

JSR A

E-ISSN: 2687-6167
Number 57
June 2024

JOURNAL OF
SCIENTIFIC REPORTS A

Journal of Scientific Reports-A, June 2024, Number 57



Galuh Dumipagar University Scientific Reports A
Educa Center Campus, Tasikmalaya Road, No. 496, 41220 Nuratapa
Phone: 02710-443 11-42
E-mail: journals@dmu.ac.id
journals.dmu.ac.id
Dumipagar University Press





Owner

On Behalf of Kütahya Dumlupınar University
Prof. Dr. Süleyman KIZILTOPRAK (Rector),
On Behalf of Institute of Graduate Studies
Assoc. Prof. Dr. Eray ACAR (Director)

Editorial Board

Önder UYSAL	Kütahya Dumlupınar University
Fatih ŞEN	Kütahya Dumlupınar University
Oktay ŞAHBAZ	Kütahya Dumlupınar University
Nevzat BEYAZIT	Ondokuz Mayıs University
Onur KARAMAN	Akdeniz University
Cafer ÖZKUL	Kütahya Dumlupınar University
Levent URTEKİN	Ahi Evran University
Ümran ERÇETİN	Kütahya Dumlupınar University
Ceren KARAMAN	Akdeniz University
Durmuş ÖZDEMİR	Kütahya Dumlupınar University
Fatih Yavuz ILGIN	Erzincan Binali Yıldırım University
Güray KAYA	Kütahya Dumlupınar University
Pelin Çağım TOKAT BİRGİN	Kütahya Dumlupınar University
Nataliia BALYTSKA	Zhytomyr State Technological University
Natalia ZUIEVSKA	National Technical University of Ukraine 'Igor Sikorsky Kyiv Polytechnic Institute'
Oksana VOVK	National Technical University of Ukraine 'Igor Sikorsky Kyiv Polytechnic Institute'
Nodor SULASHVILI	The University of Georgia
Csoknyai TAMAS	Budapest University of Technology and Economics
Tibor POOS	Budapest University of Technology and Economics
Sait ALTUN	Kütahya Dumlupınar University
Sevgi KARACA	Kütahya Dumlupınar University
Ramazan BAYAT	Kütahya Dumlupınar University
Muhammed BEKMEZCİ	Kütahya Dumlupınar University
Ayşenur AYGÜN	Kütahya Dumlupınar University
Safa DÖRTERLER	Kütahya Dumlupınar University
Seyfullah ARSLAN	Kütahya Dumlupınar University
Büşra TUTUMLU	Kütahya Dumlupınar University
Merve ARSLAN	Kütahya Dumlupınar University
Bahadır YÖRÜR	Kütahya Dumlupınar University
Naciye Nur ARSLAN	Kütahya Dumlupınar University

Journal of Scientific Reports-A started its publication life in 2000 as name of Journal of Science and Technology of Dumlupınar University and is a national peer-reviewed journal published regularly twice a year in June and December. The language of the journal is English. Articles submitted to the journal are evaluated by at least two referees who are experts in the subject and selected by the editorial board. All articles submitted to the journal are evaluated by the double-blind method. Articles submitted to our journal for review should not be previously published, accepted for publication and in the process of being evaluated for publication in another journal. All responsibility for the articles published in the journal belongs to the author(s).

The journal aims to share scientific studies carried out in the fields of science and engineering at national and international level with scientists and the public. Original research articles, review articles and short notes in science and engineering disciplines are accepted for the journal. Original research articles are expected to contain theoretical and experimental results and should not be published in other journals. In the review articles, it is expected that scientific, technological and current developments on a specific subject are reflected by using an extensive bibliography and made a satisfying evaluation of these. Short notes should be brief writings prepared to announce the first findings of an original study.

Editorial Policy

The journal is open access and the article evaluation period is between 1-2 months.

Correspondence Address: Kütahya Dumlupınar Üniversitesi Evliya Çelebi Yerleşkesi Fen Bilimleri Enstitüsü
43270 KÜTAHYA

E-mail: joursra@gmail.com

Phone: 0 274 443 19 42

Webpage: gsjsra.com

Fax: 0 274 265 20 60

Section Editors

Civil Engineering Prof. Dr. M. Çağatay KARABÖRK	Kütahya Dumlupınar University
Mechanical Engineering Prof. Dr. Ramazan KÖSE	Kütahya Dumlupınar University
Electrical-Electronics Engineering Assist. Prof. Kadir VARDAR	Kütahya Dumlupınar University
Computer Engineering Assoc. Prof. Doğan AYDIN	Kütahya Dumlupınar University
Industrial Engineering Assist. Prof. Üyesi Kerem CİDDİ	Kütahya Dumlupınar University
Mining Engineering Assist. Prof. Uğur DEMİR	Kütahya Dumlupınar University
Geology Engineering Assist. Prof. Muzaffer ÖZBURAN	Kütahya Dumlupınar University
Metallurgical and Materials Engineering Prof. Dr. İskender IŞIK	Kütahya Dumlupınar University
Food Engineering Prof. Dr. Muhammet DÖNMEZ	Kütahya Dumlupınar University
Environmental Engineering Assoc. Prof. Dr. Nevzat BEYAZIT	Ondokuz Mayıs University
Mathematics Assist. Prof. Cansu KESKİN	Kütahya Dumlupınar University
Physics Assoc. Prof. Huriye Sanem AYDOĞU	Kütahya Dumlupınar University
Chemistry Assoc. Prof. Bülent ZEYBEK	Kütahya Dumlupınar University
Biology Assist. Prof. Nüket Akalın BİNGÖL	Kütahya Dumlupınar University
Biochemistry Assoc. Prof. Derya KOYUNCU ZEYBEK	Kütahya Dumlupınar University
Occupational Health and Safety Prof. Dr. Cem ŞENSÖĞÜT	Kütahya Dumlupınar University
Software Engineering Assist. Prof. Şerif Ali SADIK	Kütahya Dumlupınar University

Advisory Board

Şükrü ASLAN	Sivas Cumhuriyet University/ Turkey
Erdal ÇELİK	Ankara Yıldırım Beyazıt University/ Turkey
Cemal PARLAK	Ege University/ Turkey
Muhammet DÖNMEZ	Kütahya Dumlupınar University/ Turkey
İhsan ÖZKAN	Konya Technical University/ Turkey
Ercan ARPAZ	Kocaeli University/ Turkey
Yavuz GÜL	Sivas Cumhuriyet University/ Turkey
Ataç BAŞÇETİN	İstanbul Technical University/ Turkey
Taner ERDOĞAN	Kocaeli University/ Turkey
Derek ABBOTT	University of Adelaide/ Australia
Kristian ALMSTRUP	Copenhagen University Hospital/ Denmark
Josette Camilleri	University of Birmingham/ UK
Yan-Ru LOU	Fudan University/ China
Ken HAENEN	Hasselt University/ Belgium
Fanming JIN	Shanghai Jiao Tong University/ China
Suneel KODAMBAKA	Florida International University/ USA
Hyoyoung LEE	Sungkyunkwan University/ Republic of Korea
Vinod TIWARI	Banaras Hindu University/ India
Sabine WURMEHL	Leibniz Institute/ Germany
Kai XIAO	Oak Ridge National Laboratory/ USA
Shahid ADEEL	Government College University/ Pakistan
J. Marty ANDERIES	Arizona State University/ USA
Ayaga BAWAH	University of Ghana/ Ghana
Lilong CHAI	University of Georgia/ USA
Idiano D'ADAMO	Sapienza University of Rome/ Italy
Sanjit DEB	Texas Tech University/ USA
Caroline HACHEM-VERMETTE	University of Calgary/ Canada
Marlia Mohd HANAFIAH	The National University of Malaysia/ Malaysia
Nick HOLDEN	University College Dublin/ Ireland
Chang-Wei HU	Sichuan University/ China
Masashi KATO	Nagoya University/ Japan
Tafadzwanashe MABHAUDHI	University of KwaZulu-Natal/ South Africa
Mubarak MUJAWAR	Universiti Teknologi Brunei/ Brunei
Nidhi NAGABHATLA	United Nations University CRIS/ Belgium
Gunnar SEIDE	Maastricht University/ Netherlands
Jonathan Wong	Hong Kong Baptist University/ Hong Kong
Yenchun Jim WU	National Waiwan Normal University/ Taiwan
Jie ZHUANG	University of Tennessee/ USA

JOURNAL OF SCIENTIFIC REPORTS-A
E-ISSN: 2687-6167

CONTENTS

RESEARCH ARTICLES

- Studies for alternative anti-caking additives used in the production of ammonium nitrate* 1-11
Burak LOK, Meric GEDİKAĞAOĞLU, Cengiz YENİKAYA*, Fatih ŞEN*
- Unified voice analysis: speaker recognition, age group and gender estimation using spectral features and machine learning classifiers* 12-26
Kaya Akgün, Şerif Ali SADIK*
- Non-linear behavior of functionally graded elastoplastic beam under torsion* 27-50
Murat KARACA, Bahadır ALYAVUZ*
- Tribological and mechanical performance evaluation of hybrid reinforced copper composites* 51-67
Esad KAYA, Pelin Çağım TOKAT_BİRGİN*
- A research on the production, storage and germination of synthetic seeds in tea plant (Camellia sinensis [L.] O. Kuntze)* 68-80
Begüm GÜLER*, Aynur GÜREL
- The effect of foundation type selection on approximate cost of reinforced concrete buildings: the role of soil classes and number of floors* 81-96
Uğur KAFKAS*
- A hybrid approach to obesity level determination with decision tree and pelican optimization algorithm* 97-109
Nagihan YAĞMUR*
- Synthesis, characterization, and investigation of antibacterial and antifungal properties of salt and metal complexes of 2-amino-5-chloropyridine and 2,6-pyridinedicarboxylic acid* 110-120
Ayşe POLAT*, Halil İLKİMEN, Beyza YILMAZ, Elif YURT, Aysel GÜLBANDILAR

<i>Conway-Maxwell-Poisson profile monitoring with rk-Shewhart control chart: a comparative study</i> Ulduz MAMMADOVA*	121-132
<i>Examination of the effect of ANN and NLPCA technique on prediction performance in patients with breast tumors</i> Canan DEMİR*	133-143
<i>Chemical structure and characterization of bio-oils isolated from walnut shells by different processes</i> Yunus BAŞAR, Mehmet Salih NAS, Mehmet Hakkı ALMA, İbrahim DEMİRTAŞ, Mehmet Harbi ÇALIMLI*	144-152
<i>Investigation of the alloying elements effect in the flux-cored wire and submerged arc welding flux combination</i> Erhan ÖZKAN*	153-168



Contents lists available at *Dergipark*

Journal of Scientific Reports-A

journal homepage: <https://dergipark.org.tr/pub/jsr-a>



E-ISSN: 2687-6167

Number 57, June 2024

RESEARCH ARTICLE

Receive Date: 18.01.2023

Accepted Date: 14.03.2023

Studies for alternative anti-caking additives used in the production of ammonium nitrate

Burak Lok^a, Meric Gedikagaoglu^b, Cengiz Yenikaya^{*c}, Fatih Sen^{*d}

^aİGSAŞ Kütahya Factory R&D Center, Çalca Mh. Eskişehir Karayolu Bul No:89 43100, Kütahya, Türkiye, ORCID:0000-0002-1439-2805

^bİGSAŞ Kütahya Factory R&D Center, Çalca Mh. Eskişehir Karayolu Bul No:89 43100, Kütahya, Türkiye, ORCID:0000-0001-7503-3665

^cKütahya Dumlupınar University, Graduated Institute, Department of Chemistry, Kütahya, Türkiye, ORCID:0000-0002-5867-9146

^dKütahya Dumlupınar University, Graduated Institute, Department of Chemistry, Kütahya, Türkiye, ORCID:0000-0001-9929-9556

Abstract

In the production of ammonium nitrate, powdered, caking, and grain size to the desired standards cause great problems in prilling and granulation processes. In this study, the problems of caking were discussed in the final product in ammonium nitrate production. Additives are added at certain stages of production to reduce and eliminate the problems of caking. The product is usually passed through a drum where it is fed with anti-caking additives with the help of a dosing system before the packaging process. At the next stage, it is stored under appropriate conditions and placed on the market.

In this study, mixtures containing different components, petroleum-derived chemicals (liquid and solid paraffin), and inorganic salts were formed, and their physical properties were determined by standard analysis methods. A quick caking measurement test was performed by dosing operations providing ammonium nitrate product remained within the range standard specifications. For the ammonium nitrate product without anti-caking agent dosage, the caking percentage was determined as 68.27%. The commercial anti-caking agent is dosed at a rate of 0.05% and has 40.84%, a 0.10% caking ratio of 39.05%. In the final product, caking was reduced by 29.22%. Six prescriptions based on ANO, a petroleum-derived chemical, were prepared (R17-R22). Effective results were obtained in commercial product comparison in ANO mold caking performance tests. While the % caking ratio of R18 is 15.33 according to the 1:1000 dose amount, this value is 13.07% for the commercial anti-caking agent.

The study was completed by identifying the mixtures that give the best results.

© 2023 DPU All rights reserved.

Keywords: ammonium nitrate, agglomeration, pollution, prilling process, granulation.

* Corresponding author. phone.: +90-5059184498

E-mail address: fatihsen1980@gmail.com, cengiz.yenikaya@dpu.edu.tr

1. Introduction

Ammonium nitrate is a chemical compound with the formula NH_4NO_3 . It is a white crystalline solid composed of ammonium and nitrate ions. Although it does not hydrate as a hygroscopic solid, it is very soluble in water. It is mainly used as a high-nitrogen fertilizer in agriculture. Another important use is as a component of explosives (ANFO) mixtures used in mining, quarrying, and building construction. ANFO is ammonium nitrate impregnated with fuel oil [1].

In our country, ammonium nitrate is produced in high capacities by companies such as İGSAŞ İstanbul Fertilizer Industry Inc., BAGFAŞ Bandırma Fertilizer Factories Inc., Toros Tarım Inc., and Gemlik Fertilizer Inc.

The raw material of ammonium nitrate is ammonia and nitric acid. In industry, nitric acid production begins with the combustion of ammonia over platinum-rhodium-palladium catalysts in ammonia combustion reactors to form nitrogen monoxide. At high temperatures, nitrogen monoxide gases from the ammonia combustion reactors first pass through the cascade heat exchangers. The next operation of the process is the oxidation stage. In the oxidation phase, nitrogen monoxide is oxidized by oxygen and converted to nitrogen dioxide. After the oxidation operation, nitrogen dioxide is absorbed with water, and nitric acid is produced. The production of ammonia, another raw material, starts with the reaction of natural gas in the steam reformer reactor, releasing hydrogen, carbon dioxide, carbon monoxide, hydrogen sulfide, and trace amounts of hydrocarbon gases ($\text{CH}_4 + \text{H}_2\text{O} \rightarrow \text{CO} + 3\text{H}_2$). Hydrogen sulfide is separated from the syngas by desulfurization. Carbon monoxide is oxidized to carbon dioxide. Carbon dioxide is sent to the urea plant for urea production. The remaining hydrogen is reacted with nitrogen from the air separation unit to produce ammonia.

Ammonium nitrate (AN) was first prepared in the 16th century. Its early industrial development was primarily for use in explosives. Its use as a fertilizer developed rapidly in the 1940s. Ammonium nitrate is mainly produced by the reaction of gaseous ammonia with aqueous nitric acid [2]. The production of ammonium nitrate begins with the formation of ammonium nitrate solution after 78 % conversion of ammonia and nitric acid in a 1:1 ratio in a stoichiometric reactor at a temperature of approximately 3.5 bar and 180 °C. Then, 78 % by mass of ammonium nitrate solution is sent to the first evaporation stage. In the first evaporation, 78 % by mass of ammonium nitrate is concentrated and increased to 95 % concentrations. In this process, waste steam from the reactors is fed to the evaporators. In the second evaporation, 95 % ammonium nitrate solution is concentrated and increased to 99 % concentration. 99 % ammonium nitrate solution is sent to the prill tower for prilling. The ammonium nitrate sprayed down from the tower takes the form of prill. Afterward, it is presented to the market by physical processes such as drying, cooling, dosing, and packaging.

Agglomeration occurs with the help of either natural forces or applied forces. For example, if it rains on a dusty road, the wet dust sticks together and then the dust stays stuck to each other even if the water evaporates and escapes from the environment. Here, water has created a natural agglomeration force [3].

The caking of ammonium nitrate fertilizer (ANG) is agglomeration and occurs with the effect of one or the other or both of the above two groups of forces [4]. The main ingredient used to make ammonium nitrate fertilizers is ammonium nitrate. However, at room temperature it exhibits some undesirable physicochemical properties, including hygroscopicity and phase change, resulting in an undesirable agglomeration phenomenon. Incineration changes the properties of the fertilizer, resulting in material loss. As a result, both the producer and the end customer suffer financial losses. Currently, anti-caking chemicals are the best approach to prevent fertilizers from clumping. Depending on the type of fertilizer and the anti-caking agent, the finished fertilizer granules are sprayed with the required amounts of these substances [5].

Most fertilizers tend to clump or clump (caking) during storage. The caking mechanism in fertilizers is mostly attributed to the formation of salt bridges and/or capillary adhesion. The severity of agglomeration can be affected by several factors including chemical composition, moisture content, particle structure, mechanical strength, hygroscopic properties, product temperature, ambient conditions, storage time, and storage pressure. Various methods of reducing or eliminating caking in fertilizers mainly involve process control, storage/packaging conditions, and/or the addition of anticaking agents [6].

The fact that fertilizers have a propensity to clump together while being transported and stored is one of the biggest issues facing the industry. Interaction between solid fertilizer particles at their places of contact leads to agglomeration. Certain fertilizer characteristics and environmental factors trigger these interactions, also known as contact mechanisms. An essential area of study that guarantees the use of the anti-caking mechanism while also having a direct impact on the end product's quality and financial worth [7].

To lessen hygroscopicity, a physical coating technique was created to replace the surface of ammonium nitrate particles with various surfactants. The surfactants that were employed were tetradecyl amine, dodecyl amine, tetradecanoyl, palmitic acid, lauric acid, stearic acid, and stearyl alcohol. Tests were conducted on the hygroscopicity of coated and uncoated ammonium nitrate [8].

Granular fertilizers have a tendency to clump when being stored, particularly those based on ammonium nitrate (AN). The goal was to create efficient anti-caking coatings for fertilizers containing ammonium nitrate while simultaneously enhancing fertilizer quality and perfecting the anti-caking coatings' composition. Response surface methodology (RSM) employing Box-Behnken design (BBD) was used to examine the impact of the manufactured organic coatings' composition on the anti-caking efficacy of fertilizers. Furthermore, the impact of the created anti-caking agents on the quality of the fertilizer was assessed by gauging the granules' crushing strength [9].

The flocculation of calcium ammonium nitrate (CAN) fertilizer, the flocculation mechanism, the factors causing caking, and remedial measures are discussed. The two theories regarding the aggregation mechanism are the capillary adhesion theory and the crystal bridging theory. Factors affecting caking are humidity, external humidity, the physical shape of the product, calcium nitrate formation, thermal shocks, heap height in storage, temperature fluctuation range, inefficient product conditioning, and seamless linings in bags. Anti-caking agents used to coat fertilizer particles to reduce caking are of two types: inert and active. The first includes finely divided powders such as clays or talc, and the second includes surfactants and water-resistant materials. Primary fatty amines play a key role in the anti-caking treatment of CAN [10].

Caking of Ammonium Nitrate Fertilizer (ANG); It is an agglomeration event caused by some factors, especially humidity, temperature, and pressure, from time to time in factory and customer warehouses.

This fertilizer; is produced as granules (grain) for reasons such as storage, filling, transportation, and agricultural application convenience, prevention of deterioration, and keeping waste at a low level. It has long been known to the research bodies of the manufacturing companies that caking shows some differences depending on whether the filler is limestone dolomite or another inert material. Many research attempts to eliminate petrification have either been hidden as private secrets of the relevant factories or have been patented and both legally secured and turned into a means of earning for the relevant organization.

It can be said that studies on this subject continue even today. For this reason, it is a research principle to always try to achieve better results with good results. The subject of this article is a new-generation product development study to be used in the anti-cake dosing process, which is a physical operation. Organic and inorganic materials were used in the studies. Anti-caking agent mixtures were formed with paraffin forms, which are organic substances.

Finally, samples made with a mixture of commercial product ANO, stearic acid, and naphthalene derivative chemicals (SNS) were applied to ammonium nitrate and effective results were observed. Istanbul Fertilizer Industry Inc. The commercial anticaking agent used in the ammonium nitrate plant and the samples made in the study were compared.

2. Experimental Studies

In this study, mixtures containing different components preventing the caking of ANG were formed from petroleum-derived chemicals (liquid and solid paraffin) and mixtures containing inorganic salts under laboratory conditions.

Experimental studies consist of five main steps;
Prescription Preparation Phases
Physical Determination and Comparison Studies

Suggestion and Preparation of New Prescriptions
Application of Appropriate Prescription
Measuring Cake Performance in the Final Product

2.1. Materials and methods

Anti-caking chemicals [11] used during the studies were provided in analytical and technical purity. Anti-caking mixtures were prepared by using these chemicals in different ratios. The commercial anti-caking agent used in the Ky 230 Fertilizer Plant was analyzed (Table 2.1). It was tried to find the product closest to the physical properties of the commercial product from the anti-cake agent mixtures with appropriate content prepared in the studies.

Table 2.1. Commercial Product Properties Used as Anti-Caking Agent.

Ingredients	Color	Density(g/cm ³)	Pour Point °C ASTM D97	Melting Point °C ASTM D127	Viscosity cSt ASTM D721	Oil Content % ASTM D127
Commercial Anticaking Agent	Dark Brown	0.83	38-41	66-77	Max 30	-

2.1.1. Chemicals

2.1.1.1. Ammonium nitrate

The ammonium nitrate used in the experiments and produced in our facility was taken from the dryer trammel outlet of the production. The reason why it is taken from this stage is that anti-caking agent dosing has not been performed yet. The product temperature is high at this point (90-110 °C). In the experiments, the product was used for cooling.

2.1.1.2. Solid paraffin

Paraffin wax (or petroleum wax) is a soft, colorless solid obtained from petroleum, coal, or oily things, consisting of a mixture of hydrocarbon molecules containing 20 to 40 carbon atoms. It is solid at room temperature and begins to melt above about 37 °C (99 °F) [12]. It differs from kerosene and other petroleum products, sometimes called paraffin [13]. The solid paraffin product obtained from Merck in granular form was used at high rates in the prepared mixtures. For this alkane with a high carbon number, a melting process was applied in the experiments.

2.1.1.3. Liquid paraffin

Liquid paraffin, also known as paraffin oil, liquid paraffin oil, or Russian mineral oil, is a highly refined mineral oil used in cosmetics and medicine. Cosmetic or medical liquid paraffin should not be confused with paraffin (ie kerosene) used as a fuel. The generic meaning of paraffin, meaning alkane, has led to regional differences in the meanings of both paraffin and paraffin oil. It is a transparent, colorless, almost odorless, and oily liquid consisting of saturated hydrocarbons derived from petroleum. This product, which is supplied by Merck in liquid form, has been used at a high rate in the prepared mixtures. No melting process was applied for this alkane with a low carbon number.

2.1.1.4. ANO material

ANO material, which is a commercial product, is the material that has the closest physical properties to the anti-caking agent product and liquid paraffin applied in the enterprise. Its pour point is 40 °C, flash point is 200 °C.

2.1.1.5. SNS material

For this naphthalene-derived chemical, which is used as a porous agent in the production of PPAN (Prill Porous Ammonium Nitrate), data on reducing caking were obtained in previous GPAN (Granular Porous Ammonium Nitrate) studies. Since it is an organic substance, it can be easily dissolved in ANO and paraffin substances.

2.1.1.6. Stearic acid

Stearic acid is obtained from fats and oils by saponification of triglycerides using hot water (approximately 100 °C). The resulting mixture is then distilled [14]. Commercial stearic acid is usually a mixture of stearic and palmitic acids, although purified stearic acid is available. Commercially, oleic acid found in dates and soybeans can be hydrogenated to yield stearic acid. Stearic acid, a plasticizer, has been used for pour point adjustment in studies.

2.1.1.7. Other inorganic salts

Both by powdering and before the prilling phase, they are added to the ammonium nitrate solution and added to the prepared anti-caking agent mixtures at certain rates, since they increase the strength of the product. These chemical salts; are sodium bisulfite, potassium sulfate, potassium hydroxide, ammonium sulfate, sodium phosphate, calcium nitrate, magnesium nitrate, and magnesium oxide.

2.1.2. Methods

In the preparation phase of anti-sealing agent mixtures with different compositions, a magnetic heater mixer with a digital display was used. A kinematic viscosity bath, oil content solvent extraction tester in waxes drop melting point tester, and internally cooled pour point tester were used to be used in physical determinations. Air spray guns and pipette, spray nozzles were used in spray experiments. A pilot drum with speed and angle adjustment was used to simulate the anti-slip drum used in the enterprise. Finally, a caking oven was used for caking performance measurements.

2.2. Experimental methods

Physical determinations in the studies were made according to ASTM standards. After the appropriate products were prepared, a certain amount of ammonium nitrate without additives was placed in the pilot drum (trammel), which simulates the operation in the enterprise, and the dosing process was carried out with the help of a spray gun and pipette. Finally, the caking performance of the ammonium nitrate samples, which were coated with an anticaking agent, was measured by using a caking oven and by applying the rapid caking method.

2.3. Rapid cake tests method

The rapid caking test method is a method used in IGSAŞ Central Laboratory. The sample is taken 300 grams in special stainless-steel containers. The lid of the stainless-steel container is closed. 300 grams of mass is put on it. It is then placed in the caking oven. The caking oven starts its process cycle at 15 °C, the temperature rises to 40 °C within 1 hour. The temperature drops again from 40 °C to 15 °C and thus the oven has made 1 cycle. 1 cycle is about 2.4 hours. By making 10 cycles in one day, the sample is quickly caked. At the end of 1 day, the sample is taken out

of the oven. The caking mass is weighed. The caking percentage is calculated. In cases where caking is not observed, the processes are repeated.

2.4. Recipe preparation

In the study, 22 different prescriptions were created. 8 of them are based on solid paraffin, 8 are based on liquid paraffin, and 6 are based on ANO. In the tables (2.2-2.4), recipe contents are given as percent by mass.

Table 2.2. Solid paraffin-based Recipes (R1 – R8)

Recipe No	Physical Appearance	Solid Paraffin %	Stearic Acid %	Sodium bi sulfide %	Potassium Sulfate %	Potassium Hydroxide %	Ammonium Sulfate %	Sodium Phosphate %	Calcium Nitrate %	Magnesium Nitrate %	Magnesium Oxide %	SNS %	Total %
R1	Solid	60	30	10	-	-	-	-	-	-	-	-	100
R2	Solid	60	20	10	10	-	-	-	-	-	-	-	100
R3	Solid	60	10	10	10	10	-	-	-	-	-	-	100
R4	Solid	60	5	10	10	10	5	-	-	-	-	-	100
R5	Solid	60	-	-	-	-	30	10	-	-	-	-	100
R6	Solid	60	-	-	-	-	20	10	10	-	-	-	100
R7	Solid	60	-	-	-	-	10	10	10	10	-	-	100
R8	Solid	60	-	-	-	-	5	10	10	10	5	5	100

Depending on the prescriptions, some inferences were made based on the observations made during the preparation phase. For example, NH_3 output in R5 and R6 was sensed by smell. The reason for this is thought to be the degradation of ammonium sulphate with sodium phosphate. Since the ammonium sulphate ratio is low in R7 and R8, even if NH_3 was formed, its smell was not felt. In recipe 6, calcium nitrate was not homogenized in solid paraffin. Non-homogenized mixtures are also not very suitable for spraying. However, these products were subjected to physical determinations (pour point, melting point, oil content, density, and viscosity) in subsequent studies. In these mixtures with a high solid paraffin ratio, (R1-R8) samples with a melting point around solid paraffin (80°C) (Table 2.5) are not considered suitable for spraying applications, which is the third phase of the trials. The reason for this is that in the application of these recipes as anti-caking agents, the operating cost for the industrial facility will be higher than the commercial anti-caking agent and other recipes. At the same time, there is a homogenization problem in these recipes. The melting points of the products were determined qualitatively based on observations and measurements (Table 2.5). As a result, R1-R8 prescriptions were not found suitable.

Recipes (R9-R16) prepared with liquid paraffin and related components are given in Table 2.3.

Table 2.3. Liquid paraffin-based Recipes (R9 – R16)

Recipe No	Physical Appearance	Liquid Paraffin %	Stearic Acid %	Sodium bi sulfide %	Potassium Sulfate %	Potassium Hydroxide %	Ammonium Sulfate %	Sodium Phosphate %	Calcium Nitrate %	Magnesium Nitrate %	Magnesium Oxide %	SNS %	Total %
R9	Solid	60	30	10	-	-	-	-	-	-	-	-	100
R10	Solid	60	20	10	10	-	-	-	-	-	-	-	100
R11	Liquid	60	10	10	10	10	-	-	-	-	-	-	100

R12	Liquid	60	30	-	-	-	-	-	-	-	-	10	100
R13	Liquid	60	20	-	-	-	-	-	-	-	-	20	100
R13.1	Liquid	60	25	-	-	-	-	-	-	-	-	15	100
R14	Liquid	60	10	-	-	-	-	-	-	-	-	30	100
R15	Liquid	60	-	-	-	-	-	-	-	-	-	40	100
R16	Solid	50	30	-	-	-	-	-	-	-	-	20	100

2.5. Physical Determination and Comparison Studies

Physical determinations were performed on the prepared recipes according to ASTM standards. Viscosity determinations were determined according to the ASTM D445 standard [15]. Density determinations were measured in g/cm^3 with the help of a simple measuring tape.

Melting point determinations were determined with the help of a drop melting point test device according to ASTM D127 standards [16].

Pour point determinations were made with a pour point tester by ASTM D97 standard [17].

Table 2.4. Physical Properties of Anticaking Agents.

Ingredients	Physical Appearance	Color	Density(g/cm^3)	Pour Point °C ASTM D97	Melting Point °C ASTM D127	Viscosity cSt ASTM D721	Oil Content % ASTM D127
Commercial Anticaking Agent	Liquid	Dark Brown	0.83	38-41	66-77	Max 30	-
R1	Solid	White	0.50	47-50	51-57	-	-
R2	Solid	White	0.55	49-52	54-61	-	-
R3	Solid	White	0.55	52-55	58-62	-	-
R4	Solid	White	0.62	54-57	58-62	-	-
R5	Solid	White	0.59	53-56	56-61	-	-
R6	Solid	White	0.49	51-54	54-58	-	-
R7	Solid	White	-	-	-	-	-
R8	Solid	White	0.80	54-57	57-61	-	-
R9	Liquid	White	0.72	54-57	-	-	-
R10	Liquid	White	0.82	55-58	-	-	-
R11	Liquid	Light Brown	-	-	-	-	-
R12	Liquid	Light Brown	0.88	52-55	-	-	-
R13	Liquid	Light Brown	0.76	50-53	-	-	-
R13.1	Liquid	Light Brown	0.81	38-41	-	-	-
R14	Liquid	Light Brown	0.89	33-36	-	-	-
R15	Liquid	Light Brown	0.94	-7—4	-	-	-
R16	Solid	Light Brown	0.93	8-10	-	-	-
R17	Solid	Dark Brown	1.06	50	50-55	-	-
R18	Liquid	Dark Brown	1.00	35	-	-	-
R19	Liquid	Dark Brown	0.91	36	-	-	-
R20	Liquid	Dark Brown	0.89	38	-	-	-
R21	Liquid	Dark Brown	0.89	40	-	-	-
R22	Liquid	Dark Brown	0.88	41	-	-	-

2.6. Suggestion and preparation of new prescriptions

Depending on the prescriptions, some inferences were made based on the observations made during the

preparation phase. After prescriptions 9,10,11, the contents of the prescription were evaluated. By selecting the key compounds in the commercial product, recipes 13-22 were prepared with three components (ANO, Stearic acid, SNS). As a result of the trials on liquid paraffin and ANO-based recipes, products physically close to the commercial product were obtained. It was decided that the fourth component could be urea in terms of providing the ammine requirement. For color compatibility, the possibility of the fifth component being molasses was considered. A recipe containing molasses and urea was prepared. However, since homogenization could not be achieved, it was removed, and the use of molasses was abandoned.

Commercial product ANO material with the same properties was used instead of liquid paraffin. Recipes were prepared with ANO substance, stearic acid, and SNS. ANO-based prescriptions are given in Table 2.5.

Table 2.5. ANO based Recipes (R17-R22).

Recipe No	Physical Appearance	ANO %	Stearic Acid %	Sodium bi sulfide %	Potassium Sulfate %	Potassium Hydroxide %	Ammonium Sulfate %	Sodium Phosphate %	Calcium Nitrate %	Magnesium Nitrate %	Magnesium Oxide %	SNS %	Total %
R17	Solid	60	35	-	-	-	-	-	-	-	-	5	100
R18	Liquid	60	30	-	-	-	-	-	-	-	-	10	100
R19	Liquid	60	25	-	-	-	-	-	-	-	-	15	100
R20	Liquid	60	20	-	-	-	-	-	-	-	-	20	100
R21	Liquid	60	15	-	-	-	-	-	-	-	-	25	100
R22	Liquid	60	10	-	-	-	-	-	-	-	-	30	100

2.6. Application of appropriate prescriptions

22 samples (solid paraffin-based, liquid paraffin-based, ANO-based) prepared in section 2.4 were applied on ammonium nitrate by the operating dosing amounts (400 L/min) in this section. A pilot drum device was used in the experiments.

A pilot drum device was specially manufactured for these trials. This device is the prototype of the Anti-cake trammel at the Ky-230 Plant. The pilot drum device has features such as speed adjustment, direction adjustment, and angle adjustment. The pilot drum device is made of 316 L stainless steel considering the corrosive properties of ammonium nitrate.

Ammonium nitrate product without any additive applied after the dryer equipment of the Ky-230 Plant was used in the experiments for the application of appropriate recipes. In these studies, 5000 grams of ammonium nitrate without anti-caking was weighed and placed in the pilot drum device. The device was operated by adjusting the speed and angle settings. After 15 minutes, approximately 100 grams of samples are taken from the samples, brought to the appropriate dosing temperature under operating conditions (80 °C), and ammonium nitrate is placed in the pilot drum with an automatic pipette at the rates determined according to the operating conditions (these rates are in the form of the amount of anticaking agent/amount of AN, gram Doses applied in /gram were 1/1000 (0.1%), 2.5/1000 (0.25%) and 5/1000 (0.5%) sprayed. Trials were completed for all samples by providing a homogeneous mixture. Antique ammonium nitrate samples were taken and tested for caking performance in the final product.

2.7. Measuring cake performance in the final product

In this part of the study, caking performances for all samples are shown in Section 2.3. It was determined with the

help of the Rapid Stuttering Test Method in The caking performance measurements for R13.1 and R18-22 recipes are given in Tables 2.6 and 2.7, respectively

Table 2.6. Caking Performance for Recipe 13.1

Sample Dozing (%)	Caking Material (g)	Caking Percent (%)
0	204.80	68.27
0.05	122.52	40.84
0.10	117.14	39.05

Table 2.7. Caking Performance Results for ANO-based materials, Commercial Anticaking Agents and Ammonium Nitrate

No	Name and No	Dosage Amount (%)	Caking Material (g)	Caking Percent (%)
-	Ammonium Nitrate	-	204.80	68.27
-	Ammonium Nitrate	-	211.60	70.53
-	Ammonium Nitrate	-	209.84	69.95
-	Commercial Anticaking Agent	0.10	39.20	13.07
-	Commercial Anticaking Agent	0.25	38.12	12.71
-	Commercial Anticaking Agent	0.50	37.22	12.41
R18	Sample 18	0.10	45.98	15.33
R18	Sample 18	0.25	35.84	11.95
R18	Sample 18	0.50	28.20	9.41
R19	Sample 19	0.10	64.69	21.56
R19	Sample 19	0.25	64.15	21.38
R19	Sample 19	0.50	54.37	18.12
R20	Sample 20	0.10	51.59	17.20
R20	Sample 20	0.25	42.42	14.14
R20	Sample 20	0.50	32.32	10.77
R21	Sample 21	0.10	54.94	18.31
R21	Sample 21	0.25	47.56	15.85
R21	Sample 21	0.50	26.70	8.90
R22	Sample 22	0.10	73.26	24.42
R22	Sample 22	0.25	92.78	30.93
R22	Sample 22	0.50	92.46	30.82

3. Conclusions and Suggestions

In this study, alternative mixtures were prepared to eliminate caking, which is an important problem in ammonium nitrate production. Physical analyses were made for the anticaking agent currently used in the Ky-230 Fertilizer Plant. By carrying out literature studies [18] and reverse engineering studies, anti-caking agent mixtures were formed in appropriate compositions.

In the light of physical determinations, the density of the prescriptions made with solid paraffin material is lower than the anti-caking agent currently used. While the density for the currently used anticaking agent is 0.83 g/cm³, the

density in the recipes prepared with solid paraffin remained in the range of 0.49-0.62 g/cm³. Melting points are not at the desired level. For the existing anticaking agent, which is in the range of 66-77 °C, this value remained in the range of 51-62 °C in recipes prepared with solid paraffin. At the same time, the pour points are higher than the commercial anticaking agent (47°C-54°C) according to the pour point determinations made according to the ASTM D97 standard. The anticaking agent pour point value is in the range of 38 °C-41 °C. Table 2.2 Samples prepared with solid paraffin were not applied to ammonium nitrate as they did not have the desired properties as a result of physical analysis.

Density values for the samples prepared with liquid paraffin were close to the anticaking agent used in the enterprise (0.88-0.94 g/cm³). The pour point value varied according to the stearic acid ratio in the samples prepared with liquid paraffin. As the stearic acid ratio increased on the samples, the pour point also increased (Table 2.4). The caking performance test was applied for recipe 13.1, whose physical properties were closest to the commercial product (Table 2.6).

According to the values in the table, while the percentage of caking was 68.27 % for the undosed ammonium nitrate product, 40.84 % caking was observed at a 0.05 % dosage rate and 39.05 % at the rate of 0.10 %. The caking was reduced by 29.22 %.

Six recipes based on ANO were prepared (R17-R22). Physical determinations were applied to the samples. Their densities are close to 0.88-1.00 g/cm³ of commercial product. The R17 is in solid physical appearance. The caking test was not applied due to commercial concerns. R18-22 is in the liquid phase. For R18-22, caking performance tests were performed for the available commercial anticaking agent and ant exhaust ammonium nitrate (Table 2.7).

ANO-based samples gave effective results in caking performance tests compared to the commercial product. While the % caking rate of R18 is 15.33 according to 1/1000 dosage amount, this value is 13.07% for commercial anti-caking agents. As the dosage amount increased, caking decreased in the ammonium nitrate sample applied to recipe 18. It gave more effective results than the commercial product. In the ammonium nitrate product, the dosing standard is a maximum of 0.125 % under operating conditions. Doses applied above this value deteriorate the product specifications (moisture, density, etc.) of the ammonium nitrate product supplied to the market. However, despite this, the reason for applying high dosages in this study is to observe the effect of samples on ammonium nitrate caking in wide ranges. Much research has been done on Ammonium Nitrate caking. The different aspect of this study is that all of the experiments covering the study were carried out in the factory that produces ammonium nitrate. The products have been tested in laboratory and production applications, and by obtaining effective results, contributions have been made to the literature and the archives of the institution.

Conflict of Interest

The authors declare that they have no conflict of interest.

Author Contributions

Conceptualization, B.L., and M.G., and F.S.; formal analysis, B.L., M.G., C.Y., and F.S.; investigation, B.L., and M.G; resources, B.L., and F.S., writing-original draft preparation, C.Y., and F.S.; writing-review and editing, C.Y., and F.S.; supervision. All authors have read and agreed to the published version of the manuscript.

Acknowledgment

TÜBİTAK TEYDEB PRESIDENCY for the project numbered 3190751 and would like to thank Yıldızlar Investment Holding.

References

[1] Z. Karl-Heinz, W. Karl-Heinz, S. Manfred, S. Kimihiko, S. Herbert, Z. Werner, C. Ruthild and L. Herbert., "Ammonium Compounds," in

Ullmann's Encyclopedia of Industrial Chemistry, Wiley, 2000. doi: 10.1002/14356007.a02_243

[2] "Ammonium Nitrate," in *Synthetic Nitrogen Products*, Boston: Kluwer Academic Publishers, pp. 251–265.

[3] F. Patat, "Ullmanns Enzyklopädie der technischen Chemie," *Zeitschrift für Elektrochemie, Berichte der Bunsengesellschaft für Phys. Chemie*, vol. 60, no. 9–10, pp. 1207–1208, Nov. 1956, doi: 10.1002/bbpc.19560600957.

[4] Kirk Othmer, *Encyclopedia of Chemical Technology*, vol. 22. 2004.

[5] A. Tyc, S. Penkala, Ma. Biegun, and D. Niewes, "The effectiveness of commercial anticaking agents for ammonium nitrate fertilizers," *Ecol Chem Eng A.*, vol. 26, no. (1-2), pp. 127–135, 2019, doi: 10.2428/ecea.2019.26(1-2)11.

[6] D. W. Rutland, "Fertilizer caking: Mechanisms, influential factors, and methods of prevention," *Fertil. Res.*, vol. 30, no. 1, pp. 99–114, Oct. 1991, doi: 10.1007/BF01048832.

[7] A. Ulusal and C. Avsar, "Understanding Caking Phenomena in Industrial Fertilizers," *Chem. Biochem. Eng. Q.*, vol. 34, no. 4, pp. 209–222, 2021, doi: 10.15255/CABEQ.2020.1866.

[8] B. I. Elzaki and Y. J. Zhang, "Surface modification of ammonium nitrate by coating with surfactant materials to reduce hygroscopicity," *Def. Technol.*, vol. 15, no. 4, pp. 615–620, Aug. 2019, doi: 10.1016/j.dt.2019.01.004.

[9] A. Tyc, D. Nieweś, E. Pankalla, M. Huculak-Mączka, K. Hoffmann, and J. Hoffmann, "Anti-Caking Coatings for Improving the Useful Properties of Ammonium Nitrate Fertilizers with Composition Modeling Using Box–Behnken Design," *Materials (Basel)*, vol. 14, no. 19, p. 5761, Oct. 2021, doi: 10.3390/ma14195761.

[10] M. Ahmed, "Caking of CAN fertilizer & its prevention.," *J. Technol. Dev.*, vol. 15, no. 1, pp. 75–84, 1990.

[11] K. PI, "Non-Caking Fertilizers from Ammonium Nitrate and Supplementary Nutrients," *J. Univ. Chem. Technol. Metall.*, vol. 40, no. 3, pp. 209–212, 2005.

[12] M. Freund, R. Csikós, S. Keszthelyi, and G. Y. Mózes, "Paraffin Products Properties, Technologies, Applications," *Paraffin Prod. Technol. Appl.*, vol. Volume 14, p. 337, 1982.

[13] C. B. Willingham, W. J. Taylor, J. M. Pignocco, and F. D. Rossini, "Vapor pressures and boiling points of some paraffin, alkylcyclopentane, alkylcyclohexane, and alkylbenzene hydrocarbons," *J. Res. Natl. Bur. Stand. (1934)*, vol. 35, no. 3, p. 219, Sep. 1945, doi: 10.6028/jres.035.009.

[14] F. Sharif, E. Crushell, K. O'Driscoll, and B. Bourke, "Liquid paraffin: a reappraisal of its role in the treatment of constipation," *Arch. Dis. Child.*, vol. 85, no. 2, pp. 121–124, Aug. 2001, doi: 10.1136/adc.85.2.121.

[15] Anonim, "ASTM D445-19 Standard Test Method for Kinematic Viscosity of Transparent and Opaque Liquids (and Calculation of Dynamic Viscosity)," 2021.

[16] ASTM D127-08 - Standard Test Method for Drop Melting Point of Petroleum Wax, Including Petrolatum. 2021.

[17] ASTM D97-11 - Standard Test Method for Pour Point of Petroleum Products. 2021.

[18] Anonim, *TÜGSAŞ İşletme Bültenleri*. 1964.



Contents lists available at *Dergipark*

Journal of Scientific Reports-A

journal homepage: <https://dergipark.org.tr/pub/jsr-a>



E-ISSN: 2687-6167

Number 57, June 2024

RESEARCH ARTICLE

Receive Date: 19.01.2024

Accepted Date: 12.02.2024

Unified voice analysis: speaker recognition, age group and gender estimation using spectral features and machine learning classifiers

Kaya Akgün^a, Şerif Ali Sadık^{b*}

^a*Kütahya Dumlupınar University, Faculty of Engineering, Computer Engineering Dept., 43100, Kütahya, Türkiye, ORCID: 0000-0001-5678-9643*

^b*Kütahya Dumlupınar University, Faculty of Engineering, Software Engineering Dept., 43100, Kütahya, Türkiye, ORCID: 0000-0003-2883-1431*

Abstract

Predicting speaker's personal traits from voice data has been a subject of attention in many fields such as forensic cases, automatic voice response systems, and biomedical applications. Within the scope of this study, gender and age group prediction was made with the voice data recorded from 24 volunteers. Mel-frequency cepstral coefficients (MFCC) were extracted from the audio data as hybrid time/frequency domain features, and fundamental frequencies and formants were extracted as frequency domain features. These obtained features were fused in a feature pool and age group and gender estimation studies were carried out with 4 different machine learning algorithms. According to the results obtained, the age groups of the participants could be classified with 93% accuracy and the genders with 99% accuracy with the Support Vector Machines algorithm. Also, speaker recognition task was successfully completed with 93% accuracy with the Support Vector Machines.

© 2023 DPU All rights reserved.

Keywords: Gender estimation; Age group estimation; Speaker recognition; Support vector machine; k-nearest neighbors; gradient boosting; Classification and regression tree

* Corresponding author. Tel.: +90 274 443 4330; fax: +90 274 265 20 13.

E-mail address: serifali.sadik@dpu.edu.tr

<http://dx.doi.org/10.1016/j.cviu.2017.00.000>

1. Introduction

With the advancements in machine learning (ML) studies, the use of ML algorithms in applications such as classification, recognition, prediction and forecasting are increasing in recent years[1-5]. The most important parameters for ML applications are data and their features. Machines can be trained with data from past events, just like in the human learning process. Thus, in newly encountered events, the machine can now perform tasks such as prediction or classification, based on the features of the training data. Nowadays, digital data such as text, image, video or sound can be used as ML training data for the solution of many different problems [6].

Among these data types, human beings have been interacting with sound data for a very long time. Sound, which has been our communication tool since the first ages of history, has also enabled us to comprehend many events that exist around us. When the sounds are examined in terms of their sources, they can be examined in three groups. While the natural and artificial sounds we hear from our environment constitute the first two groups, the human voice can be classified as the third group [7]. Examples of natural sounds include thunder, wind, waves, and animal sounds. Artificial sounds, on the other hand, are mostly human-induced examples such as traffic sounds, machine noises and instrument sounds. Finally, when we say human voice, examples such as speaking, singing, coughing and sneezing can be given. In addition, other human-induced sounds such as heart sound and respiratory sound have been the subject of many studies[7-10]. Various studies have been carried out on the recognition, tagging and classification of all these sounds, and the determination of the events that may cause them. With the popularization of ML methods in the recent past, the focus of these studies has been ML applications using audio data [11-14].

Recognition or classification of natural sounds has been widely used in acoustic event classification (AEC) studies. In particular, studies to classify the sounds made by other living things with which we share our world are important for reasons such as analyzing biodiversity and getting to know the ecosystem better. In a study conducted in 2007, support vector machines (SVM) algorithm was used to classify the sounds of bird species given in two different datasets. With the mixed model prepared using different spectral and temporal features and the extracted Mel-frequency cepstral coefficients (MFCC) features the classification accuracy up to 98% was achieved [16]. In another study, classification of frog sounds using threshold-crossing rate, spectral centroid and signal bandwidth as distinctive features was carried out. The k nearest neighbor (kNN) and SVM algorithms were used as classifiers and their performances were compared. As a result of the comparative analysis, 89.05% and 90.30% classification accuracy were obtained by using kNN and SVM algorithms, respectively [17]. The classification of the sounds of bats, which also use sound waves for different purposes, has undoubtedly been a remarkable subject in AEC studies. In a study conducted in 2010, the performance of four different algorithms (SVM, artificial neural networks – ANN, discriminant function analysis – DFA and random forests - RF) were comparatively analyzed to classify the echolocation sounds of bats. In 5 different classification tasks defined, classification process could be performed with accuracies ranging from 84% to 96% [18]. In a study in 2015, syllable features such as frequency modulation, energy modulation, duration of syllable, dominant frequency, oscillation rate were used to classify frog sounds. With the kNN classifier algorithm, classification success was achieved as 90.5% [19]. In another study, Ribeiro et al. used RF and SVM algorithms for classification of fish sounds and obtained 96.9% classification accuracy [20]. Ribeiro et al. used the SVM algorithm to classify the sounds of tomato-pollinating bees and achieved a classification success of 73.39% [21]. In a recent study, the performances of RF, SVM and kNN algorithms for the classification of different animal sounds were compared using three different datasets. The comparative analysis showed that 99% classification success was achieved with SVM and kNN algorithms [22].

In addition to the studies on the classification of natural sounds, the environmental sound classification (ESC) has also been one of the highlights in this area of research. The focus of these studies are mostly publicly available datasets such as ESC-10, ESC-50 [23] and UrbanSound8k [24]. In a comparative study, Mushtaq et al. applied their proposed data augmentation method to all 3 datasets mentioned above and performed ESC with transfer learning method with deep networks. Researchers have achieved classification accuracy of 99% in the ESC-10 and UrbanSound8k datasets, and 97% in the ESC-50 dataset [25].

Undoubtedly, the subject of automatic speaker recognition (ASR) attracts the most attention in studies on sound. Since the larynx size, the anatomy of the vocal cords, the internal structure of the mouth or the anatomy of other organs that influence voice formation may be different in each person, the human voice has distinctive features. In addition, the human voice can convey characteristics such as the ethnicity, age and gender of the person, as well as having personal characteristics [26]. Studies on ASR, which has attracted the attention of researchers for about 50 years, have gained great momentum thanks to developments in digital signal processing and artificial intelligence [27]. Thanks to this automation, automatic voice or speaker recognition methods have been frequently used, especially in authentication, personalization, surveillance and forensic case applications [26].

Speaker recognition, which initially attracted the attention of researchers due to the need in forensic cases [28], continues to be widely studied today thanks to the ease of digital signal processing, extraction of qualified features, and feature selection. Looking at recent studies, Krishnamoorthy et al. obtained 78.20% accuracy by extracting MFCCs as features with limited data set and using Gaussian Mixture Model-Universal Background Model (GMM-UBM) as a classifier. In addition, they tried to overcome the limited data problem with the data augmentation method by adding white noise, and they achieved 80% accuracy with the data with noise added [29]. In another study focusing on the speaker recognition problem using MFCC features and a combination of Generalized Fuzzy Model (GFM) and HMM, a success rate of 93% was achieved [30]. In a study using neural networks (NN), MFCC features were extracted with two different methods and a 93.2% success rate was obtained using the second MFCC feature extraction method proposed in [31]. In 2018, a text-independent speaker recognition problem using a dataset of 24 volunteers was presented as a master's thesis. Feature vectors combining linear prediction cepstral coefficient (LPCC), MFCC, Higuchi fractal dimension (HFD), variance of fractal dimension (VFD), zero crossing rate (ZCR) and number of turns led to a recognition accuracy of 91.6%. [32]. The MFCC features were combined with the power normalization cepstral coefficient (PNCC) for speaker recognition and classification accuracies of 97.52% and 85% were achieved with the extreme learning machine (ELM) using clean sounds and noisy sounds, respectively in [33]. Ayvaz et al. achieved a classification accuracy of 90.2% using a Multilayer Perceptron (MLP) network as the model for a speaker recognition study with MFCC features derived from the voice data of Turkish speakers. [34]. Another recent research focused on speaker identification using artificial intelligence algorithms and feature extraction methods, specifically MFCC and Multiband spectral entropy (MSE), from speech signals. Machine learning algorithms like k Nearest Neighbors, Random Forest, Deep Neural Networks, and Decision Trees were employed for classification. Experiments conducted on LibriSpeech and ELSDSR databases included speaker identification in a group of 20 participants, among men, among women, and by gender. Notably, using the ELSDSR database, the experiment for speaker recognition by gender achieved a precision of 93.99% [35]. Another paper aimed to boost speaker recognition by utilizing rich audio-visual data. It introduced a two-branch network to learn joint face and voice representations in a multimodal system. Extracted features from the network trained a speaker recognition classifier. Evaluation on VoxCeleb1 dataset yielded a notable 91% identification performance using solely audio features [36].

The brief literature review shows that studies on voice/speaker recognition have been carried out for many years, and with the popularity of artificial intelligence, it has still been a remarkable issue in recent years. In this study, MFCC features were extracted from audio files recorded with 12 male and 12 female participants. In addition, formant frequencies and fundamental frequency features are extracted, and all obtained features are fused. The obtained features were given as input values to train the classifier algorithms of SVM, kNN, Classification and Regression Tree (CART) and Gradient Boosting Classifier (GBC) to estimate the gender and age group and the speaker from voice data. Lastly the test results obtained with 4 different algorithms were compared. This study addresses a comprehensive analysis of speaker trait prediction, specifically focusing on gender and age group estimation using voice data. While prior research has touched upon aspects of speaker recognition, this study uniquely combines hybrid time/frequency domain features (MFCC) with fundamental frequencies and formants, offering a more robust and accurate approach. The integration of these diverse features into a unified pool, coupled with the application of four distinct machine learning algorithms, sets our study apart. Notably, the results showcase

better accuracy than reviewed literature, with 93% precision in age group classification, a 99% precision in gender estimation and 93% accuracy in speaker recognition task, using the Support Vector Machines algorithm.

The rest of the paper was organized as follows. In Section 2, the materials and methods which are the dataset, the feature extraction methods and the machine learning algorithms are explained briefly. In Section 3, the training, validation and test results obtained are given comparatively. In the last section, the results are discussed and ideas for future studies are made.

2. Material and methods

Fig.1 shows the block diagram of this study. Firstly, MFCCs, the fundamental frequencies and the formants were extracted as features from human voice data belong to the dataset. The extracted features were fused together and one final feature vector was obtained. With the help of the feature vector obtained, 4 different ML algorithms were trained to predict the age group and gender of the individuals and the classification performances of the ML algorithms were evaluated with the test data excluded from the training procedure.

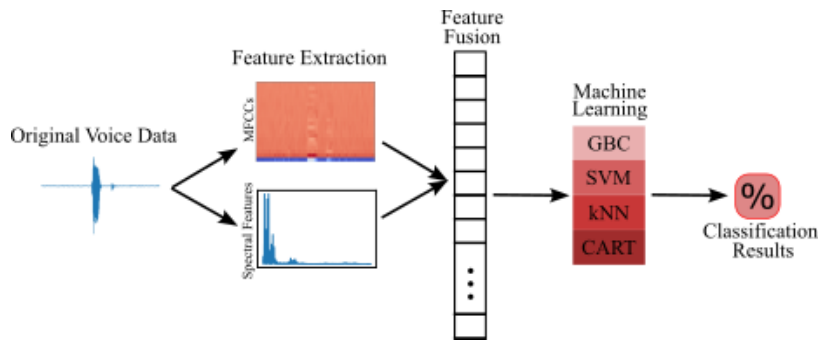


Fig.1. Block diagram of the classification problem in this study.

2.1. Dataset

A publicly available human voice dataset [37] was used in this study. In the data set, there are 1056 waveform audio file format (wav) files for the pronunciation of 44 English words recorded with 24 volunteers. Of the volunteers, 12 are men and 12 are women. While 7 of the female volunteers are younger than 25 years old, 5 are individuals over 25 years old. With male volunteers, there is a 6:6 ratio between individuals older and younger than 25 years old. All 24 volunteers are individuals born and raised in Manitoba, Canada. The sampling frequency of recorded audio files is 44.1 kilo-samples per second. All audio files are 2 seconds long. Fig.2 shows the waveforms of the pronunciations of the word “Book” by two different individuals from the dataset used.

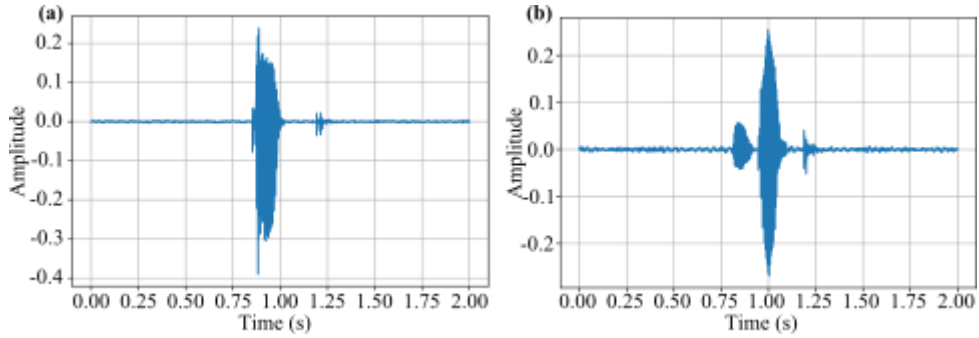


Fig.2. Waveform of the audio file recorded at the moment of pronunciation of the word "Book" (a) for a young male individual (b) for a young female individual.

2.2. Extracted features

The main purpose of machine learning is to train the machine with the help of data from past events and make it capable of making predictions for new or future events. However, raw data from past incidents can contain a lot of information, including some that may not be of use to the machine for its task. Therefore, with feature extraction more informative and distinctive features should be revealed from the raw data for a particular machine learning task. A feature chosen to suit the specific task can represent the raw data in a much more compact way [38]. Successful classification results of machine learning algorithms depend on the extraction of relevant features from the data. By extracting features that are relevant to the target labels, complex data can be analysed more easily, thus shortening the training process of the model. [39].

Research on sound analysis has focused primarily on extracting features from the time domain [40] over time, and as signal processing techniques have improved, features in the frequency domain have gained importance [41]. In recent studies, features that contain information from both time and frequency domains have become prominent [42].

In this study, a hybrid feature pool was created by extracting fundamental frequency and formant features that contain information from the frequency domain and MFCC features that can show changes in time-frequency domains.

2.2.1. Mel-frequency cepstral coefficients (MFCC)

MFCCs visualize the distribution of the energy of an audio signal in the frequency spectrum. MFCCs are extracted from the audio signal using 6 fundamental steps. Firstly, the audio signal is divided into frames, typically 20-30 milliseconds long. By dividing the signals into short "frames", reliable and stable time frames can be obtained where the raw data signal is long and shows frequent changes over time. On each frame, a window which are generally Hanning and Hamming windows, is applied to narrow the signal. Secondly, a power spectrum is computed for each frame. To calculate the power spectrum, Discrete Fourier Transform (DFT) is commonly used. Then the power spectrum is converted to a mel (short for melody) scale, which is a non-linear scale that is more closely aligned with human perception of pitch [43]. The mel scale can be obtained with equation (1).

$$mel = 2595 \log_{10} \left(1 + \frac{f}{700} \right) \quad (1)$$

Then the logarithm values of all mel filter banks is calculated. For the fifth step, a discrete cosine transform (DCT) is applied to the mel-scaled power spectrum to select most accelerative coefficients. And lastly, the first few

DCT coefficients are retained as the MFCCs. MFCCs are typically represented as a vector of 12-20 coefficients. The first few coefficients are the most important, as they capture the most significant information about the spectral envelope. MFCCs are invariant to changes in pitch and volume, which makes them well-suited for speech recognition and other tasks where the speaker or audio source may vary. They are also relatively robust to noise, which is another important property for many applications [44].

2.2.2. Frequency domain features

The distinctive features of audio data may be hidden in characteristic features in the frequency domain rather than changes in the time domain. Therefore, frequency domain features come to the fore in studies on audio signal processing. The most basic tools for extracting frequency domain features are Fourier transform and autocorrelation analysis [38]. In this study, fundamental frequency and formant features were extracted using these tools. The fundamental frequency (f_0), also known as the first harmonic, is the lowest frequency of a periodic waveform and can be determined by autocorrelation analysis using the periodic structure of the signal [45]. Formants are frequency components that result from changes in the shape and size of the human vocal tract. The first three formants (f_1 , f_2 , f_3) are the most important for speech recognition and are related to tongue height, tongue backing and lip roundness, respectively [46].

2.3. Machine learning algorithms

In this study, a hybrid feature space generated from human voice data is used for speaker recognition and classification of age and gender of speakers using machine learning algorithms. For this purpose, proven classifier algorithms used in human voice data classification studies in the literature were used and their performances were compared.

2.3.1. K-nearest neighbors

The kNN algorithm tries to solve the classification problem by calculating the distances between the points in the sample space with methods such as Euclidean distance or Hamming distance and establishing a "neighborhood" relation between the sample points. To determine the class of a new data point, it finds the k closest points in the sample space and uses these neighbors to predict the label of the new point. The main criterion that determines the classification performance of the kNN algorithm is a user-defined hyperparameter called k. The value of k can be optimized according to the type of data and the distribution of labels in the data space. As the k value increases, the effect of noise or outliers in classification will decrease. As the k value becomes smaller, the size of the neighborhoods in the data space will decrease and the distribution of the labels in space will be scattered [47], [48].

In the kNN algorithm used in this study, k=5 was chosen. The weight function is determined as uniform. In a uniform weight distribution, all points in each neighborhood are weighted equally. Additionally, Euclidean distance was used as the distance metric between points.

2.3.2. Gradient boosting classifier

The gradient boosting classifier (GBC) is an ensemble learning algorithm, which combines the predictions of multiple weak learners to produce a more accurate prediction. The GBC works by iteratively training a weak learner on the residuals which are the errors made by the previous learner. The goal of the gradient boosting classifier is to minimize the loss function. The GBC minimizes the loss function by iteratively moving in the direction of the negative gradient of the loss function. The negative gradient of the loss function points in the direction of the steepest descent of the loss function. The learning rate controls the size of the steps that the GBC takes in the direction of the negative gradient of the loss function. A higher learning rate will result in the GBC taking larger steps and vice versa [49,50].

In the GBC algorithm used in this study, the number of estimators was selected as 100. The learning rate was set

to 0.1.

2.3.3. Support vector machine

The support vector machine (SVM) algorithm, which has been studied in many different fields in the literature, tries to obtain an optimal hyperplane to separate different classes in the sample space while classifying. While determining this hyperplane, it tries to maximize the distance between the data points closest to the plane, which also gives the algorithm its name as support vectors [51-53]. In the SVM used in this study, the regularization parameter was selected as 100. The kernel function was chosen as radial basis function.

2.3.4. Classification and regression tree

The classification and regression tree (CART) algorithm recursively splits the data into subsets based on a criterion called the Gini impurity and continues to split until only data belonging to one class remains in the subsets, called leaf nodes. The Gini impurity value represents the proportion of data in a node that belongs to the same class. The closer the impurity value is to 0, the more likely it is that the data in that node belongs to the same class, and the closer it is to 1, the more likely it is that the node is "impure". Thus, nodes with high impurity continue to be split [54,55].

3. Results

In this study, a data set consisting of audio data recorded while each of 24 volunteers was pronouncing 44 English words was used. First, MFCC, fundamental frequency and formant features were extracted from the data and a feature pool was created by combining these features. The resulting 1056 samples were divided into training and test data in a ratio of 8:2. Using the 5-fold cross-validation method with the training data obtained, kNN, GBC, SVM and CART algorithms were trained to classify the genders and age groups of the volunteers. The classification performances of the algorithms were tested with the remaining test data that had not been seen before by the classification algorithms. All ML algorithms mentioned above and used in this study was trained and tested with Python (v.3.9.7) [56].

3.1. Gender classification

Firstly, gender classification was performed from the voice data recorded from the volunteers. With the training data created, 4 classifier algorithms were trained with the 5-fold cross-validation method. The distribution of accuracies obtained with the training data as a result of 5-fold cross-validation is given in Fig.3. As can be seen from the figure, the highest accuracy was obtained with the SVM algorithm, while the CART algorithm gave the lowest accuracy. The mean value and standard deviations of the accuracies of the 5-fold cross-validation step are also given in Table 1.

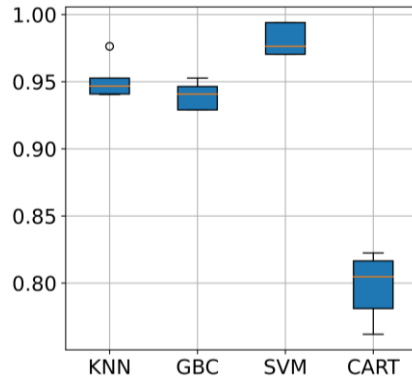


Fig.3. 5-fold cross-validation results of the gender classification.

Table 1. Mean and standard deviation values of the accuracies of the 5-fold cross-validation training process of the gender classification

Accuracy	kNN	GBC	SVM	CART
Mean Value	0.951	0.940	0.981	0.797
Standard Dev.	0.013	0.009	0.011	0.023

The confusion matrices of classifications belong to the gender prediction are given in Fig.4. One can see from the figure that, highest test accuracy was achieved with SVM algorithm with a true positive value of 102 and true negative value of 107.

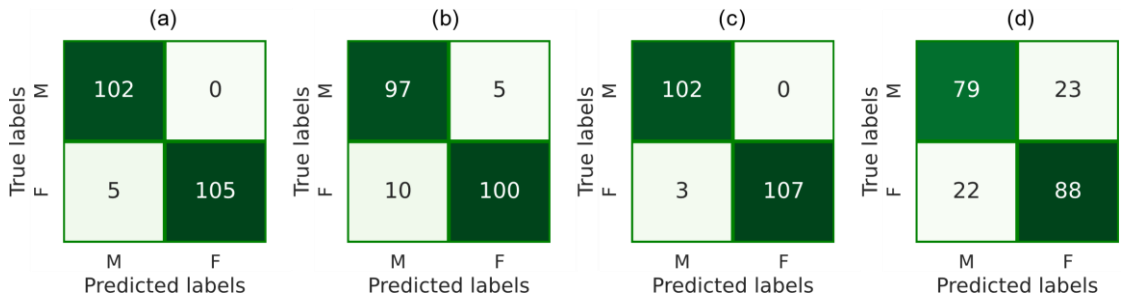


Fig.4. Confusion matrices of the gender classification test results (a) kNN (b) GBC (c) SVM (d) CART.

Table 2 gives the test results of the gender classification in terms of precision, recall, F1-score and accuracy. It can be seen from the table that the highest test accuracy of 0.99 was obtained with the SVM algorithm, which coincides with the complexity matrices.

Table 2. Evaluation metrics of the test process of the gender classification.

Classifier	Precision	Recall	F1-Score	Accuracy
kNN	0.98	0.98	0.98	0.98

GBC	0.93	0.93	0.93	0.93
SVM	0.99	0.99	0.99	0.99
CART	0.79	0.79	0.79	0.79

3.2. Age group classification

In the second part of the study, age group classification was performed from the voice data recorded from the volunteers. Data labels were divided into two groups according to the age of the participants: youth (18 - 25) and adults (25-50). As in the first part, 4 classifier algorithms were trained using the 5-fold cross-validation method with the training data. The distribution of training accuracies obtained as a result of cross-validation is given as a box plot in Fig.5.

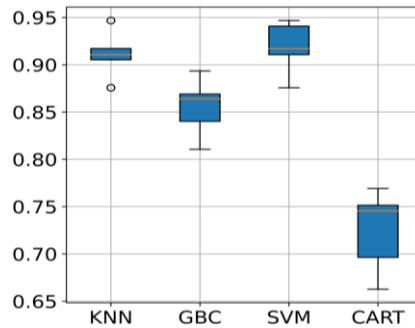


Fig.5. 5-fold cross-validation results of the age group classification.

As can be seen from the Fig.5, the algorithms that gave training accuracy above 90% were SVM and kNN, respectively. The mean accuracy values and standard deviations obtained as a result of 5-fold cross-validation are given in the Table 3. The table shows that 92% training accuracy was achieved with the SVM algorithm. The lowest accuracy was obtained as 73% with the CART algorithm.

Table 3. Mean and standard deviation values of the accuracies of the 5-fold cross-validation training process of the age group classification.

Accuracy	kNN	GBC	SVM	CART
Mean Value	0.911	0.855	0.918	0.725
Standard Dev.	0.023	0.028	0.025	0.039

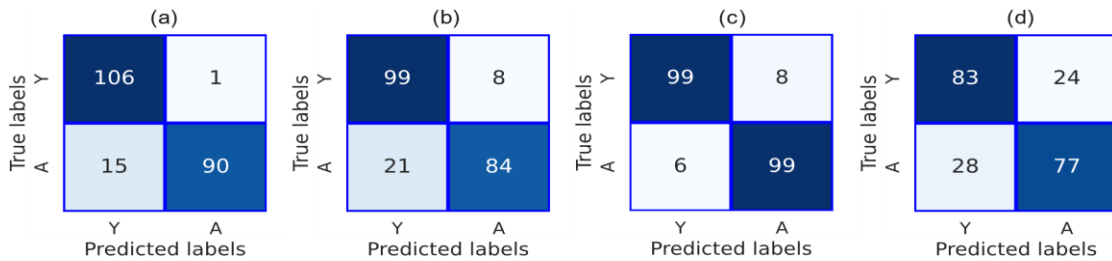


Fig.6. Confusion matrices of the age group classification test results (a) kNN (b) GBC (c) SVM (d) CART.

The confusion matrices of test results belong to the age group classification are given in Figure 6. One can see from the figure that, highest test accuracy was achieved with SVM algorithm with a true positive value of 99 and true negative value of 99. Among the labels in the confusion matrices, A indicates the adult group and Y indicates the youth group.

Table 4. Evaluation metrics of the test process of the gender classification.

Classifier	Precision	Recall	F1-Score	Accuracy
kNN	0.88	0.99	0.93	0.92
GBC	0.82	0.93	0.87	0.86
SVM	0.94	0.93	0.93	0.93
CART	0.75	0.78	0.76	0.75

Lastly, Table 4 gives the test results of the age group classification in terms of precision, recall, F1-score and accuracy. It can be seen from the table that the highest test accuracy of 0.93 was obtained with the SVM algorithm, which coincides with the complexity matrices.

3.3. Speaker recognition

The final objective of this study is speaker recognition from voice data. We classified the voices of 24 volunteers using four distinct classification algorithms (kNN, GBC, SVM, and CART). Similar to two-class classification scenarios, the four classifiers underwent sequential training with dedicated training data. We assessed the training performance of the algorithms using a 5-fold cross-validation approach.

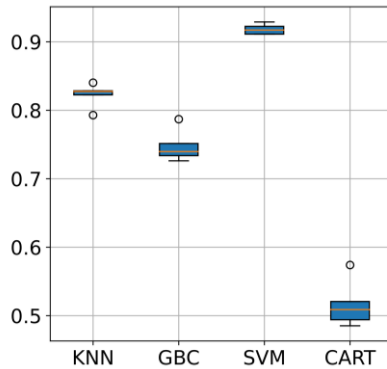


Fig.7. 5-fold cross-validation results of the speaker recognition.

Fig.7 displays a box plot illustrating the distribution of accuracies for each classifier algorithm during the cross-validation stages. The SVM algorithm exhibited the highest accuracy (>90%) in 5-fold cross-validation, while the kNN algorithm secured the second-highest accuracy, averaging over 80% in training performance. In line with two-class classification scenarios, the CART algorithm displayed the lowest accuracy.

Table 5. Mean and standard deviation values of the accuracies of the 5-fold cross-validation training process of the speaker recognition.

Accuracy	kNN	GBC	SVM	CART
----------	-----	-----	-----	------

Mean Value	0.822	0.748	0.918	0.517
Standard Dev.	0.015	0.021	0.006	0.031

Table 6 assesses the test results for speaker recognition based on precision, sensitivity, F1-Score, and Accuracy metrics. The SVM algorithm achieved the highest accuracy at 93%, while the CART algorithm yielded the lowest accuracy at 50%.

Table 6. Evaluation metrics of the test process of the speaker recognition.

Classifier	Precision	Recall	F1-Score	Accuracy
kNN	0.88	0.85	0.86	0.85
GBC	0.75	0.74	0.73	0.74
SVM	0.94	0.93	0.93	0.93
CART	0.52	0.50	0.50	0.50

Concluding the analysis, the confusion matrix of the classification performed using the SVM algorithm, known for providing the highest accuracy in speaker recognition, is presented In Fig.8. A detailed examination of the confusion matrix reveals the capability of accurately classifying the voice data of all 24 speakers.

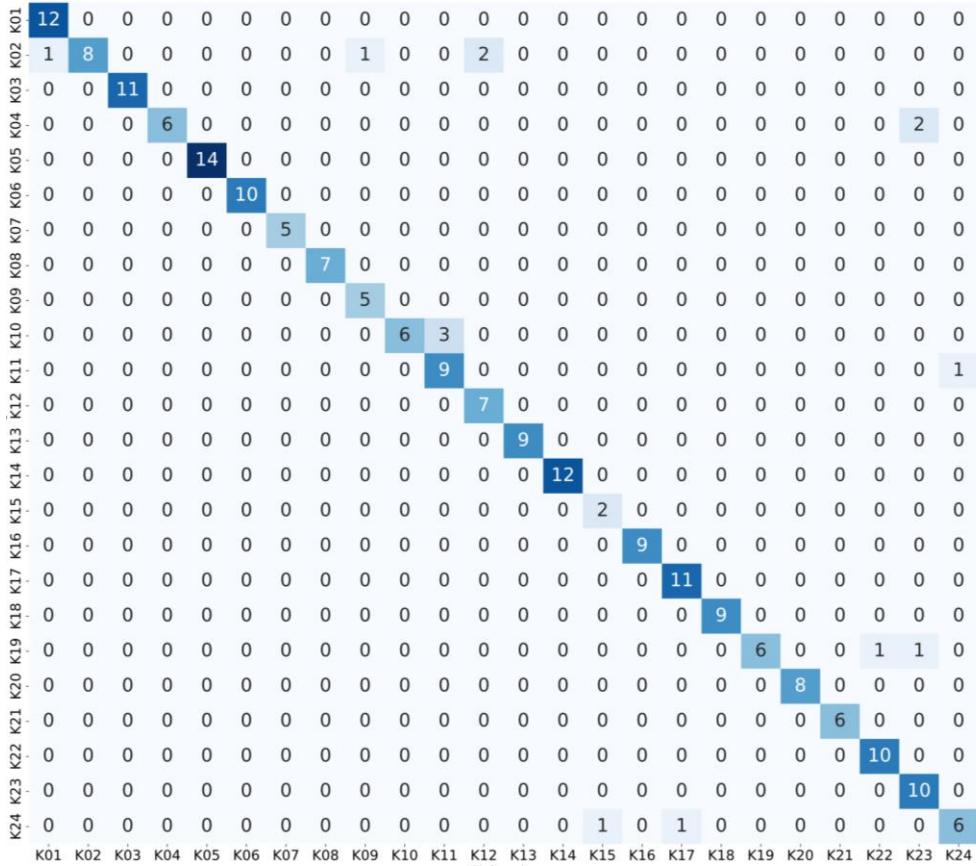


Fig.8. Confusion matrix of the speaker recognition test results for SVM classifier.

3.4. Comparison with the literature

As highlighted in the introduction, the identification of speakers from voice data or the determination of demographic characteristics, such as age and gender, holds significance in various applications like interactive voice response systems, forensic cases, e-marketing, and online banking. However, as indicated in the table, research in this domain remains limited, underscoring the importance of this study in addressing gaps within the existing literature related to Automatic Speaker Recognition (ASR) systems. A notable contribution of this research lies in demonstrating that speaker recognition can achieve high accuracy even with a restricted dataset, utilizing spectral features. Furthermore, the study undertakes a comparison by employing four widely used classification algorithms with distinct methodologies and principles: CART relies on decision trees, SVM seeks optimal hyperplanes, GBC forms an ensemble of weak learners, and kNN classifies based on the majority of nearest neighbors. Notably, the SVM classifier demonstrated the highest accuracy, precision, recall, and F1 score values among these algorithms. A comparative analysis with other studies in the literature is presented in the Table 7 for reference.

Table 7. Comparison of the speaker recognition results with existing literature works.

Reference	Method	Dataset	Features	Accuracy Score
Krishnamoorthy et al.,	GMM-UBM	100 speakers from TIMIT database	MFCC	78.20% with limited data

2011 [29]				80% with noise added data
Bhardwaj et al., 2013 [30]	HMM and GFM	VoxForge speech corpus A subset of NIST 2003 database	MFCC	90% - 93%
Soleymanpour & Marvi, 2017 [31]	NN	ELSDSR database that consists of 22 speakers	MFCC	91.9 % and 93.2 %
Sedigh, 2018 [32]	SVM	Manitoban voice dataset with 24 volunteers	LPCC, MFCC, HFD, VFD ZCR, turns count	91.60%
Bharath & Rajesh Kumar, 2020 [33]	ELM	124 speakers from TIMIT, SITW-2016	MFCC, PNCC	97.66% highest
Ayvaz et al., 2022 [34]	MLP	Turkish voice dataset is collected from 15 people	MFCC	90.2%
Ramírez-Hernández et al., 2023 [35]	NN, kNN, DT, RF	ELSDSR database	MFCC, MSE	78.92% speaker recognition 93.99% gender classification
Shah et al., 2023 [36]	SVM	VoxCeleb1	MFCC	91% with only sound data
This study	kNN, GBC, SVM, CART	Manitoban voice dataset with 24 volunteers	MFCC, Fundamental Freq., Formants	92% age group classification 93% speaker recognition 99% gender classification

4. Conclusion

The use of machine learning algorithms is becoming widespread in many application areas such as speaker recognition, speech-to-text, music analysis, and environmental sound classification by using audio data, and it can be predicted that these studies will expand further. In particular, detecting characteristics such as gender, age group, accent and emotion from the human voice has become a practical and reliable method in biomedical applications, forensic cases or interactive voice response systems. This study focuses on gender and age group prediction from voice data. In the dataset used in this study, voice data were recorded from each of 24 volunteers while pronouncing 44 English words. The MFCC feature, which contains frequency and time domain information, was extracted from the audio data, and the fundamental frequency and formant features were extracted from the frequency domain. A hybrid feature space was created by combining the extracted features. The data were labeled according to the gender and age groups of the volunteers, and classification was carried out with machine learning algorithms. In the study, k nearest neighbors, gradient boost classifier, support vector machines and classification and regression tree algorithms were used and their performances were comparatively analyzed. In the gender prediction study, the SVM algorithm gave the highest accuracy, as 99%. In addition, the highest accuracy in age group classification was achieved as 93% with the SVM algorithm. Finally, in the speaker recognition task from the voice data of 24 volunteers, the SVM algorithm managed to achieve high accuracy with 93%. In order to expand the scope of the study, it is planned to enlarge the dataset, collect data from volunteers with different ethnic identities or accents, and add noise to the data in future studies.

Acknowledgements

There is no conflict of interest with any person/institution in the prepared article. This study did not receive any specific funding or financial assistance from governmental, commercial, or non-profit organizations.

References

- [1] A. Rana, A. Dumka, R. Singh, M. Rashid, N. Ahmad, and M. K. Panda, "An Efficient Machine Learning Approach for Diagnosing Parkinson's Disease by Utilizing Voice Features," *Electronics (Basel)*, vol. 11, no. 22, p. 3782, 2022.
- [2] E. H. Houssein, A. Hammad, and A. A. Ali, "Human emotion recognition from EEG-based brain-computer interface using machine learning: a comprehensive review," *Neural Comput Appl*, vol. 34, no. 15, pp. 12527–12557, 2022.
- [3] E. Dritsas and M. Trigka, "Stroke risk prediction with machine learning techniques," *Sensors*, vol. 22, no. 13, p. 4670, 2022.
- [4] M. M. Kumbure, C. Lohrmann, P. Luukka, and J. Porras, "Machine learning techniques and data for stock market forecasting: A literature review," *Expert Syst Appl*, vol. 197, p. 116659, 2022.
- [5] N. N. Arslan, D. Ozdemir, and H. Temurtas, "ECG heartbeats classification with dilated convolutional autoencoder," *Signal Image Video Process*, vol. 18, no. 1, pp. 417–426, 2024, doi: 10.1007/s11760-023-02737-2.
- [6] S. B. Kotsiantis, I. Zaharakis, and P. Pintelas, "Supervised machine learning: A review of classification techniques," *Emerging artificial intelligence applications in computer engineering*, vol. 160, no. 1, pp. 3–24, 2007.
- [7] S. Duan, J. Zhang, P. Roe, and M. Towsey, "A survey of tagging techniques for music, speech and environmental sound," *Artif Intell Rev*, vol. 42, no. 4, pp. 637–661, 2014, doi: 10.1007/s10462-012-9362-y.
- [8] S. Jayalakshmy and G. F. Sudha, "GTCC-based BiLSTM deep-learning framework for respiratory sound classification using empirical mode decomposition," *Neural Comput Appl*, vol. 33, no. 24, pp. 17029–17040, 2021, doi: 10.1007/s00521-021-06295-x.
- [9] R. Palaniappan, K. Sundaraj, and N. U. Ahamed, "Machine learning in lung sound analysis: A systematic review," *Biocybern Biomed Eng*, vol. 33, no. 3, pp. 129–135, 2013, doi: <https://doi.org/10.1016/j.bbe.2013.07.001>.
- [10] M. Tschannen, T. Kramer, G. Marti, M. Heinzmann, and T. Wiatowski, "Heart sound classification using deep structured features," in *2016 Computing in Cardiology Conference (CinC)*, 2016, pp. 565–568.
- [11] M. Xiang *et al.*, "Research of heart sound classification using two-dimensional features," *Biomed Signal Process Control*, vol. 79, p. 104190, 2023, doi: <https://doi.org/10.1016/j.bspc.2022.104190>.
- [12] S. Esmer, M. K. Uçar, İ. Çil, and M. R. Bozkurt, "Parkinson hastalığı teşhisi için makine öğrenmesi tabanlı yeni bir yöntem," *Düzce Üniversitesi Bilim ve Teknoloji Dergisi*, vol. 8, no. 3, pp. 1877–1893, 2020.
- [13] A. F. R. Nogueira, H. S. Oliveira, J. J. M. Machado, and J. M. R. S. Tavares, "Sound Classification and Processing of Urban Environments: A Systematic Literature Review," *Sensors*, vol. 22, no. 22, p. 8608, 2022.
- [14] Y. R. Pandeya, D. Kim, and J. Lee, "Domestic cat sound classification using learned features from deep neural nets," *Applied Sciences*, vol. 8, no. 10, p. 1949, 2018.
- [15] K. J. Piczak, "Environmental sound classification with convolutional neural networks," in *2015 IEEE 25th international workshop on machine learning for signal processing (MLSP)*, IEEE, 2015, pp. 1–6.
- [16] S. Fagerlund, "Bird species recognition using support vector machines," *EURASIP J Adv Signal Process*, vol. 2007, pp. 1–8, 2007.
- [17] C.-J. Huang, Y.-J. Yang, D.-X. Yang, and Y.-J. Chen, "Frog classification using machine learning techniques," *Expert Syst Appl*, vol. 36, no. 2, Part 2, pp. 3737–3743, 2009, doi: <https://doi.org/10.1016/j.eswa.2008.02.059>.
- [18] D. W. Armitage and H. K. Ober, "A comparison of supervised learning techniques in the classification of bat echolocation calls," *Ecol Inform*, vol. 5, no. 6, pp. 465–473, 2010, doi: <https://doi.org/10.1016/j.ecoinf.2010.08.001>.
- [19] J. Xie, M. Towsey, A. Truskinger, P. Eichinski, J. Zhang, and P. Roe, "Acoustic classification of Australian anurans using syllable features," in *2015 IEEE Tenth International Conference on Intelligent Sensors, Sensor Networks and Information Processing (ISSNIP)*, 2015, pp. 1–6. doi: 10.1109/ISSNIP.2015.7106924.
- [20] M. Malfante, J. I. Mars, M. Dalla Mura, and C. Gervaise, "Automatic fish sounds classification," *J Acoust Soc Am*, vol. 143, no. 5, pp. 2834–2846, May 2018, doi: 10.1121/1.5036628.
- [21] A. P. Ribeiro, N. F. F. da Silva, F. N. Mesquita, P. de C. S. Araújo, T. C. Rosa, and J. N. Mesquita-Neto, "Machine learning approach for automatic recognition of tomato-pollinating bees based on their buzzing-sounds," *PLoS Comput Biol*, vol. 17, no. 9, pp. e1009426-, Sep. 2021, [Online]. Available: <https://doi.org/10.1371/journal.pcbi.1009426>
- [22] U. Haider *et al.*, "Bioacoustics Signal Classification Using Hybrid Feature Space with Machine Learning," in *2023 15th International Conference on Computer and Automation Engineering (ICCAE)*, 2023, pp. 376–380. doi: 10.1109/ICCAE56788.2023.10111384.
- [23] K. J. Piczak, "ESC: Dataset for environmental sound classification," in *Proceedings of the 23rd ACM international conference on Multimedia*, 2015, pp. 1015–1018.
- [24] J. Salamon, C. Jacoby, and J. P. Bello, "A dataset and taxonomy for urban sound research," in *Proceedings of the 22nd ACM international conference on Multimedia*, 2014, pp. 1041–1044.
- [25] Z. Mushtaq, S.-F. Su, and Q.-V. Tran, "Spectral images based environmental sound classification using CNN with meaningful data augmentation," *Applied Acoustics*, vol. 172, p. 107581, 2021.
- [26] R. Mohd Hanifa, K. Isa, and S. Mohamad, "A review on speaker recognition: Technology and challenges," *Computers & Electrical Engineering*, vol. 90, p. 107005, 2021, doi: <https://doi.org/10.1016/j.compeleceng.2021.107005>.
- [27] S. Furui, "40 Years of Progress in Automatic Speaker Recognition," in *Advances in Biometrics*, M. Tistarelli and M. S. Nixon, Eds., Berlin, Heidelberg: Springer Berlin Heidelberg, 2009, pp. 1050–1059.
- [28] N. Singh, A. Agrawal, and R. Khan, "The development of speaker recognition technology," *IJARET*, no. May, 2018.
- [29] P. Krishnamoorthy, H. S. Jayanna, and S. R. M. Prasanna, "Speaker recognition under limited data condition by noise addition," *Expert Syst Appl*, vol. 38, no. 10, pp. 13487–13490, 2011, doi: <https://doi.org/10.1016/j.eswa.2011.04.069>.

- [30] S. Bhardwaj, S. Srivastava, M. Hanmandlu, and J. R. P. Gupta, "GFM-Based Methods for Speaker Identification," *IEEE Trans Cybern*, vol. 43, no. 3, pp. 1047–1058, 2013, doi: 10.1109/TSMCB.2012.2223461.
- [31] M. Soleymanpour and H. Marvi, "Text-independent speaker identification based on selection of the most similar feature vectors," *Int J Speech Technol*, vol. 20, no. 1, pp. 99–108, 2017, doi: 10.1007/s10772-016-9385-x.
- [32] S. Sedigh, "Application of polyscale methods for speaker verification," Master Thesis, The University of Manitoba, Winnipeg, 2018.
- [33] K. P. Bharath and M. Rajesh Kumar, "ELM speaker identification for limited dataset using multitaper based MFCC and PNCC features with fusion score," *Multimed Tools Appl*, vol. 79, no. 39, pp. 28859–28883, 2020, doi: 10.1007/s11042-020-09353-z.
- [34] U. Ayvaz, H. Gürüler, F. Khan, N. Ahmed, T. Whangbo, and A. Bobomirzaevich, "Automatic speaker recognition using mel-frequency cepstral coefficients through machine learning," *CMC-Computers Materials & Continua*, vol. 71, no. 3, 2022.
- [35] J. I. Ramírez-Hernández, A. Manzo-Martínez, F. Gaxiola, L. C. González-Gurrola, V. C. Álvarez-Oliva, and R. López-Santillán, "A Comparison Between MFCC and MSE Features for Text-Independent Speaker Recognition Using Machine Learning Algorithms," in *Fuzzy Logic and Neural Networks for Hybrid Intelligent System Design*, O. Castillo and P. Melin, Eds., Cham: Springer International Publishing, 2023, pp. 123–140. doi: 10.1007/978-3-031-22042-5_7.
- [36] S. H. Shah, M. S. Saeed, S. Nawaz, and M. H. Yousaf, "Speaker Recognition in Realistic Scenario Using Multimodal Data," in *2023 3rd International Conference on Artificial Intelligence (ICAI)*, 2023, pp. 209–213. doi: 10.1109/ICAI58407.2023.10136626.
- [37] S. Sedigh and W. Kinsner, "A Manitoban Speech Dataset," *IEEE DataPort*, January, 2018, doi: 10.21227/H2KM16.
- [38] G. Sharma, K. Umopathy, and S. Krishnan, "Trends in audio signal feature extraction methods," *Applied Acoustics*, vol. 158, p. 107020, 2020, doi: <https://doi.org/10.1016/j.apacoust.2019.107020>.
- [39] S. Khalid, T. Khalil, and S. Nasreen, "A survey of feature selection and feature extraction techniques in machine learning," in *2014 science and information conference*, IEEE, 2014, pp. 372–378.
- [40] K. N. Stevens, "Autocorrelation analysis of speech sounds," *J Acoust Soc Am*, vol. 22, no. 6, pp. 769–771, 1950.
- [41] G. Tzanetakis and P. Cook, "Musical genre classification of audio signals," *IEEE Transactions on speech and audio processing*, vol. 10, no. 5, pp. 293–302, 2002.
- [42] M. Sahidullah and G. Saha, "Design, analysis and experimental evaluation of block based transformation in MFCC computation for speaker recognition," *Speech Commun*, vol. 54, no. 4, pp. 543–565, 2012.
- [43] P. Pedersen, "The mel scale," *Journal of Music Theory*, vol. 9, no. 2, pp. 295–308, 1965.
- [44] Z. K. Abdul and A. K. Al-Talabani, "Mel Frequency Cepstral Coefficient and its Applications: A Review," *IEEE Access*, vol. 10, pp. 122136–122158, 2022, doi: 10.1109/ACCESS.2022.3223444.
- [45] M. Lahat, R. Niederjohn, and D. Krubsack, "A spectral autocorrelation method for measurement of the fundamental frequency of noise-corrupted speech," *IEEE Trans Acoust*, vol. 35, no. 6, pp. 741–750, 1987.
- [46] I. V. Bele, "The speaker's formant," *Journal of Voice*, vol. 20, no. 4, pp. 555–578, 2006.
- [47] G. Batista and D. F. Silva, "How k-nearest neighbor parameters affect its performance," in *Argentine symposium on artificial intelligence*, Citeseer, 2009, pp. 1–12.
- [48] O. Kramer, "K-Nearest Neighbors," in *Dimensionality Reduction with Unsupervised Nearest Neighbors*, O. Kramer, Ed., Berlin, Heidelberg: Springer Berlin Heidelberg, 2013, pp. 13–23. doi: 10.1007/978-3-642-38652-7_2.
- [49] C. Bentéjac, A. Csörgő, and G. Martínez-Muñoz, "A comparative analysis of gradient boosting algorithms," *Artif Intell Rev*, vol. 54, pp. 1937–1967, 2021.
- [50] A. Natekin and A. Knoll, "Gradient boosting machines, a tutorial," *Front Neurorobot*, vol. 7, p. 21, 2013.
- [51] M. A. Hearst, S. T. Dumais, E. Osuna, J. Platt, and B. Scholkopf, "Support vector machines," *IEEE Intelligent Systems and their applications*, vol. 13, no. 4, pp. 18–28, 1998.
- [52] D. A. Pisner and D. M. Schnyer, "Support vector machine," in *Machine learning*, Elsevier, 2020, pp. 101–121.
- [53] S. Suthaharan and S. Suthaharan, "Support vector machine," *Machine learning models and algorithms for big data classification: thinking with examples for effective learning*, pp. 207–235, 2016.
- [54] W. Loh, "Fifty years of classification and regression trees," *International Statistical Review*, vol. 82, no. 3, pp. 329–348, 2014.
- [55] E. Şahin Sadık, H. M. Saraoğlu, S. Canbaz Kabay, M. Tosun, C. Keskinçiliç, and G. Akdağ, "Investigation of the effect of rosemary odor on mental workload using EEG: an artificial intelligence approach," *Signal Image Video Process*, vol. 16, no. 2, pp. 497–504, 2022.
- [56] F. Pedregosa *et al.*, "Scikit-learn: Machine learning in Python," *the Journal of machine Learning research*, vol. 12, pp. 2825–2830, 2011.



E-ISSN: 2687-6167

Number 57, June 2024

RESEARCH ARTICLE

Receive Date: 05.01.2024

Accepted Date: 15.04.2024

Non-linear behavior of functionally graded elastoplastic beam under torsion

Murat Karaca^a, Bahadır Alyavuz^{b,*}

^aGazi University, Graduate School of Natural and Applied Sciences, Ankara, Türkiye, ORCID: 0009-0009-6465-1818

^bGazi University, Faculty of Engineering, Department of Civil Engineering, Ankara, Türkiye, ORCID: 0000-0003-4643-4368

Abstract

The torsional behavior of beams graded in one and two directions under large displacements and angular deformations was analyzed using the power law and sinusoidal functions. Functionally graded material is elastoplastic, consisting of ceramic and metal. A nonlinear finite element method with isoparametric hexahedral elements was used. The finite element formulation was developed by using the updated Lagrangian formulation based on the virtual displacement principle. An iterative solution using Newton-Raphson and updated Newton-Raphson methods was used to solve the nonlinear equation system. The propagation of the plastic region was calculated based on the flow theory of plasticity. Elastoplastic behavior and effective material properties were determined according to the TTO model. Numerical investigations have shown that functionally graded beams behave quite differently from homogeneous beams under torsion. Yielding of the material starts at the outer boundaries of the section of the homogeneous beams, and the plastic region propagates symmetrically. On the other hand, yielding and propagation of plastic regions tend to shift to regions with more ceramic volume with higher effective Young modulus in functionally graded beams. Beams graded in the axial direction have a non-linear variation of rotation angle along the axial direction, unlike beams graded in section and pure metal beams. The amount of non-linearity increases with increasing volume of the ceramic material, which has higher torsional stiffness. Unlike homogeneous beams, the largest shear stresses can occur within the section rather than at the outer boundaries of the section. In beams graded from ceramic to metal using the power law, the section moves along the transverse direction in addition to the rotation. This transverse displacement occurs in the grading direction, and its magnitude is about 3% of the thickness at 12.5° rotation angle. Also, the shear stresses are not zero in the section's midpoint. The effects of material distribution on displacements, stresses, and plastic region propagation were examined, and essential points were reported.

© 2023 DPU All rights reserved.

Keywords: Functionally graded material, torsion, hexahedral finite element.

* Corresponding author.

E-mail address: balyavuz@gazi.edu.tr

1. Introduction

Functionally graded material (FGM) was proposed by Japanese material scientists to prepare thermal barrier materials in 1984 [1]. Unlike layer-by-layer designs, a functionally graded single material structure emerges in FGM.

The use of FGMs has made it possible to eliminate apparent boundaries between layers of multilayer composites through functions called grading rules. One of these rules, the power law model, was presented at an early FGM symposium in 1990 [2]. This model is often preferred because of its wide range of material distribution. It is possible to create continuously varying material using different values of power law index [3, 4]. In addition to the power law, other functions such as exponential and sinusoidal are also used. Boggarapu et al. [5] have included the most commonly used functions in their review. Simply, these rules yield the volume fractions of the constituent materials at any point in the structure.

The effective material properties of FGM are determined through the homogenization schemes. Initial studies aimed to determine material properties up to their linear limits. A rough approach that directly relates the effective material properties to the volume fraction of materials is the scheme known as the Voigt model or the rule of mixtures. Hill [6] proposed the self-consistent scheme for materials with similar volume fractions, in which the constituents cannot be separated into the main phase and inclusion phase. Mori and Tanaka [7] later presented the Mori-Tanaka scheme for composition, in which the material microstructure can be described by the main phase and a minor inclusion phase. Since the variation of the microstructure along the grading axis limits the use of these conventional homogenization schemes, different approaches have been developed. Gasik and Lilius [8] proposed the LRVE scheme, a more comprehensive approach for FGMs. Reiter and Dvorak [9] used an approach based on combining Mori-Tanaka and self-consistent schemes. Determination of elastoplastic effective properties of non-homogeneous materials is more complicated due to additional parameters. In order to define the effective properties of elastoplastic materials in metal alloys, the scheme called TTO (Tamura-Tomota-Ozawa) model or the rule of improved mixtures, was proposed by Tamura et al. [10]. This scheme was used by Williams et al. [11] for ceramic-metal FGMs. It is based on determining effective stress and strain using the volume fractions of materials. It has been used to determine effective material properties outside the elastic limit for ceramic-metal FGMs with low ceramic volume fraction, and it is well accepted in the literature [12,13,14].

Initial studies on the torsional behavior of FGM were conducted under uniform torsion and without exceeding linear limits. Rooney and Ferrari [15] presented the analytical solution of the torsional behavior of linear elastic functionally graded (FG) bars graded in the section plane. Horgan and Chan [16] analyzed FG linear elastic bars graded in the section plane under torsion by generalizing the classic approach to inhomogeneous material. Unlike homogeneous materials, they showed that maximum shear stresses may not occur at the section boundaries. Horgan [17] later developed an analytical solution for non-isotropic FG rods. Batra [18] presented an analytical solution for a linear elastic circular cylindrical rod graded in the axial direction. Anita [19] formulated the torsional behavior of FG bars using a meshless method. Hematiyan and Estakhrian [20] presented analytical solutions for FG open section members. Nguyen et al. [21] presented analytical modeling for thin-walled FG beams. Ecsedi and Baksa [22] presented an analytical solution for the torsion of non-isotropic circular FG cylinders. Nie et al. [23] gave analytical solutions for conical cylinders graded in two directions. Akinlabi et al. [24] formulated the torsion of FG bar with a triangular cross-section. Ecsedi [25] gave the analytical solution of FG bars with elliptical cross-sections under non-uniform torsion. Tsiatas and Babouskos [26] examined the plastic region distribution under the torsional behavior of elastoplastic beams with rectangular and triangular cross-sections using the boundary element method based on the Analog Equation Method. They also included an FG beam with a rectangular cross-section in their study. Aminbaghai et al. [27] performed non-uniform torsion analyses of functionally graded I and box section beams using the power law model in the axial direction. They developed a beam element for the finite element analysis. Singh et al. [28] examined the torsional behavior of beams of various cross-sections with two homogeneous material layers in the height direction and a functionally graded transition zone between them. Chen et al. [29] proposed a

one-dimensional beam model based on the hierarchical Legendre expansion, and they examined the non-uniform torsional behavior of FG beams with various cross-sections and demonstrated the reliability of their proposed model. Mahmoodi and Malekzadeh [30] gave the analytical solutions of cracks and cavities in a rectangular cross-section bar coated by a functionally graded layer under Saint-Venant torsion. They showed FG coating layer can significantly improve the torsional behavior of isotropic bars weakened by cracks and cavities. Ecdesi and Baksa [31] gave the analytical solution for radially functionally graded orthotropic piezoelectric hollow circular cylinder under Saint-Venant torsion. They investigated the dependence of mechanical and electric fields from the power index of the radial inhomogeneity. There are also studies examining the buckling behavior of FGMs under torsional load [32,33,34].

The objective of this study is to investigate the torsional behavior and plastic region propagation of elastoplastic FG beams under large displacements and angular deformations using hexahedral finite elements. Additionally, the study aims to analyze the shear stress distribution and axial displacement distribution of elastoplastic FG beams graded according to different functions and directions.

2. Functionally graded beam

Functionally graded materials are defined by functions that eliminate material boundaries on a macro scale. In this study, the torsional behavior of beams graded using the power law and sinusoidal functions was examined. In this direction, a ceramic-metal functional graded beam was considered. The geometric properties of the beam are shown in Fig. 1. The boundary conditions are applied as a torsional loading at the $x_1=0$ and a fully clamped end at the $x_1=l$. Material grading, which differ depending on the selected function and direction, are shown in Fig. 2.

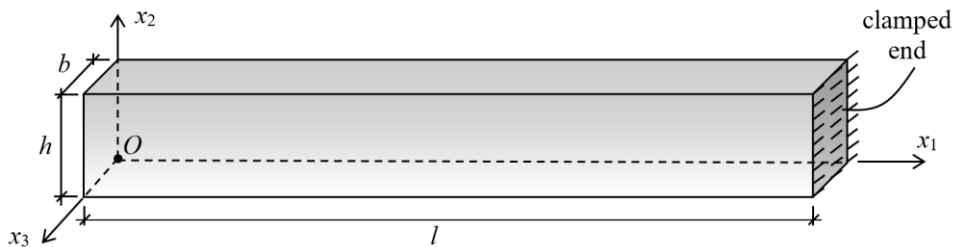


Fig. 1. Functionally graded beam.

2.1. HP-beam material grading

The beam graded using the power law along the beam height is expressed as HP-beam. The cross-section of such a beam is shown in Fig. 3a. This beam has ceramic material on the top surface and metal on the bottom. The ceramic material volume fraction and the corresponding metal material volume fraction are given in Eq. 1, and Eq.2 respectively.

$$V_c(x_2) = \left(\frac{x_2}{h}\right)^n \tag{1}$$

$$V_m(x_2) = 1 - V_c(x_2) \tag{2}$$

Positive-definite n is the parameter that determines the material distribution. V_c refers to the ceramic volume fraction and V_m refers to the metal volume fraction. If $n=1$, the amount of ceramic and metal materials used in the

beam are equal. The variation of ceramic volume fraction with the beam height for different n values is shown in Fig. 2a.

2.2. LP-beam material grading

The beam graded using the power law along the beam length is expressed as LP-beam, and it is shown in Fig. 3b. The end of the beam, where the torsional load is applied, is metal. The fully clamped end of the beam is ceramic. Ceramic volume fraction according to the power law can be calculated using Eq. 3.

$$V_c(x_1) = \left(\frac{x_1}{l}\right)^n \quad (3)$$

The variation of ceramic volume fraction along the beam for different n values is shown in Fig. 2a.

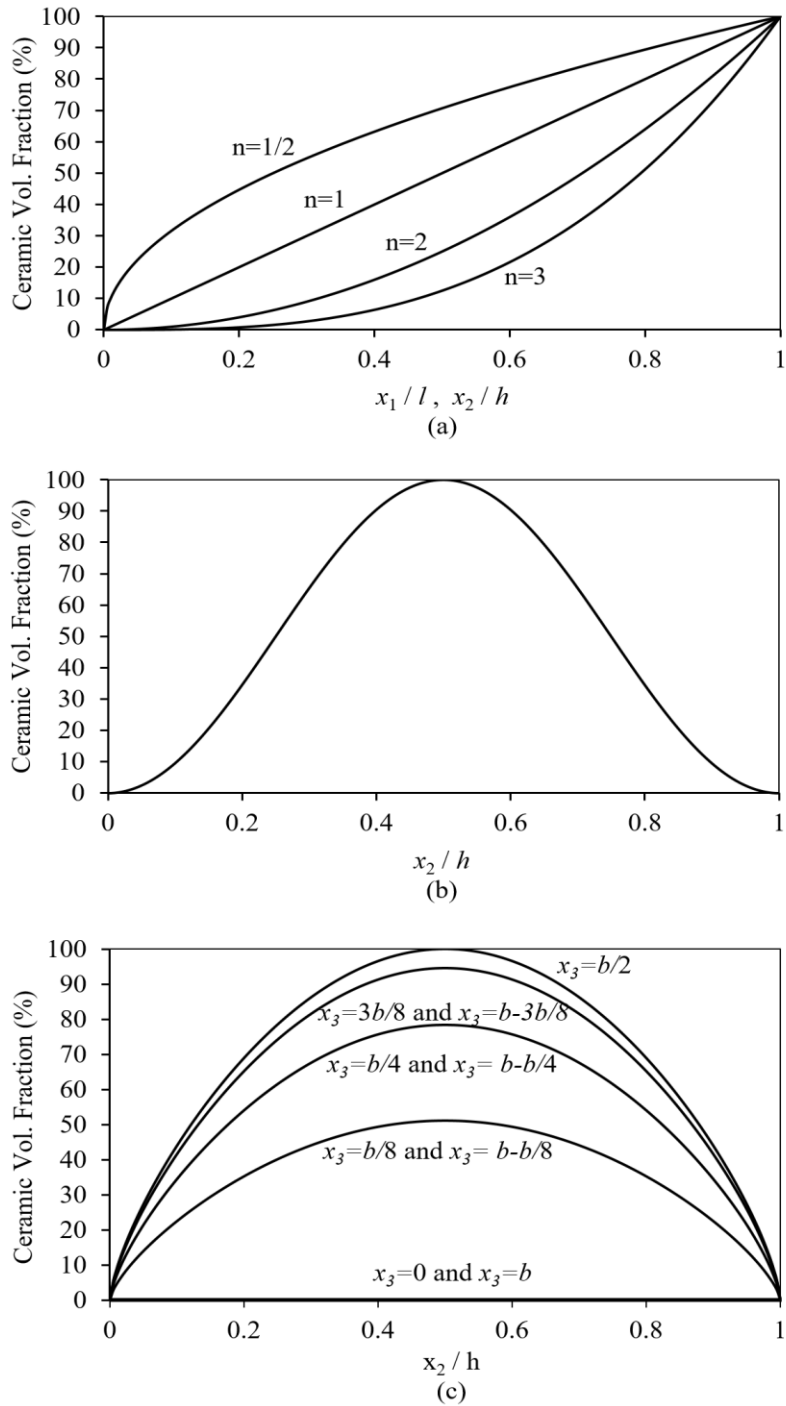


Fig. 2. The variation of ceramic volume fraction (a) HP-beam and LP- beam; (b) HS-beam; (c) HBS-beam.

2.3. HS-beam material grading

A sinusoidal grading function was used for the beam shown in Fig. 3c, with metal top and bottom surfaces. The same amount of ceramic and metal materials are used in the beam. The variation of ceramic volume fraction with the beam height is shown in Fig. 2b. Ceramic volume fraction according to the power law can be calculated using Eq. 4.

$$V_c(x_2) = \left(\sin \left(\frac{\pi(2x_2-h)}{2h} + \frac{\pi}{2} \right) \right)^2 \quad (4)$$

2.4. HBS-beam material grading

Fig. 3d shows a beam graded in two directions, i.e., height and width. The metal material was used on the outer edges, and the ceramic was in the mid-region of the section. The sinusoidal function given in Eq. 5 was used as a grading function. The variation of ceramic volume fraction with beam height for specific x_3 values in the section is shown in Fig. 2c.

$$V_c(x_2, x_3) = \left(\sin \left(\frac{\pi(2x_2-h)}{2h} + \frac{\pi}{2} \right) \sin \left(\frac{\pi(2x_3-b)}{2b} + \frac{\pi}{2} \right) \right)^{0.7} \quad (5)$$

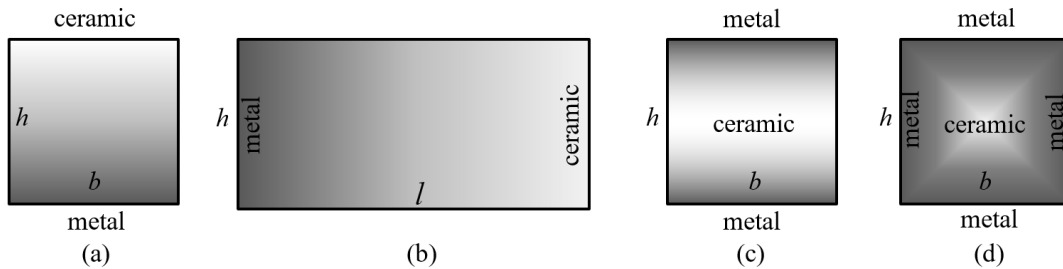


Fig. 3. Beam material gradings (a) HP-beam; (b) LP-beam; (c) HS- beam; (d) HBS- beam.

3. Effective elastoplastic properties

The elastoplastic behavior of the FG beam is described by the TTO scheme. Based on the flow theory of plasticity, this scheme is used to determine the effective material properties of FGMs beyond the elastic limits, where the ceramic ratio is not very dominant [37]. The yield condition can be divided into two parts and written as follows.

$$F(\boldsymbol{\sigma}, \kappa) = f(\boldsymbol{\sigma}) - k(\kappa) = 0 \quad (6)$$

Here, $f(\boldsymbol{\sigma})$ is the yield criterion, and $k(\kappa)$ is the yield stress curve obtained from uniaxial test data. Experimental observations have shown that the plastic deformation of metals is independent of hydrostatic pressure [38]. Any stress tensor can be divided into hydrostatic and deviatoric parts and expressed as in Eq. 7.

$$\sigma_{ij} = \delta_{ij} \sigma_m + \sigma'_{ij} \quad (7)$$

In the above equation, δ_{ij} is the Kronecker delta, $\sigma_m = \sigma_{ii}/3$ is the hydrostatic pressure or mean stress, and σ'_{ij} is the deviatoric stress tensor.

When the yield criterion reaches the yield surface, as in Eq. 7, it remains on the surface with a slight stress increase, and plastic deformation begins. In the updated Lagrangian (UL) formulation, when the effective plastic strain does not exceed 2% [37], the change in total strain can be divided into elastic and plastic parts and expressed as follows.

$$d\boldsymbol{\varepsilon} = d\boldsymbol{\varepsilon}^e + d\boldsymbol{\varepsilon}^p \quad (8)$$

In the flow theory of plasticity, stresses are related to the change in strain. For isotropic materials, according to Hooke's law, the change in the elastic part of the strain can be written as in Eq. 9 related to the change in stress.

$$d\varepsilon_{ij}^e = \frac{d\sigma'_{ij}}{2G} + \frac{(1-2\nu)\delta_{ij}d\sigma_{kk}}{3E} \quad (9)$$

Where $d\sigma'_{ij}$ is the change in deviatoric stress tensor, $d\sigma_{kk}$ is the change in mean stress, G , E and ν are the shear modulus, elastic modulus and Poisson's ratio of the material, respectively. The associated flow rule for deformations of the material in the plastic region is as follows.

$$d\boldsymbol{\varepsilon}^p = d\Lambda \left[\frac{\partial f}{\partial \boldsymbol{\sigma}} \right] \quad (10)$$

Here, $d\Lambda$ is the hardening parameter. $\partial f/\partial \boldsymbol{\sigma}$ corresponds to a vector perpendicular to the yield surface at the corresponding stress point and determines the direction in the flow rule. The following equation can be written by determining the yield criterion according to the J_2 yield criterion.

$$d\varepsilon_{ij}^p = d\Lambda \frac{\partial J_2}{\partial \sigma_{ij}} = d\Lambda \sigma'_{ij} \quad (11)$$

In the above equation, J_2 is the second invariant of the deviatoric stress tensor. The effective stress change and effective strain change are as shown in Eq. 12 and Eq.13, respectively.

$$\bar{\sigma} = \sqrt{3J_2} \quad (12)$$

$$\overline{d\varepsilon}^p = \sqrt{\frac{2}{3} d\varepsilon_{ij}d\varepsilon_{ij}} \quad (13)$$

The plastic modulus, E_p , relating the stress change and plastic strain change, is expressed as follows.

$$E_p = \frac{d\bar{\sigma}}{d\overline{\varepsilon}^p} = \frac{EE_T}{E-E_T} \quad (14)$$

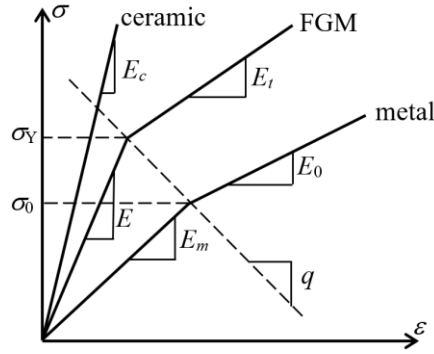


Fig. 4. Bi-linear stress-strain graph according to TTO scheme.

The elastoplastic constitutive equation is written as follows.

$$d\varepsilon_{ij} = \frac{d\sigma'_{ij}}{2G} + \frac{(1-2\nu)\delta_{ij}d\sigma_{kk}}{3E} + \frac{3d\bar{\sigma}}{2\bar{\sigma}E_p} \sigma'_{ij} \quad (15)$$

In the TTO model, the ceramic material is linearly elastic, as shown in Fig. 4. It is accepted that the functionally graded material will behave according to the J_2 flow theory, as in metals, when the yielding limit is exceeded. According to the model, the uniaxial stress and strain of the graded material with isotropic hardening are related to the volume fraction of the materials [11].

$$\sigma = \sigma_c V_c + \sigma_m V_m \quad (16)$$

$$\varepsilon = \varepsilon_c V_c + \varepsilon_m V_m \quad (17)$$

In above equations σ_c , σ_m ve ε_c , ε_m are the uniaxial stress and strain of the ceramic and metal, respectively. The stress and strain relationship is provided by the modulus denoted by positive definite q . This modulus is written as,

$$q = \frac{\sigma_c - \sigma_m}{|\varepsilon_c - \varepsilon_m|} \quad (18)$$

According to the TTO model, the effective material properties are defined using the material properties forming the FGM, volume fractions, and modulus q as follows.

$$E = \left[E_m V_m \frac{q + E_c}{q + E_m} + E_c V_c \right] / \left[V_m \frac{q + E_c}{q + E_m} + V_c \right] \quad (19)$$

$$\sigma_y = \sigma_0 \left[V_m + \frac{q + E_m}{q + E_c} \frac{E_c}{E_m} V_c \right] \quad (20)$$

$$E_t = \left[E_0 V_m \frac{q + E_c}{q + E_0} + E_c V_c \right] / \left[V_m \frac{q + E_c}{q + E_0} + V_c \right] \quad (21)$$

The effective Poisson's ratio can be written by following the Voigt model as [38],

$$\nu = \nu_c V_c + \nu_m V_m \quad (22)$$

4. Incremental finite element formulation

The notation of formulation used here includes the tensor notation. The lower right indices represent the coordinates in the three-dimensional Euclidean space, taking values from 1 to 3. The comma between the coordinate indices indicates the partial derivative with respect to position. The lower left symbol refers to the reference time step, and the upper left symbol refers to the current time step. The presence of a single superscript on the left indicates that the referenced geometry and the corresponding geometry are the same. The presence of a single subscript and no symbols on the left side describe the quantity change relative to the reference time step and the current time step, respectively. The index appearing twice on only one side of the equation requires the summation convention. The time step corresponds also to the load level since static analysis is performed.

The incremental finite element formulation is based on the solutions of linearized equations for times 0, Δt , $2\Delta t$, t . In case of UL formulation, the variables are referred to the last calculated configuration in the solution. With arbitrarily chosen virtual displacements and displacement boundary conditions satisfied, the principle of virtual displacements requires the following equation for the time $t+\Delta t$ [37].

$$\int_{tV} {}^{t+\Delta t}S_{ij} \delta {}^{t+\Delta t}\epsilon_{ij} d^tV = {}^{t+\Delta t}\mathcal{R} \quad (23)$$

Here, tV is the volume of the continuum, ${}^{t+\Delta t}\mathcal{R}$ is the external virtual work. δ shows that the quantity is virtual. The relation between Green-Lagrange strain tensor, ${}^{t+\Delta t}\epsilon_{ij}$, and second Piola-Kirchhoff stress tensor, ${}^{t+\Delta t}S_{ij}$, is as follows.

$${}^{t+\Delta t}S_{ij} = {}^{t+\Delta t}C_{ijrs}^{EP} {}^{t+\Delta t}\epsilon_{rs} \quad (24)$$

The elements of elastoplastic constitutive tensor ${}^{t+\Delta t}C_{ijrs}^{EP}$ depends on the location because of the material grading. Since the Second Piola-Kirchhoff stress tensor ${}^tS_{ij}$ for the configuration at time t corresponds to the Cauchy stress tensor ${}^t\tau_{ij}$, the Second Piola-Kirchhoff stress tensor in the incremental formulation at time $t+\Delta t$ is written as [37].

$${}^{t+\Delta t}S_{ij} = {}^t\tau_{ij} + {}^tS_{ij} \quad (25)$$

The incremental representation of the Green-Lagrange strain tensor and its expression using its linear and nonlinear parts are given below, respectively.

$${}^{t+\Delta t}\epsilon_{ij} = {}^t\epsilon_{ij} \quad (26)$$

$${}^t\epsilon_{ij} = {}^t\epsilon_{i,j} + {}^t\eta_{i,j} \quad (27)$$

These linear and nonlinear parts can be written as shown in Eq. 28 and Eq. 29, respectively, using the displacement vector \mathbf{u} as,

$${}^t\epsilon_{ij} = \frac{1}{2}({}^t\mathbf{u}_{i,j} + {}^t\mathbf{u}_{j,i}) \quad (28)$$

$${}^t\eta_{ij} = \frac{1}{2} {}^t\mathbf{u}_{k,i} {}^t\mathbf{u}_{k,j} \quad (29)$$

The equation of motion in virtual displacements principle using the incremental UL formulation becomes as in Eq. 30.

$$\int_{tV} {}_tS_{ij} \delta {}_t\varepsilon_{ij} d^tV + \int_{tV} {}_t\tau_{ij} \delta {}_t\eta_{ij} d^tV = {}^{t+\Delta t}\mathcal{R} - \int_{tV} {}_t\tau_{ij} \delta {}_te_{ij} d^tV \quad (30)$$

The linearized equation of motion can be written using the approximations ${}_tS_{ij} = {}_tC_{ijrs} {}_te_{rs}$ and ${}_te_{ij} = {}_te_{ij}$ as,

$$\int_{tV} {}_tC_{ijrs}^{EP} {}_te_{rs} \delta {}_te_{ij} d^tV + \int_{tV} {}_t\tau_{ij} \delta {}_t\eta_{ij} d^tV = {}^{t+\Delta t}\mathcal{R} - \int_{tV} {}_t\tau_{ij} \delta {}_te_{ij} d^tV \quad (31)$$

This equation is fundamental in isoparametric finite element analysis [37]. Since external loads are torsional loads, the applied load follows the deformations and is updated at each solution step, as shown in Fig. 5.

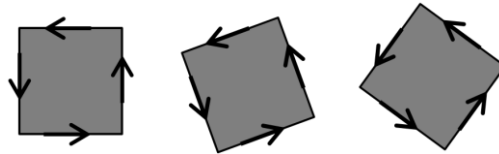


Fig. 5. Representation of loads following the deformation.

$$h_k = (1 + \xi\xi_k)(1 + \eta\eta_k)(1 + \zeta\zeta_k)/8 \quad (32)$$

In above equation, $k=1, 2, \dots, 8$ represents the node numbers of hexahedral finite element, as shown in Fig. 6. ξ, η, ζ are isoparametric coordinates and $\xi_k, \eta_k, \zeta_k = \pm 1$. Linear and nonlinear strain-displacement transformation matrices, ${}^t\mathbf{B}_L$ ve ${}^t\mathbf{B}_{NL}$, can be written by taking partial derivatives with respect to the coordinates as in Eq. 33 and Eq. 34.

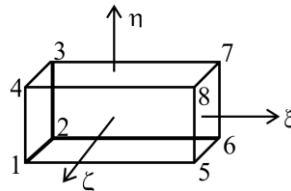


Fig. 6. Isoparametric finite element.

$${}^t\mathbf{B}_L = \begin{bmatrix} {}_th_{1,1} & 0 & 0 & {}_th_{2,1} & \dots & 0 \\ 0 & {}_th_{1,2} & 0 & 0 & \dots & 0 \\ 0 & 0 & {}_th_{1,3} & 0 & \dots & {}_th_{m,3} \\ {}_th_{1,2} & 0 & 0 & {}_th_{2,2} & \dots & 0 \\ 0 & {}_th_{1,3} & {}_th_{1,2} & 0 & \dots & {}_th_{m,2} \\ {}_th_{1,3} & 0 & {}_th_{1,1} & {}_th_{2,3} & \dots & {}_th_{m,1} \end{bmatrix} \quad (33)$$

$${}^t\mathbf{B}_{NL} = \begin{bmatrix} {}^t\tilde{\mathbf{B}}_{NL} & \tilde{\mathbf{0}} & \tilde{\mathbf{0}} \\ \tilde{\mathbf{0}} & {}^t\tilde{\mathbf{B}}_{NL} & \tilde{\mathbf{0}} \\ \tilde{\mathbf{0}} & \tilde{\mathbf{0}} & {}^t\tilde{\mathbf{B}}_{NL} \end{bmatrix} \quad (34)$$

where,

$${}^t\tilde{\mathbf{B}}_{NL} = \begin{bmatrix} {}^th_{1,1} & 0 & 0 & \cdots & {}^th_{m,1} \\ {}^th_{1,2} & 0 & 0 & \cdots & {}^th_{m,2} \\ {}^th_{1,3} & 0 & 0 & \cdots & {}^th_{m,3} \end{bmatrix} \quad (35)$$

The linearized version of equation of motion given in Eq. 31 becomes,

$$\underbrace{\left(\int_{tV} {}^t\mathbf{B}_L^T {}^t\mathbf{C}^{EP} {}^t\mathbf{B}_L d^tV \right) \hat{\mathbf{u}}}_{{}^t\mathbf{K}_L \hat{\mathbf{u}}} + \underbrace{\left(\int_{tV} {}^t\mathbf{B}_{NL}^T {}^t\boldsymbol{\tau} {}^t\mathbf{B}_{NL} d^tV \right) \hat{\mathbf{u}}}_{{}^t\mathbf{K}_{NL} \hat{\mathbf{u}}} = {}^{t+\Delta t}\mathbf{R} - \underbrace{\int_{tV} {}^t\mathbf{B}_L^T {}^t\hat{\boldsymbol{\tau}} d^tV}_{{}^t\mathbf{F}} \quad (36)$$

where ${}^t\mathbf{C}^{EP}$ is the incremental elastoplastic constitutive matrix and $\hat{\mathbf{u}}$ represents vectors. Since the virtual displacements can be chosen as arbitrary unit vectors, they can be eliminated from the equation. The integrals were calculated using Gauss quadrature method with Gauss integration order of $n=3$ and each finite element has 27 Gauss integration points. The effective material properties due to the material grading were calculated at each Gauss integration point. Finite element formulation in Eq. 36 can be written as,

$$({}^t\mathbf{K}_L + {}^t\mathbf{K}_{NL})\mathbf{U} = {}^{t+\Delta t}\mathbf{R} - {}^t\mathbf{F} \quad (37)$$

where ${}^t\mathbf{K}_L$ and ${}^t\mathbf{K}_{NL}$ are linear and nonlinear strain incremental stiffness matrices, respectively. ${}^t\mathbf{F}$ are nodal point loads at time t and ${}^{t+\Delta t}\mathbf{R}$ is deformation following external forces. The unknown displacements in Eq. 37 were calculated using Newton-Raphson and modified Newton-Raphson iteration methods together.

5. Numerical analysis

A code in Java SE [39] programming language was developed in the Netbeans [40] environment in order to perform numerical analyses. The code produces the result with the formulation given above. Three-dimensional visualization of the plastic region propagation was carried out through the code created in the Matlab [41] environment.

The reliability of the code developed based on the given formulation was determined by comparing the work of Nguyen et al. [42], examining the nonlinear bending behavior of elastoplastic FG beams. The clamped beam shown in Fig. 7 is functionally graded from ceramic to metal using the power law in the height direction. Axial stress values were compared at points P1 and P2 shown on the beam with their coordinates on Fig. 7. Different power law distribution parameter values (n) were used in this comparison. Additionally, two different external load values were used. The results are shown in Table 1. The maximum difference between stresses was calculated as 4.5%. In the normalized load - dimensionless displacement graph shown in Fig. 8, the difference between the maximum dimensionless displacements is 4.6%.

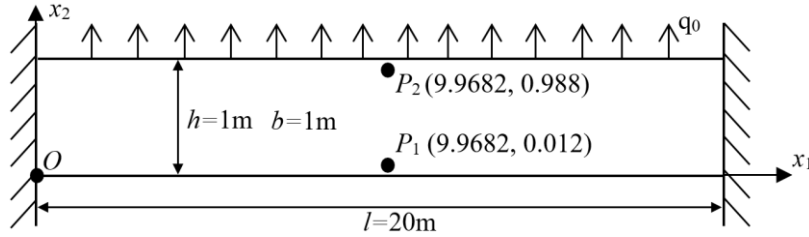


Fig. 7. Problem geometry used in comparison [42].

Table 1. Axial stresses under uniformly distributed load (MPa).

n	Point	q_0 (kN/m)					
		1500			3500		
		Code	Nguyen et al. [42]	Difference %	Code	Nguyen et al. [42]	Difference %
0.5	P_1	-95.59	-92.83	2.97	-219.85	-213.43	3.01
0.5	P_2	208.64	216.40	3.58	493.81	512.67	3.68
2	P_1	-113.97	-114.96	0.86	-262.62	-266.12	1.31
2	P_2	258.26	268.52	3.82	602.18	628.08	4.12
5	P_1	121.94	-122.83	0.72	-282.63	-287.43	1.67
5	P_2	295.64	309.56	4.49	651.76	681.06	4.30

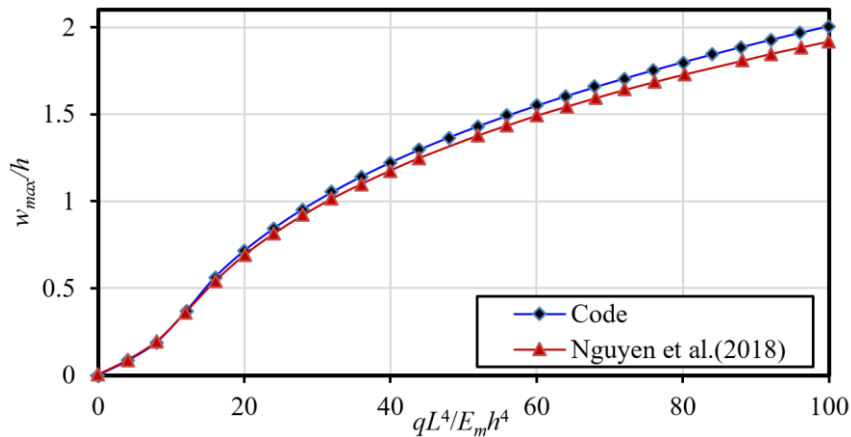


Fig. 8. Variation of maximum dimensionless displacement with normalized load [42].

5.1. Functionally graded square section beam

The torsion behavior of the functionally graded beams given in Section 1 has been examined numerically. The dimensions of the beam shown in Fig. 9 are $b = 210$ mm, $h = 210$ mm, and $l = 1440$ mm. Torsional loading was applied using deformation-following forces located on the rigid elements. Since axial displacements are not prevented, plane sections no longer remain plane. The section corresponding to the $x_1=0$ plane, where the load is

applied to the FG beam, is named CS1. The behavior was examined by applying a torsional loading that would cause this section to rotate around the longitudinal axis by $\phi = 12.5^\circ$. Stress values were read in Gaussian points. At each load step, the load increment that would create the same angular deformation increment was calculated by extrapolation and applied to the system.

1617 finite elements were used in the analysis. Finite element dimensions are $b_e=30$ mm, $h_e=30$ mm, and $l_e=45$ mm. 2176 nodal points and 43659 Gauss integral points were created.

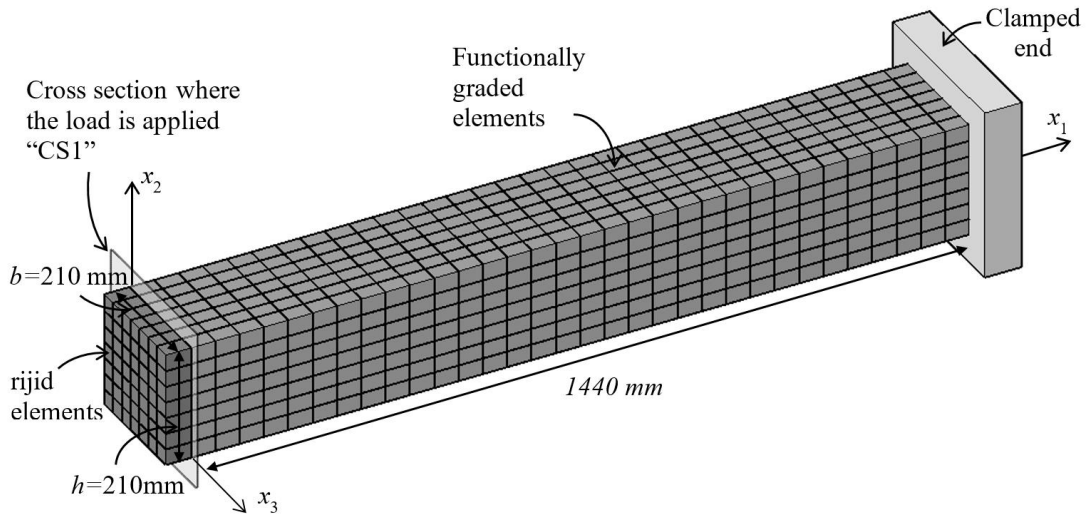


Fig. 9. Finite element model used in numerical analysis.

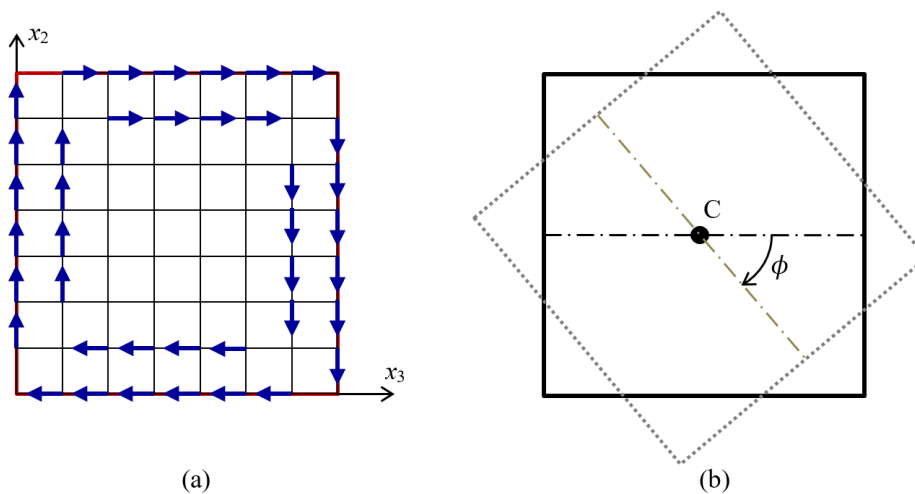


Fig. 10. (a) Loading to create torsional moment; (b) Angle of rotation.

In the beam with one end clamped, the loads deformation-following loading were applied as concentrated forces on the nodes in the CS1 section at the free end, as shown in Fig. 10a. Thus, a torsional moment is created.

Elastoplastic properties for the TiB-Ti (Titanium Boride-Titanium) material used in the analysis [12] are $E_c=375$ GPa (TiB), $E_m=107$ GPa (Ti), $E_0=14$ GPa, $\sigma_0=450$ MPa, $q=4.5$ GPa, $\nu_m=0.34$, and $\nu_c=0.14$. Rigid elements were considered as linear elastic and their mechanical properties are $E=50000$ GPa and $\nu=0.001$.

The variation of the normalized load with the angle of rotation of the CS1 section is shown in Fig. 11 for different beam gradings. With the onset of plastic deformation, the loading-rotation angle graph slope decreases. The decrease in the slope of the graph started when 80% of the total load level was reached for the all-metal beam. The decrease in the slope of the graph started when the load level reached approximately 60% for the HP-beam. For other beams, a decrease in the slope of the graph was observed between these two values. In Appendix A, the propagation of the plastic region in the beams is shown in detail by visualizing the results for different rotation angles. The HP beam with the largest torsional stiffness starts plastic deformation at the smallest rotation angle. In the metal beam with the lowest torsional stiffness, the plastic flow starts at large rotation angle.

Table 2. Torsional moment values versus the angle (ϕ) formed at CS1 section.

FD beam torsional moment (kNm)					
ϕ	Metal	HP n=1	LP n=1	HS	HBS
0.5	58.06	107.26	96.73	97.25	88.53
1.0	116.13	214.52	193.47	194.50	177.07
1.5	174.19	321.20	290.20	291.75	265.60
2.0	232.25	424.60	386.93	388.12	354.13
2.5	290.32	518.61	481.89	480.41	442.66
3.0	348.38	598.32	559.60	566.71	531.19
3.5	406.44	666.31	614.80	646.09	615.30
4.0	463.94	723.16	657.55	713.31	665.56
4.5	514.35	770.65	690.51	757.59	695.36
5.0	555.27	812.31	718.52	789.48	720.52
5.5	588.49	849.16	742.98	817.26	744.00
6.0	616.12	882.19	765.53	842.97	764.81
6.5	639.56	913.42	786.14	866.62	783.40
7.0	659.62	943.28	805.48	888.84	801.25
7.5	675.80	971.46	823.90	910.14	818.31
8.0	691.30	998.91	841.68	930.55	834.61
8.5	704.96	1025.84	858.79	950.78	850.56
9.0	717.41	1052.13	875.48	970.90	866.25
9.5	729.18	1078.11	891.88	990.92	881.90
10.0	740.79	1103.70	908.03	1010.81	897.46
10.5	751.62	1128.92	923.99	1030.63	912.93
11.0	761.65	1153.79	939.81	1050.37	928.33

11.5	771.38	1178.36	955.52	1069.98	943.71
12.0	780.72	1202.71	971.13	1089.48	959.05
12.5	789.91	1226.94	986.65	1108.89	974.36

Torsional moments corresponding to the rotation angle ϕ in the CS1 section, obtained by grading with different functions for beams with equal amounts of metal and ceramic materials in total, are given in Table 2. The moment value required to create the same angle of twist was highest for the HP-beam. As the ceramic ratio on the outer walls increases and the effective material modulus of elasticity increases, the resistance to torsion increases. The HP-beam is followed by the HS-beam. Among the FG beams graded on the transverse cross-section, the HBS-beam, which has metal on all four outer walls and turns to ceramic towards the middle of the section, shows the lowest resistance to torsion.

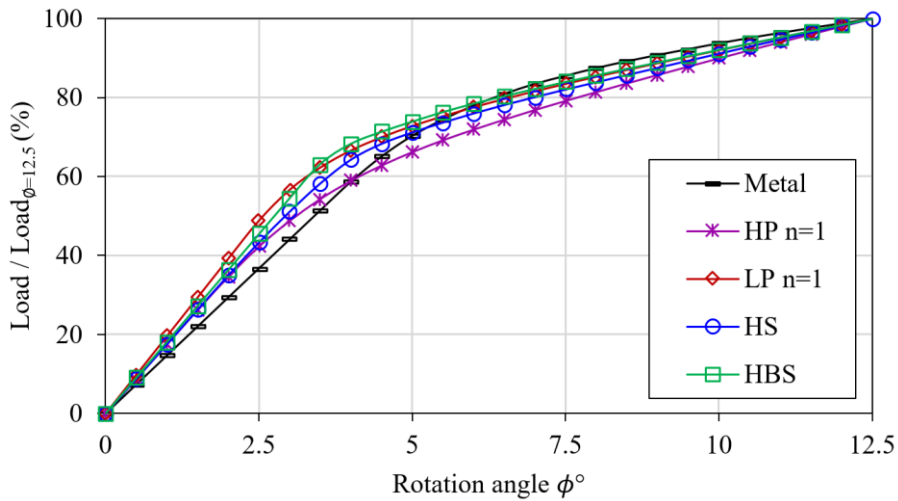


Fig. 11. Variation of the normalized load with the rotation angle of the beam end.

The torsion-induced angular deformation along the FG beam, from CS1 section to the clamped end, for $\phi=12.5^{\circ}$ is given in Fig. 12. For beams made of pure metal and graded in the cross-sectional plane, the angle variation along the beam is linear, whereas for LP-beams the variation is non-linear. In these beams, the angle variation along the beam for different values of n is also non-linear as shown in Fig. 13, and the curvature of the graph increases with increasing ceramic content in the beam. If the ceramic volume fraction increases in a section, the angle of rotation decreases.

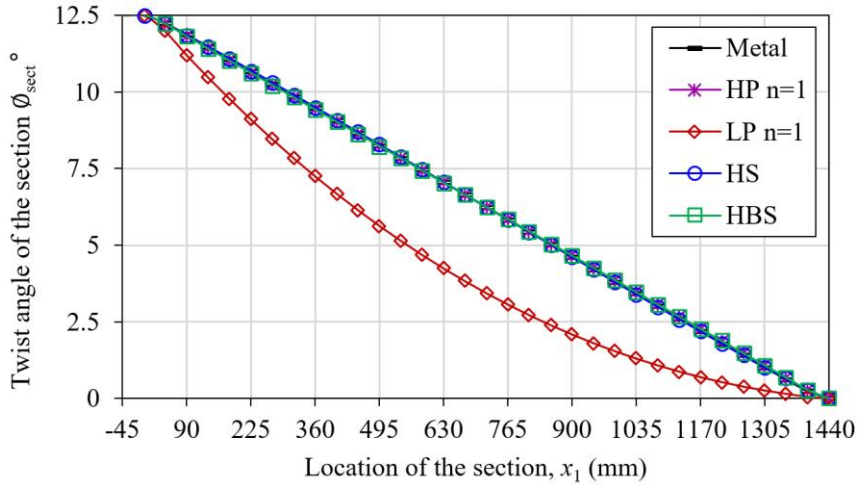


Fig. 12. Variation of angle of twist along the beam length for different FG beams.

In the region where torsional load is applied on FG beams, the change of s_{12} shear stresses in the x_3 direction for $\phi=12.5^\circ$ at Gaussian points on the horizontal line passing through the center of the section ($x_2=105$ mm) is given in Fig. 14. Unlike homogeneous beams, in functionally graded beams, there are cases where the largest shear stresses do not occur at the outer boundaries of the section. In the HBS-beam, the largest shear stresses occur in the inner region of the section. Fig. 15 shows that the largest s_{13} shear stresses read at the Gaussian points on the vertical line passing through the center of the same section ($x_3=105$ mm) do not occur at the outer boundaries of the section for HBS- and HS-beams. This behavior, which is different from homogeneous beams, can also be seen in the s_{12} shear stress values read at the Gaussian points on the diagonal of the section in this region as shown in Table 3.

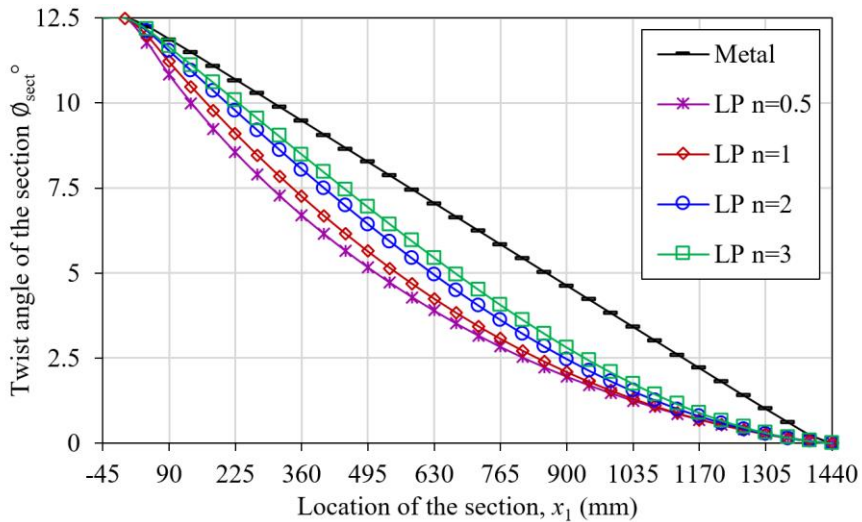


Fig. 13. Variation of angle of twist along the beam length for LP-beams.

Table 3. s_{12} shear stress values at Gaussian points on the cross-section diagonal for $\phi=12.5^\circ$ in the region where the load is applied.

Point	Coordinates (mm)			s_{12} shear stress (MPa)				
	x_1	x_2	x_3	Metal	HP n=1	LP n=1	HS	HBS
1	5.072	3.381	3.381	180.398	142.221	214.506	191.653	183.971
2	5.072	26.619	26.619	170.765	140.885	199.092	179.993	186.106
3	5.072	33.381	33.381	170.689	141.063	197.798	181.179	192.598
4	5.072	56.619	56.619	159.782	123.158	179.359	166.570	206.610
5	5.072	63.381	63.381	158.174	115.967	175.330	162.131	216.493
6	5.072	86.619	86.619	71.646	66.484	151.111	157.045	224.011
7	5.072	105.0	105.0	0.0	-38.559	0.0	0.0	0.0
8	5.072	123.381	123.381	-71.646	-204.215	-151.111	-157.045	-224.011
9	5.072	146.619	146.619	-158.174	-284.833	-175.330	-162.131	-216.493
10	5.072	153.381	153.381	-159.782	-292.982	-179.359	-166.570	-206.610
11	5.072	176.619	176.619	-170.689	-395.976	-197.798	-181.179	-192.598
12	5.072	183.381	183.381	-170.765	-419.03	-199.092	-179.993	-186.106
13	5.072	206.619	206.619	-180.398	-1156.22	-214.506	-191.653	-183.971

In the HP-beam, unlike other FG beams and the metal beam, shear stresses are not zero at the center of the section geometry, as seen in Fig. 14 for s_{12} and in Fig. 15 for s_{13} . This can also be seen for point 7 on the HP-beam in Table 3. The shift of the point where the stress is zero increases as the power law distribution coefficient (n) changes to increase the ceramic ratio, as shown in Fig. 16.

This situation occurs when the cross-section is not symmetric in terms of volume fractions with respect to both horizontal and vertical axes. This causes the section to behave as a geometrically non-symmetrical section. The shear center is no longer the geometric center of the section. As shown in Fig. 17, the cross-section is displaced in the transverse direction, in the direction of the material gradation relative to the initial position, towards the material with smaller effective material properties. Unlike other beams, these transverse displacement values in the HP-beam can reach 3% of the section height, as seen in Fig.18.

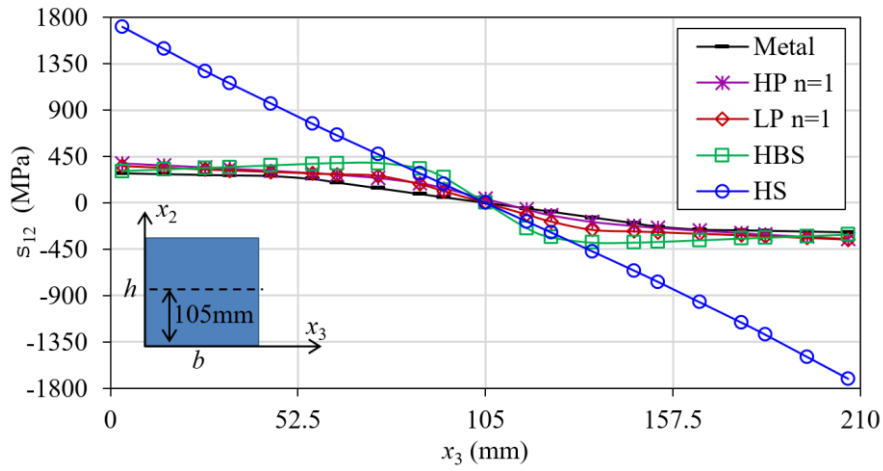


Fig. 14. Variation of shear stress (s_{12}) at $x_2=105$ mm with x_3 in the loading region.

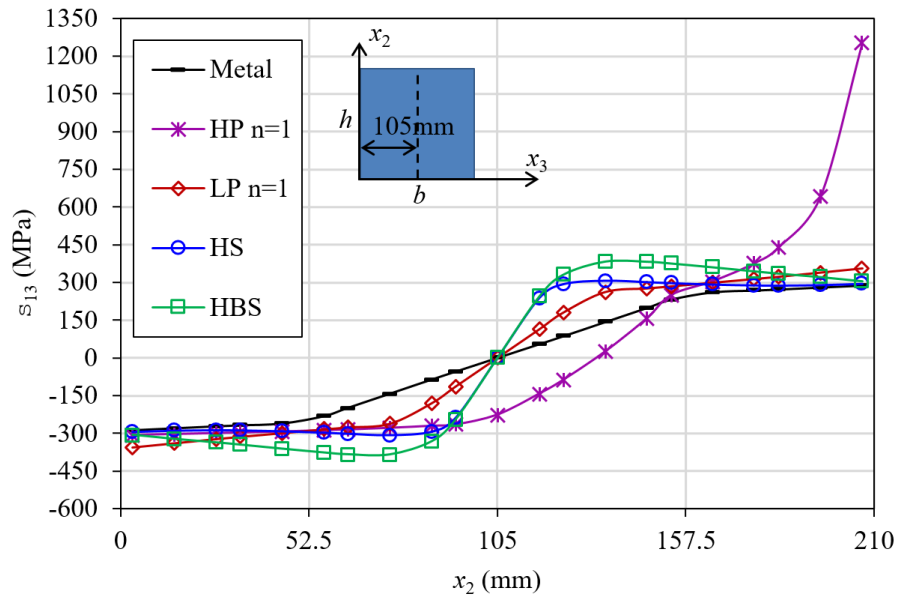


Fig. 15. Variation of shear stress (s_{13}) at $x_3=105$ mm with x_2 in the loading region.

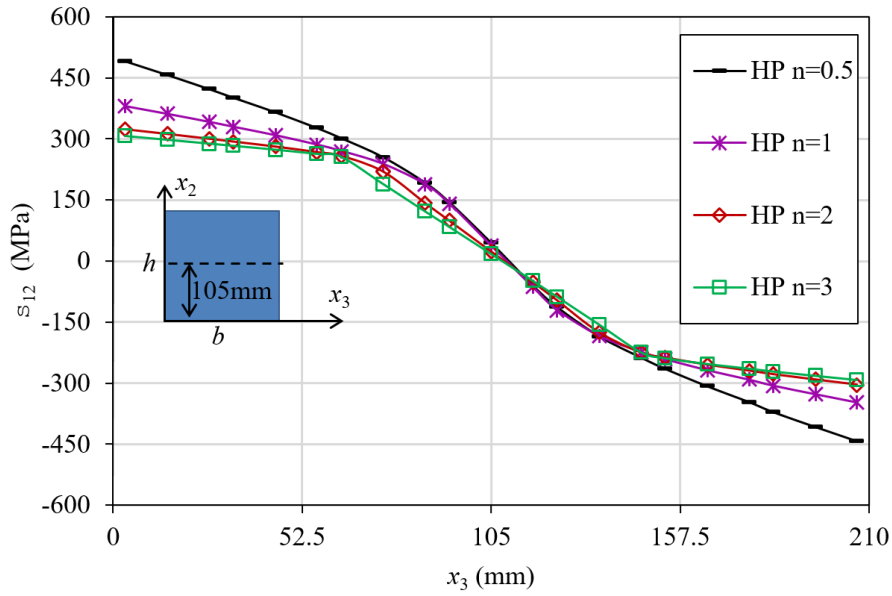


Fig. 16. Variation of shear stress (s_{12}) at $x_2=105$ mm with x_3 in the loading region for HP-beams.

Fig. 19 shows the axial displacements at the nodes on the diagonal of the CS1 section for the rotation angle of $\phi=12.5^\circ$. The distribution of axial displacements in sections that are symmetrical with respect to any axis within the section is similar to a homogeneous metal beam. Axial displacements tend to decrease towards the middle of the section in the homogeneous beam. In the HP-beam, they are high in regions where the metal ratio is high and low in regions where the ceramic ratio is high.

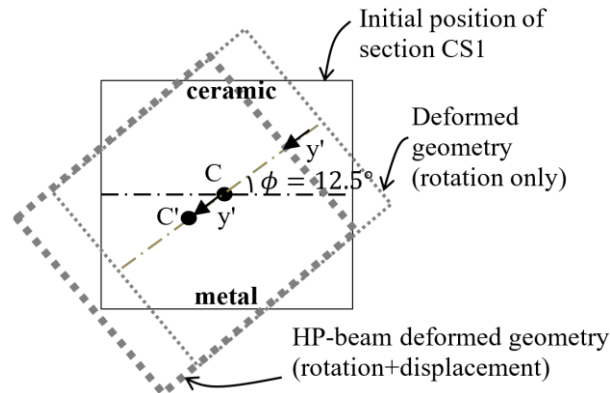


Fig. 17. CS1 section transverse displacement in the direction of material gradation for HP-beams.

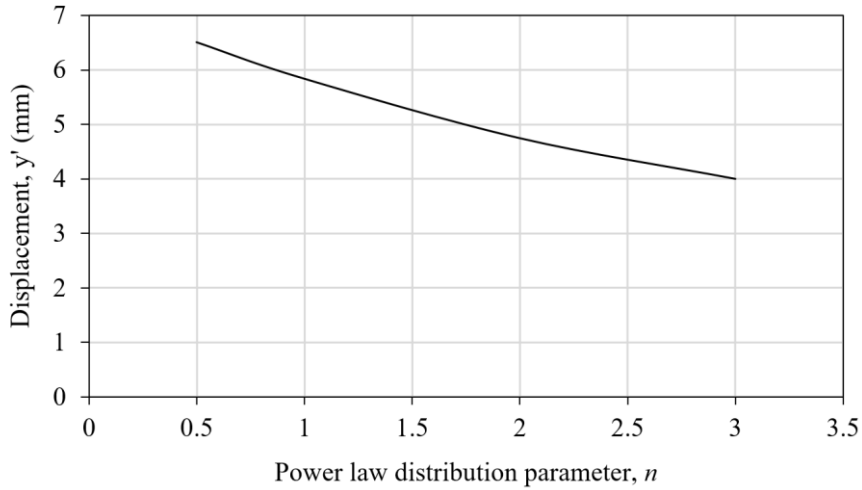


Fig. 18. HP-beam CS1 section transverse displacement, y' (mm), for different n values at $\phi=12.5^\circ$.

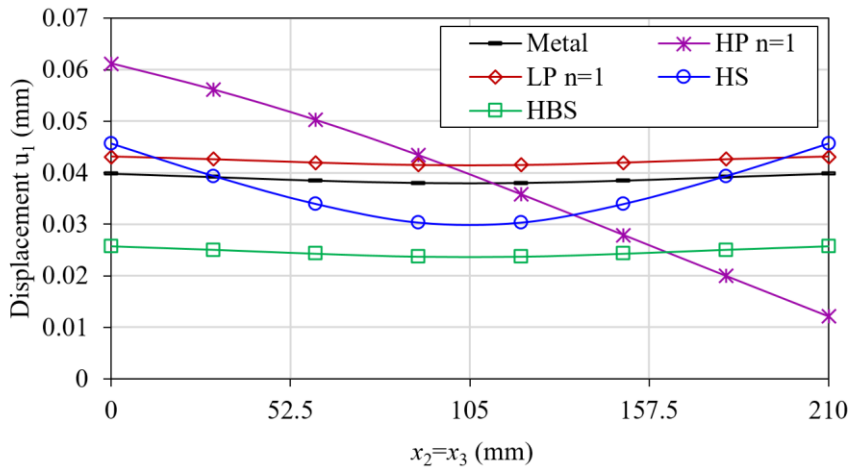


Fig. 19. Axial displacements at points on the cross-section diagonal for $\phi = 12.5^\circ$ in CS1 section.

6. Conclusion

The torsional behavior of functionally graded ceramic-metal elastoplastic beams was investigated using the nonlinear finite element method. Effective elastoplastic properties were obtained using the TTO scheme. The nonlinear finite element formulation was created with the updated Lagrangian formulation based on the virtual displacement principle. An iterative solution based on Newton-Raphson and updated Newton-Raphson methods was used to solve the nonlinear equation system. Effective material properties were calculated at Gaussian points.

The torsional behavior of FG beams differs from homogeneous beams depending on the material distribution used. According to the material distribution, the largest shear stresses are not at the outer boundaries of the section, unlike the homogeneous beam. In the FG beam, graded from metal to ceramic from outer walls towards the middle

of the section, with a sinusoidal function, the largest shear stresses occur in the region close to the mid-region of the section. The HP-beam, which is graded from ceramic to metal in the direction of the cross-section height according to the power law, is displaced in the transverse direction relative to its initial position under torsional loads, unlike the homogeneous beam and the FG beams that have two or more symmetries in the section plane. In addition, shear stresses are not zero in the center of the section. In the LP-beam with material grading along the longitudinal direction, the change of the rotation angle along the beam, unlike other beams, is not linear and varies according to the material distribution.

The distribution of the plastic regions in FG beams was also examined for different material distributions. Although the distribution of the plastic region in the LP-beam graded in the axial direction is similar to the homogeneous beam, in the beams graded in the section plane, the distribution of the plastic region varies depending on the material distribution. The plastic region shifts towards ceramic-dense regions with higher effective Young modulus. However, yielding begins close to the outer boundaries of the section.

Acknowledgements

This research received no specific grants from any funding agency in public, commercial or non-profit sectors.

References

- [1] M. Koizumi, "FGM activities in Japan," *Composites Part B*, vol. 28, no. 1, pp. 1-4, 1997, doi: 10.1016/S1359-8368(96)00016-9.
- [2] T. Hirai, "Functional gradient materials," in. *Materials Science and Technology*, 3 b., vol. 17B, R. J. Brook, Ed., Weinheim, VCH Verlagsgesellschaft mbH, 1996, pp. 293-341.
- [3] S. H. Chi and Y. L. Chung, "Mechanical behavior of functionally graded material plates under transverse load-Part I: Analysis," *International Journal of Solids and Structures*, vol. 43, no. 13, pp. 3657-3674, June 2006, doi: 10.1016/j.ijsolstr.2005.04.011.
- [4] F. Tornabene and E. Viola, "Free vibrations of four-parameter functionally graded parabolic panels and shells of revolution," *European Journal of Mechanics A/Solids*, vol. 28, no. 5, pp. 991-1013, Sept. 2009, doi: 10.1016/j.euromechsol.2009.04.005.
- [5] V. Boggarapu, R. Gujjala, S. Ojha, S. Acharya, P. V. Babu, S. Chowdary and D. k. Gara, "State of the art in functionally graded materials," *Composite Structures*, vol. 262, p. 113596, April 2021, doi: 10.1016/j.compstruct.2021.113596.
- [6] R. Hill, "A self-consistent mechanics of composite materials", *J. Mech. Phys. Solids*, vol. 13, no. 4, pp. 213-222, Aug. 1965, doi: 10.1016/0022-5096(65)90010-4.
- [7] T. Mori and K. Tanaka, "Average stress in matrix and average elastic energy of materials with misfitting inclusions," *Acta Metallurgica*, vol. 21, no. 5, pp. 571-574, May 1973, doi: 10.1016/0001-6160(73)90064-3.
- [8] M. M. Gasik and K. R. Lilius, "Evaluation of properties of W-Cu functional gradient materials by micromechanical model," *Computational Materials Science*, vol. 3, no. 1, pp. 41-49, Sept. 1994, doi: 10.1016/0927-0256(94)90151-1.
- [9] T. Reiter and G. J. Dvorak, "Micromechanical models for graded composite materials: II. thermomechanical loading," *J. Mech. Phys. Solids*, vol. 46, no. 9, pp. 1655-1673, Sept. 1998, doi: 10.1016/S0022-5096(97)00039-2.
- [10] I. Tamura, Y. Tomota and H. Ozawa, "Strength and ductility of Fe-Ni-C alloys composed of austenite and martensite with various strength," *Proceeding of the Third International Conference on Strength of Metals and Alloys*, Cambridge Institute of Metals, vol. 1, pp. 611-615, 1973.
- [11] R. L. Williamson, B. H. Rabin and J. T. Drake, "Finite element analysis of thermal residual stresses at graded ceramic metal interfaces. Part I. Model description and geometrical effects," *Journal of Applied Physics*, vol. 74, pp. 1310-1320, July 1993, doi: 10.1063/1.354910.
- [12] H. Huang and Q. Han, "Elastoplastic buckling of axially loaded functionally graded material cylindrical shells," *Composite Structures*, vol. 117, pp. 135-142, Nov. 2014, doi: 10.1016/j.compstruct.2014.06.018.
- [13] Y. Zhang, H. Huang and Q. Han, "Buckling of elastoplastic functionally graded cylindrical shells under combined compression and pressure," *Composites: Part B*, vol. 69, pp. 120-126, Feb. 2015, doi: 10.1016/j.compositesb.2014.09.024.
- [14] H. Zafarmand and M. Kadkhodayan, "Nonlinear material and geometric analysis of thick functionally graded plates with nonlinear strain hardening using nonlinear finite element method," *Aerospace Science and Technology*, vol. 92, pp. 930-944, Sept. 2019, doi: 10.1016/j.ast.2019.07.015.
- [15] F. J. Rooney and M. Ferrari, "Torsion and flexure of inhomogeneous elements," *Composites Engineering*, vol. 5, no. 7, pp. 901-911, 1995, doi: 10.1016/0961-9526(95)00043-M.
- [16] C. O. Horgan and A. M. Chan, "Torsion of functionally graded isotropic linearly elastic bars," *Journal of Elasticity*, vol. 52, pp. 181-199, Aug. 1998, doi: 10.1023/A:1007544011803.
- [17] C. O. Horgan, "On the torsion of functionally graded anisotropic linearly elastic bars," *IMA Journal of Applied Mathematics*, vol. 72, pp. 556-562, Oct. 2007, doi: 10.1093/imamat/hxm027.
- [18] R. C. Batra, "Torsion of a functionally graded cylinder," *AIAA Journal*, vol. 44, no. No.6, pp. 1363-1365, June 2006, doi: 10.2514/1.19555.
- [19] U. Anita, "Implementation of the method of fundamental solutions and homotopy analysis method for solving a torsion problem of a rod

- made of functionally graded material,” *Advanced Materials Research*, vols. 123-125, pp. 551-554, Aug. 2010, doi: 10.4028/www.scientific.net/AMR.123-125.551.
- [20] M. R. Hematiyan and E. Estakhrian, “Torsion of functionally graded open-section members,” *International Journal of Applied Mechanics*, vol. 4, no. 2, p. 1250020, June 2012, doi: 10.1142/S1758825112500202.
- [21] T. T. Nguyen, N. I. Kim and J. Lee, “Analysis of thin-walled open-section beams with functionally graded materials,” *Composite Structures*, vol. 138, pp. 75-83, March 2016, doi: 10.1016/j.compstruct.2015.11.052.
- [22] I. Ecdesi and A. Baksa, “Torsion of Functionally Graded Anisotropic Linearly Elastic Circular Cylinder,” *Engineering Transactions*, vol. 66, no. 4, pp. 413-426, 2018, doi: 10.24423/EngTrans.923.20181003.
- [23] G. J. Nie, A. Pydah and R. C. Batra, “Torsion of bi-directional functionally graded truncated conical cylinders,” *Composite Structures*, vol. 210, pp. 831-839, Feb. 2019, doi: 10.1016/j.compstruct.2018.11.081.
- [24] E. T. Akinlabi, M. N. Mikhin and E. V. Murashkin, “Functionally graded prismatic triangular rod under torsion,” *Journal of Physics: Conf. Series*, vol. 1474, p. 012003, 2020, doi: 10.1088/1742-6596/1474/1/012003.
- [25] I. Ecdesi, “Non-uniform torsion of functionally graded anisotropic bar of an elliptical cross section,” *Acta Mech*, vol. 231, pp. 2947-2953, July 2020, doi: 10.1007/s00707-020-02682-y.
- [26] G. C. Tsiatas and N. G. Babouskos, “Elastic-plastic analysis of functionally graded bars under torsional loading,” *Composite Structures*, vol. 176, pp. 254-267, Sept. 2017, doi: 10.1016/j.compstruct.2017.05.044.
- [27] M. Aminbaghai, J. Murin, V. Kutis, J. Hrabovsky, M. Kostolani and H. A. Mang, “Torsional warping elastostatic analysis of FGM beams with longitudinally varying material properties,” *Engineering Structures*, vol. 200, p. 109694, Dec. 2019, doi: 10.1016/j.engstruct.2019.109694.
- [28] P. K. Singh, M. Kumar and S. Mishra, “Finite element analysis of functionally graded bar under torsional load,” *Materials Today: Proceedings*, vol. 56, pp. 2960-2966, 2022, doi: 10.1016/j.matpr.2021.11.012.
- [29] X. Chen, G. Nie and Z. Wu, “Non-uniform torsion analysis of functionally graded beams with solid or thin-walled section using hierarchical Legendre expansion functions,” *Mechanics of Advanced Materials and Structures*, vol. 29, no. 14, pp. 2074-2097, 2022, doi: 10.1080/15376494.2020.1851828.
- [30] E. Mahmoodi and P. Malekzadeh, “Analytical solutions of multiple cracks and cavities in a rectangular cross-section bar coated by a functionally graded layer under torsion,” *Arch Appl Mech*, vol. 91, pp. 2189-2209, May 2021, doi: 10.1007/s00419-020-01877-y.
- [31] I. Ecdesi and A. Baksa, “Saint-Venant torsion of functional graded orthotropic piezoelectric hollow circular cylinder,” *International Journal on Applied Physics and Engineering*, vol. 2, pp.22-27, 2023, doi: 10.37394/232030.2023.2.4.
- [32] F. Mehralian and Y. T. Beni, “Size-dependent torsional buckling analysis of functionally graded cylindrical shell,” *Composites*, vol. Part B, no. 94, pp. 11-25, June 2016, doi: 10.1016/j.compositesb.2016.03.048.
- [33] T.-T. Nguyen, P. T. Thang and J. Lee, “Flexural-torsional stability of thin-walled functionally graded open-section beams,” *Thin-Walled Structures*, vol. 110, pp. 88-96, Jan. 2017, doi: 10.1016/j.tws.2016.09.021.
- [34] Y. Wang, C. Feng, Z. Zhao, F. Lu and J. Yang, “Torsional buckling of graphene platelets (GPLs) reinforced functionally graded cylindrical shell with cutout,” *Composite Structures*, vol. 197, pp. 72-79, Aug. 2018, doi.org/10.1016/j.compstruct.2018.05.056.
- [35] M. Bocciarelli, G. Bolzon and G. Maier, “A constitutive model of metal-ceramic functionally graded material behavior: Formulation and parameter identification,” *Computational Materials Science*, vol. 43, pp. 16-26, July 2008, doi: 10.1016/j.commatsci.2007.07.047.
- [36] D. Owen and E. Hinton, *Finite Elements in Plasticity: Theory and practice*. Swansea: Pineridge Press Limited, 1980.
- [37] K.-J. Bathe, *Finite Element Procedures*. New Jersey: Prentice-Hall Inc., 1996.
- [38] Z.-H. Jin, G. H. Paulino and R. H. D. Jr., “Cohesive fracture modeling of elastic-plastic crack growth in functionally graded materials,” *Engineering Fracture Mechanics*, vol. 70, no. 14, pp. 1885-1912, Sept. 2003, doi: 10.1016/S0013-7944(03)00130-9.
- [39] Oracle Corporation, *JAVA SE*. Version 18.0.0, Programming Language.
- [40] The Apache Software Foundation, *NETBEANS IDE*. Version 13, Integrated Development Environment.
- [41] The Math Works Inc., *MATLAB*. Version 2023a, Computer Software.
- [42] D. K. Nguyen, K. V. Nguyen, V. M. Dinh, B. S. Gan and S. Alexandrow, “Nonlinear bending of elastoplastic functionally graded ceramic-metal beams subjected to nonuniform distributed loads,” *Applied Mathematics and Computation*, vol. 333, pp. 443-459, Sept. 2018, doi: 10.1016/j.amc.2018.03.100.

Appendix A. Plastic region propagation

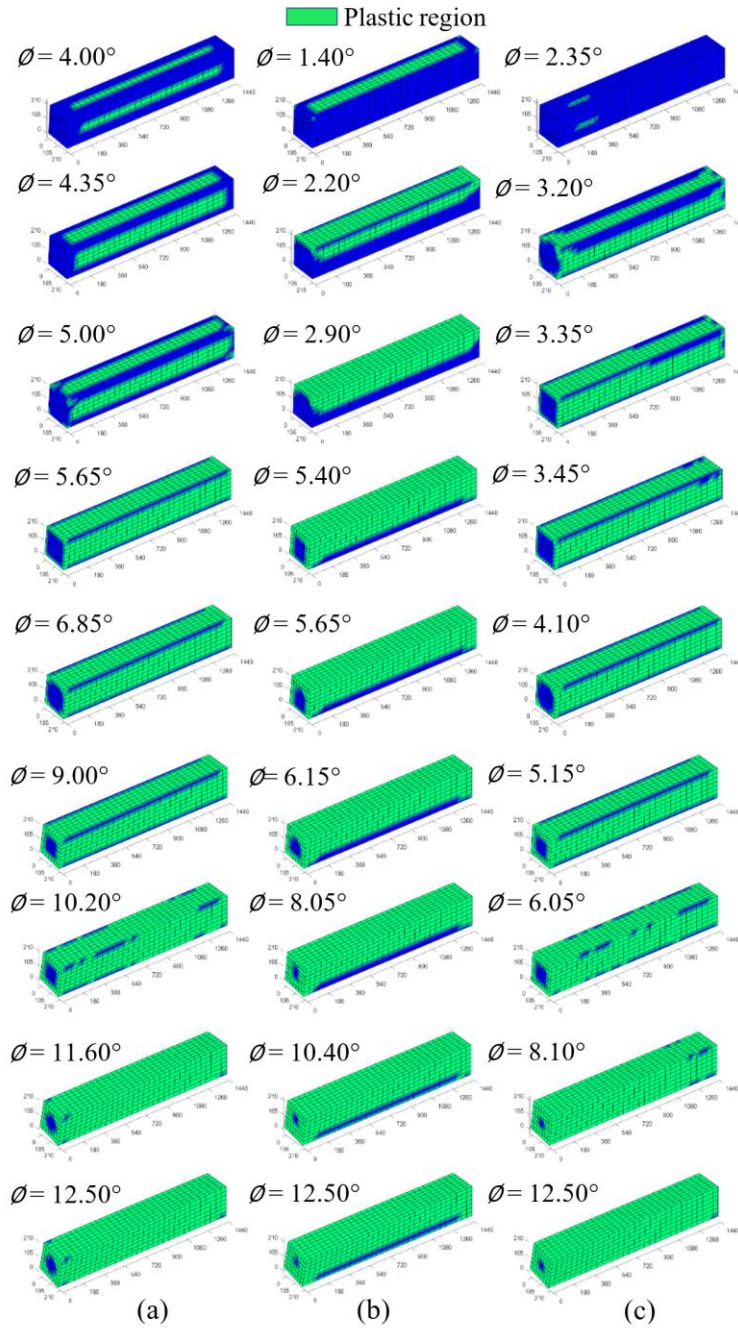


Fig. A1. Distribution of plastic regions in FG beams (a) metal; (b) HP $n=1$; (c) LP $n=1$.

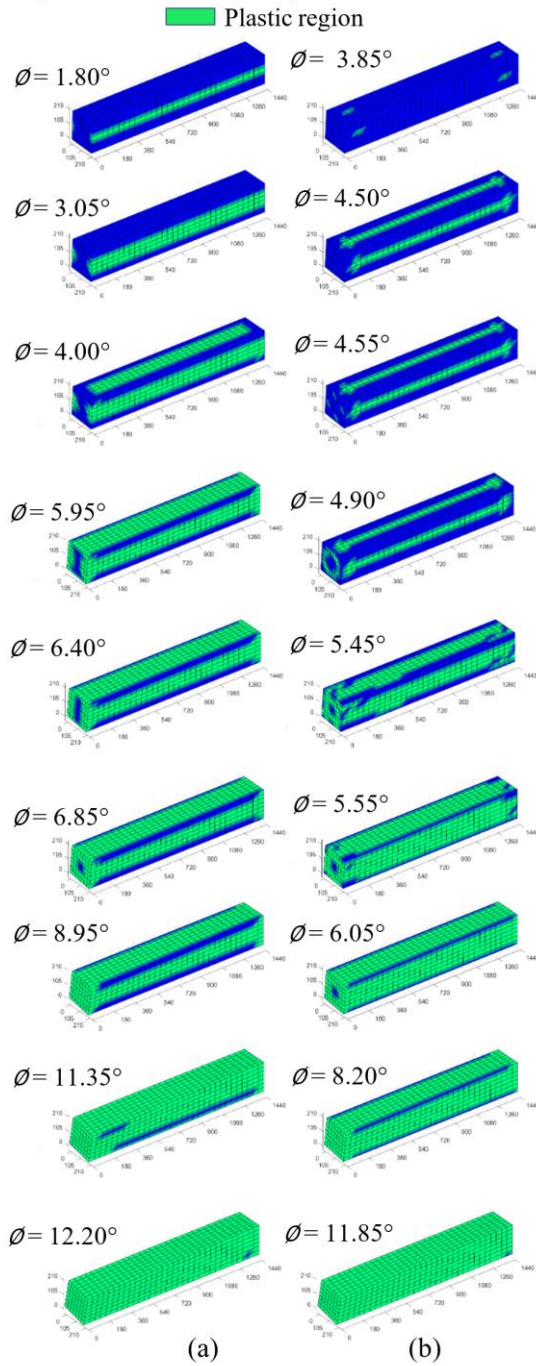


Fig. A2. Distribution of plastic regions in FG beams (a) HS; (b) HBS.



Contents lists available at *Dergipark*

Journal of Scientific Reports-A

journal homepage: <https://dergipark.org.tr/pub/jsr-a>



E-ISSN: 2687-6167

Number 57, June 2024

RESEARCH ARTICLE

Receive Date: 04.03.2024

Accepted Date: 15.04.2024

Tribological and mechanical performance evaluation of hybrid reinforced copper composites

Esad Kaya^a, Pelin Çağım Tokat-Birgin^{b*}

^a *Eskişehir Osmangazi University, Department of Mechanical Engineering, Eskişehir, Türkiye,*
ORCID: 0000-0002-7332-6154

^b *Kütahya Dumlupınar University, Department of Metallurgy and Material Engineering, Kütahya, Türkiye,*
ORCID: 0000-0001-9806-3381

Abstract

The powder metallurgy technique is utilized in this study to produce Cu matrix hybrid composites with ZrO₂ reinforcements and graphite additives. This study compares composites' microstructural (theoretical, experimental, and relative density, phase morphology, type, chemical content), mechanical (microhardness), and tribological behavior (wear and friction) with 5, 10, and 15 wt% reinforcement, together with and without the effect of 2 wt% graphite additives. Homogenously ZrO₂ added copper alloy was successfully produced. All samples were produced at least %90 relative density. The XRD analyses also validate the phase presence of reinforcement phase. Also the graphite was added to samples which provides self-lubrication. The graphite addition improves friction behaviour. The hardness of the composites increased as the amount of ZrO₂ increased with the addition of graphite. The wear resistance of ZrO₂-added copper samples was improved between 1.32 and 4.84 times better than that of copper without reinforcement.

© 2023 DPU All rights reserved.

Keywords: Powder metallurgy; Metal matrix composites; Wear resistance; Friction

1. Introduction

Copper matrix composites have had many uses in recent years due to their superior mechanical, physical, and chemical properties [1]. Copper matrix composites are produced by adding many different reinforcement elements. Some of these are SiC [1], Al₂O₃ [2], MgO [3], and graphite composites [4]. Due to their superior thermal and electrical conductivity, copper-based metal matrix composites are very popular in the electrical and electronics industry [4]. Different carbide and oxide structures are used as reinforcement to improve both thermal and

mechanical properties [2]. Today, Cu-based composites manufacture brushes widely used in automotive applications such as door locks, starter motors, and blower motors [5-7]. As can be seen, the components mentioned are machine parts that operate at high speed and are subject to friction and wear. In the literature, the benefits of oxides integrated to the Cu structure have been revealed by different studies. Alumina particles have special qualities when distributed throughout the copper matrix, including potent strength, outstanding resistance to annealing, and high electrical and thermal conductivity. A study used the traditional and spark plasma sintering methods to generate an Al₂O₃-reinforced copper matrix in three distinct atmospheres: argon, nitrogen, and hydrogen. Using a hydrogen atmosphere, an issue of weak interfacial bonding in the nitrogen and argon atmosphere has been partially resolved. EDS analysis validates the same problem as well. The degree of bonding deteriorated during sintering in nitrogen and argon atmosphere due to the formation of Cu₂O [2]. Improvements in the Cu–Al₂O₃ system's compressive strength, hardness, and wear resistance were demonstrated by Fathy et al. [8]. A comparison was made between Cu–Al₂O₃ and copper alloy's wear resistance, and it was observed that the copper alloy without Al₂O₃ had the lowest wear resistance. Furthermore, it has been found that wear resistance increases with an increase in the Al₂O₃ ratio. The copper matrix composite samples with 2.5%, 7.5%, and 12.5% Al₂O₃ possess the following relative densities, in that order: 92%, 90%, and 88%. It is observed that the relative density is highest in pure copper alloy and lower in copper composites containing Al₂O₃, and this decrease continues as the additive ratio increases. It was determined that Brinell hardness values increased with increasing Al₂O₃ ratio. The hardness value of the pure copper alloy is 53.7HB, and the hardness of the copper matrix composite samples containing 2.5%, 7.5%, and 12.5% Al₂O₃ are 59.8HB, 67.9HB, and 79.4HB.

Due to its unique characteristics, which include high hardness, low coefficient of friction (COF), high elastic modulus, chemical inertness, and high melting point, zirconia is a ceramic material with a wide range of applications [9]. Studies using copper matrix composite materials with different reinforcements, including SiC, Y₂O₃, and TiO₂, have been published in the literature [1-4, 10, 11]. These reinforcements have significantly increased the hardness values of composite materials. Nevertheless, a literature review reveals that adding graphite to copper matrix composites increases their ability to resist friction and wear. [12, 13]. Studies have shown that graphite additive in Cu matrix composites reduces the alloy's hardness and increase wear resistance by acting as a solid lubricant. Based on this situation, the hardness of the composite samples is predicted to be increased by adding reinforcements such as ZrO₂ into the copper matrix. At the same time, the wear resistance of the samples was increased by adding 2-3% graphite by volume. The samples were made using and without the addition of ceramic reinforcement-graphite addition. The effect of graphite and ceramic additives on microstructural (SEM-EDS and XRD analysis), tribological (wear rate, friction coefficient behavior), and mechanical (hardness) performance was investigated and relatively compared.

2. Material and method

Cu powder (NaNokar, 44 µm, 99.9%), ZrO₂ (Metco, 25 µm, 99.99%), and graphite (Alfa Easer, 44 µm, 99.5 %) were prepared according to calculated stoichiometric ratios. The starting powder materials were homogenized in 10 ml polyethylene containers for 12 hours at 150 rpm using a Retsch PM 400 planetary mill machine. The samples were pressed with a Calver manual press in a diameter of 1 cm. The shaped samples were pressurized to 200 MPa using a cold isostatic press (MSE-CIP) to make them more dense. In this study, the samples were produced utilizing a Protherm tube furnace operated in an argon atmosphere for two hours at 900 °C. The experimental densities of the samples were calculated using Archimedes' method [14]. PanAnalytical X-ray diffraction (XRD) was conducted at 30 kV and 30 mA with a Cu Kα radiation source. The FEI NovaNanoSEM650 scanning electron microscope (SEM) and the EDAX Trident energy scattering X-ray spectrometry (EDS) were used concurrently. The data regarding the microstructural characteristics and the location of the reinforcement (ZrO₂ and graphite) in the matrix (Cu) of the samples were gathered. The microhardness measurement technique was performed using Future Tech FM-800 equipment. Hardness evaluation tests were done at 25 gf load and 10 seconds of dwelling time. Also, the tribological

performance of all samples was evaluated. ASTM G99 test standard was used. The pin-on-disk type test method was selected and carried out in the CSM Tribometer device. A hardened 3 mm diameter 100Cr6 bearing steel ball was used as the counterbody. 3N was used as a test load. All wear tests were performed with a 6 mm diameter projectile circle. Wear test performed at 3 cm/sec (about @ 196 RPM). The total test distance was 50 meters. During the test, the COF was recorded instantly. In order to calculate the wear rate in a volumetric loss per load and distance, a cross-section of the worn surface was measured using a Mitutoyo SJ-400 surface roughness profilometer. Gaussian filtering techniques were used to determine of the average surface profile. Subsequently, after the wear test, SEM and EDS analyses were evaluated on the worn surfaces. The wear mechanism is characterized. The chemical composition of the produced samples were added to Table 1.

Table 1. The chemical composition of the produced samples.

Sample Code	Cu (% vol.)	ZrO ₂ (%vol.)	Graphite(%vol.)
S-0	100	none	none
S-1	Balance	none	2
S-2	Balance	5	none
S-3	Balance	10	none
S-4	Balance	15	none
S-5	Balance	5	2
S-6	Balance	10	2
S-7	Balance	15	2

3. Result and discussion

The theoretical and relative densities of the samples were calculated, and experimental densities were measured. Density values are compared in Figure 1. The relative density of the copper sample S-0 is at its maximum compared to the other samples. Graphite and ceramic additives led to a decrease in the relative density. As the additional amount of ZrO₂ increases (S-2, S-3, and S-4, respectively), the relative density value is expected to decrease compared to other added compounds, while the relative densities of samples S-2 and S-3 are the same. In ceramic-reinforced metal matrix composites, 100% wetting between ceramic and metal may not be achieved. As ceramic reinforcement increases, the relative density of the composite may decrease. The relative densities of ZrO₂/graphite added copper matrix composite specimens are also expected to decrease with increasing ZrO₂ addition, while the relative density of specimen S-6 increased very slightly. S-7 showed a decrease, as expected. Considering the margins of error, there is no inconsistency in the result.

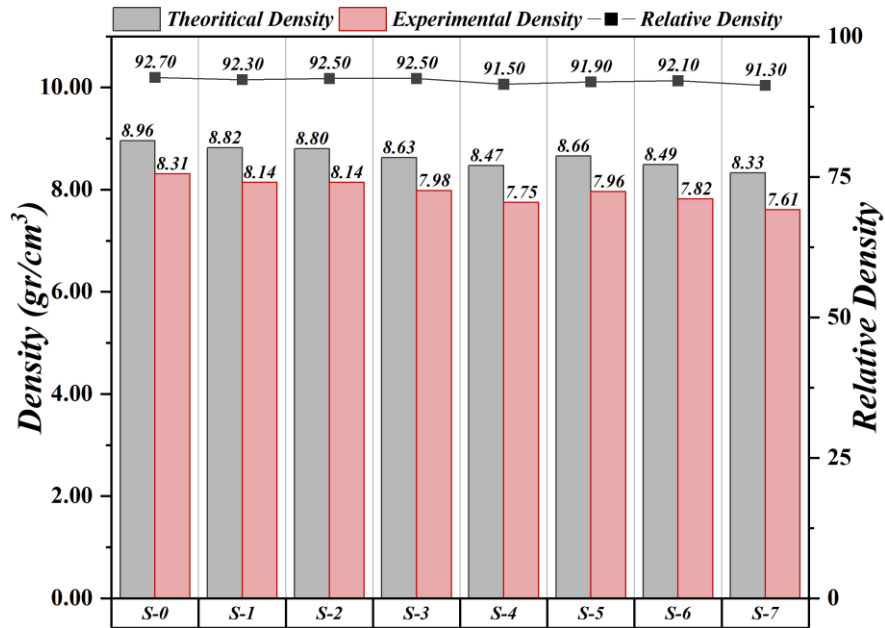


Fig. 1. Theoretical, experimental, and relative densities of ZrO₂ and ZrO₂/graphite added copper matrix composite samples.

Figure 2 shows SEM images of the composite samples. Figure 2a presents SEM images of the undoped sample, Figure 2b, 2c and 2d present SEM images of the samples containing 5%, 10% and 15% ZrO₂, respectively. The amount of ZrO₂ in the composites is directly proportional to the amount of ZrO₂ in the microstructures in the SEM images. In Figure 2b, the amount of ZrO₂ grains is relatively less, in Figure 2c it is slightly increased, and in Figure 2d it is slightly increased. The samples in Figure 2e, 2f, 2g, and 2h contain 2% graphite and 0%, 5%, 10% and 15% ZrO₂, respectively. Similar to the SEM images of the samples without graphite addition, as the amount of ZrO₂ in the graphite and ZrO₂-added composites increased, the amount of ZrO₂ grains in the microstructures also increased (figures 2f, 2g and 2h, respectively). Figure 2e shows that the grain boundaries of the graphite-containing sample are more indistinct than in Figure 2a and that the graphite is homogeneously distributed in the copper matrix. In images b, c, f, and g, it is evident that the ZrO₂ grains retain their structural integrity. In the study by Elmahdy et al., It was mentioned that due to their high melting point, high hardness, exceptional thermal stability, and chemical inertness, ZrO₂ grains are present in the Cu matrix whereas no melting occurs. It was mentioned that the reinforcement grains increase the strength of the sample by preventing the movement of dislocations [15]. The SEM images obtained in the study are similar to those in the literature. It is clear from the microstructure analysis that the samples are sintered and well-densified.

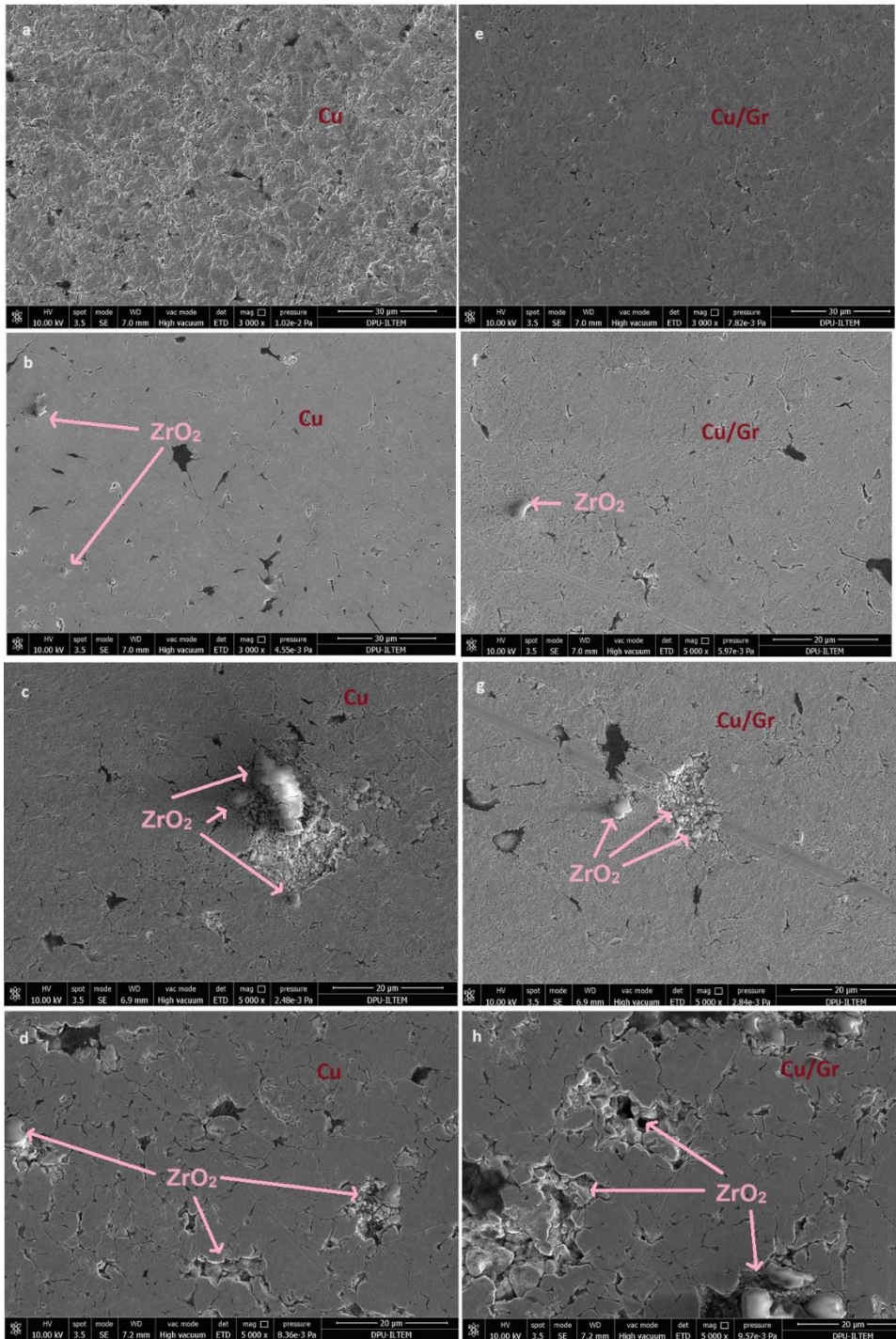


Fig. 2. SEM images of (a) S-0, (b) S-1, (c) S-2, (d) S-3, (e) S-4, (f) S-5, (g) S-6, (h) S-7.

Data from the SEM/EDX analysis in Figures 3a and 3b are shown. The principal Cu, C, O, and Zr peaks were found, which correspond to the ZrO_2 particle and Cu matrix compositions, respectively. For both samples, two spot analyses and one field analysis were performed. The peak intensities and numerical data obtained agree with the of stoichiometry composition.

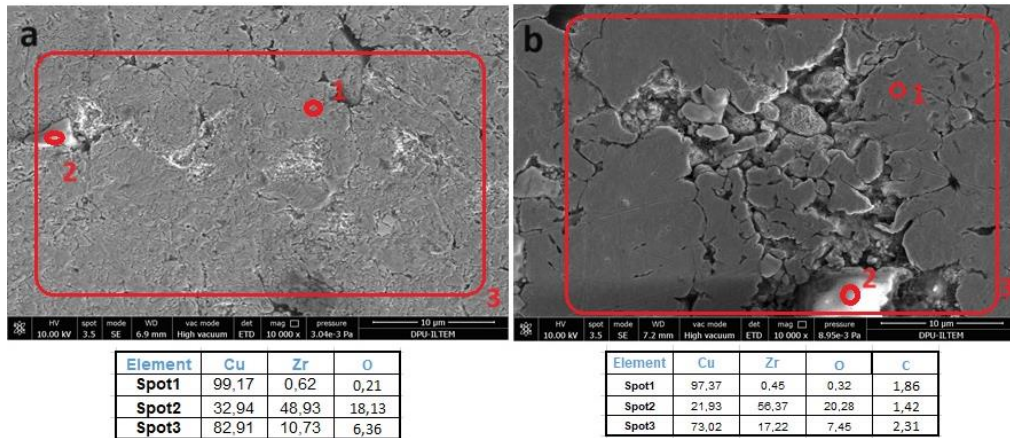


Fig. 1. SEM-EDX images of (a) S-4, (b) S-7 samples.

The field emission SEM micrograph and matching map analysis used to ascertain the distribution of the composite's elemental parts are displayed in Figure 4. The elemental components of the structure are distributed uniformly, according to the surface scan results. Nearly the entire surface is covered in copper and zirconium and are readily apparent at a particular location in the surface scan. A low level of carbon and oxygen content were also detected. The carbon content was detected as % 3.13. One can be infer that the low atomic diameter elements (such as C, B, and O) s are hard to detect precise exact chemical composition

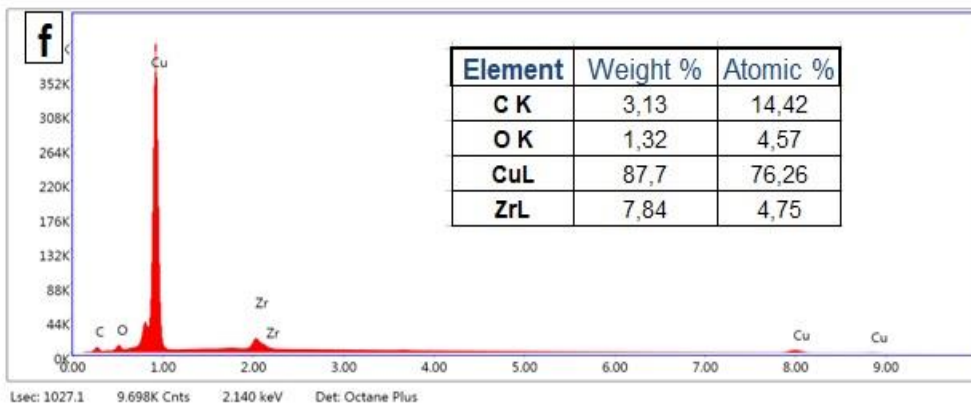
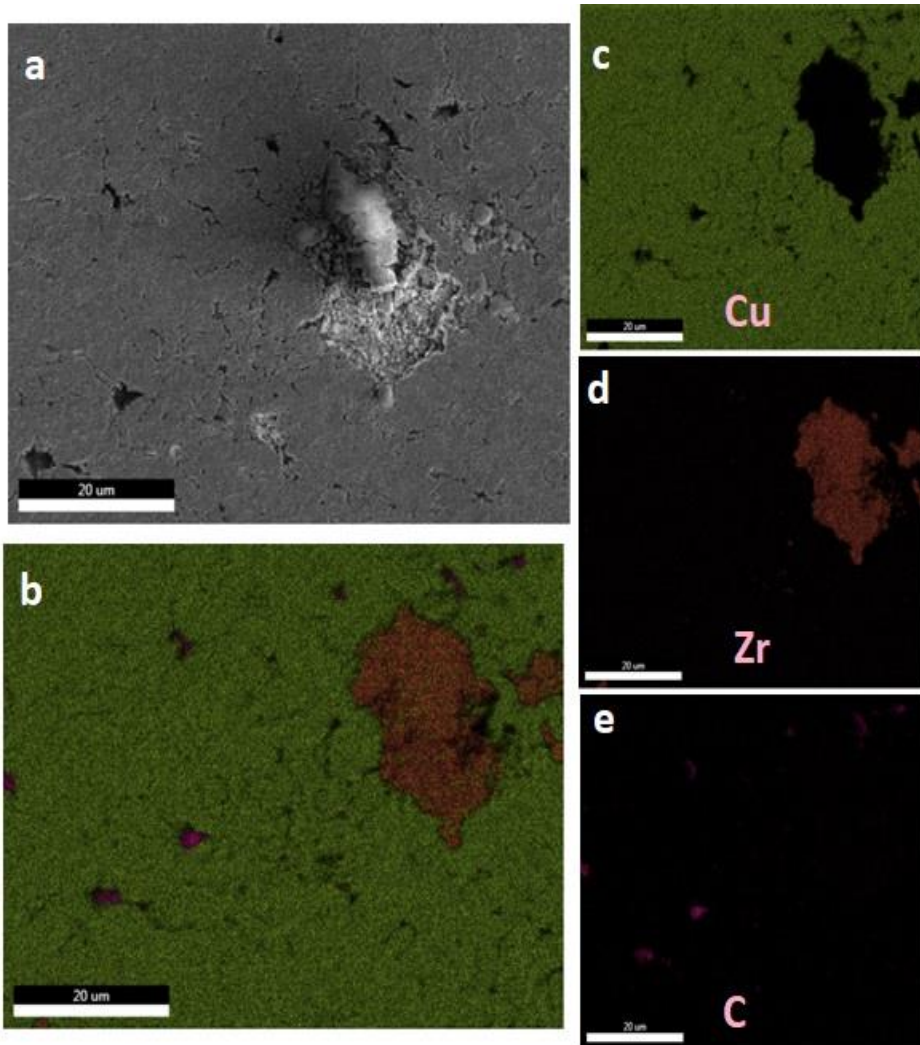
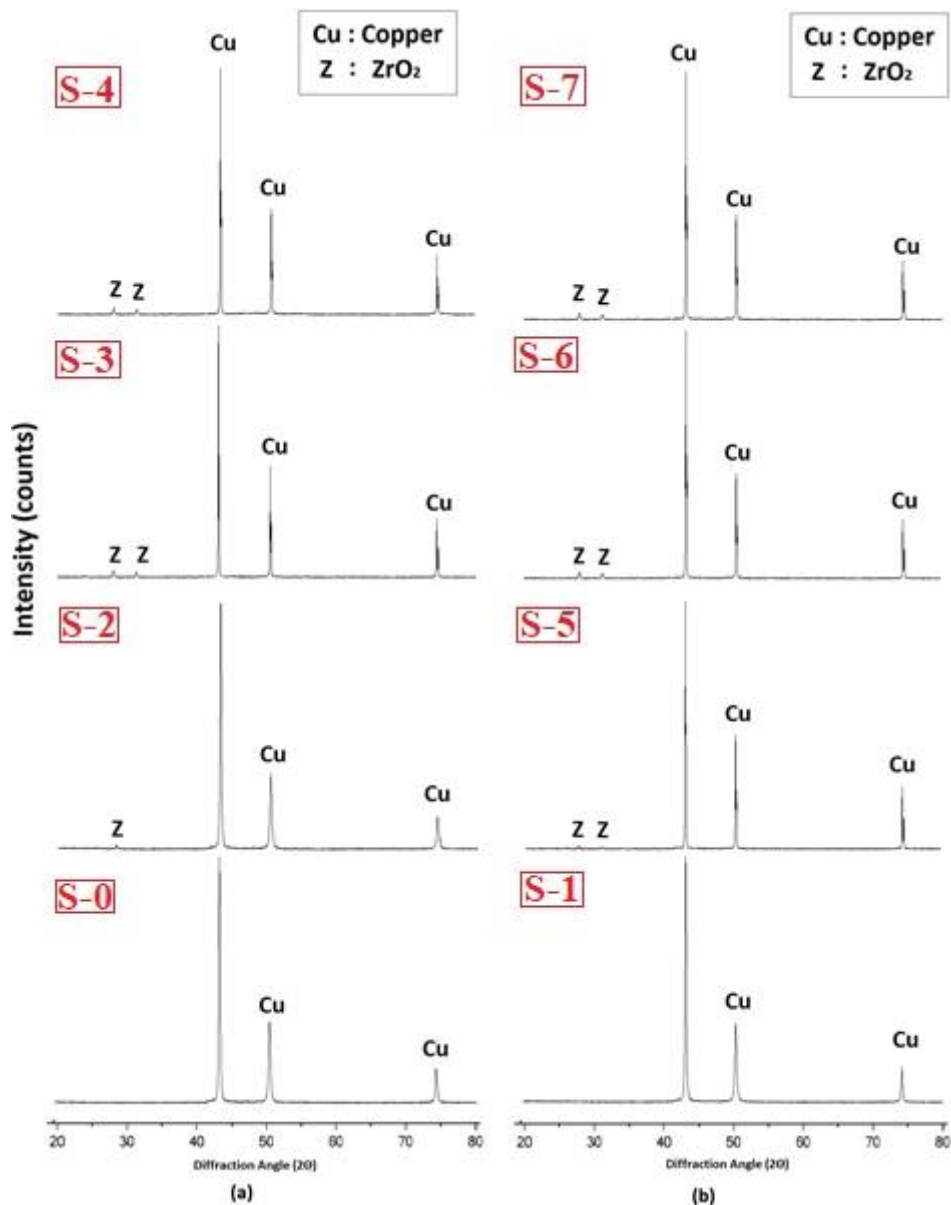


Fig. 4. (a) SEM image of the sample S-7, (b) elemental mapping of sample S-7, (c) the element mapping of Cu in (a), (d) the element mapping of Zr in (a); (e) the element mapping of C in (a), (f) the element mapping spectrum of sample S-7.

The data obtained after X-ray diffraction (XRD) analysis of ZrO_2 and ZrO_2 -graphite added copper matrix samples are shown in figures (a) and (b), respectively. For the ZrO_2 -added samples, the primary phase is copper, and the peaks of the copper phase are observed at $2\theta = 43.3^\circ$, 50.4° , and 74.7° , similar to the other reinforced samples. Sample Z-2 does not appear to have a 100% zirconia peak. All ZrO_2 -containing samples, including sample Z-5 with the same ratio, have this peak and a minimal zirconia peak at 31.7° . As the reinforcement addition of ZrO_2 increases, the peaks of the zirconia phase also increase minimally. Due to the high intensity of Cu peaks and low level of the graphite content, it is thought that the peak of graphite phases settled in the background in ZrO_2 -graphite added copper matrix composites. The elements added below 2% could not be detected as they were below the detection limit of the XRD.



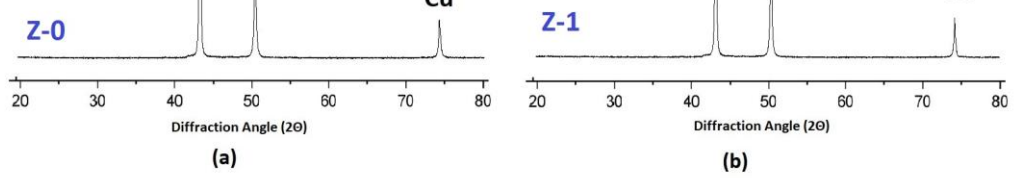


Figure 6 shows the microhardness properties of the produced samples. The lowest hardness was measured in S-0 sample which pure copper. The sample with graphite content (S-1) has a particularly lower hardness value than the pure copper sample (S-0). The main reason for this situation is graphite couldn't affinity to copper elements in the microstructure. When the ZrO_2 addition rate increases by 5%, 10%, and 15%, the hardness change increases significantly. As the amount of ZrO_2 increased, the hardness of the samples increased linearly as the reinforcement distribution increase general stiffness was increased. The hardness value of graphite/ ZrO_2 added samples (S-5, S-6, and S-7) is higher than that of only ZrO_2 added (S-2, S-3 and S-4). The addition of graphite is increased general stiffness due to integration to grain boundaries. It is higher than the copper composite sample (S-1) containing only graphite.

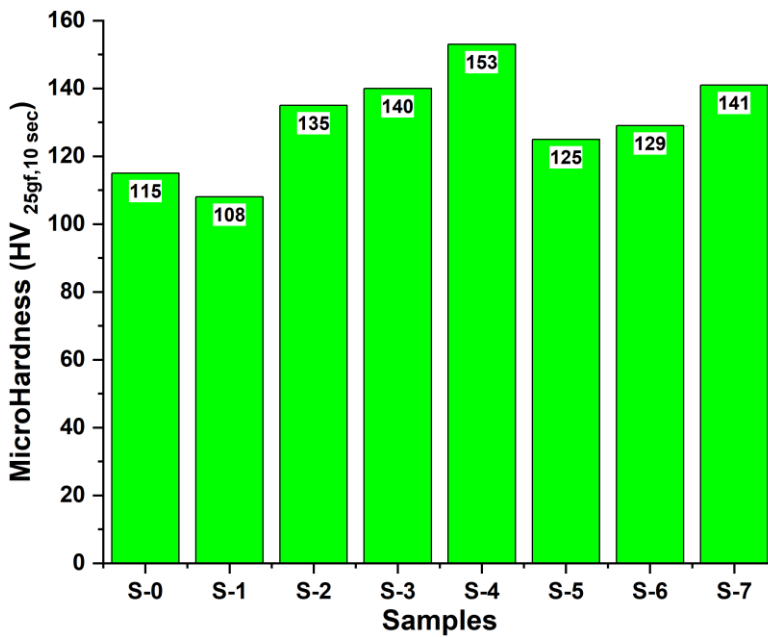


Fig. 6. Hardness of of ZrO_2 and ZrO_2 /graphite added copper matrix composite samples.

Figure 7 shows the wear resistance-COF alteration graph of samples containing Cu matrix, ZrO_2 ceramic reinforcement phase, and Graphite additive at different rates. The diagram is reported as wear rate and average friction coefficient. Higher wear rates mean inferior wear resistance. Wear rates are calculated by taking the average value of the applied load, distance, wear scar diameter, and the resulting wear channel. Equation 1, given below, shows the formulation used in wear rates. D is the diameter of wear track that used in the test (mm), A is the surface cross section worn surface obtained by surface profilometer (mm^2), P is the normal load that used in the test (N), L is the wear test distance as meter.

$$Wear Rate = \left(\frac{\pi \cdot D \cdot A}{P \cdot L}, \frac{mm^3}{N \cdot m} \right) \quad (1)$$

As can be seen from the diagram, ceramic reinforcement added to the structure at different rates dramatically improves the wear resistance of the structure. Due to increased ceramic particle reinforcement, wear rates have significantly improved in all reinforced groups over and plain graphite-added Cu alloys. Wear performance improvements in samples produced by adding different amounts of ZrO_2 to the microstructure vary between %132 to %484 comparison to the lean Cu sample (S0). Only ZrO_2 reinforcements improve wear resistance %136 to %331. ZrO_2 reinforcement and the graphite addition improved the wear resistance %132 to %484. One can infer that combining oxide and graphite improve wear resistance more efficiently. However, adding lean graphite did not directly improve the wear resistance; on the contrary, it caused a decrease in the wear performance. When the wear rate and average friction coefficient of the lean graphite added sample (S-1) are examined, it is seen that it shows a high wear rate. However, this sample had the lowest friction coefficient among all groups. The friction coefficient is not an exact material property but the response of the created tribological coupled system. The friction coefficient graph of this sample is examined (Fig. 8), showing that the friction behavior is stable after 10 meters. The EDS analysis of the worn surface showed that the presence of oxide layers formed on the surface is seen. Wear increased with the first contact but decreased with increasing test distance due to graphite-based oxides formed on the direct metal-metal contact surfaces. The structure's absence of a hard reinforcement phase (such as ZrO_2 for this case) increased the actual contact area on the interface. Although graphite, known to be soft and able to move within its own layers, prevents direct metal-metal contact on surfaces, it does not directly affect wear resistance. Thus, the wear rate deteriorated. This situation is thought to be due to the formation of tertiary particles by graphite combining with O in the ambient atmosphere during the test. The resulting complex tribochemical oxides caused abrasive damage to the pure Cu matrix and caused worsening wear. Graphite is known to be an excellent solid lubricant with the ability to move through layers. For this reason, graphite plastered on the surfaces reduced the friction.

When the wear performances of ceramic particle-reinforced samples are compared to the reference sample, the wear rates are improved by approximately 1.36 to 4.84 times. Ceramic particles placed in the Cu matrix increased the load-carrying ability of the surface. Similarly, the increasing amount of ceramic particles within the structure had a linear effect on wear performance. Samples containing plain ceramic particles are coded as S-2, S-3, and S4, and with increasing amounts of ceramic additives, wear rates decreased, and wear resistance improved in all samples. In addition to ceramic additives, the effect of ceramic particles and graphite reinforcement on wear and friction was also examined in the experiments. For this reason, the wear behavior of samples containing graphite with different amounts of ceramic particle reinforcement was characterized using the same test parameters. These samples are coded as S-5, S-6, S-7. Graphite additives do not have the same effect in every ceramic particle system. Graphite content in ZrO_2 -reinforced samples had a positive effect and reduced friction.

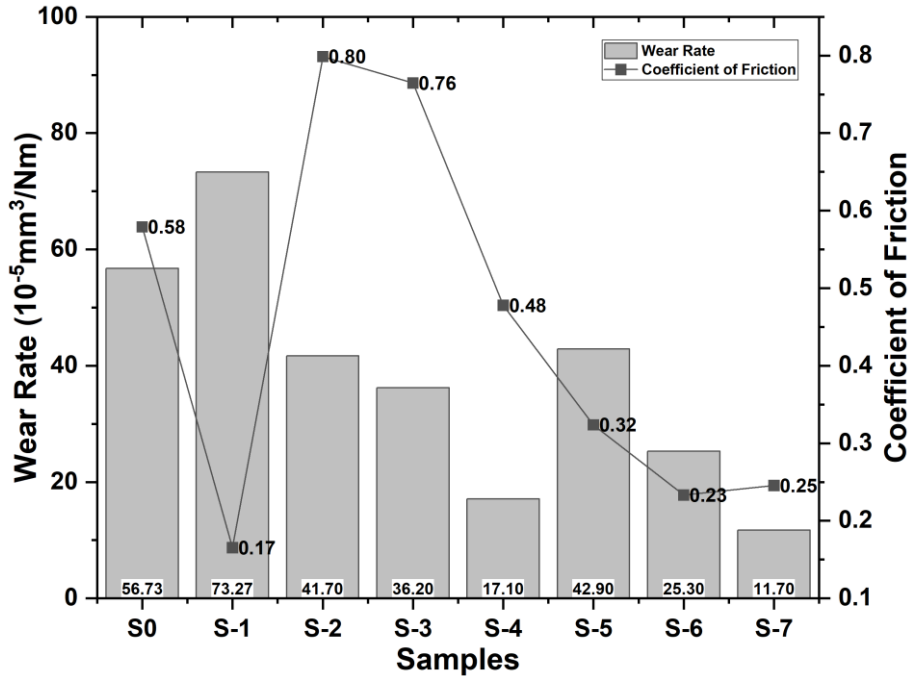


Fig. 7. The comparative wear rate of ceramic particle-reinforced alloy systems at different rates.

Figure 8 shows the distance-dependent COF alteration graphs of samples containing different ratios of ZrO_2 ceramic reinforcement phase and graphite additive. When the graphs are examined in general, it is seen that the friction behaviors enter a regular regime called the incubation period after passing the static friction point. Friction behavior in all samples showed stable behavior at the end of the test except for the S-6. This case indicates that the selected test distance is optimum for the specified load and speed values. S-2 sample which has contains lowest reinforcement ratio, exhibits higher steady regime comparison to other samples. A high friction regime was observed in the S-0 sample for the first 20 meters which is the reference sample. During the mid-regime of the test, the COF behavior getting stabilized. The situation shows that third bodies at the interfaces were extracted from the worn surfaces. Thus the COF behavior was stabilized with the help of copper-based oxides. Although sample S-1 has a high wear rate, it has a low COF—this situation affects the graphite present in the structure. Samples S-2, 3, and 4 are ceramic-added samples that do not contain graphite. As expected, the average COF behavior of these samples is higher than those containing graphite. Among the graphite-added samples, the system showing the highest oscillation is the S-5 and S-6. This situation develops due to oxides breaking and breaking with continuous contact at increasing wear test distance. Particles that break off and remain on the rubbing interface cause an increase in the friction force due to compression and cause fluctuations. Sample S-7 is the sample with the lowest wear rate. Similarly, it exhibited the relatively steady friction behavior in the ZrO_2 -reinforced groups. High and hard ceramic grains in the microstructure reduced the deteriorating effects of the wear. It also reduced the COF by reducing the actual contact rate.

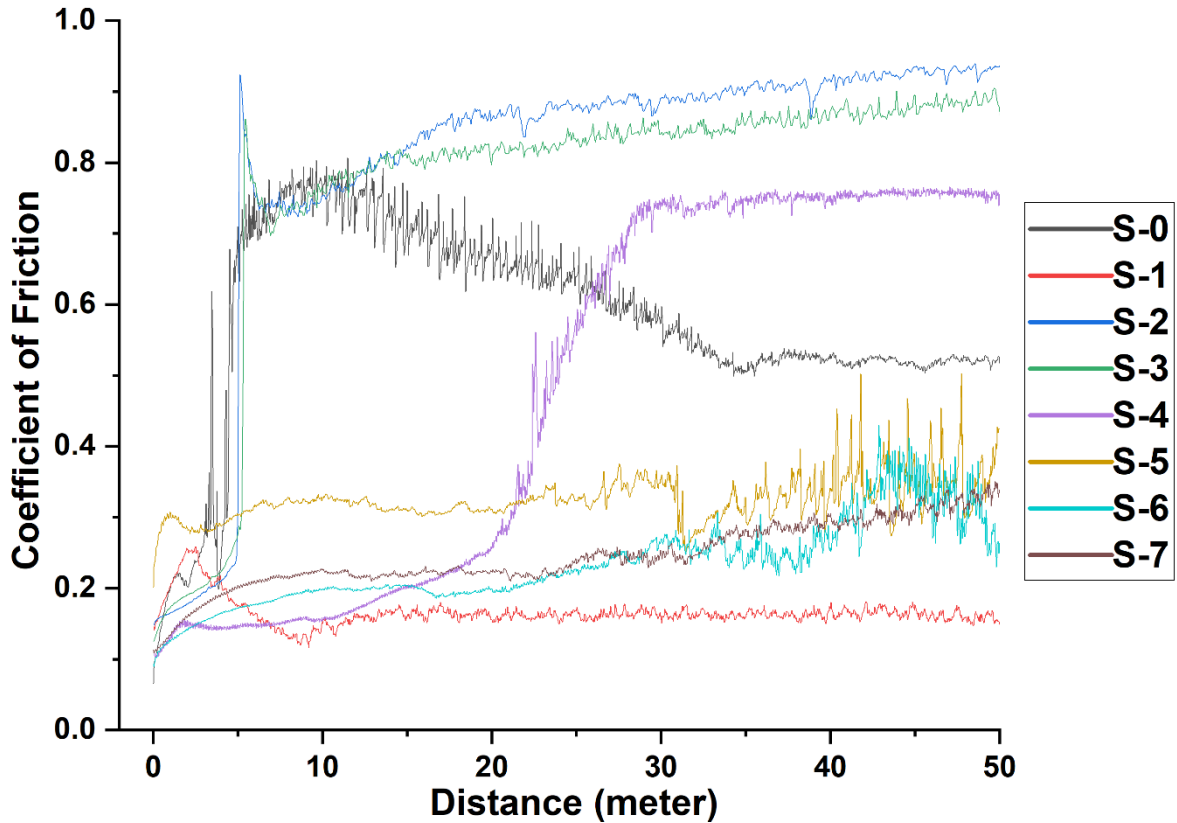


Fig. 8. The COF behavior is based on the distance of the samples.

Figure 9 shows the worn surface SEM-EDS analysis of the reference sample without additives (S-0) and the graphite-added sample (S-1). When the wear surface of the reference sample is examined, it is seen that the wear mechanism is primarily oxidative in places. These formed oxides are brittle and break at increasing wear distances. These broken pieces remained on the surface, allowing three-body abrasive wear to begin. Although the dominant wear mechanism in the reference sample is oxidative, abrasive effects are also observed. When the SEM-EDS analysis of the wear surface of the graphite-added reference sample is examined, it is clear that the wear mechanism is entirely abrasive. There is also superficial oxide formation on the surfaces. There is graphite found in the structure. Graphite incorporated into the structure is a type of solid lubricant and is one of the main topics known in the literature. The solid lubricity of graphite occurs due to the weak interlayer bonds. Graphite inside the microstructure is plastered on both surfaces. Graphite moving between layers after plastering ensured low friction on the surface. However, the absence of a reinforcement phase supporting the matrix within the structure poses a negative situation regarding load-bearing ability. With increasing wear test distances and wear load, also the plastic deformation mechanism of abrasive wear deformed the surface. For this reason, the wear performance of the plain graphite added sample performed weak weak wear resistance compared to the reference sample.

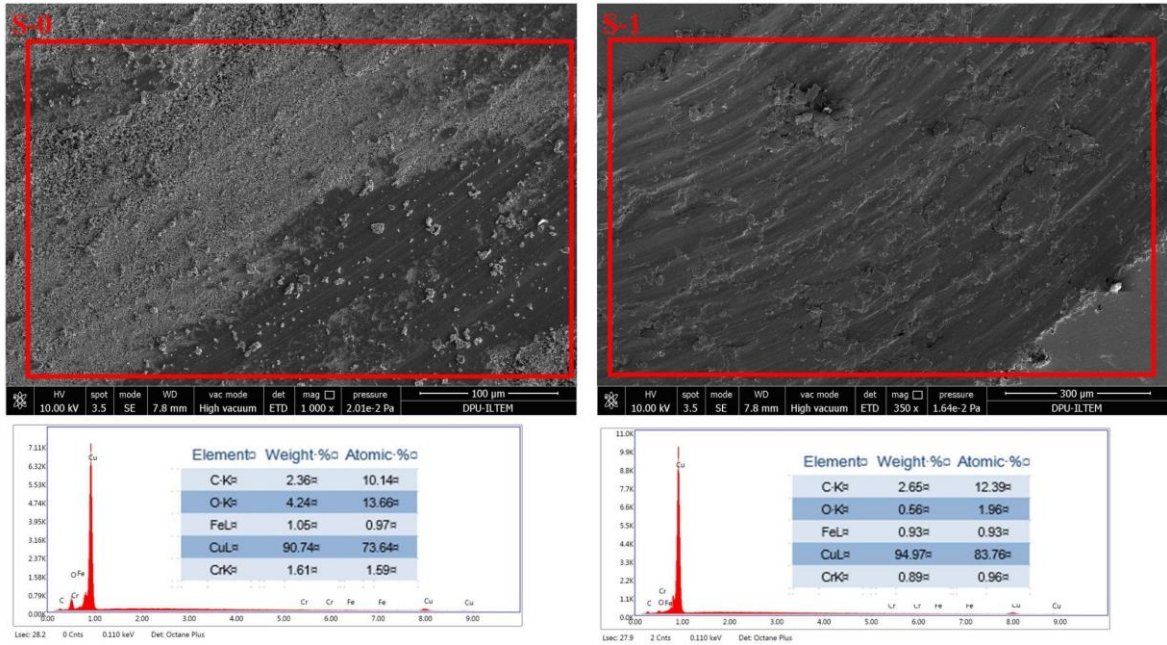


Fig. 9. Worn surface SEM-EDS analysis of reference sample (S-0) and graphite added sample (S-1).

SEM and EDS analyses of worn surfaces are shown in Figures 9, 10 and 11 respectively. Figure 9 exhibits SEM-EDS analysis of the worn surface of S-0 and S-1 which are lean copper and graphite added copper samples. Figure 10 and 11 shows SEM and EDS analyses of worn surface of different amounts of ZrO₂ reinforced samples. When the plain ceramic added group is examined, it is seen that the wear resistance is lower than the graphite added group. This sample group is the group characterized as having the lowest wear resistance. As can be seen, when the surfaces of these samples containing different amounts of ceramic reinforcement are examined, microcracks caused by contact are pretty visible. These microcracks occur after continuous contact with the high-hardness areas of both sides. It is a type of damage mechanism caused by surface fatigue. This situation indicates that the surface's load-bearing ability is low. Similarly, cleavages, indicators of brittle fracture, are frequently seen on the surfaces. In addition, despite the increased reinforcement ratio, oxidative wear on the surfaces was practical in all sample groups. The high wear appears to be three-body abrasive wear, which starts with oxidative origin and turns abrasive.

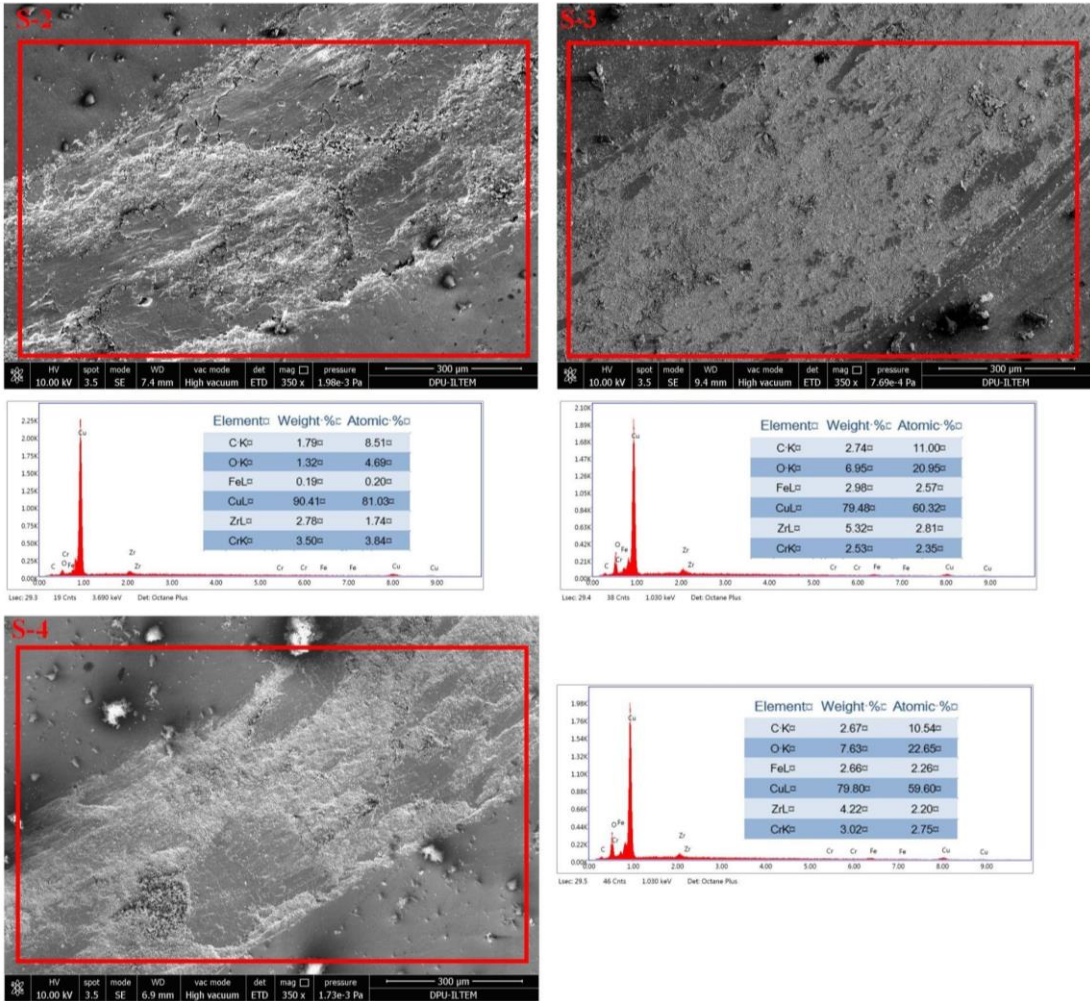


Fig. 10. Worn surface SEM and EDS analyses of samples containing different amounts of ZrO₂ additives.

The worn surface analysis photographs of both ceramic and graphite-added samples are given in Figure 11. Similarly, wear performance improved with increasing reinforcement ratio. The effect of graphite addition was observed very clearly in this alloy system. A decrease in the channel width was observed in all graphite-added samples. This situation is an indication that friction is decreasing. Surface damage in graphite-added ceramic particle-reinforced samples turned into an abrasive character. It is seen that the surface damage occurs superficially after increasing the reinforcement ratio. Increasing ceramic additive in the produced samples increased the probability of contact with the counter object, and wear decreased. Additionally, graphite smearing and interlayer movement reduced the actual contact zone and improved wear performance.

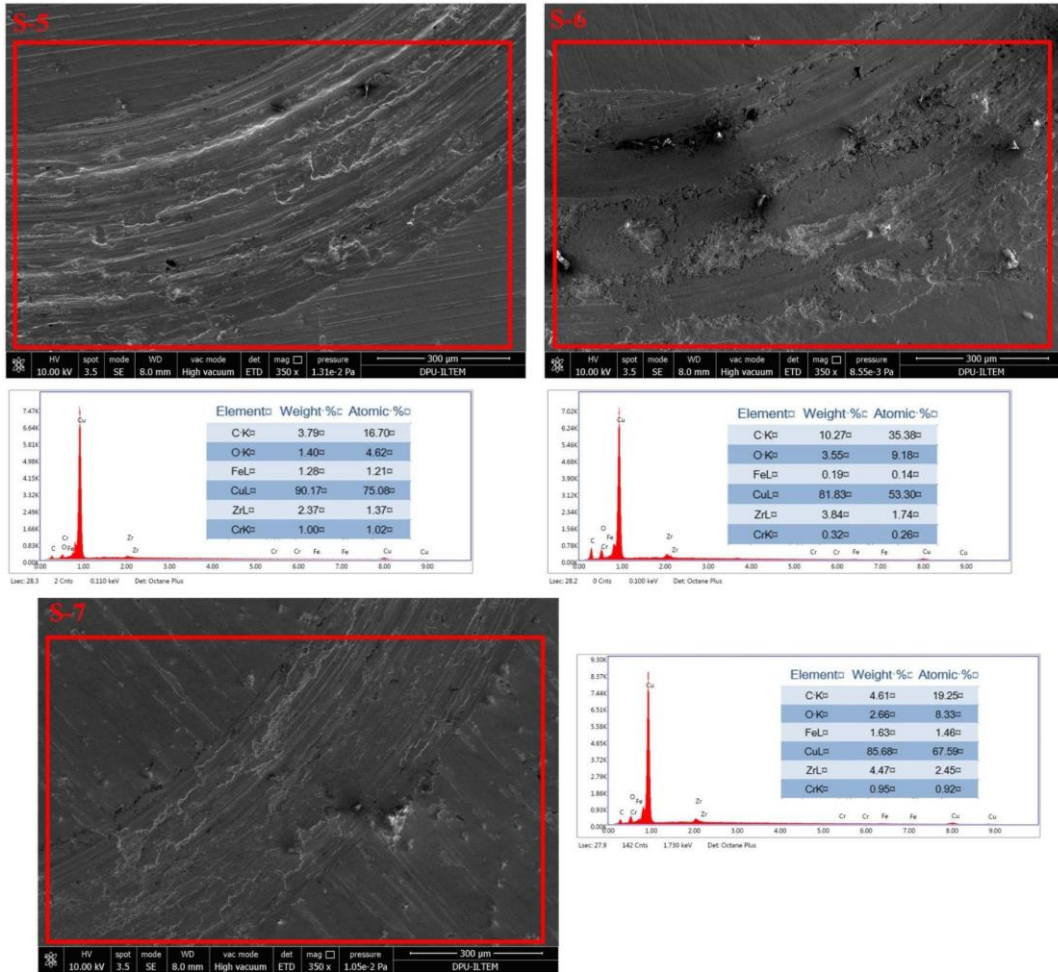


Fig. 11. Worn surface SEM and EDS analyses of samples containing different amounts of ZrO₂ and graphite.

4. Conclusions

Copper and copper matrix composites containing 5%, 10%, and 15% ZrO₂ by volume have been successfully produced via powder metallurgy. In addition to these samples, 2% graphite was added to each sample, and the mechanical properties of the samples were compared. Analysis and characterization methods such as XRD, theoretical, experimental, relative density, hardness, SEM, EDX, elemental EDX mapping, and wear were applied to the produced samples. If the results obtained are examined in detail, the following conclusions are drawn:

- When the theoretical, experimental, and relative densities of the produced Cu/ZrO₂ added and reference samples were compared, it was observed that the density values decreased with the addition of reinforcement. The average values of pure copper, ZrO₂, and both ZrO₂ and graphite-reinforced samples were 92.5%, 92.17%, and 91.77%, respectively. The relative densities of the specimens were found to be suitable by performing the specimens first and then cold isostatic pressing and pressing twice.

- As a result of the electron microscopy analysis, it was observed that the graphite was distributed in copper and homogeneously distributed. In contrast, in the samples containing ZrO₂, ZrO₂ was homogeneously distributed without dissolution, preserving the grain structure. The Cu, Zr, O, and C quantities obtained from the elemental analysis of the samples are consistent with each other and with the initial stoichiometries. Electron microscopy analysis supports the successful production of ZrO₂ and graphite reinforcements in all samples with homogeneous dispersion in the Cu matrix.

- XRD analysis shows that copper matrix composites containing ZrO₂ and copper matrix composites containing ZrO₂ and graphite were successfully fabricated.

- Samples with ZrO₂ reinforcement increased the hardness value considerably compared to the copper sample. Unsurprisingly, the hardness value of the samples containing 2% graphite additives increased, and the wear resistance decreased slightly compared to those without graphite.

- It has been observed that graphite additive positively affects wear resistance and friction behavior. No significant results regarding wear performance were obtained in the plain graphite additive sample.

- In samples containing graphite additives and ceramic additives, the coefficient of friction was reduced, and wear resistance was improved.

- With the study, the wear performance of Cu alloys was improved between 1.32 and 4.84 times. Wear resistance improved proportionally with increasing ceramic particle reinforcement.

- By evaluating microstructural, mechanical, and tribological properties, optimum chemical content was determined as %15 ZrO₂ reinforcement with the graphite additives. The material composition of S-7 sample could be utilized where wear resistance and friction behavior are important.

Conflicts of interest

The authors declare no conflicts of interest.

Acknowledgments

The Kutahya Dumlupinar University BAP (Scientific Research Project-Career Start Project) number 2022-32 provided funding for this work. For SEM, EDX, and mapping analysis, we are pleased to use the DPU-ILTEM (Kutahya Dumlupinar University-Advanced Technologies Research Center).

References

- [1] F. Kennedy, A. Balbahadur, and D. Lashmore, "The friction and wear of Cu-based silicon carbide particulate metal matrix composites for brake applications," *Wear*, vol. 203, no. 5, pp. 715-721, March 1997, doi: 10.1016/S0043-1648(96)07384-X.
- [2] K. Dash, B.C. Ray, and D. Chandra, "Synthesis and characterization of copper-alumina metal matrix composite by conventional and spark plasma sintering," *J. Alloys Compd.*, vol. 516, no. 1, pp. 78-84, March 2012, doi: 10.1016/j.jallcom.2011.11.136.
- [3] X. Guo, K. Song, S. Liang, C. Zheng, "Thermal expansion behavior of MgO/Cu composite with lower MgO volume fraction," *Mater. Res. Bull.*, vol. 47, no. 11, pp. 11-15, November 2012, doi: 10.1016/j.materresbull.2012.08.012.
- [4] C. Samal, J. Parihar and D. Chandra, "The effect of milling and sintering techniques on mechanical properties of Cu-graphite metal matrix composite prepared by powder metallurgy route," *J. Alloys Compd.*, vol. 569, no. 1, pp. 95-101, August 2013, doi: 10.1016/j.jallcom.2013.03.122.
- [5] J. Márquez, N. Antón, A. Jimenez, M. Madrid, M. Martínez, J. Bas, "Viability study and mechanical characterisation of copper-graphite electrical contacts produced by adhesive joining," *J. Mater. Process. Technol.*, vol. 143, no. 1, pp. 290-293, December 2003, doi : 10.1016/S0924-0136(03)00476-X.
- [6] S. Hong, and B. Kim, "Fabrication of W-20 wt % Cu composite nanopowder and sintered alloy with high thermal conductivity," *Mater. Lett.*, vol. 57, no. 18, pp. 61-67, May 2003, doi: 10.1016/S0167-577X(03)00071-5.
- [7] H. Mallikarjuna, C.S. Ramesh, P. Koppad, R. Keshavamurthy, D. Sethuram, "Nanoindentation and wear behaviour of copper based hybrid composites reinforced with SiC and MWCNTs synthesized by spark plasma sintering," *Vacuum*, vol. 145, no. 1, pp. 320-333, November 2017, doi: 10.1016/j.vacuum.2017.09.016.

- [8] A. Fathy , F. Shehata, M. Abdelhameed, M. Elmahdy, “Compressive and wear resistance of nanometric alumina reinforced copper matrix composites,” *Materials & Design*, vol. 36, no. 1, pp. 100-107, April 2012, doi: 10.1016/j.matdes.2011.10.021.
- [9] M. Khaloobagheri, B. Janipour, and N. Askari, “Electrical and Mechanical Properties of Cu Matrix Nanocomposites Reinforced with Yttria-Stabilized Zirconia Particles Fabricated by Powder Metallurgy,” *Adv. Mater. Res.*, vol. 829, no. 1, pp. 610-615, November 2013, doi: /10.4028/www.scientific.net/AMR.829.610.
- [10] J. Mirazimi, P. Abachi, and K. Purazrang, “Spark Plasma Sintering of Ultrafine YSZ Reinforced Cu Matrix Functionally Graded Composite,” *Acta Metall. Sin.*, vol. 29, no. 12, pp. 1169-1176, November 2016, doi: 10.1007/s40195-016-0512-0.
- [11] Y. Qin, Y. Tian, Y. Zhuang, L. Luo, X. Zan, Y. Cheng, “Effects of solid–liquid doping and spark plasma sintering on the microstructure and mechanical properties of Y_2O_3 -doped copper matrix composites,” *Vacuum*, vol. 192, no. 110, pp. 436-445, October 2021, doi: 10.1016/j.vacuum.2021.110436
- [12] H. Imai , Y. Kosaka, A. Kojima, S. L. K. Kondoh, J. Umeda, H. Atsumi, “Characteristics and machinability of lead-free P/M Cu60–Zn40 brass alloys dispersed with graphite,” *Powder Technol.*, vol. 198, no. 3, p. 417-421, 2010, doi: 10.1016/j.powtec.2009.12.010.
- [13] H. Imai, L. Shufeng, H. Atsumi, Y. Kosaka, A. Kojima, K. Kondoh, “Development of Lead-Free Machinable Brass with Bismuth and Graphite Particles by Powder Metallurgy Process,” *Mater. Trans.*, vol. 51, no. 5, pp. 855-859, May 2010, doi: 10.2320/matertrans.MH200907.
- [14] H. Aydin and P. Birgin, “Properties of Al/Al₂O₃-TiO₂ composites prepared by powder metallurgy processing,” *Kovove Mater.*, vol. 59, no. 2, pp. 99-107, January 2021, doi: 10.4149/km 2021 2 99
- [15] M. Elmahdy, G. Abouelmagd, A. Mazen, “Microstructure and properties of Cu-ZrO₂ nanocomposites synthesized by in situ processing,” *Materials Research*, vol. 21, no. 1, pp. December 2018, doi: 10.1590/1980-5373-mr-2017-0387



Contents lists available at *Dergipark*

Journal of Scientific Reports-A

journal homepage: <https://dergipark.org.tr/pub/jsr-a>



E-ISSN: 2687-6167

Number 57, June 2024

RESEARCH ARTICLE

Receive Date: 09.02.2024

Accepted Date: 25.03.2024

A research on the production, storage and germination of synthetic seeds in tea plant (*Camellia sinensis* [L.] O. Kuntze)

Begüm Güler^{a,*}, Aynur Gürel^b

^a*Kırşehir Ahi Evran University Faculty of Engineering and Architecture, Genetic and Bioengineering Department, Kırşehir, Türkiye, ORCID: 0000-0002-9970-2111*

^b*Ege University, Faculty of Engineering, Bioengineering Department, İzmir, Türkiye, ORCID: 0000-0002-7002-9752*

Abstract

Tea plant, is one of the most popular beverages consumed worldwide because of its rich and pleasant flavors and numerous health benefits. In this study, we performed production, storage and germination of synthetic seeds in the tea plant by encapsulation of somatic embryos. In our research, after the encapsulation of the mass-produced embryogenic calli with different doses of sodium alginate (NaAlg) and CaCl₂, they were stored at different temperatures and at different times, and then transferred to different nutrient media after the expiry of the different storage period to determine the most suitable nutrient composition for germination. The resulting embryogenic calli were stored after encapsulation and then transferred to germination media. Although there was very little germination in long-term storage, the data obtained were found to be statistically insignificant. The germination rate of the beads, which were transferred directly to the germination medium without storage and encapsulated using 3% Na-Alg and 50 mM CaCl₂·2H₂O, was determined as 44.44% in the MS medium containing 3 mg/L BAP and 1 mg/L IBA. In addition, it was observed in the study that increasing storage time increased the darkening of the beads, while increasing NaAlg and CaCl₂ doses caused obtaining harder and more nontransparent beads. Hyperhydricity problem was not encountered in any trial in the study. This study, carried out with our local tea variety.

© 2023 DPU All rights reserved.

Keywords: Tea plant; synthetic seed; encapsulation; somatic embryo; storage period

* Corresponding author. Tel.: +90-386-280-2256;

E-mail address: begum.guler@ahievran.edu.tr

1. Introduction

Tea plant (*Camellia sinensis* [L.] O. Kuntze), which belongs to the Theaceae family, is one of the most important economic plants in the world due to its numerous medicinal benefits and being the most consumed product as a beverage [1]. The tea plant, which is a perennial and evergreen plant, also has many medicinal properties. Black tea, obtained by brewing processed leaves, is the most consumed beverage all over the world. Medicinal use of tea dates back 4700 years. Today, it is included in the daily diet of people in many regions, especially in Asia. Apart from China, India, Sri Lanka, Kenya, Japan, Indonesia, Malawi and Türkiye are the largest tea producers in the World [2].

Tea propagation is carried out in two different ways: generative (seed) and vegetative (cutting, grafting and tissue culture) [3]. Most of its production is carried out with seeds. However, seed production causes problems such as genetic variations, yield differences and changes in quality characteristics [4]. For this reason, seed production is not one of the preferred production techniques. Vegetative techniques also cause various problems. Due to reasons such as dormancy and drought, there are no suitable seedlings in some tea gardens. Low rooting percentage and reproduction rates similarly constitute disadvantages of vegetative production techniques. When these disadvantages are examined, tissue culture applications stand out as the most effective production technique among all production methods [3].

Among tissue culture techniques, synthetic seed technology (also called “synseed” or “artificial seed”) is a valuable alternative technique for micropropagation and conservation of important agro-economic plants [5]. Synthetic seed is defined as the synthetic encapsulation of somatic embryo, shoot tip, cell aggregate or other tissues that has the potential to turn into a full plant under *in vitro* and *ex vitro* conditions and can continue to show this feature after long-term storage [6]. “Synthetic seed technology” has many advantages, such as providing a protective coating that encapsulates the reproductive structures with the necessary nutrients, maintaining their strong and high adaptability during storage, and providing ease of packaging, storage and transportation [7]. With the use of synthetic seeds, the regenerable meristematic parts within the synthetic seed can be stored for different time periods and also ensure mass multiplication and preservation of germplasm [8].

In general, plant seeds have embryos containing one or two cotyledons connected to the endosperm, which serves as a nutrient reservoir for the development of the embryos. This structure is covered with a hard structure called testa, which protects the inner sensitive structure from injuries and ensures that the embryo remains alive until the germination period [9]. Although synthetic seeds have similar properties to natural seeds, there are also some distinct differences between them. T. Murashige put forward the first idea about synthetic seeds in 1977 [10]. He first expressed his idea about synthetic seeds at the "Symposium on the Tissue Culture for Horticultural" held in Genth, Belgium, on 6-9 September 1977. In this speech, while talking about the features that synthetic seed technology should have, the researcher stated that the production method should be extremely fast, allow a large number of production in a day, and should be competitive with the seed production technique [6]. The first synthetic seed production was carried out by Kitto and Janick in carrot somatic embryos in 1982. In this study, polyoxyethylene was used as the coating material [9].

Although somatic embryos were generally used in the first studies on synthetic seeds, many plant parts are used for encapsulation purposes today. Somatic embryos are followed by shoot tip and axillary shoots, respectively. Protocorm-like structures, nodal segments, and callus are also explant sources used in the production of synthetic seeds. Plant lines obtained through somatic embryos can maintain their regeneration capacity for a very long time, and also prevents dedifferentiation at the callus stage, thus ensuring the preservation of the genetic structure and the formation of a uniform genetic structure. [6, 11]. The synthetic seed containing the somatic embryo can be encapsulated directly into the synthetic shell, or it can be coated after being partially dehydrated [5]. Somatic embryos continue to form in cell masses and thus it is possible to produce several thousand embryos per gram in a culture. This makes somatic embryos a good source. Since the plant parts used in synthetic seed production are generally produced by *in vitro* clonal propagation techniques, they do not include meiotic recombination (during crossing-over) and gametic fusion (during cross-pollination), which are the two basic steps of sexual reproduction.

For this reason, new plants produced through synthetic seed technology have characteristics true to their name. Synthetic seeds are covered with a coating material that will provide the protection needed during storage, shipping and transportation. In some cases, this coating material may also contain plant nutrients and plant growth regulators [12].

Dried artificial seeds are naked. The drying process can be carried out quickly or by leaving it to dry overnight in lidless petri dishes or slower under more controlled conditions by reducing the humidity. In addition to the use of high osmotic potential, sublethal stress conditions such as nutrient deprivation or low temperature are used to induce tolerance to desiccation. High gel strength or osmotic agents such as mannitol or sucrose are used to increase the osmotic potential [6, 9]. Hydrogel capsules are a method used to encapsulate plant parts that are recalcitrant and sensitive to drying [6]. The method may also vary depending on the type of encapsulation preferred in synthetic seed production. While only a single coating layer is used in the single-layer encapsulation method, a second coating is applied on the coated material in the double-layer coating technique. The hollow beads technique is generally not preferred because it is laborious and costly, and the seeds cannot be protected well enough [13].

For the purpose of synthetic seed production, it has been determined that the most suitable material among many coating materials such as agar, alginate, carboxyl methyl cellulose, sodium pectate, gelrite, guar gum, etc. is alginate [6, 9]. Generally, 100 mM Ca^{+2} is used as a complementary solution with 2% NaAlg. This composition creates a protective layer as well as nutritional elements, and the seeds are easier to use and store. The basic principle in performing alginate encapsulation is based on the displacement of Na^+ ions in NaAlg and Ca^{+2} ions in $\text{CaCl}_2 \cdot 2\text{H}_2\text{O}$ solution when NaAlg solution containing plant parts is dropped into $\text{CaCl}_2 \cdot 2\text{H}_2\text{O}$ solution. Endosperm-like structure formed as a result of coating can be used to carry microorganisms, nutrients, antibiotics, plant growth regulators, pesticides and fungicides. Endosperm may contain plant growth regulators and carbon sources not only for the physical protection of embryos but also for germination and plant growth [6]. In encapsulation, the coating material may contain nutrients, biological fertilizer, pesticides, nitrogen-fixing bacteria, antibiotics or other necessary components [14]. In a study conducted by Khor an Loh, they determined that the transformation potential and viability of synthetic seeds increased when the coating material and activated carbon were used together [15]. They attributed this to the fact that activated carbon breaks the alginate and the embryo in the synthetic seed can breathe more easily in this way. The covering material should not harm the embryo, allow germination, but should be resistant to the difficulties encountered during production, storage, transportation and planting processes, as well as providing nutrients to the embryo for germination [9].

The reason why alginate is frequently preferred is its suitable viscosity, low toxicity, fast gelling and low cost. It also better protects the explant it covers against mechanical damage. The state of the encapsulated beads depends on the concentrations of NaAlg and calcium chloride, but also on the mixing time based on the plant species and explant source [11]. Redenbargh et al. stated that alginate hydrogels are the most suitable encapsulation material with their properties such as light viscosity, low toxicity and rapid gelation [16]. Nair and Reghunanth determined that 4% NaAlg and 100 mM $\text{CaCl}_2 \cdot 2\text{H}_2\text{O}$ were coating materials of similar quality and suitability for *Clitoria teretea* and *Indigofera tinctoria*, respectively [17, 18]. At low concentrations of NaAlg and CaCl_2 , irregularly shaped, brittle beads are formed, while at high concentrations, beads with a hard structure that do not allow germination are formed [19]. Mohanraj et al. determined that the use of high NaAlg reduced the germination frequency of beads [20]. In their study, Lulsdorf et al., found a high recycling rate after 4 weeks of storage at 4°C. Similarly, [22] stored synthetic seeds obtained from olive somatic embryos at 2 or 4°C for 23 months and determined a germination rate of 61% [21].

Synthetic seed applications have many advantages. By directly encapsulating and using somatic embryos, the number of subculture processes required for the production of plants obtained from embryos through regeneration is reduced. Additionally, meiotically unstable elite genotypes can be protected with adjuvants such as plant growth regulators and pesticides. In addition to determining the role of seed coat formation and endosperm in embryo development and germination, synthetic seed technologies can be used to obtain information on plant development. While allowing large-scale production, synthetic seeds can also be used for germplasm preservation, medium-long

term or cold storage and disease eradication. Seeds can be produced in every season and every period, regardless of the season. Seed production can be achieved in a very short time and it is extremely easy to apply and has low cost. Seed production can be achieved with low cost and high efficiency [6, 12, 23].

In addition to their many advantages, synthetic seeds also have some disadvantages. The biggest problems experienced in synthetic seed technology are listed as the need to improve storage conditions due to dormancy problems, problems in ensuring synchronization in somatic embryo regenerations, improper maturation, low conversion rate to plants, problems in the acclimatization of weak plants due to lack of lignification and low cuticle formation [6]. Additionally, the rooting needs of non-embryogenic plant parts indicate the need for further research, especially in woody plants [11].

In a study conducted by Seran et al., with zygotic embryos of the tea plant, synthetic seeds coated with 2, 3, 4% (w/v) NaAlg and 100 and 50 mM $\text{CaCl}_2 \cdot 2\text{H}_2\text{O}$, 3 mg/L BAP and 0.5 mg /L was germinated on MS media with and without IBA [24]. As a result of the study, it was determined that synthetic seeds produced with 3% NaAlg + 100 mM $\text{CaCl}_2 \cdot 2\text{H}_2\text{O}$ had the most suitable coating form, and for germination, MS medium containing growth regulators showed a higher germination rate [24].

In this study carried out by us, it was aimed to produce synthetic seeds and determine appropriate storage and germination conditions. For this purpose, encapsulation process was carried out with different ratios of NaAlg and CaCl_2 , the produced beads were stored for different periods and conditions and germinated in different nutrient media. There are somatic embryogenesis studies in the tea plant. In addition, different explant sources were used in synthetic seed studies in tea. Our study is a pioneer in the production of synthetic seeds in tea plants by encapsulation of somatic embryos.

2. Methods

2.1. Material

In the studies, leaf explants of the *Camellia sinensis* [L.] O. Kuntze cv. Ali Rıza Erten were used to produce somatic embryos. Ali Rıza Erten variety is a local variety developed by Rize Tea Research Institute. Tea plantlets under *in vitro* conditions were purchased from Dikili Ciftlik company and propagated clonally.

2.2. Production of somatic embryos

40-day-old plantlets under *in vitro* conditions were subcultured in a laminar flow cabinet. To ensure the continuity of stock plants during this subculture process, shoot tip and node explants were cultured in MS [25] medium containing 0.6 mg/L BAP and 0.1 mg/L NAA, while leaf explants were injured and transferred to MS medium containing 4 mg/L BAP, 1.5 mg/L IBA and 30 g/L sucrose. After callus initiation was achieved in this environment, the callus clusters were transferred to MS medium containing 4 mg/L BAP, 1.5 mg/L IBA and 50 g/L sucrose for secondary embryogenesis. Embryos with secondary embryogenesis observed in nutrient medium and at the globular stage were used in the production of synthetic seeds.

2.3. Production of synthetic seeds

In synthetic seed experiments, a pasteur pipette with a cut off tip was used to form beads. To sterilize the Pasteur pipette, its entirety (including its inner part) was treated with plenty of 70% ethyl alcohol solution and then subjected to UV sterilization for 15 minutes. Then, a large amount of bleach (commercial bleach containing 5% NaOCl) was taken into a straw in the cabin and allowed to come into contact with all surfaces. To remove the bleach, rinse with sterile distilled water until the foam was completely gone. It was decided that this process was sufficient for surface sterilization of the Pasteur pipette.

As a result of the literature research [24, 26], it was decided to use 50 mM and 100 mM CaCl_2 and 3, 4 and 5% NaAlg for coating purposes. After the embryos were separated from each other in the cabin with the help of a scalpel, they were transferred to autoclaved NaAlg solution. After all embryos were transferred to the NaAlg solution, they were dropped into the CaCl_2 solution in a beaker on the magnetic stirrer with the help of a Pasteur pipette with the tip cut off and sterilized with bleach in the cabinet. Mixing with orbital shaker was continued for 30-40 minutes for the beads to harden. At the end of 40 minutes, the CaCl_2 solution was removed with the help of a sterile filter and the beads were rinsed 3 times with sterile distilled water to remove excess CaCl_2 . Then, the beads were placed on a sterile napkin and waited for a short time (1-2 min) to remove excess water. After this process, if the beads were to be stored, they were placed in a sterile petri dish and stored in the place where they would be stored, or they were transferred directly to germination media.

2.4. Storage and germination of synthetic seeds

The obtained beads were stored in dark conditions at 4°C (refrigerator) and 25°C (cabinet) for 0, 15, 30 and 60 days to determine the appropriate storage condition. As a result of the storage period, the synthetic seeds were transferred to the designated germination media (Table 1). The culture vessels were placed on culture shelves at 24±2°C under 16-hour light/8-hour dark photoperiod conditions to ensure germination. Observations were made once a week and the cracking of the beads and the conditions of the embryos were noted. The experiments were set up according to the fully randomized trial design and were planned with 3 replications, with 3 beads in each replication. Minitab 17 Statistical Software (Minitab Inc, PA, USA) was used to evaluate the data obtained.

Table 1. Germination media compositions*.

Code	Germination media
ÇG1	0.5 mg/L GA3
ÇG2	1 mg/L GA3
ÇG3	1.5 mg/L GA3
ÇG4	3 mg/L BAP + 0.5 mg/L IBA
ÇG5	3 mg/L BAP + 1 mg/L IBA
ÇG6	3 mg/L BAP + 2 mg/L IBA
ÇG7	2 mg/L BAP + 1 mg/L IBA
ÇG8	1 mg/L BAP + 1 mg/L IBA
ÇG9	0.5 mg/L BAP + 1 mg/L IBA

* In all experiments, MS (Murashige and Skoog, 1962) was used as the basic nutrient medium, 30 g/L sucrose as the carbon source, and 3 g/L Gelrite as the gelling agent. pH:5.8

2.5. Statistical evaluation of data

All *in vitro* treatments were applied in a randomized plot design with three replications. The data obtained from the applications were evaluated with the Minitab 17 (Minitab®, LLC, Pennsylvania, USA, 2015) program.

3. Results

The synthetic seeds obtained in the study were coated using different concentrations of NaAlg and CaCl_2 . The obtained beads were stored at different temperatures for different periods of time and transferred to different nutrient media in order to crack the beads as a result of the storage period. By determining the cracked (germinated) beads of these beads, an attempt was made to determine the most suitable NaAlg and CaCl_2 concentration, the most suitable storage time and temperature, as well as the most suitable nutrient medium. Due to the intense amount of contamination seen in the embryogenic calli of the tea plant, the problem that these contaminations can remain hidden for a long time and emerge in unexpected situations has been encountered in many studies [27]. A similar

situation was encountered in this study conducted by us. While no contamination was observed in the previous stages of the study, contamination occurred during the storage of synthetic seeds. While a higher rate of contamination was observed especially in beads stored at 24°C, it was determined that both contamination and darkening were less in beads stored at 4°C. Increasing storage time also caused the darkening problem to be observed. In addition, since the size of the beads formed is related to the diameter of the pipette, it was observed that their sizes were distributed in the range of 3-5 mm on average. Preliminary studies showed that the mixing process should be fast enough to prevent the beads from piling up and sticking, but not so fast as to create shear stress on the bead surface and prevent its shape from becoming more elliptical. In addition, it was determined that the coldness of the CaCl₂ solution used had an effect on the beads having a more stable round shape/hard structure, and therefore keeping them at 4°C overnight after the autoclaving process was important for bead formation (Fig 1).

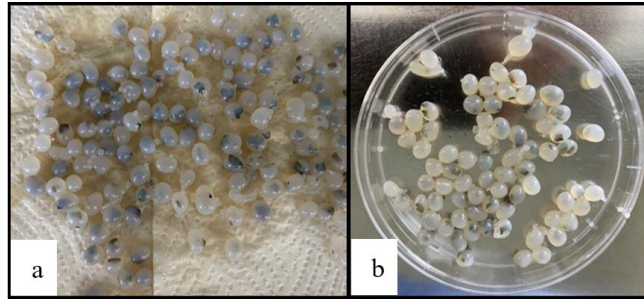


Fig 1. Synthetic seeds a) beads after rinsing, b) beads ready for storage.

In the study, data regarding the percentage of germinating beads were examined. When NaAlg values were examined, the highest germination rate was detected in 3% trials (2.46%). At CaCl₂ doses, the highest germination rate of 1.54% was obtained in the 50 mM experiment. When the storage periods were evaluated, the highest germination rate was observed in the trials with no storage (0 day), while the data obtained was not found to be statistically different, although there was germination (0.21%) in the 60-days trials (Table 2). As a result of the experiments carried out within the scope of the study, CaCl₂ doses and various interactions were also examined. When the relationship between NaAlg and CaCl₂ was examined, 4.63% germination rate occurred in beads produced with 3% NaAlg and 50 mM CaCl₂. When all trials were evaluated, the highest germination rate of 6.17% was obtained in trials without storage. When 100 mM and 50 mM trials were compared, the highest germination rate (1.54%) was detected in 50 mM CaCl₂ trials. There was no statistically significant difference between the data obtained at different storage temperatures.

Table 2. Data on the binary interactions of different CaCl₂ doses on the percentage (%) of germinating (cracked) seeds in synthetic seed experiments*.

	C	50 mM	100mM	Average
A	3%	4.63 a	0.31 b	2.46 a
	4%	0.00 b	0.92 b	0.46 b
	5%	0.00 b	0.00 b	0.00 b
	0	6.17 a	1.23 b	3.70 a
S (days)	15	0.00 b	0.00 b	0.00 b
	30	0.00 b	0.00 b	0.00 b
	60	0.00 b	0.41 b	0.21 b
	Average	1.54 a	0.41 b	

* Applications were performed in triplicate and 3 beads were used for each replication. The differences between the values indicated with different letters are significant at the p<0.0.1 level according to the Duncan multiple comparison test. A: NaAlg dose, C: CaCl₂ dose, S: Storage time

In this study, comparisons with different interactions were also examined to determine the effect of media

composition on germination. When the media composition and NaAlg interaction were examined, the best germination percentage (5.55%) was observed in ÇG5 medium in 3% NaAlg trials. When media composition and CaCl₂ interaction were evaluated, the best result was found in the ÇG5*50 mM trials (3.70%). When the relationship between media composition and storage time was examined, it was concluded that storage reduced germination. In trials without storage, 7.41% germination rate was achieved in ÇG5 medium. Although 0.92% germination rate occurred in 60-day trials on ÇG8 medium, the difference was not statistically significant (Table 3). When the media compositions were evaluated in general, it was determined that the most suitable germination medium was MS medium (ÇG5) containing 3 mg/L BAP and 1 mg/L IBA. As a result of the analysis of variance performed, NaAlg dose (A), CaCl₂ dose (C) and storage time (S) were found to be statistically significant. Additionally, A*C, A*S, A*medium composition (M), C*S, C*M, A*C*S, A*S*M, C*S*M and A*C*S*M interactions were also found to be statistically significant. When all conditions were examined in detail, synthetic seeds coated with 50 mM CaCl₂ and 3% NaAlg gave the best results with a germination rate of 44.44% in conditions without storage in ÇG5 medium (Table 4).

Table 3. Data on the binary interactions of percentage (%) germination (cracking) bead rates in synthetic seed experiments in different media*.

M	A			T		C		S (days)				Average
	%3	%4	%5	4°C	24°C	50 mM	100 mM	0	15	30	60	
ÇG1	1.39 bcd	0.00 d	0.00 d	0.46	0.46	0.92 bc	0.00 c	1.85 cd	0.00 c	0.00 c	0.00 c	0.46 ab
ÇG2	2.78 abcd	0.00 d	0.00 d	0.92	0.92	1.85 abc	0.00 c	3.70 bc	0.00 c	0.00 c	0.00 c	0.93 ab
ÇG3	0.69 cd	0.00 d	0.00 d	0.00	0.46	0.00 c	0.46 c	0.00 c	0.00 c	0.00 c	0.92 cd	0.23 ab
ÇG4	4.17 ab	0.00 d	0.00 d	1.39	1.39	2.77 ab	0.00 c	5.55 ab	0.00 c	0.00 c	0.00 c	1.39 ab
ÇG5	5.55 a	0.00 d	0.00 d	1.85	1.85	3.70 a	0.00 c	7.41 a	0.00 c	0.00 c	0.00 c	1.85 a
ÇG6	4.17 ab	0.00 d	0.00 d	1.39	1.39	2.77 ab	0.00 c	5.55 ab	0.00 c	0.00 c	0.00 c	1.39 ab
ÇG7	0.00 d	0.00 d	0.00 d	0.00	0.00	0.00 c	0.00 c	0.00 c	0.00 c	0.00 c	0.00 c	0.00 b
ÇG8	3.47 abc	0.00 d	0.00 d	1.39	0.92	1.85 abc	0.46 c	3.70 bc	0.00 c	0.00 c	0.92 cd	1.16 ab
ÇG9	0.00 d	4.17 ab	0.00 d	1.39	1.39	0.00 c	2.77 ab	5.55 ab	0.00 c	0.00 c	0.00 c	1.39 ab

*Applications were performed in triplicate and 3 beads were used for each replication. The differences between the values indicated with different letters are significant at the p<0.0.1 level according to the Duncan multiple comparison test. M: Medium code, A: NaAlg dose, C: CaCl₂ dose, S: Storage time, T: storage temperature

Table 4. Data on the percentage (%) of germinating (cracked) beads in synthetic seed trials*.

A C T	M	3%					4%					5%							
		50 mM		100 mM		Avg	50 mM		100 mM		Avg	50 mM		100 mM		Avg	AVG		
		4°C	24°C	4°C	24°C		4°C	24°C	4°C	24°C		4°C	24°C	4°C	24°C				
S (days)	0	ÇG1	11.11 cd	11.11 cd	**	**	**	**	**	**	**	**	**	**	**	**	**	**	
		ÇG2	22.22 bc	22.22 bc	**	**	**	**	**	**	**	**	**	**	**	**	**	**	
		ÇG3	**	**	**	**	**	**	**	**	**	**	**	**	**	**	**	**	
		ÇG4	33.33 ab	33.33 ab	**	**	**	**	**	**	**	**	**	**	**	**	**	**	
		ÇG5	44.44 a	44.44 a	**	**	9.26 a	**	**	**	**	**	**	**	**	**	**	0.00 b	3.70 a
		ÇG6	33.33 ab	33.33 ab	**	**	**	**	**	**	**	**	**	**	**	**	**	**	**
		ÇG7	**	**	**	**	**	**	**	**	**	**	**	**	**	**	**	**	**
		ÇG8	22.22 bc	22.22 bc	**	**	**	**	**	**	**	**	**	**	**	**	**	**	**
		ÇG9	**	**	**	**	**	**	**	33.33 ab	33.33 ab	**	**	**	**	**	**	**	**
15	ÇG1	**	**	**	**	**	**	**	**	**	**	**	**	**	**	**	**		
	ÇG2	**	**	**	**	0.00 b	**	**	**	**	**	**	**	**	**	**	0.00 b	0.00 b	
	ÇG3	**	**	**	**	**	**	**	**	**	**	**	**	**	**	**	**		

	ÇG4	**	**	**	**	**	**	**	**	**	**	**	**				
	ÇG5	**	**	**	**	**	**	**	**	**	**	**	**				
	ÇG6	**	**	**	**	**	**	**	**	**	**	**	**				
	ÇG7	**	**	**	**	**	**	**	**	**	**	**	**				
	ÇG8	**	**	**	**	**	**	**	**	**	**	**	**				
	ÇG9	**	**	**	**	**	**	**	**	**	**	**	**				
	ÇG1	**	**	**	**	**	**	**	**	**	**	**	**				
	ÇG2	**	**	**	**	**	**	**	**	**	**	**	**				
	ÇG3	**	**	**	**	**	**	**	**	**	**	**	**				
	ÇG4	**	**	**	**	**	**	**	**	**	**	**	**				
30	ÇG5	**	**	**	**	0,00 b	**	**	**	**	0,00 b	**	**	**	**	0,00 b	0,00 b
	ÇG6	**	**	**	**	**	**	**	**	**	**	**	**	**	**	**	**
	ÇG7	**	**	**	**	**	**	**	**	**	**	**	**	**	**	**	**
	ÇG8	**	**	**	**	**	**	**	**	**	**	**	**	**	**	**	**
	ÇG9	**	**	**	**	**	**	**	**	**	**	**	**	**	**	**	**
	ÇG1	**	**	**	**	**	**	**	**	**	**	**	**	**	**	**	**
	ÇG2	**	**	**	**	**	**	**	**	**	**	**	**	**	**	**	**
	ÇG3	**	**	**	11,11 cd	**	**	**	**	**	**	**	**	**	**	**	**
	ÇG4	**	**	**	**	**	**	**	**	**	**	**	**	**	**	**	**
60	ÇG5	**	**	**	**	0,02 b	**	**	**	**	0,00 b	**	**	**	**	0,00 b	0,21 b
	ÇG6	**	**	**	**	**	**	**	**	**	**	**	**	**	**	**	**
	ÇG7	**	**	**	**	**	**	**	**	**	**	**	**	**	**	**	**
	ÇG8	**	**	**	11,11 cd	**	**	**	**	**	**	**	**	**	**	**	**
	ÇG9	**	**	**	**	**	**	**	**	**	**	**	**	**	**	**	**
	AVG			2,46 a				0,46 b						0,00 b			

*Applications were performed in triplicate and 3 beads were used for each replication. The differences between the values indicated with different letters are significant at the $p < 0.01$ level according to the Duncan multiple comparison test. M: Medium code, A: NaAlg dose, C: CaCl_2 dose, S: Storage time, T: storage temperature
 ** 0.00 d

The values of different interactions with storage temperature were also examined within the scope of the study. No statistical difference was determined between the data in the C*T interaction. When the effect of storage periods was examined, day 0 trials were in the first group with both temperature values of 3.70%. Although 0.2% value was obtained for both storage temperatures in the 60-day trials, they were included in the last group along with the other trials (Fig 2).

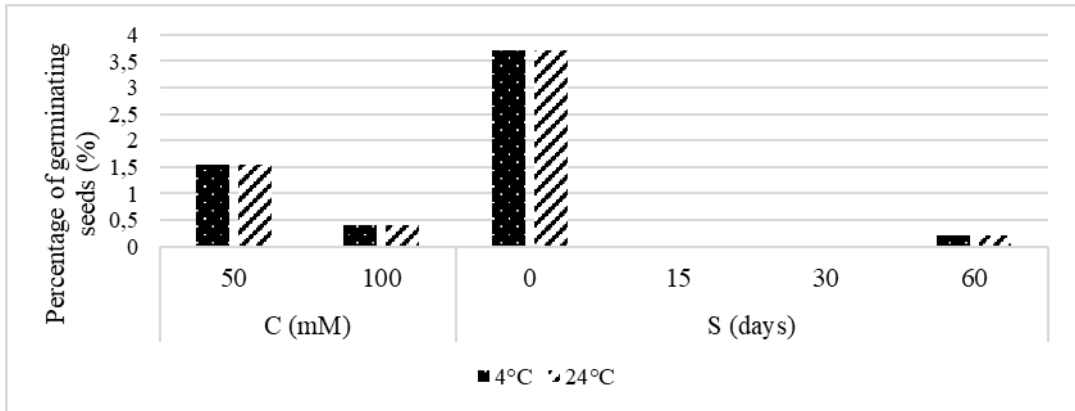


Fig 2. Graph of the percentage (%) data of germinating beads in the interactions of different CaCl₂ doses, alginate dose and storage times.

Various observations were made regarding the forms of the beads during the experiments. The beads produced with different amounts of NaAlg and CaCl₂ had different hardness and different degrees of opacity. Especially in low CaCl₂ and low NaAlg amounts, the beads were extremely soft and elliptical in shape, while harder and rounder shaped beads were formed with increasing CaCl₂ amounts (Fig 3). In addition, at high CaCl₂ molarity, the beads had a matte appearance, while as the amount decreased, the degree of transparency increased (Fig 4). While transparent beads were softer, as the opacity increased, the hardness of the beads increased. Increasing hardness in the beads had a negative effect on germination. As a result of all the experiments, the germinating seeds were determined and the most suitable coating method, storage condition and duration were determined (Fig 5).

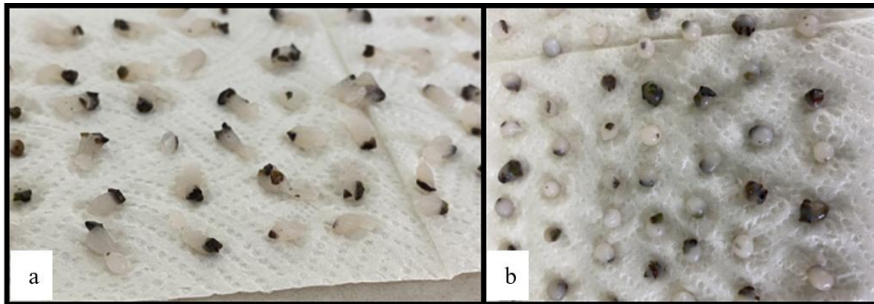


Fig 3. Synthetic seeds in different shapes and hardness states a) 50 mM CaCl₂ and 3% Na-Alg b) 100 mM CaCl₂ and 3% Na-Alg.

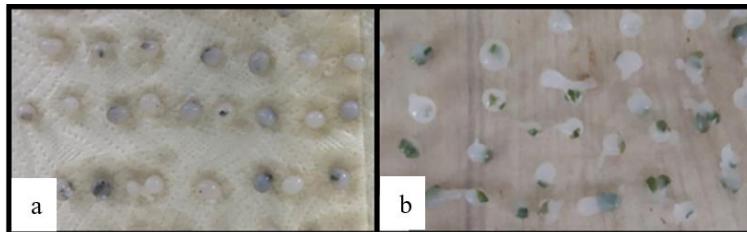


Fig 4. Synthetic seeds with different degrees of opacity a) 100 mM CaCl₂ and 3% Na-Alg b) 50 mM CaCl₂ and 3% Na-Alg.

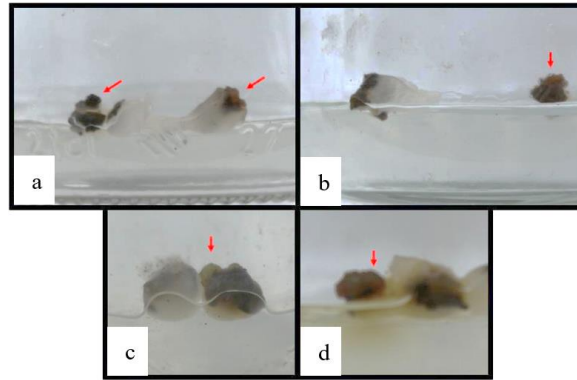


Fig 5. Some synthetic seeds germinating in different nutrient media as a result of storage period a) Seeds coated with 50 mM CaCl_2 +3% NaAlg and stored for 0 days and germinated in ÇG9 medium, b) Seeds coated with 50 mM CaCl_2 +3% NaAlg and stored at 4°C for 15 days and germinated in ÇG4 medium, c) Seeds coated with 100 mM CaCl_2 +3% NaAlg and stored at 4°C for 15 days and germinated in ÇG1 medium, d) Seeds coated with 50 mM CaCl_2 +3% NaAlg and stored at 4°C for 60 days and germinated in ÇG9 medium (indicated by red arrow).

4. Discussion

Somatic embryos produced in *in vitro* conditions in the tea plant were coated using different doses of NaAlg and CaCl_2 and synthetic seeds were obtained. The obtained synthetic seeds were germinated in nutrient media with different compositions after being stored under different conditions and for different periods of time. In this way, a new biotechnological method has been developed that allows it to be used in germplasm preservation in tea plants and facilitates the storage-transport stages.

Contamination is one of the problems frequently encountered in plant tissue culture studies. Contaminations in many cases prevent the growth and development of plants and cause loss of vitality [28]. In many cases, contamination can be seen quickly from the very beginning of the culture during *in vitro* studies, but in some cases, hidden contamination can become evident in later subcultures [27]. This situation was also seen in the study conducted by us. While no contamination was encountered in somatic embryo studies of the tea plant, yeast contamination was encountered in synthetic seed studies. The higher incidence of contamination, especially in beads stored at 24°C, can be explained by the fact that the ambient temperature provides suitable conditions for the growth of contaminants.

As a result of the study, although germination occurred in long-term storage, the data were not found to be statistically significant. This situation was thought to be related to intense darkening. In the study, a higher average germination rate (2.46%) was observed in the lowest dose alginate applications, while the germination rate decreased with increasing doses. It was determined that the most suitable encapsulation was obtained in the experiments carried out with 3% Na-Alg and 50 mM CaCl_2 , and in the germinations carried out without storage, the MS nutrient medium containing 3 mg/L BAP and 1 mg/L IBA was the most suitable germination medium. In the experiments, it was determined that an average of 1.333 out of 3 beads remained alive, and the viability rate was determined as 44.44%. Additionally, when CaCl_2 doses were compared, the average of 50 mM applications was found to be 1.54%, while this rate decreased to 0.41% in 100 mM trials. Another situation observed in the study is that increasing Na-Alg and CaCl_2 doses cause the formation of more round-shaped but harder beads. In encapsulations at lower doses, the shapes of the beads became more elliptical, but softer beads were obtained. Additionally, the opacity of the beads also varied. While the beads coated with higher molarity CaCl_2 had a more matte appearance, it was observed that the beads coated with lower molarity were more transparent.

Seran et al. carried out a study on the encapsulation of zygotic embryogenic parts of the tea plant [24]. In the study, it was determined that the most suitable encapsulation was obtained in the combination of 3% NaAlg and 100 mM CaCl_2 and the highest germination rate was in MS medium containing 3 mg/L BAP and 0.5 mg/L IBA. Similarly, in the study conducted by us, 3% NaAlg was found to be suitable and the suitable nutrient medium

content for germination was also similar. However, while [24] found the germination rate to be 93%, the germination rate in this study conducted by us was lower. It was thought that this situation was due to the difference in the encapsulated explant. In addition, it was observed in the study that harder and matte beads were obtained in high NaAlg and CaCl₂ combinations. [24] carried out experiments on MS nutrient media with and without plant growth regulators for germination and stated that exogenous plant growth regulators were needed for organ formation in tea plantlets. Similarly, in our study, regeneration did not occur in all experiments that did not contain plant growth regulators.

Gantait and Kundu, examined the polymerization abilities of different NaAlg doses in their studies on encapsulation [10]. In the study, experiments were carried out based on the knowledge that the bonding resulting from ion exchange between sodium (Na) and calcium (Ca) affects the form and hardness of synthetic seeds. In experiments using less than 3% NaAlg, it was observed that alginate lost its gelling feature and beads that were too soft and amorphous to hold were obtained. It was determined that the most suitable bead form was obtained in experiments using 3% NaAlg and 75 or 100 mM CaCl₂. At these doses, the shape of the beads was determined to be extremely solid, round in shape, light colored and uniform. This is thought to be due to the fact that the coating provides better protection as well as allowing nutrient transport between the explant and the nutrient medium without damaging the bead shape. It has been stated that with increasing doses of NaAlg, opacity increases and germination decreases in direct proportion to the dose. In addition, it was not preferred in the study because it showed toxic effects at high CaCl₂ doses. The information obtained from this study is parallel to the information obtained by us.

The genus *Camellia* is considered one of the most complex plant taxa. This complexity was achieved first by high hybridization and then by polyploidization. The new genetic materials created are preserved by clonal propagation methods. It has been suggested that organogenic calli can be used in micropropagation and long-term storage of tea.

5. Conclusion

Tea plant is an important agricultural plant worldwide with its socio-economic potential. Problems experienced in tea production necessitated the use of biotechnological methods. In our study, synthetic seeds were obtained by encapsulating somatic embryos produced from tea plantlets under *in vitro* conditions, and experiments were carried out to determine the most suitable coating method, storage time, storage condition and germination environment. In the light of the data obtained as a result of the study, the appropriate coating procedure and the appropriate nutrient medium composition for germination were determined. As a result of long storage, germination was observed in synthetic seeds, albeit at a low rate. This data shows that a study has been carried out that will lead to the development of an effective protocol for storage and transportation in the tea plant by applying synthetic seed technology. In addition, the fact that temperature was not determined as an effective factor is an indication that the protocol is economically low-cost. From now on, it is recommended to carry out experiments regarding the coating dose for encapsulation purposes and the use of alternative equipment in addition to the pasteur pipette in coating. In this way, a more practical application method can be used. Additionally, there is a need to carry out experiments by adding NaAlg or CaCl₂ or PPMTM to the nutrient medium in order to reduce contamination or browning.

Acknowledgements

This study was supported within the scope of TUBITAK-2211/C National PhD Scholarship Program in the Priority Fields in Science and Technology. This research was derived from Begüm Güler's doctoral thesis.

References

- [1] S.S. Chaeikar and K. Falakro, "Effect of colchicine treatment and polyploidy induction on some morphological, physiological and phytochemical characteristics of *Camellia sinensis* cv. Kashaf. ". *Journal of Plant Process and Function Iranin Society of Plant Physiology*, vol. 12, no. 54, pp. 203-218, 2023. doi: <http://jispp.iut.ac.ir/article-1-1738-en.html>
- [2] Direkvand-Moghdam, M.H. Mirjalili, M.N. Padasht Dehkai, H. Hassan Rezadoost. "Aromatic composition, catechins content, and metal elements profiling of forty-three Iranian black tea (*Camellia sinensis* L.) samples." *Journal of Medicinal Plants*, vol. 22, no. 85, pp. 76-88, 2023. doi: 10.61186/jmp.22.85.76
- [3] B. Can, B. Güler, and A. Gürel, "Globular embryo regeneration from callus in the tea plant (*Camellia sinensis* [L.] O. Kuntze)." *Indian Journal of Plant Sciences*, vol.11, pp. 62-73. 2022.
- [4] Ş.G. İzmirli and S. Gül, "Modeling of current and future distributions of *Camellia sinensis* in Türkiye under climate change." *Theoretical and Applied Climatology*, 2023. <https://doi.org/10.1007/s00704-023-04627-6>
- [5] P. Mangena, "Potential role of somatic embryo-generated synthetic seed production on mass propagation of recalcitrant grain legume crops in Sub Saharan Africa—A review article." *International Journal of Agricultural Technology*. vol. 17, no. 3, pp. 959-976, 2021.
- [6] K. Chandra, A. Pandey and P. Kumar, "Synthetic seed-Future prospects in crops improvement." *International Journal of Agriculture Innovations and Research*, vol. 6, no. 4, pp. 2319-1473, 2018.
- [7] T.K. Mondal, A. Bhattacharya, A. Sood, and P.S. Ahuja, "Factors affecting induction and cold storage of encapsulated tea (*Camellia sinensis* (L.) O. Kuntze) somatic embryos." *Tea*. vol, 21, pp. 92-100, 2000.
- [8] A. Ray and S. Bhattacharya, "Storage and plant regeneration from encapsulated shoot tips of *Rauwolfia serpentina*-An effective way of conservation and mass propagation." *South African Journal of Botany*, vol. 74, pp. 776-779, 2008.
- [9] P. Nongdam, "Development of synthetic seed technology in plants and its applications: A Review." *International Journal of Current Science*, vol. 19, no. 4, pp. E 86-101, 2016.
- [10] S. Gantait and S. Kundu, "Artificial seed technology for storage and exchange of plant genetic resources." *Advanced Technologies for Crop Improvement and Agricultural Productivity* (Edts: C.P. Malik, S.H. Wani, H. Bhati Kushwaha, R. kaur,), 2017, SBN No.: 978-93-81191-17-0. 2017.
- [11] A.A. Qahtan, E.M. Abdel-Salam, A.A. Alatar, Q.C. Wang and M. Faisal, "An introduction to synthetic seeds: production, techniques, and applications (Synthetic Seeds: Germplasm Regeneration, Preservation and Prospects)". Edts: M. Faisal, A.A. Alatar, 2019.Springer. ISBN 978-3-030-24630-3
- [12] P. Sharma, B. Roy, M. Roy, and G.S. Sundarrao, "Synthetic seed technology in horticultural crops for conservation and utilisation of germplasm." *International Journal of Agriculture Innovations and Research*, vol. 9, no. 3, pp. 2319-1473, 2020.
- [13] M.Ş. Özdemir, "Bazı colchium türlerinde somatik embriyogenesis, histolojik analizler ve sentetik tohum üretiminin araştırılması," Çukurova Üniversitesi Fen Bilimleri Enstitüsü Bahçe Bitkileri Anabilim Dalı. Yüksek Lisans Tezi (Danışman: Prof. Dr. Yeşim Yalçın Mendi). 2021.
- [14] V.A. Bapat, "Synthetic seeds: A novel concept in seed biotechnology." *Bhabha Atomic Research Centre Newsletter* vol. 200, pp. 7-111, 2000.
- [15] E. Khor and C.S. Loh, "Artificial seeds. In: Applications of Cell Immobilisation Biotechnology" Eds. V. Nedović and R.Willaert, *Focus on Biotechnology*, vol. 8B, 2005.Springer, Dordrecht. https://doi.org/10.1007/1-4020-3363-X_31.
- [16] K. Redenbaugh, J.A. Fujii, and D. Slade, "Hydrated coatings for synthetic seeds. In: Synseeds" Edt. K. Redenbaugh (CRC Press, Boca Raton). pp. 35-46, 1993.
- [17] D.S. Nair and B.R. Reghunanth, "Effective use of encapsulation dehydration technique in cryopreserving somatic embryos of butt erfly pea (*Clitoria ternatea* L.)." *Journal of Herbs, Spices & Medicinal Plants*, vol. 13, pp. 83-95, 2007.
- [18] D.S. Nair and B.R. Reghunanth, "Cryoconservation and regeneration of axillary shoot meristems of *Indigofera tinctoria* (L.) by encapsulation-dehydration technique." *In Vitro Cellular & Developmental Biology*, vol. 45, pp. 565-573, 2009.
- [19] A. Saxena, M. Shukla and P. Saxena, "Synthetic Seeds: Relevance to Endangered Germplasm Conservation *In Vitro* (Synthetic Seeds:Germplasm Regeneration, Preservation and Prospects)" Edts: M. Faisal and A.A. Alatar, 2019. Springer. ISBN 978-3-030-24630-3.
- [20] R. Mohanraj, R. Ananthan and V.N. Bai, "Production and storage of synthetic seeds in *Coelogyne breviscapa* Lindl." *Asian Journal of Biotechnology*, pp. 124-128, 2009.
- [21] M.M. Lulsdorf, T.E. Tautorus, S.I. Kikcio, T.D. Bethuni and D.I. Dunstan, "Germination of encapsulated embryos of interior spruce (*Picea glauca* engelmanni complex) and black spruce (*Picea mariana* Mill.)". *Plant Cell Reports*, vol. 12, pp. 385-389, 1993.
- [22] M.M.M. Micheli and A. Standardi, "Encapsulation of *in vitro* proliferated buds of olive." *Advances in Horticultural Science*, vol. 12, pp. 163-168, 1998.
- [23] B. Yücesan,"Synseed: A new trend in seed technology." In:Synthetic Seeds. Edts. M. Faisal and A. Alatar, Springer, Cham. 2019 https://doi.org/10.1007/978-3-030-24631-0_3
- [24] T.H. Seran, K. Hırmburagama, and M.T.K. Gunasekare, "Encapsulation of embryonic axes of *Camellia sinensis* (L.) O. Kuntze (tea) and subsequent *in vitro* germination." *Journal of Horticultural Science & Biotechnology*, vol. 80, no. 1, pp. 154-158, 2005.
- [25] T. Murashige, and F. Skoog, "A revised medium for rapid growth and bioassay with tobacco tissue cultures." *Physiologia Plantarum*, vol. 15, pp. 473-497, 1962.
- [26] N. Onishi, Y. Sakamoto and T. Hirosawa "Synthetic seeds as an application of mass production of somatic embryos". *Plant Cell, Tissue and Organ Culture* vol. 39, pp. 137-145, 1994.
- [27] B. Güler, Çay (*Camellia sinensis* [L.] O. Kuntze) bitkisinde geçici daldırma sistemine dayalı biyoreaktörler aracılığıyla sentetik tohumların üretilmesi. Ege Üniversitesi Fen Bilimleri Enstitüsü Biyomühendislik Anabilim Dalı Doktora Tezi (Danışman: Prof. Dr. Aynur Gürel). 2022.

[28] M.B. Pithiye, S.K. Sharma, M. Sharma, M., Sharma and N. Kotwal “Advancement and Challenges in Plant Tissue Culture: A Comprehensive Overview”. *Journal of Plant Biota*, vol. 1, no. 1, pp. 12-16, 2022. <https://doi.org/10.51470/JPB.2022.1.1.12>



Contents lists available at *Dergipark*

Journal of Scientific Reports-A

journal homepage: <https://dergipark.org.tr/pub/jsr-a>



E-ISSN: 2687-6167

Number 57, June 2024

RESEARCH ARTICLE

Receive Date: 21.03.2024

Accepted Date: 22.04.2024

The effect of foundation type selection on approximate cost of reinforced concrete buildings: the role of soil classes and number of floors

Uğur Kafkas^{a*}

^a*Kütahya Dumlupınar University, Kutahya Voc. School of Technical Sciences, Kutahya, Türkiye, ORCID: 0000-0003-1730-7810*

Abstract

This study investigates the choice of foundation type, which is one of the factors affecting the approximate cost of rough construction of buildings with reinforced concrete structural systems. In the study, isolated, continuous and raft foundation types are discussed comparatively for buildings with different numbers of floors (1-4 floors above the basement) and different soil classes (ZB-ZE). In the literature, there is no study in which the effects of foundation type, number of floors and soil classes on the approximate cost of a building are analyzed together. This study aims to fill this gap in this field. Reinforced concrete design and analysis were performed using Protastructure 2022 software; concrete, formwork and reinforcing steel quantities were calculated, and approximate costs were calculated with the Republic of Türkiye Ministry of Environment, Urbanization and Climate Change 2024 Construction and Installation Unit Prices (TCÇŞİDB 2024) and the results were presented in tables and graphs. According to the study's findings, as the soil class improves, isolated foundations are more economical than other foundations. In contrast, the cost of isolated foundations increases significantly as the soil class deteriorates and the number of floors increases, while the cost difference between continuous foundation and raft foundation decreases.

© 2023 DPU All rights reserved.

Keywords: Foundation type selection; Approximate cost, Soil classes, Number of floors, Cost analysis

* Corresponding author. Tel.: +90-274-443-6203.
E-mail address: ugur.kafkas@dpu.edu.tr

1. Introduction

The construction sector is one of the essential sectors for the development and sustainability of modern societies. It is an important source of economic growth and employment while enabling the realization of infrastructure and superstructure projects that affect daily life. Completing construction projects requires intensive efforts from engineers and other industry stakeholders. All processes are critical in this context, from the initial design phase of construction projects to the final turnkey delivery. Safety, aesthetics, and economy are the most important principles to consider during the design phase of construction projects. Especially in the design of structural bearing systems, the most critical factor is safety, but cost is also an important consideration in engineering practice [1]. The cost of a project starts with the cost of the land on which the project will be realized and ends with the completion and delivery of the entire construction. These costs can generally be grouped as land costs, costs incurred for plans, projects and permits, rough construction costs and acceptable construction costs.

Rough construction is an early phase of the construction project, focusing on durability and structural integrity rather than visual aesthetics. Notably, the cost of the rough construction part, where the manufacturing of support systems is done, is a significant component of a construction project's total cost. Generally, the share of rough construction within the total cost of a construction project can vary significantly from project to project. Many variables, from the size and complexity of the project to the condition of the support system, soil characteristics, and materials used, influence the cost of rough construction. For example, interior design and materials may carry more weight in a luxury housing project. In contrast, in an industrial facility project, the rough construction cost may constitute a more significant percentage of the total cost.

The primary aim of this study is to thoroughly examine the impact of different types of surface foundations on the approximate cost of rough construction for single and multi-story reinforced concrete-bearing system buildings with basements. As known, the most crucial task of foundations in structures is to safely transfer the loads from the superstructure and any other potential forces that may arise to the ground. The choice of foundation type is not only dependent on the superstructure but also heavily relies on the condition of the soil. Therefore, the class of soil on which the structure will be established, and its physical properties are significant factors that influence the choice of foundation type.

Foundations can generally be divided into two main groups: shallow and deep. As the name suggests, the shallow foundations discussed in this study are those established closer to the ground surface. The types of foundations used in this study have been selected as isolated (pad), continuous (strip), and raft (mat) foundations, per market conditions. Understanding the impact of these foundation types on the rough construction cost of a building, especially under different soil conditions, is crucial for the cost estimates and budget planning of construction projects. The rough construction cost includes the concrete, construction steel, and formwork quantity and expenses used to construct the building's support system. This study will address these elements in detail, providing cost analyses for different foundation types, total building heights, number of floors, and different soil classes.

Türkmen and Tekeli [2] and Türkmen et al. [3] examined the cost variations of reinforced concrete buildings with 4-8 floors and a standard floor plan of 248 m², conducting static and reinforced concrete designs for buildings with two apartments per floor in earthquake-prone and non-earthquake-prone areas, with and without irregularities, and for different soil types. Their research, conducted using the Probing Orion 2000 software and the equivalent static earthquake load method, found that the additional load imposed by earthquake-resistant design increased the total cost by only 4-8%. Through regression analysis, Dorum et al. [4] explored the variations in rough construction costs for reinforced concrete buildings depending on soil class and earthquake zone, highlighting the differences between soil classes and earthquake zones per the 1998 Turkish Regulation on Buildings to be Constructed in Disaster Areas. Dikmen and Özek [5] investigated the effect of soil classes on the cost of industrial-type buildings with different column spacings. The designs of single-story buildings with varying support systems were compared based on approximate costs for different soil classes according to the 2007 Turkish Earthquake Regulation. Azimi et al. [1] analyzed the cost of reinforced concrete support systems for buildings with varying numbers of floors and soil types

using acceleration spectra. They found a significant cost difference in buildings designed with 5 floors as the soil structure became more stable. Eroğlu and İpek [6] examined the effects of soil class and different foundation types (isolated, continuous, and raft foundations) on structural behavior. Focusing on the interaction between soil and structure, their research aimed at decision-making regarding foundation systems relative to soil, considering soil classes and the requirements of the 2018 Turkish Building Earthquake Code (TBDY), with supporting system designs completed using the IDE-CAD software.

The number of floors in a building type is significant for construction costs. In a study that changed only the building geometry while keeping the floor areas constant, structural designs using the tunnel form system demonstrated the effect of both the number of floors and building height on costs, showing that the cost per area decreases up to a certain number of floors, particularly after 15 floors, the unit cost increases [7]. Another study on the effect of soil classes on foundation design costs, particularly for buildings on soils with different sand densities, was conducted by Azhim and Prakoso [8]. Their research in various cities in Indonesia revealed that the soil's friction angle and elasticity modulus were the primary factors affecting the cost of the designed foundations. In research on the impact of foundation types on building costs [9], the effect of different foundation types on the construction cost of a 5-story building was examined. Excluding the foundation type, all other variables were kept constant, and the raft foundation was more economical than other foundations. Various studies have also been conducted on the effects of different earthquake zones, soil parameters, and soil classes on building costs [10-14].

When the literature above is examined, there is no study in which the effects of foundation type, number of floors and soil class on the approximate cost of the building are studied together. This study aims to fill this gap in this field. At different soil classes and different numbers of floors, i.e., total heights of the building, the foundation type to be determined at the design stage will have a significant effect on the approximate cost of the building. This effect is revealed in this study. This study selected an architectural project of a building with a uniform, symmetrical form. It addressed situations with basements and one or more floors (2-4) according to the selected floor plan. For each different number of floors, the analyses of the building were redone, followed by reinforced concrete design and analysis for various foundation types. Then, concrete, steel reinforcement, and formwork quantities were calculated separately. Subsequent analyses repeated for different soil classes and physical properties led to comparisons between the same and different foundation types under various soil classes and conditions. This research aims to evaluate the suitability of different foundation types for buildings with varying numbers of floors and soil class designs, focusing on design and cost optimization.

2. Material and method

Within the scope of this study, the floor plan of the architectural project selected is presented in Fig. 1, and the base area of the project is 341.90 m², with a floor height of 2.80 m for each floor. The ground floor reinforced concrete formwork plan is also given in Fig. 2. Considering the construction will occur in Kütahya, the material properties and the earthquake parameters determined according to the TBDY [15] were used during the reinforced concrete design and calculation stages. As material parameters, the concrete class was taken as C30, the reinforcement steel class as S 420 and earthquake parameters as Building Usage Class 3 and Earthquake Design Class 1.

Within this study's scope, the project features a symmetrical structure and is an apartment project with four units on each floor. Reinforced concrete designs and solutions for 1-4 floors, including a basement, were performed using Protastructure 2022 software (version 6.0.647). Protastructure 2022 is a domestically developed software with thousands of users worldwide, facilitating the design and analysis of steel and reinforced concrete. This software has superior features such as fast, efficient, robust analysis capabilities, integration with building information modeling, optimization tools, and collaboration ease. Thus, it allows for the more reliable and sustainable management of complex projects and assists in designing reinforced concrete structures per various regulations.

One of the most critical aspects of structural design is the foundation design. Foundations are the load-bearing elements that transfer the weight and loads of the structure to the ground. Therefore, they are essential parts of the support system that ensure the structure stands as designed. Surface foundation types such as isolated, continuous, and raft have been used in this study. Fig. 3 provides examples of 3D drawings from the design and analyses performed with the foundation types used within the scope of the study.

The primary task of foundations is to safely carry the mass of the structure, the loads arising from this mass, and the loads that may be induced by external factors, transferring them to the ground on which they sit. In particular, from a geographical standpoint, Turkey is a region that experiences many disasters, including earthquakes [16]. At this point, the characteristics of the soils on which the foundations rest are as crucial as the design of the foundations themselves. The ability of the soils to bear the loads transferred by the foundations is one of the most essential aspects in the design of foundations. According to the TBDY [15], soil classification is given in Table 1. The part with a thickness of 30 meters below the foundation subgrade level should be used for soil classification. Here, $(V_s)_{30}$ represents the average shear wave velocity for 30 meters, $(N_{60})_{30}$ represents the average standard penetration blow count for 30 meters, and $(c_u)_{30}$ represents the average undrained shear strength for 30 meters. Soils have been classified from A to F according to their strength.

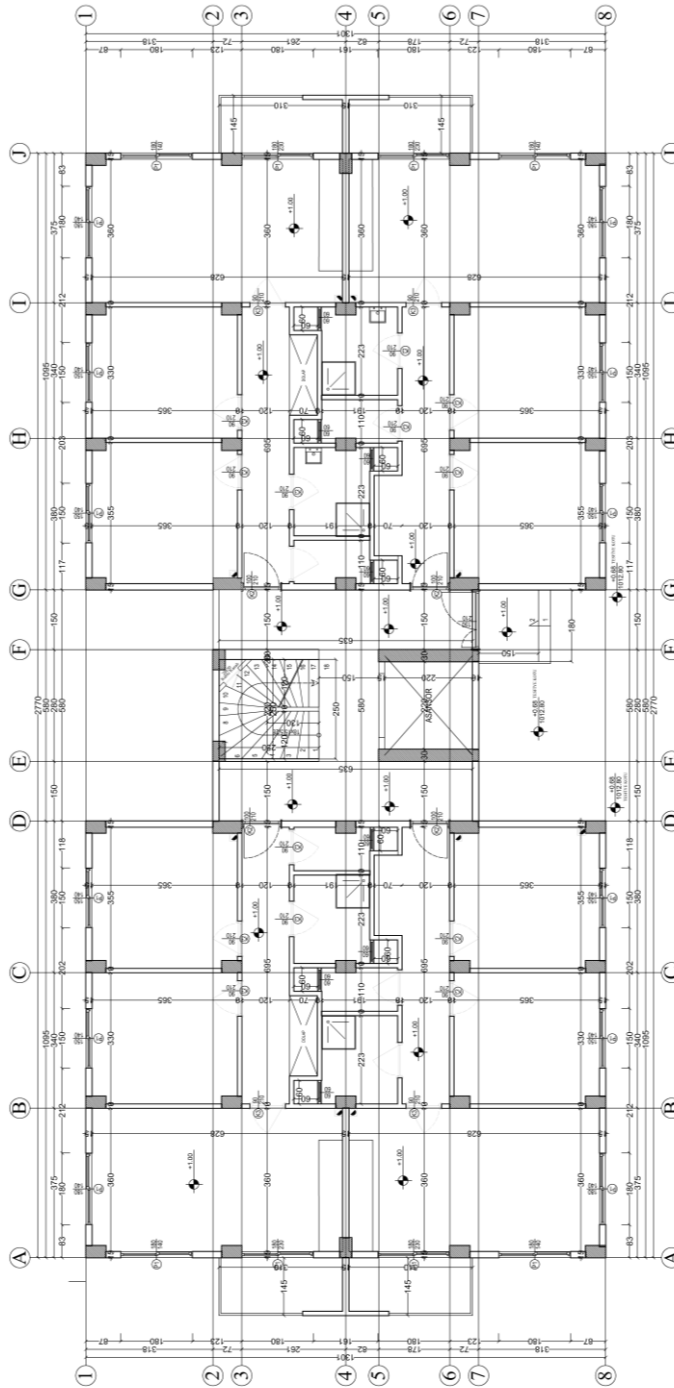


Fig. 1. Architectural floor plan.

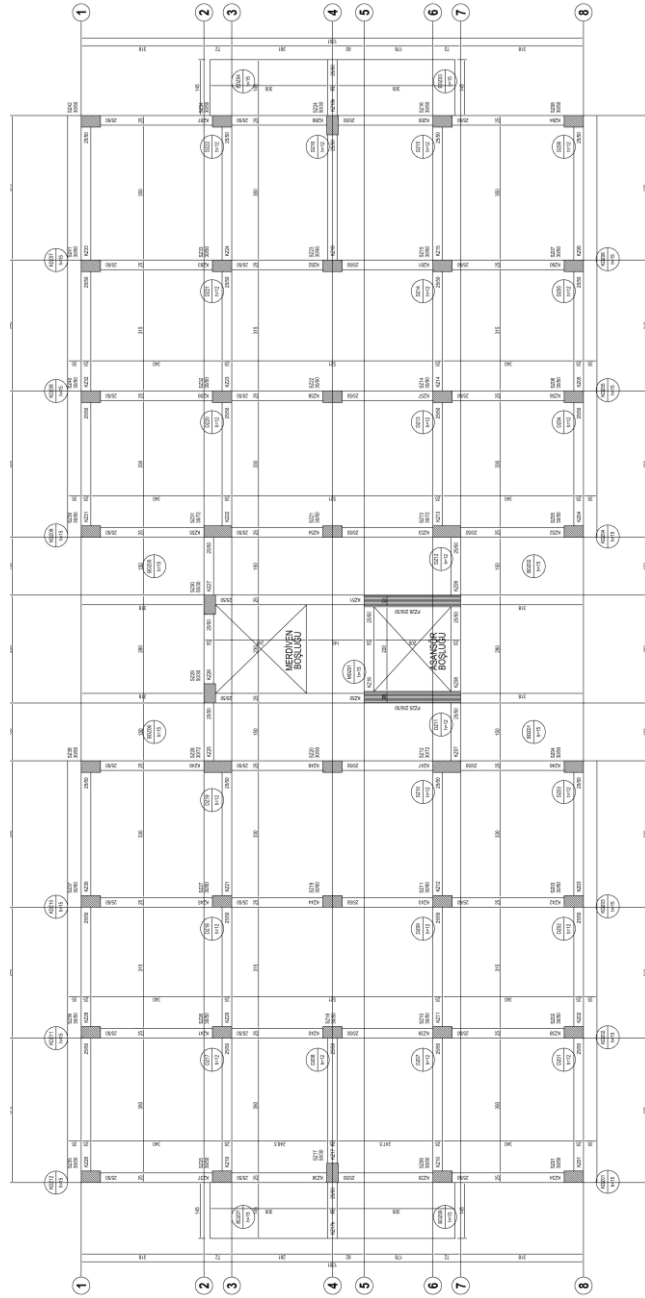


Fig. 2. Reinforced concrete formwork plan.

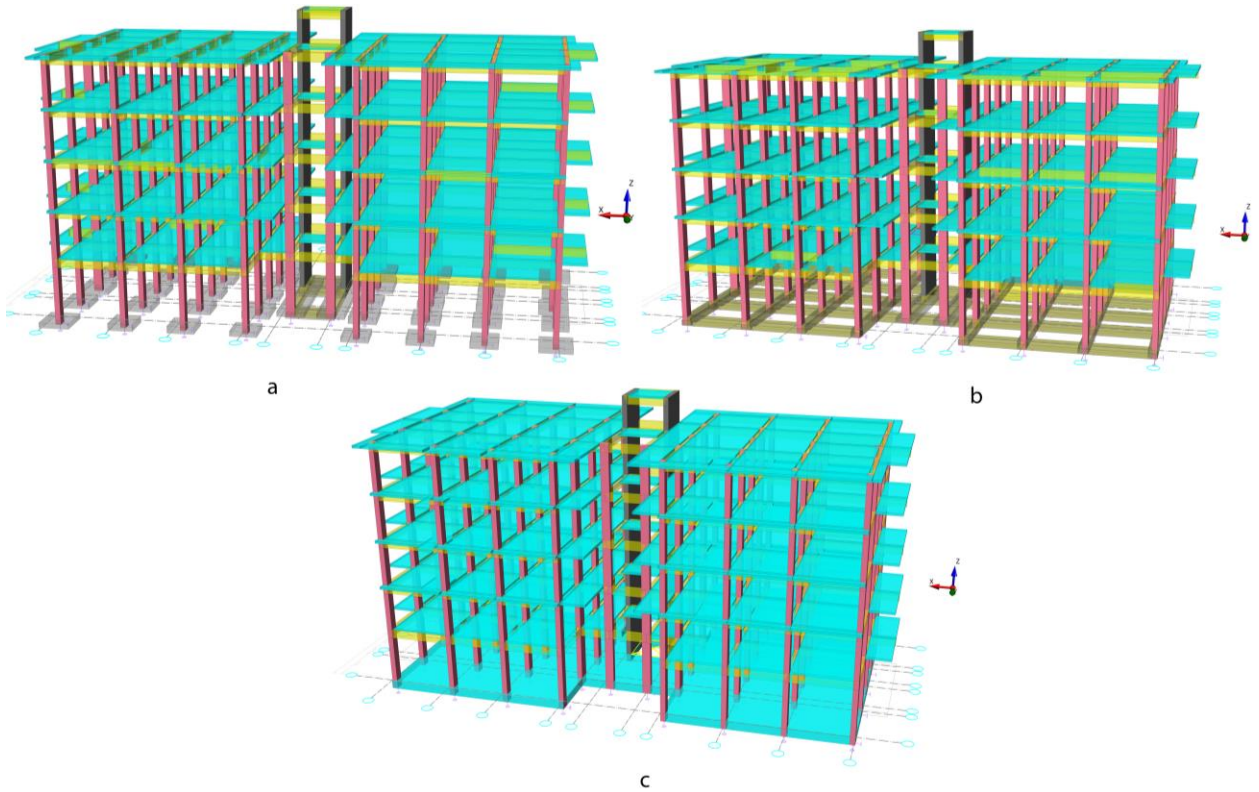


Fig. 3. Examples of reinforced concrete design; (a) Isolated foundation; (b) Continuous foundation; (c) Raft foundation.

Table 1. Local soil classes [15].

Local soil class	Floor-type	Average at upper 30 meters		
		$(V_s)_{30}$ (m/s)	$(N_{60})_{30}$ (pulse /30 cm)	$(c_u)_{30}$ (kPa)
ZA	Sturdy, hard rocks	> 1500	–	–
ZB	Slightly decomposed, moderately solid rocks	760 – 1500	–	–
ZC	Layers of very tight sand, gravel and hard clay, or weak rocks with decomposed, very cracked	360 – 760	> 50	> 250
ZD	Medium tight – layers of tight sand, gravel or very solid clay	180 – 360	15 – 50	70 – 250
ZE	Profiles containing layers of loose sand, gravel or soft–solid clay or a layer of soft clay thicker than 3 meters in total ($c_u < 25$ kPa) satisfying conditions of $PI > 20$ and $w > 40\%$	< 180	< 15	< 70
ZF	Soils requiring site-specific research and evaluation			

In the context of the study, initially, the design and analyses for the said project were carried out on a rock soil with soil class ZB, and the design strengths and coefficient of soil reactions were selected according to this soil. Subsequent analyses were performed for soil classes such as ZC, ZD, and ZE. The necessary parameters for the soil classes used in these analyses were obtained from previous soil survey reports in Kütahya. In this context, the design strengths and coefficient of soil reactions received from the reports were calculated separately for different foundation types as specified in TBDY [15]. As known, TBDY [15] explains how to calculate the design strength, and here, the differences that may arise in terms of foundation types begin primarily with foundation geometry and dimensions. Different design strength values and coefficient of soil reactions emerge when considering different geometries or sizes for various foundation types to be constructed on the same soil.

It should also be noted that the calculations during structural design and analysis consider continuous boundary values. In other words, while performing calculations with different foundation types for each building solution, the minimum values have been selected by TBDY [15], the Provision for the Design and Construction of Reinforced Concrete Structures (TS 500) [17], and minimum values have been used until a safe solution is obtained.

According to TS 500 [17], when designing isolated foundations, the smallest dimension in the plan cannot be less than 70 cm, and the foundation area cannot be less than 1 m². The foundation depth cannot be less than 25 cm and cannot be smaller than 1/4 of the cantilever span. Similarly, for continuous foundations, according to TS 500 [17], if the foundation is beam-designed, the thickness of the foundation beam cannot be less than 1/10 of the free span, and the plate thickness cannot be less than 20 cm; if it is designed without beams, then the plate thickness cannot be less than 30 cm. Thus, the minimum design dimensions were selected in this way. The thickness of the raft foundation also started from a minimum of 30 cm. After the analysis and calculations, if the dimensions were insufficient, they were increased and analyzed again. Increases were made using as small numbers as possible. For example, raft thicknesses were increased by 1-2 cm increments, and the analyses were repeated. It should be noted here that in market conditions, raft thicknesses are generally increased in 5-10 cm increments rather than making such increments. After completing the design, analysis, and calculations, the concrete, formwork, and steel reinforcement quantities for all the designed reinforced concrete structures were extracted. Then, these quantities were multiplied by the TCCŞİDB 2024 to obtain approximate costs. Subsequently, the necessary comparisons were made with these costs.

3. Material and method

This section presents the results and findings of analyses conducted on the selection of foundation type - one of the factors influencing the approximate rough construction cost of buildings with a reinforced concrete support system -. In the study, isolated, continuous, and raft foundation types have been comparatively considered for buildings with different numbers of floors (1-4 floors above the basement) and various soil classes (ZB-ZE). The soil parameters used in the analyses are given separately for the local soil classes applied in Table 2. The variations in values calculated according to TBDY [15] are due to the inclusion of foundation geometry and foundation dimensions in the calculation of design strength.

Table 2. Utilized soil parameters.

Local soil classes	Unit weight (t/m ³)	Isolated foundation		Continuous foundation		Raft foundation	
		Design strength (t/m ²)	Coefficient of soil reaction (t/m ³)	Design strength (t/m ²)	Coefficient of soil reaction (t/m ³)	Design strength (t/m ²)	Coefficient of soil reaction (t/m ³)
ZB	2.49	41.80	2341	39.00	2184	40.40	2262
ZC	2.24	34.50	1932	29.50	1652	31.50	1764

ZD	1.87	25.50	1428	20.50	1148	22.50	1260
ZE	1.92	21.00	1176	18.40	1030	19.20	1075

As a result of the analyses, the quantities of concrete, formwork, and reinforcement steel, along with their total approximate costs obtained by multiplying these quantities by TCÇSİDB 2024, are given separately for each soil class in Tables 3-6. The graphical representation of the data in the tables is provided in Figs. 4-7.

Table 3. ZB local soil class for floor level specific concrete, formwork, and reinforcement steel quantities and total cost.

Number of floors (excluding basement)	Foundation type	Concrete volume (m ³)	Formwork area (m ²)	Construction steel (Ø 8-12 mm) (tn)	Construction steel (Ø 14-28 mm) (tn)	Approximate total cost (TL)
1	Isolated	251.127	1,731.11	16.185	8.395	2,590,006.15
	Continuous	223.763	1,905.27	14.812	9.717	2,623,786.94
	Raft	282.040	1,609.50	21.827	5.074	2,677,158.01
2	Isolated	326.306	2,455.07	22.999	10.161	3,537,558.44
	Continuous	311.011	2,632.75	21.236	12.776	3,635,064.46
	Raft	367.555	2,336.56	28.801	7.125	3,669,149.16
3	Isolated	410.281	3,187.14	30.045	12.044	4,525,526.48
	Continuous	406.363	3,355.31	28.722	16.160	4,711,182.77
	Raft	469.393	3,068.71	36.395	9.304	4,733,290.62
4	Isolated	497.994	3,923.15	36.849	13.466	5,502,992.40
	Continuous	498.127	4,083.51	35.447	19.574	5,756,720.65
	Raft	571.231	3,800.85	44.416	11.282	5,805,199.42

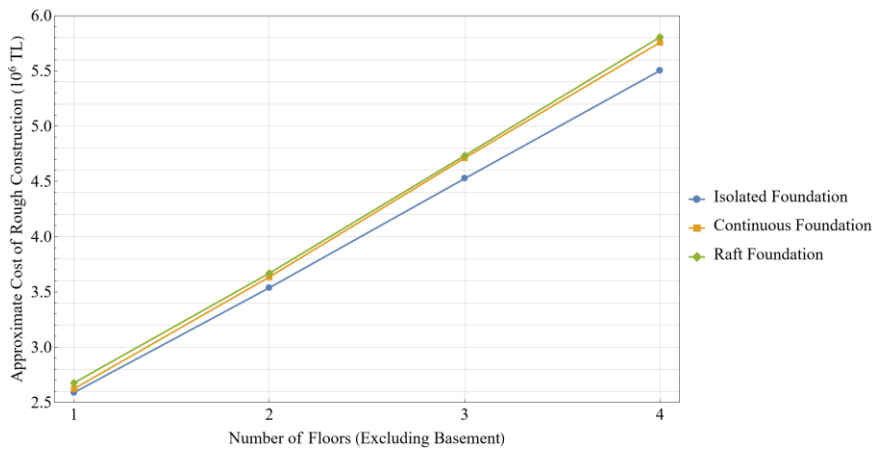


Fig. 4. Changes in approximate cost depending on foundation type and number of floors in local soil class ZB.

According to Table 3, as expected, buildings on ZB class soil with higher foundation strength and coefficient of soil reaction isolated foundations have a lower cost than others. The difference between the costs widens as the floor count increases. In the case of a building on a single basement floor, isolated foundations are approximately 1.2875% less expensive than continuous foundations and about 3.2554% less than raft foundations. However, this difference grows as the number of floors increases, with the cost of isolated foundations being approximately 4.4075% lower than continuous and about 5.2058% lower than raft foundations for a four-story building above the basement.

Table 4. ZC local soil class for floor level specific concrete, formwork, and reinforcement steel quantities and total cost.

Number of floors (excluding basement)	Foundation type	Concrete volume (m ³)	Formwork area (m ²)	Construction steel (Ø 8-12 mm) (tn)	Construction steel (Ø 14-28 mm) (tn)	Approximate total cost (TL)
1	Isolated	325.623	1,811.41	17.167	10.372	2,938,759.89
	Continuous	224.214	1,905.41	14.851	9.685	2,625,346.97
	Raft	282.084	1,609.50	21.446	6.532	2,711,901.70
2	Isolated	446.768	2,593.89	24.527	14.313	4,136,227.65
	Continuous	313.836	2,633.31	21.731	13.103	3,670,237.23
	Raft	377.375	2,339.61	29.091	8.942	3,766,334.69
3	Isolated	508.595	3,292.90	31.258	16.226	5,034,023.93
	Continuous	411.536	3,356.23	29.345	16.992	4,773,645.65
	Raft	472.666	3,069.72	36.658	11.033	4,807,776.33
4	Isolated	567.790	4,002.47	37.933	18.113	5,928,696.31
	Continuous	507.343	4,085.20	35.856	20.681	5,832,319.26
	Raft	577.778	3,802.89	44.150	13.746	5,895,298.50

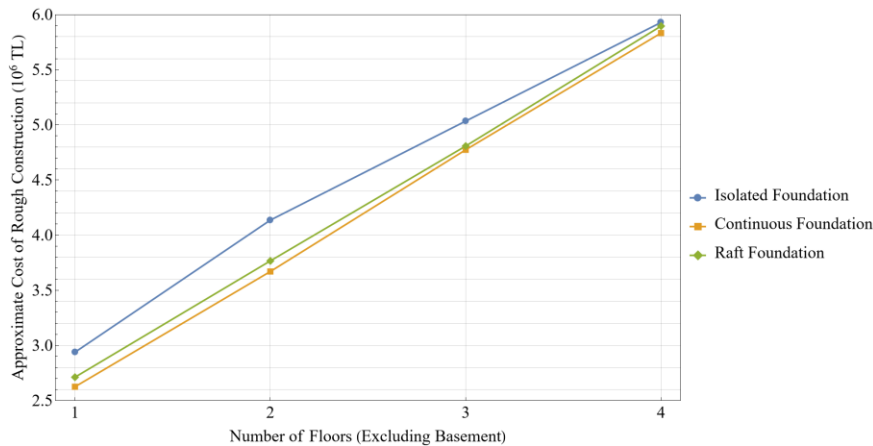


Fig. 5. Changes in approximate cost depending on foundation type and number of floors in local soil class ZC.

In Table 4, the quantities of concrete, formwork, and reinforcement steel, along with their approximate costs, are shown for a building designed on ZC-class soil with different numbers of floors and foundation types. As shown in

Fig. 4, on ZB-type soil, as the number of floors increases, using isolated foundations significantly reduces the approximate rough construction cost to the extent reinforced concrete design allows. However, as the soil parameters decrease, the soil becomes less resistant, and the cost of isolated foundations increases considerably, as seen in Table 4 and Fig. 5.

For ZC class soils, it is understood from Table 4 and Fig. 5 that continuous foundations are the most cost-effective option. Looking at the cost between raft and continuous foundations, the cost difference decreases significantly as the number of floors increases. For example, while the difference in approximate cost for a building designed on a single basement floor is about 3.3%, this difference falls below 0.75% for three floors above the basement. It should not be forgotten that the calculated approximate costs only pertain to concrete, formwork, and reinforcement steel; when considering the total cost of the building, this percentage difference will be even lower.

Table 5. ZD local soil class for floor level specific concrete, formwork, and reinforcement steel quantities and total cost.

Number of floors (excluding basement)	Foundation type	Concrete volume (m ³)	Formwork area (m ²)	Construction steel (Ø 8-12 mm) (tn)	Construction steel (Ø 14-28 mm) (tn)	Approximate total cost (TL)
1	Isolated	358.480	1,841.35	17.610	11.509	3,098,022.36
	Continuous	228.568	1,906.45	15.276	9.764	2,654,522.63
	Raft	282.084	1,609.50	21.823	6.702	2,730,059.61
2	Isolated	505.339	2,644.28	25.005	16.503	4,413,158.66
	Continuous	331.419	2,636.75	22.122	13.230	3,737,023.41
	Raft	383.921	2,341.65	29.441	8.948	3,797,184.58
3	Isolated	638.888	3,371.24	32.317	21.045	5,626,729.08
	Continuous	436.353	3,361.03	29.558	16.831	4,845,415.03
	Raft	489.033	3,074.81	37.150	11.693	4,893,025.96
4	Isolated	708.586	4,076.48	39.000	23.178	6,555,220.77
	Continuous	538.741	4,091.18	36.182	20.799	5,935,387.40
	Raft	590.739	3,806.96	42.465	16.882	5,978,296.87

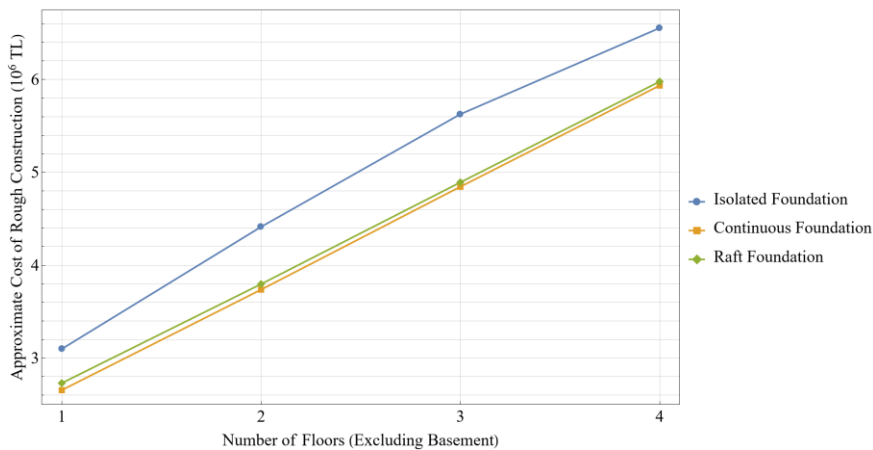


Fig. 6. Changes in approximate cost depending on foundation type and number of floors in local soil class ZD.

The quantity results and approximate costs for a building designed on ZD-class soil are presented in Table 5, with the graphical representation provided in Fig. 6. It is noteworthy that as the soil's design strength and soil reaction coefficient values decrease. The soil class worsens, and the cost difference between continuous and raft foundations decreases even when the number of floors is low. Continuous foundations emerge as the most cost-effective foundation type for ZD class soil, where the approximate cost of isolated foundations is again very high due to soil conditions. However, while the price of raft foundations is about 2.85% higher than continuous foundations for a single floor above the basement, this excess cost drops to around 0.73% for four floors above the basement.

Finally, Table 6 presents the results for a building designed and analyzed for construction on ZE class soil, which has the lowest soil parameters in the study. The graph created based on these results is provided in Fig. 7. The outcomes observed for ZD class soil are similarly applicable for ZE class soil. Again, continuous foundations stand out as the most cost-effective, while the cost difference compared to raft foundations continues to decrease. As previously mentioned, as the soil class weakens in strength, the heightened cost of isolated foundations, which are not very sensible in design and production under such conditions, also becomes noteworthy.

Table 6. ZE local soil class for floor level specific concrete, formwork, and reinforcement steel quantities and total cost.

Number of floors (excluding basement)	Foundation type	Concrete volume (m ³)	Formwork area (m ²)	Construction steel (Ø 8-12 mm) (tn)	Construction steel (Ø 14-28 mm) (tn)	Approximate total cost (TL)
1	Isolated	407.960	1,884.06	18.025	13.252	3,328,965.83
	Continuous	234.929	1,907.71	15.492	9.905	2,684,281.03
	Raft	282.084	1,609.50	21.843	6.782	2,733,347.26
2	Isolated	592.598	2,714.75	25.718	19.794	4,823,733.04
	Continuous	342.506	2,638.89	22.173	13.281	3,771,594.03
	Raft	393.741	2,344.70	30.062	8.953	3,846,526.37
3	Isolated	747.122	3,482.55	32.978	27.611	6,224,470.09
	Continuous	453.932	3,364.46	29.774	16.931	4,905,408.50
	Raft	501.983	3,078.88	35.417	14.974	4,979,077.18
4	Isolated	873.159	4,209.07	40.063	29.613	7,327,373.02
	Continuous	560.361	4,095.18	36.387	20.602	5,996,627.98
	Raft	603.963	3,811.03	43.156	16.938	6,041,456.33

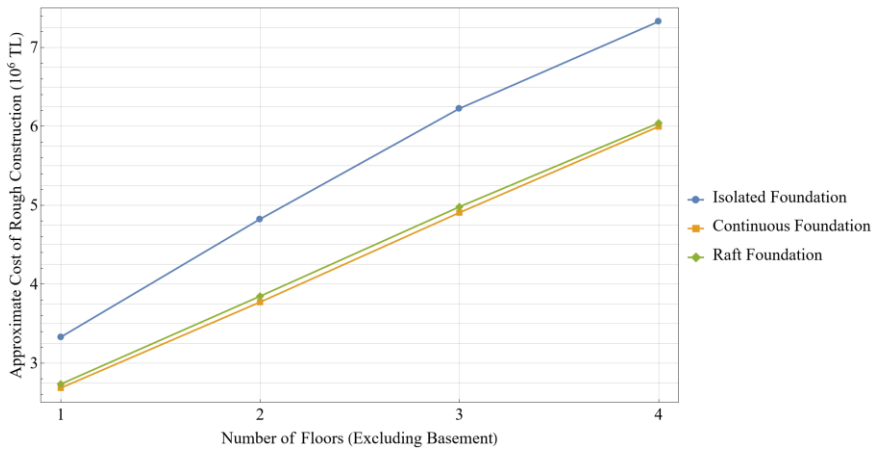


Fig. 7. Changes in approximate cost depending on foundation type and number of floors in local soil class ZE.

Another point regarding Tables 4-6 that should be addressed pertains to isolated foundations. Suppose the quantities and approximate costs associated with isolated foundations are examined. In that case, it is noticeable that as the number of floors increases, the difference from other types of foundations relatively decreases. Upon investigation, this phenomenon is attributed to eccentricity in the design of isolated foundations. Due to the geometric design requirements of isolated foundations, especially under seismic loadings, the forces generated often result in isolated foundations for lower numbers of floors being as large or even more significant than those for buildings with higher floors.

Figures 8-11 graphically present the cost variations for different floor counts according to various local soil classes.

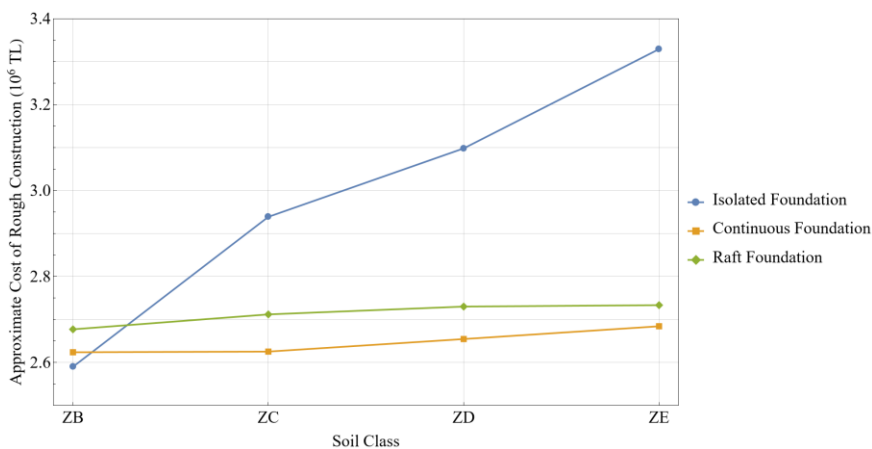


Fig. 8. Cost changes depending on foundation type and soil class for a single floor above the basement.

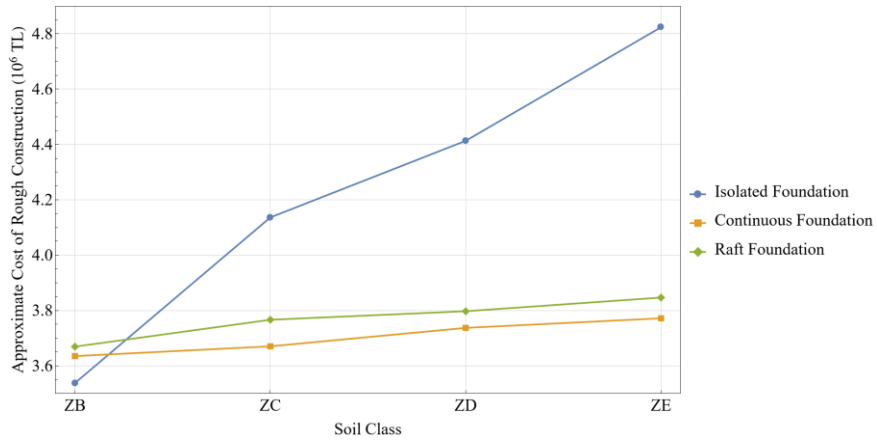


Fig. 9. Cost changes depending on foundation type and soil class for 2 floors above the basement.

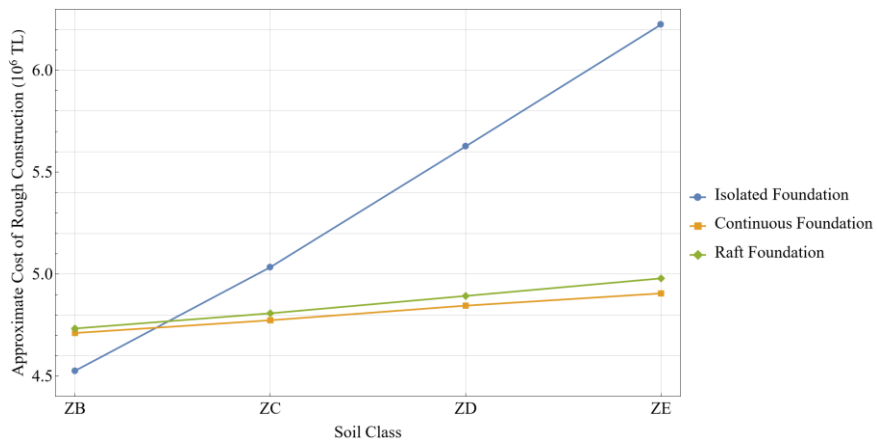


Fig. 10. Cost changes depending on foundation type and soil class for 3 floors above the basement.

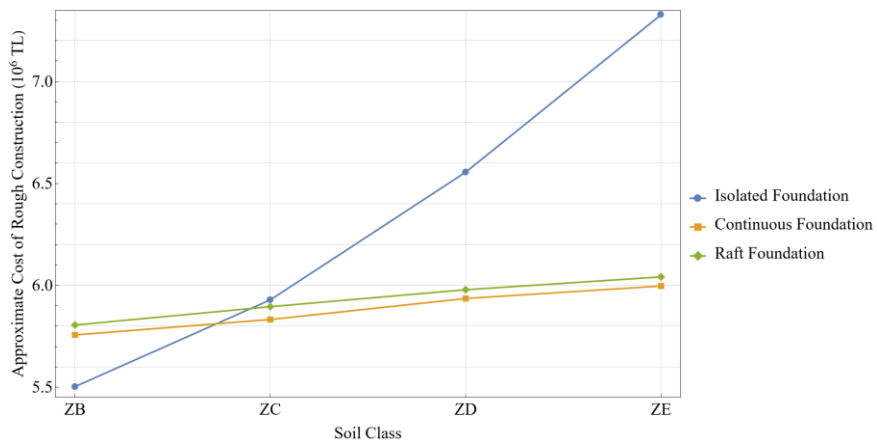


Fig. 11. Cost changes depending on foundation type and soil class for 4 floors above the basement.

One of the most significant findings emerging from the design and analyses conducted within the scope of the study is that for structures to be constructed on soils with higher bearing capacity, such as ZA and ZB classes, designs utilizing isolated foundations tend to be more cost-effective. This is mainly due to the influence of dimension restrictions during the design phase as per the regulations in Turkey. Continuous foundations emerge as the most cost-effective foundation for soils with lower bearing capacities. Moreover, raft foundations also appear as the main competitors to continuous foundations regarding the cost of these types of soils.

4. Conclusions

This study has investigated the impact of different shallow foundation types on the approximate rough construction cost of buildings with reinforced concrete support systems. Isolated, continuous, and raft foundations were comparatively analyzed for buildings with varying floors and soil classes. Isolated foundations emerge as the most cost-effective foundation type regardless of the number of stories on soils with higher bearing capacities. A significant reason for this is the minimum size rules applied to continuous and raft foundations as per TS 500 [17]. As soil-bearing capacity decreases, continuous foundations become more cost-effective.

The analyses have shown that raft foundations are more expensive than continuous foundations. However, it is crucial to note that this cost difference only encompasses concrete, formwork, and steel reinforcement quantities. When comparing the costs of these quantities, particularly as the number of stories increases, the cost difference significantly decreases. Considering the local soil classes of ZC, ZD, and ZE, the cost difference for a single-floor building above the basement is approximately 2.657% on average, 2.072% for two floors, 1.067% for three floors, and 0.850% for four floors. As the number of stories increases, the cost difference between continuous and raft foundations significantly diminishes. Moreover, it is evident that when considering the overall building (both fine and rough construction) costs, the percentage cost difference between the raft and continuous foundations will further decrease.

Another point that stands out when examining Tables 3-6 is the formwork quantities. As expected, the formwork quantities are lower for raft foundations than other types. One of the first and most significant effects of this situation is the reduced cost of formwork scaffolding, which directly influences the overall approximate cost of the building. The indirect effect is that formwork labor for raft foundations will be less, resulting in time savings and, consequently, shorter project delivery times.

The filling process is another significant cost difference between isolated and continuous foundations compared to raft foundations. The filling required for isolated or continuous foundations brings substantial costs and risks. Initially, there will be the cost of filling material and the cost of spreading and compacting this material. Then, the cost of wire mesh reinforcement and slab concrete will also be added. Alongside all these costs, there are risks, such as damage to column stubs during compaction of the fill and the potential for settlement of the fill material. Furthermore, the necessity of filling, like formwork labor, will also extend the project delivery times to a certain degree.

When all these risks and costs are considered, it can be said that, especially for soil class ZC and local soils with lower strength, there is no significant difference between continuous and raft foundation construction costs. Particularly in Turkey, which harbors substantial seismic risks, even if it were possible, deciding on the type of foundation solely based on the cost parameter, without considering other factors, does not entirely reflect reality; the idea that raft foundations are much more costly than other shallow foundations is not wholly accurate.

In conclusion, many factors must be carefully considered when selecting the most suitable foundation type for each project. This study aims to provide a broader perspective by including the impact of the cost factor in choosing the foundation type. It underscores the importance of assessing each project's unique needs and conditions.

Acknowledgments

This research received no specific grants from any funding agency in public, commercial or non-profit sectors.

References

- [1] P. Azimi, H. Gazi, and C. Alhan, "Effects of Soil Amplification Factors on the Seismic Performance Potential and Cost of Reinforced Concrete Structural Systems," *Teknik Dergi*, vol. 30, no. 1, pp. 8803–8834, 2019, doi: 10.18400/tekderg.308431.
- [2] M. Türkmen and H. Tekeli, "Effects of Local Soil Classification and Seismic Zone On the Cost of Building," *SDÜFBED*, vol. 9, no. 3, 2005, doi:10.19113/sdufbed.51589.
- [3] M. Türkmen, H. Tekeli, and A. Kuyucular, "Construction Costs of Multi Storey RC Buildings for Different Soil Classes and Structural Irregularities," *J. Fac.Eng.Arch. Selcuk Univ.*, vol. 21, no. 1, pp. 57–66, 2006, <https://dergipark.org.tr/tr/pub/sujest/issue/23271/248396>.
- [4] A. Dorum, Ö. Özkan, and M. Erdal, "Effects of Different Earth Quake Areas and Different Soil Classes on Basic Structure Costs," *Selcuk University Journal of Engineering Sciences*, vol. 5, no. 1, pp. 1–9, 2006, <https://sujes.selcuk.edu.tr/sujes/article/view/20>.
- [5] S. Ü. Dikmen and S. Özek, "Effects of Soil Group on the Cost of Industrial Structures," *Teknik Dergi*, vol. 22, no. 108, pp. 5543–5558, 2011, <https://dergipark.org.tr/tr/pub/tekderg/issue/12751/155191>.
- [6] İ. Eroğlu and C. İpek, "Soil And Building Interaction Under Earthquake Loads," *International Journal of New Horizons In The Sciences*, vol. 1, no. 1, pp. 18–27, 2023, doi: 10.5281/zenodo.8200563.
- [7] Z. Y. İlerisoy and M. E. Tuna, "Effects of Plane Dimensions and Number of Storeys On the Cost of Rectangular-Plane Buildings Constructed with Tunnel Form," *MEGARON / Yıldız Technical University, Faculty of Architecture E-Journal*, 2018, doi: 10.5505/megaron.2018.98698.
- [8] A. Azhim and W. A. Prakoso, "Construction cost optimization of shallow foundation for sand soil in Indonesia," *MATEC Web of Conferences*, vol. 270, p. 05005, Feb. 2019, doi: 10.1051/mateconf/201927005005.
- [9] E. Azat, "The Effect of Different Foundation Types and Different Soil Improvement Techniques on Building Cost," [Master Thesis], Bilecik Şeyh Edebali University, Bilecik, 2022.
- [10] H. Karaca, "The influence of soil parameters of TEC-2019 over the amount of structural material used and roof drift of structures, a case Study," *Journal of Polytechnic*, vol. 25, no. 2, pp. 467–475, 2022, doi: 10.2339/politeknik.680595.
- [11] İ. Teştek, "Analysis and economical comparison of a multi-story structure having reinforced concrete and steel bearing system considering the soil classes defined in 2018 Turkey Building Earthquake Code," [Master Thesis], Gümüşhane University, Gümüşhane, 2019.
- [12] Ü. Gülçiçek, "Approximate rough construction cost estimation via the change of construction parameters," [Master Thesis], Sakarya University, Sakarya, 2011.
- [13] Y. Genç, "Cost Analysis on Residential Buildings Built in Different Earthquake Regions," [Master Thesis], Harran University, Şanlıurfa, 2014.
- [14] H. İnce, E. Toy and M. Tolon, "Influence of Local Soil Conditions on the Structural Design and Associated Costs," *International Journal of Engineering and Natural Sciences*, vol. 1, no. 1, pp. 21–26, 2018, <https://dergipark.org.tr/en/pub/ijens/issue/43155/523381>.
- [15] TBDY, "Supplement Principles for The Design of Buildings Under the Influence of Earthquakes." Disaster and Emergency Management Presidency, Ankara, 2018.
- [16] M. Kalkan, A. D. Kaçar, and O. Alptekin, "Ülkelerin Deprem Sonras Yeniden Yapılaşma Süreçlerinin Karşılaştırılması: Çin, Şili ve Türkiye Örnekleri: Deprem Sonras Yeniden Yapılaşma Stratejileri," *Tasarım+ Kuram*, vol. 16, no. 31, pp. 152–169, 2020, doi: 10.14744/tasarimkuram.2020.41275.
- [17] TS 500, "Betonarme Yapıların Tasarım ve Yapım Kuralları," *Türk Standardları Enstitüsü*. 2000.



Contents lists available at *Dergipark*

Journal of Scientific Reports-A

journal homepage: <https://dergipark.org.tr/pub/jsr-a>



E-ISSN: 2687-6167

Number 57, June 2024

RESEARCH ARTICLE

Receive Date: 06.03.2024

Accepted Date: 23.06.2024

A hybrid approach to obesity level determination with decision tree and pelican optimization algorithm

Nagihan Yağmur^{a*}

*Kütahya Dumlupınar University, Faculty of Engineering, Department of Computer Engineering, Kutahya, Türkiye,
ORCID:0000-0002-6407-4338*

Abstract

Approximately 2 billion people in the world struggle with "obesity" and factors like eating lifestyle, habits, health conditions and mode of transport affect obesity. In this study, an artificial intelligence and machine learning-based model has been developed to predict obesity levels. It is proposed to create a hybrid model by combining the Decision Tree (DT) algorithm with the Pelican Optimization Algorithm (POA) on the obesity dataset of 2111 patients in SSggle. These models emphasize the critical role of parameters, aiming to achieve high performance. To solve the classification problem of multi-class obesity level determination, fuzzy logic-based parameter optimization is used to achieve high performance. While obesity rates are increasing worldwide, the study, which aims to globalize the parameters with the random discovery strategy of POA, is thought to be helpful for health professionals and decision-makers by successfully predicting obesity levels.

© 2023 DPU All rights reserved.

Keywords: Artificial intelligence, obesity, machine learning, decision tree, Pelican optimization algorithm, hybrid model

1. Introduction

Within the medical realm, the discussion on categorizing obesity as a disease has concluded, establishing a unanimous consensus: Obesity has received official recognition as a medical condition [1], [2], [3]. This view has been supported by the World Health Organization (WHO) and more recently by the European Commission. Many

* Corresponding author.

E-mail address: nagihan.yagmur@dpu.edu.tr

other health organizations have also endorsed this classification. A broad understanding of the scientific and health reasons behind defining obesity as a disease is now generally accepted in the medical community [1].

The surge in obesity rates has become a significant public health issue both nationally and globally [4], [5], [6]. Apart from imposing substantial financial burdens on the healthcare system, obesity leads to numerous detrimental health consequences, including cancers, endocrine disruptions, musculoskeletal issues, and a notable rise in premature deaths attributed to cardiovascular diseases [6], [7].

It is possible for anyone to gain weight and become obese in the context of his or her lifestyle, family history and a number of other factors according to the World Health Organization guidelines [5], [8]. The largest contributor to obesity, or the condition of uncontrolled weight gain, is excess fat [9]. There are several ways to measure excess fat in the human body [9]. Body fat is measured by a person's weight and height [9]. The most widely used scale is body mass index (BMI). Also used for measurements are skinfold thickness, bioimpedance, and waist circumference [9].

BMI furnishes crucial insights into categorizing body fat and body mass/weight, facilitating meaningful comparisons of weight across diverse groups. This helps to identify individuals at higher risk and prioritize interventions. Nevertheless, it is important to note that BMI fails to consider variations in body fat and muscle distribution, leading to the possibility that individuals with substantial muscle mass may register a high BMI even if their body fat percentage is low [9]. Waist size is another important measurement, especially used to assess overweight or obese individuals. However, it is important to understand that BMI alone is not sufficient in all cases and a more comprehensive assessment should be made by combining different measurements [9].

Obesity does not appear suddenly, but rather develops over time. It is important to apply machine learning techniques to assess a person's dietary habits and life choices. Data mining studies with the application of machine learning techniques will not only visualize changes in the follow-up of diet plans, but also allow this trend to predict negative events in the long term [9].

As engineering problems become more intricate, there is a rise in optimization challenges that classical optimization methods struggle to address. Therefore, new algorithms inspired by nature need to be developed. Among these artificial intelligence-based algorithms, there are methods inspired by nature such as POA, Butterfly Optimization Algorithm (BOA), Chicken Swarm Optimization Algorithm (CSO) [10], [11], [12].

Within data mining research, the exploration of influential attributes is commonly employed to evaluate classification outcomes. Feature selection aims to assess each parameter's impact while retaining those most critical to the model. Less impactful metrics can be excluded to focus on the most informative for categorization. Conventional logic-based methods restrict coefficients to binary values of zero or one. However, employing variably weighted coefficients permits a more nuanced assessment of each attribute's role. This finessed approach allows subtle adjustment of individual contributions to the predictive procedure. Such weighted evaluation proves vital for enhancing results and glean insights from large, complex datasets. Indeed, many published studies document the calculation of customized weights shed light on each factor's classification influence [13], [14], [15], [16], [17], [18].

The purpose of this research is to build a estimation model for assessing obesity levels based on machine learning techniques. This system accounts for an array of aspects including eating habits, lifestyle, medical conditions, and means of transportation. Here, we analyzed an obesity dataset from UCI comprising 2111 patients. The database categorizes individuals as Normal_weight, Over_weight_1, Over_weight_2, Obesity_type1, Obesity_type2, Obesity_type3 and Under_weight. To assign obesity classes, we applied the 'fitctree' method utilizing the Decision Tree algorithm within Matlab [16]. Additionally, a hybrid approach is proposed combining DT with the POA. The POA outperforms other meta-heuristic algorithms in solving optimization problems by establishing a balanced relationship between exploration and exploitation. Derived from fuzzy logic principles, these blended models diligently appraise the importance of variables through the stochastic exploration of POA. In doing so, it strives to accomplish triumphant performance in categorizing individuals across multiple obesity levels.

The main contributions of this article can be summarized as follows:

- It comprehensively reviews the studies on obesity.
- It tests classical methods commonly used in the literature for obesity level classification or other classification problems with the same dataset.
- It proposes a new hybrid model to the literature by using DT and POA metaheuristics to classify the dataset to determine the obesity level.
- Inspired by the fuzzy logic approach, the proposed model better emphasizes the importance of parameters and achieves better results than the results obtained by classical methods.
- To the best of our knowledge, there is no other work on fuzzy logic-based parameter optimization to improve decision trees for multi-class obesity level classification.
- By improving the importance score calculated by the DT method for each parameter, an enhanced DT method is introduced to the literature.

2. Literature review

An investigation has recently been conducted into the use of 3D body scans to rectify deficiencies in obesity categorization through machine learning [19]. Duo-information (on body composition), consisting of Dual-energy X-ray absorptiometry, 3D body images, and Bioimpedance Analysis, was collected from one group of South Korean subjects. Following a machine learning framework based on 3D body scanning data for obesity classification, its utility was tested using a variety of metrics such as F1-score, Accuracy, Sensitivity and Precision. VKI and BIA are compared in this lightweight. VKI created Accuracy of 0.529, Sensitivity of 0.472, F1 score of 0.462, and Precision 0.458. On the other hand, BIA bettered these figures significantly with a Accuracy of 0.752, Sensitivity 0.742, Precision 0.751, and F1 score of 0.739. Not surprisingly, the proposed model compares favourably with both VKI and BIA, achieving an Accuracy of 0.800, a Sensitivity of 0.767, Precision 0.842 and F1 score 0.792. These values surpass the effectiveness of BMI and BIA in obesity categorization. In other a study, researchers endeavored to compare machine learning algorithms for a supervised task [20]. They employed Random Forest (RF) and K-Nearest Neighbor (KNN) models, submitting each to a battery of performance metrics. RF outpaced KNN following hyperparameter tuning, a 94% average accuracy. In a research investigation centered upon classifying obesity levels, dataset has been collected from the UCI Machine Learning Repository, which served as the basis for applying diverse machine learning methods. These included the Logistic Support Vector Machine (SVM), Regression, KNN, DT, and the sophisticated RF algorithm [21]. The analysis revealed the RF model delivered the most exceptional outcomes, attaining the highest measured accuracy at a %85.58. In a research initiative presenting a deep learning model designed to predict future obesity trends using the extensive medical records of children, a prominent pediatric health system in the United States provided an unmodified dataset [22]. Taking advantage of a versatile Long Short Term Memory (LSTM) network architecture, the model data in research consisted both static and dynamic Electronic Health Records (EHR) from 1-3 years prior. The model offers elaborate information to capture the onset of obesity among all persons between the ages of 3 and 20. Comparing the efficacy of the LSTM model with the data set from relevant literature studies, the model outperformed other models across most age groups-and this means it is very good at predicting patterns of obesity which depend on historical medical records. Similar findings led to another study that applied different machine learning techniques (including ensemble learning, generalized random forest, partial least square method, linear model) to the prediction of obesity trends based on age, height and weight, and BMI indicators [23]. The study achieved an impressive accuracy rate of more than 89%, showing that this comprehensive method predicts obesity patterns effectively.

When the studies using the same dataset are examined, the highest accuracy was obtained with J48 trees with 97.4% in the study using decision trees (J48), Bayesian networks (Naïve Bayes) and logistic regression [24]. In another study, chi-square, F-classification and mutual information classification algorithms were used to identify the most critical factors associated with obesity [25]. The performance of these models was compared using a neural network trained with different feature sets. Furthermore, the hyperparameters of the models are optimized with

Bayesian optimization techniques, which are faster and more efficient than traditional methods. The results showed that the neural network predicted the level of obesity with an average accuracy of 93.06%, 89.04%, 90.32% and 86.52% using all features and the features selected by the chi-square, F-classification and mutual information classification algorithms, respectively.

The processing of biomedical digital data and the evaluation of data records in hospitals are crucial for developing decision support systems for physicians [26]. Recently, numerous studies have focused on digital data processing and the classification of patient data records. In these studies, numerical data from patients, such as blood values, are typically processed to create systems that assist doctors in responding to new patients more quickly and accurately [27]. Both classical machine learning methods, such as Naïve Bayes, SVM, KNN, and regression, as well as deep learning techniques like Convolutional Neural Networks (CNN) and Stacked Autoencoders (SAE), have been utilized (knn nbayes cnn ekle). Additionally, nature-inspired metaheuristics, including Particle Swarm Optimization (PSO), Harris Hawks Algorithm (HHA), and Artificial Bee Colony (ABC), are increasingly being employed in these studies [13], [28], [29].

Feature selection Feature selection methods are important when guiding the impact of different parameters in a dataset on classification in data mining and machine learning, and to choose significant features when looking at data records [30]. It is characterized by getting rid of the less important parameters and keeping the more important ones in order to handle big datasets issues. We need to figure out 1) how to select features 2) and weight individual input parameters Page 129 So traditional feature selection someone receives a coefficient of 0 or 1 which means it is included accounted. But instead of selecting / discarding features we actually want to say that this feature is more significant compared to the other one by multiplying them by weight vector. This way, each parameter contributes to the success (the better) of classification to different degrees. However, it is better to give low weight rather than deleting a completely trivial parameter, with the creation of a function that is as insensitive to the hypothesis as possible (least dependence on this parameter while using its real range of values).

For many years, there have been numerous studies on the binary classification of obesity records (obese/not obese) and classification based on obesity levels. The literature proposes various machine learning methods for predicting and classifying obesity. These methods include KNN, SVM, RF, DT, and Learning Vector Quantization (LVQ), among others. These techniques may not always perform well across different datasets due to varying features and characteristics. Factors such as variability in the number of patient records significantly influence the success of obesity classification methods. Therefore, it is essential to develop new techniques to account for differences in dataset features and parameter numbers [31]. The increasing complexity of engineering problems has made solving them with traditional machine learning methods more challenging. The limitations of classical methods in addressing complex problems have necessitated the development of new nature-inspired techniques. Examples of nature-inspired algorithms include JAYA, CSO and Artificial Bee Colony (ABC). These methods are frequently used in data mining. Metaheuristics are successfully applied to various problems due to their ability to avoid local optima, derivative-free nature, flexibility, and ease of implementation. However, in recent years, the use of metaheuristics for obesity classification problems has been limited.

Additionally, although machine learning has been widely applied to obesity prediction and classification, there are few studies that comprehensively investigate various important factors such as an individual's health status and dietary habits and present a hybrid method. Simultaneously, emphasizing the significance of selected parameters to improve classification accuracy is a crucial factor in enhancing obesity prediction. Therefore, this paper introduces a hybrid model designed to identify classes including Normal_weight, Over_weight_1, Over_weight_2, Obesity_type1, Obesity_type2, Obesity_type3, and Under_weight. The results of the proposed model are compared with those obtained from traditional machine learning techniques to provide a thorough comparative analysis.

Table 1. Dataset properties and types.

	Parameter	Type		Parameter	Type
1	Age	Numerical	20	CH2O_2	1 : Between 1 liter and 2lt 0 : No
2	Gender	0 : Male 1 : Female	21	CH2O_3	1 : More than 2 liters 0 : No
3	Height (metre)	Numerical	22	SCC	1 : Yes 0 : No
4	Weight (kg)	Numerical	23	FAF_1	1 : Never 0 : Others
5	FHWO	1 : Yes 0 : No	24	FAF_2	1 : 1 or 2 times a week 0 : Others
6	FAVC	1 : Yes 0 : No	25	FAF_3	1 : 2 or 3 times a week 0 : Others
7	FCVC_1	1 : Never 0 : Others	26	FAF_4	1 : 4 or 5 times a week 0 : Others
8	FCVC_2	1 : Sometimes 0 : Others	27	TUE_1	1 : Less than 1 hour 0 : Others
9	FCVC_3	1 : Always 0 : Others	28	TUE_2	1 : 1 to 3 hours 0 : Others
10	NCP_1	1 : 1 to 2 0 : Others	29	TUE_3	1 : More than 3 hours 0 : Others
11	NCP_2	1 : 2 0 : Others	30	CALC_1	1 : No 0 : Others
12	NCP_3	1 : More than 3 0 : Others	31	CALC_2	1 : Sometimes 0 : Others
13	NCP_4	1 : No answer 0 : Others	32	CALC_3	1 : Often 0 : Others
14	CAEC_1	1 : No 0 : Others	33	CALC_4	1 : Always 0 : Others
15	CAEC_2	1 : Sometimes 0 : Others	34	MTRANS_1	1 : Car 0 : Others
16	CAEC_3	1 : Often 0 : Others	35	MTRANS_2	1 : Motorcycle 0 : Others
17	CAEC_4	1 : Always 0 : Others	36	MTRANS_3	1 : Bicycle 0 : Others
18	Smoke	1 : Yes 0 : No	37	MTRANS_4	1 : Public transport 0 : Others
19	CH2O_1	1 : Less than 1 liter 0 : No	38	MTRANS_5	1 : Walking 0 : Others

When looking at the parameters in the Table 1, "FHWO" refers to "Family_history_with_overweight," "FAVC" indicates "consumption of high-calorie food," "FCVC" represents "vegetable consumption frequency," "NCP" stands for "main meal frequency," "CAEC" signifies "food consumption between meals," "Smoke" pertains to "smoking information," "CH2O" denotes daily water consumption, "SCC" refers to "Information about whether or not you consume calories," "FAF" stands for "frequency of physical activity," "TUE" indicates "Time using technology devices," "CALC" represents "alcohol consumption," and "MTRANS" signifies "transportation."

3. Materials and methods

3.1. Data preprocessing and dataset

For the investigation reported here, the source of the data set is UCI Laboratory, providing open access to its dataset [24], [32]. The dataset includes data from Mexico, Peru, and Colombia to estimate the obesity levels of individuals aged between 14 and 61 years. The data was collected using a web platform, through a questionnaire where anonymous users answered each question, and SMOTE (Synthetic Minority Over-Sampling Technique) was

used to balance the unbalanced dataset, resulting in a dataset of 17 attributes and 2111 records. However, since the variables are categorical, One Hot Encoding was applied to these variables and the categorical parameters were transformed into vector arrays consisting of 0 and 1. Thus, the number of parameters was increased to 38 as seen in Table 1. At the same time, due to the large differences between the values in the dataset, the data were normalized to 0-1 in order to make the data regular and comparable.

3.2. One hot encoding

By comparing each level of the categorical variable with a fixed reference level, it transforms a single variable with n observations and d different values into d binary variables, each with n observations [33]. The observations indicate the presence of the binary variable with 1 and its absence with 0 [33].

3.3. Decision trees

Decision trees (DTs) have gained widespread use in recent years for classification and pattern recognition, owing to their simplicity and straightforward rule-based construction [34]. DT adopts a multi-stage or sequential methodology in the classification process. A decision tree comprises three main components: nodes, branches, and leaves. Each attribute is represented by a node in the tree structure, with branches and leaves forming the additional components. The uppermost segment of the tree is denosssted as the root, while the lower portion is referred to as the leaf. The segments connecting the root to the leaves are termed branches [34], [35].

Building a decision tree entails asking a sequence of inquiries about the training data and drawing conclusions from the answers, with the objective of formulating decision rules. The classification process begins at the root node, progressing through nodes until branches or leaves without further subdivisions are encountered [34], [36]. To assess the generalization ability of the generated tree, a test dataset is employed. When a new test data point enters the tree structure established with the training data, it traverses through the tree, commencing from the root node. The new data, upon being tested at the root, is directed to a child node based on the test outcome, and this traversal continues until a specific leaf is reached. Each leaf corresponds to a single path or decision rule from the root [34], [36].

3.4. Pelican optimization algorithm

POA, conceptualized by Trojovský and Dehghani, draws inspiration from the foraging behavior of pelicans and stands as a metaheuristic optimization technique. Pelicans, renowned for their collective hunting approach, skillfully pinpoint their prey and execute a coordinated dive to capture it. These birds predominantly inhabit warm waters worldwide, favoring locations such as lakes, rivers, coasts, and marshes. Pelicans are social creatures, typically dwelling in groups, showcasing proficiency not only in flight but also in swimming [37]. Their keen eyesight and adept observation skills aid them during flight, and they primarily subsist on a diet of fish. When pelicans detect prey, they engage in a distinctive hunting behavior by running towards it from an altitude of 10-20 meters and directly diving into the water [38]. In the presence of fish schools, pelicans organize themselves into a line or U-shape formation, descending from the sky to manipulate the water with their wings. This strategic movement compels the fish to ascend, facilitating the pelicans in capturing them in their throat pouches. Pelicans' foraging behavior encompasses three distinct strategies [39].

The first strategy is the initialization step. Supposing that there are N pelicans in an M -dimensional space, the position of the i th pelican is $P_i = [p_{i1}, p_{i2}, p_{i3}, \dots, p_{im}, \dots, p_{iM}]$. Where p_{im} is i . Pelican's position in the m th dimension. Initially, the pelicans are randomly distributed in a certain range and the position update between up_m and low_m (0,1), which is the pelican's search range, is as follows.

$$P_{im} = low_m + random. (up_m - low_m) \quad i = 1, 2, \dots, M \quad (1)$$

The second strategy is to move towards its prey. In this phase, the pelican identifies its target and descends toward it from an elevated position. The adjustment of the pelican's location is formulated through Equation (2).

$$P_{im}^{t+1} = \begin{cases} P_{im}^t + rand. (S_m^t - \lambda \cdot P_m^t), & F(P_S) < F(P_i) \\ P_{im}^t + rand. (P_{im}^t - S_m^t), & F(P_S) \geq F(P_i) \end{cases} \quad (2)$$

Following the guidelines in Equation (2), where t signifies the current iteration count, the position of pelican i in dimension m , denoted as P_{im}^t , is expressed in relation to the position of the prey in dimension m , represented as S_m^t . $F(P_S)$ designates the fitness function, and λ is a random value between 0 and 2, the third strategy step corresponds to the pelicans flapping their wings on the water's surface during hunting. This behavior is mathematically expressed in Equation (3).

$$P_{im}^{t+1} = P_{im}^t + \gamma \cdot \left(\frac{T-t}{T}\right) \cdot (2 \cdot random - 1) \cdot random \cdot P_{im}^t \quad (3)$$

In line with Equation 3, the existing iteration count denoted as t , alongside the maximum iteration count T , governs the γ neighborhood radius of P_{im}^t , expressed as $\gamma \cdot \left(\frac{T-t}{T}\right)$. This quantity is derived as a randomly generated value within the range of (0,1).

The steps of POA for solving the question of classification obesity levels are divided into as following:

1st step: The dataset was split into training and testing subsets, with $xtrain$, $ytrain$ for modeling and $xtest$, $ytest$ reserved for assessment.

2nd step: We initialized the pelican population and established iterations for optimization. The population size (N) was set at 30 individuals and the algorithm run ($IteN$) for 15 generations.

3rd step: The pelican population is initialized randomly by applying the formula in Equation 1. Since the pelican population will be the weight vector we are trying to optimize, its size should be ($N \times 38$). Each row within the ($N \times 38$) matrix with $j = 1, 2, \dots, 38$ represents a weight vector, which aims to highlight the significance levels of values of parameters in the data, as stated in Equation 4.

$$d = [d_1, d_2, d_3, \dots, d_j] \quad (4)$$

4th step : As highlighted in Equation 5, the input data values are multiplied by the weight vector. Thus, significance of data parameter values is emphasized. In the study, i takes values between 1 and 2111.

$$Xtrain_{i,j} = xtrain_{i,j} * d_j \quad (5)$$

5th step: The MATLAB fitctree function is invoked, as outlined in Equation 6, to determine the fitness value linked to each member in the population, with a parameter setting of $nTrees = 50$.

$$Model = fitctree(XTrain, yTrain); \quad (6)$$

6th step : Classification is performed on the test data as in Equation 7.

$$yFound = Model.predict(xTest); \quad (7)$$

7th step: Make a comparison between y_{Found} and y_{test} . Then y is obtained by solving equation 8, which is an error value for such classifications. The hope here is to discover a weight vector leading to minimal y . Thus in these formulas Found represents the count of accurate records in the test dataset, and p_{Test} is a count of all records within the test dataset. The POA algorithm will be used to obtain the optimal solution for this weight vector.

$$y = 1 - \text{Found}/p_{Test} \tag{8}$$

8th step: A randomly chosen member from the population is designated as the prey.

9th step : When the fitness value of the prey falls below that of other individuals in the population, the individual's position undergoes an update and is subsequently stored as per Equation (2).

10th step: If the prey's value exceeds that of other individuals in the population, the individual's position is updated and recorded using Equation (3).

11th step: Evaluate the new location's fitness and compare it with the current fitness value. If the updated fitness is lower, integrate the current individual into the population, and adjust the pelican's position accordingly.

12th step: During the water surface flapping stage, recalculate and store the pelican's position based on Equation (4).

13th step: The fitness value of the new location value is compared with the old fitness value. If the new fitness value is smaller, the pelican location value is updated by adding the stored individual to the population.

14th step: Return to step 5 and repeat the process until the iteration concludes.

15th step: Ultimately, the optimal pelican location will be determined.

Table 2 outlines the values of variables crucial for identifying obesity classes.

Table 2. Parameter weights (d) found by optimizing the DT method with POA.

Parameter	Weights	Parameter	Weights
Gender	0.430	CH2O_2	0
Age	0	CH2O_3	0.489
Height	0.228	SCC	0.286
WeighT	0.010	FAF_1	0.853
Family_history_with_overweight	0.330	FAF_2	0.190
FAVC	0	FAF_3	0
FCVC_1	0	FAF_4	0.081
FCVC_2	0	TUE_1	0.797
FCVC_3	0	TUE_2	0
NCP_1	0.134	TUE_3	0.402
NCP_2	0	CALC_1	0
NCP_3	0.640	CALC_2	0.459
NCP_4	0	CALC_3	0
CAEC_1	0	CALC_4	0
CAEC_2	0.693	MTRANS_1	0.248
CAEC_3	0.624	MTRANS_2	0
CAEC_4	0.264	MTRANS_3	0
Smoke	0	MTRANS_4	0.212
CH2O_1	0.098	MTRANS_5	0.270

Observing the weight vector associated with each parameter obtained through optimizing the decision tree method with POA in Table 2 reveals that certain parameters exert a predominant influence on classification success, whereas others exhibit values of 0 or 0-1.

4. Evaluation

In this paper, a hybrid model is proposed by combining the POA metaheuristic with the decision tree method to detect Normal_weight, Over_weight_1, Over_weight_2, Obesity_type1, Obesity_type2, Obesity_type3 and Under_weight classes. The results of the proposed model are compared with the results of classical machine learning methods.

The study implemented a 5-fold cross-validation method, where the dataset was partitioned into five subsets, and each subset was iteratively employed as a test set. Consequently, each subset served as a test set once, and all possible combinations were assessed, with the results subsequently averaged. For the evaluation of performance,

The purpose of ROC analysis is to evaluate the effectiveness of the results obtained from different methods and compare them using criteria such as Accuracy, Specificity, Sensitivity, F1-Score, Precision [18], [40], [41]. The main ROC parameters used in the analysis, FN (False Negative), TN (True Negative), FP (False Positive) and TP (True Positive), serve to indicate the accuracy of the classification results through true and false predictions. It is important to select appropriate metrics such as Accuracy, Precision, Recall and F1-Score to evaluate model performance. Accuracy measures the proportion of correct predictions, while precision shows how many of the values we predict as Positive are actually Positive. Recall is a metric that shows how many of the transactions we should have predicted as Positive we actually predicted as Positive, while F1-Score is the harmonic mean of Precision and Recall. Expressions for macro metrics, calculating the unweighted mean for each tag, are elucidated in Equations (9-12).

$$\text{Accuracy} = \frac{TP + TN}{TP + TN + FP + FN} \quad (9)$$

$$\text{Recall}_m = \sum_c \frac{TP_c}{TP_c + FN_c}, c \in \text{snif} \quad (10)$$

$$\text{Precision}_m = \sum_c \frac{TP_c}{TP_c + FP_c}, c \in \text{snif} \quad (11)$$

$$\text{F1-Score}_m = \frac{2 \times \text{Precision}_m \times \text{Recall}_m}{\text{Precision}_m + \text{Recall}_m} \quad (12)$$

Within the equations, when considering the macro metric m and the classes = {Normal_weight, Over_weight_1, Over_weight_2, Obesity_type1, Obesity_type2, Obesity_type3 and Under_weight classes}, the term TP_c denotes the count of samples accurately categorized as c .

5. Experimental results

In this section, traditional methods frequently employed in the literature for obesity classification were subjected to tests using the "Classification Learner App" in Matlab [42]. The Linear Support Vector Machine, Quadratic Support Vector Machine, Cubic Support Vector Machine, Quadratic KNN models were assessed. As illustrated in Table 3, the Quadratic Support Vector Machine model demonstrated the highest accuracy rate, achieving an impressive 94.36%.

Table 3. Accuracy values of classical methods.

Model	Methods	Accuracy (%)
Model 1	LSVM	93.08
Model 2	QSVM	94.36

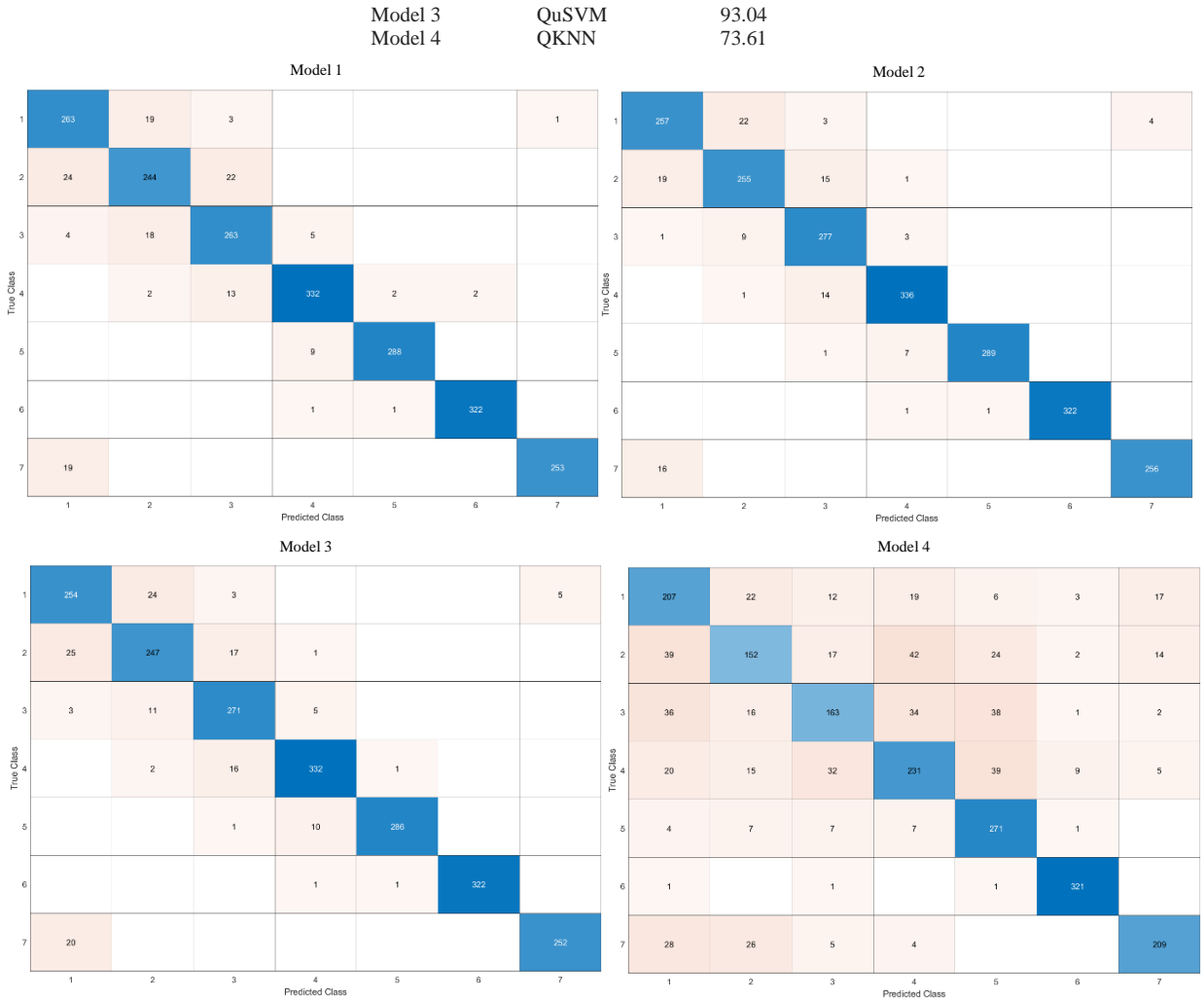


Fig. 1. Confusion matrices of classical methods; (a) Confusion matrix of Model 1, (b) Confusion matrix of Model 2, (c) Confusion matrix of Model 3, (d) Confusion matrix of Model 4..

The results obtained using only the Decision tree method for the classification of the obesity level dataset are listed in Table 4 and Figure 1.

Table 4. Results of recommended models.

Model	Description	Accuracy (%)	Macro Avg Recall (%)	Macro Avg Precision (%)	Macro Avg F1-Score (%)
DT_Model	fitctree	0.9370	0.9357	0.9361	0.9357
POA_DT_MODEL	POA+fitctree	0.9550	0.9546	0.9542	0.9543

classification instance involved 5-fold cross validation. Success was appraised by examining a handful of performance metrics (e.g., accuracy, recall, precision, F-score). Results from our experiments showed the POA_DT_Model boasting 95.4% accuracy, providing an improvement of 1.92% over the DT_Model. This relative success rate was 1.21% against classical methods. In conclusion, the hybrid approach proposed here is able to optimize very effectively the classification of obesity levels. We believe that the proposed models will improve their success performance, especially with increased parameter and data records, in future studies.

This study is suggested to be used in different data sets in the future. We believe that the proposed models will improve their performance in future studies, especially with increasing parameters and data records. The obtained results can be used to develop intelligent computational tools to determine the obesity levels of individuals and to create recommendation systems that monitor obesity levels. We believe that the hybrid approach logic presented in the literature will form the basis of different hybrid methods to be presented in the future, and parameter optimization with fuzzy logic approach will be a source of inspiration for different studies.

Author Contribution

The writing of the manuscript and all analyses were performed by Nagihan Yağmur.

Acknowledgements

In the course of this study, I would like to extend my gratitude to my cats, Karamel and Mahmutcan, for providing me with support and keeping my motivation high. Their love and loyalty strengthened me throughout this academic endeavor. Facing every challenge together made the time spent with them even more valuable.

REFERENCES

- [1] M. Steele and F. M. Finucane, "Philosophically, is obesity really a disease?," *Obesity Reviews*, p. e13590, 2023.
- [2] T. K. Kyle, E. J. Dhurandhar, and D. B. Allison, "Regarding obesity as a disease: evolving policies and their implications," *Endocrinology and Metabolism Clinics*, vol. 45, no. 3, pp. 511–520, 2016.
- [3] A. M. Jastreboff, C. M. Kotz, S. Kahan, A. S. Kelly, and S. B. Heymsfield, "Obesity as a disease: the obesity society 2018 position statement," *Obesity*, vol. 27, no. 1, pp. 7–9, 2019.
- [4] CDC, "Overweight and Obesity." Accessed: Jan. 04, 2024. [Online]. Available: <http://www.cdc.gov/obesity/data/adult.html>
- [5] WHO, "Obesity and Overweight." Accessed: Jan. 04, 2024. [Online]. Available: <https://www.who.int/en/news-room/fact-sheets/detail/obesity-and-overweight>
- [6] V. Osadchiy *et al.*, "Machine learning model to predict obesity using gut metabolite and brain microstructure data," *Sci Rep*, vol. 13, no. 1, p. 5488, 2023.
- [7] J. J. Reilly and J. Kelly, "Long-term impact of overweight and obesity in childhood and adolescence on morbidity and premature mortality in adulthood: systematic review," *Int J Obes*, vol. 35, no. 7, pp. 891–898, 2011.
- [8] S. S. Shinde and R. S. Vaidya, "Automated Obesity Detection and Classification Via Live Camera Analysis" *International Research Journal of Modernization in Engineering Technology and Science*, vol. 5, no. 11, 2023.
- [9] S. A. Alsareii *et al.*, "Machine-Learning-Enabled Obesity Level Prediction Through Electronic Health Records," *Computer Systems Science and Engineering*, vol. 46, no. 3, pp. 3715–3728, 2023.
- [10] A. A. Heidari, S. Mirjalili, H. Faris, I. Aljarah, M. Mafarja, and H. Chen, "Harris hawks optimization: Algorithm and applications," *Future generation computer systems*, vol. 97, pp. 849–872, 2019.
- [11] X. Meng, Y. Liu, X. Gao, and H. Zhang, *A new bio-inspired algorithm: chicken swarm optimization*. Springer, p. 86–94.
- [12] A. Askarzadeh, "A novel metaheuristic method for solving constrained engineering optimization problems: crow search algorithm," *Comput Struct*, vol. 169, pp. 1–12, 2016.
- [13] N. Yagmur, I. Dag, and H. Temurtas, "A new computer- aided diagnostic method for classifying anaemia disease: Hybrid use of Tree Bagger and metaheuristics," *Expert Syst*, p. e13528, 2023.
- [14] N. Yagmur, I. Dag, and H. TEMURTAŞ, "A New Computer-Aided Diagnostic Method for Classifying Anemia Disease: Hybrid Use of Tree Bagger and Metaheuristics," *Authorea Preprints*, 2023.
- [15] S.-D. H. Ö. D. T. H. DÖRTERLER, "Hybridization of k-means and meta-heuristics algorithms for heart disease diagnosis," *New Trends in Engineering and Applied Natural Sciences*, p. 55, 2022.
- [16] S. Dörterler, H. Dumlu, D. Özdemir, and H. Temurtas, "Melezlenmiş K-means ve Diferansiyel Gelişim Algoritmaları ile Kalp Hastalığının

Teşhisi,” in *International Conference on Engineering and Applied Natural Sciences içinde (ss. 1840-1844)*. Konya, 2022.

- [17] S. Dörterler, “Kanser Hastalığı Teşhisinde Ölüm Oyunu Optimizasyon Algoritmasının Etkisi,” *Mühendislik Alanında Uluslararası Araştırmalar VIII*, p. 15, 2023.
- [18] S. Dörterler, H. Dumlu, D. Özdemir, and H. Temurtas, “Hybridization of Meta-heuristic Algorithms with K-Means for Clustering Analysis: Case of Medical Datasets,” *Gazi Mühendislik Bilimleri Dergisi*, vol. 10, no. 1, pp. 1–11.
- [19] S. Jeon, M. Kim, J. Yoon, S. Lee, and S. Youm, “Machine learning-based obesity classification considering 3D body scanner measurements,” *Sci Rep*, vol. 13, no. 1, p. 3299, 2023.
- [20] T. Turan, “Optimize Edilmiş Denetimli Öğrenme Algoritmaları ile Obezite Analizi ve Tahmini,” *Mehmet Akif Ersoy Üniversitesi Fen Bilimleri Enstitüsü Dergisi*, vol. 14, no. 2, pp. 301–312.
- [21] T. Cui, Y. Chen, J. Wang, H. Deng, and Y. Huang, “Estimation of Obesity levels based on Decision trees,” in *2021 International Symposium on Artificial Intelligence and its Application on Media (ISAIAM)*, IEEE, 2021, pp. 160–165.
- [22] M. Gupta, T.-L. T. Phan, H. T. Bunnell, and R. Beheshti, “Obesity Prediction with EHR Data: A deep learning approach with interpretable elements,” *ACM Transactions on Computing for Healthcare (HEALTH)*, vol. 3, no. 3, pp. 1–19, 2022.
- [23] K. Jindal, N. Baliyan, and P. S. Rana, “Obesity prediction using ensemble machine learning approaches,” in *Recent Findings in Intelligent Computing Techniques: Proceedings of the 5th ICACNI 2017, Volume 2*, Springer, 2018, pp. 355–362.
- [24] E. De-La-Hoz-Correa, F. Mendoza Palechor, A. De-La-Hoz-Manotas, R. Morales Ortega, and A. B. Sánchez Hernández, “Obesity level estimation software based on decision trees,” 2019.
- [25] F. H. Yagin *et al.*, “Estimation of obesity levels with a trained neural Network Approach optimized by the bayesian technique,” *Applied Sciences*, vol. 13, no. 6, p. 3875, 2023.
- [26] A. Clim, R. Zota, R. Constantinescu, and I. Ilie-Nemedi, “Health services in smart cities: Choosing the big data mining based decision support,” *Int J Healthc Manag*, vol. 13, no. 1, pp. 79–87, 2020.
- [27] E. Şahin, D. Özdemir, and H. Temurtas, “Multi-objective optimization of ViT architecture for efficient brain tumor classification,” *Biomed Signal Process Control*, vol. 91, p. 105938, 2024.
- [28] N. Yağmur, “Anemi Hastalığı Sınıflandırmasında Karga Arama Optimizasyon Algoritması,” in *Mühendislik Alanında Akademik Araştırma ve Derlemeler*, 2023, pp. 291–307.
- [29] N. Yagmur, I. Dag, and H. Temurtas, “Classification of anemia using Harris hawks optimization method and multivariate adaptive regression spline,” *Neural Comput Appl*, pp. 1–20, 2024.
- [30] R.-C. Chen, C. Dewi, S.-W. Huang, and R. E. Caraka, “Selecting critical features for data classification based on machine learning methods,” *J Big Data*, vol. 7, no. 1, p. 52, 2020.
- [31] S. Kilicarslan, M. Celik, and Ş. Sahin, “Hybrid models based on genetic algorithm and deep learning algorithms for nutritional Anemia disease classification,” *Biomed Signal Process Control*, vol. 63, p. 102231, 2021.
- [32] F. M. Palechor and A. de la Hoz Manotas, “Dataset for estimation of obesity levels based on eating habits and physical condition in individuals from Colombia, Peru and Mexico,” *Data Brief*, vol. 25, p. 104344, 2019.
- [33] K. Potdar, T. S. Pardawala, and C. D. Pai, “A comparative study of categorical variable encoding techniques for neural network classifiers,” *Int J Comput Appl*, vol. 175, no. 4, pp. 7–9, 2017.
- [34] T. Kavzoğlu and İ. Çölkesen, “Karar ağaçları ile uydu görüntülerinin sınıflandırılması,” *Harita Teknolojileri Elektronik Dergisi*, vol. 2, no. 1, pp. 36–45, 2010.
- [35] J. R. Quinlan, *C4. 5: programs for machine learning*. Elsevier, 2014.
- [36] M. Pal and P. M. Mather, “An assessment of the effectiveness of decision tree methods for land cover classification,” *Remote Sens Environ*, vol. 86, no. 4, pp. 554–565, 2003.
- [37] J. G. T. Anderson, “Foraging behavior of the American white pelican (*Pelecanus erythrorhynchos*) in western Nevada,” *Colonial Waterbirds*, pp. 166–172, 1991.
- [38] J. B. E. O’Malley and R. M. Evans, “Kleptoparasitism and associated foraging behaviors in American White Pelicans,” *Colonial Waterbirds*, pp. 126–129, 1983.
- [39] W. Tuerxun, C. Xu, M. Haderbieke, L. Guo, and Z. Cheng, “A wind turbine fault classification model using broad learning system optimized by improved pelican optimization algorithm,” *Machines*, vol. 10, no. 5, p. 407, 2022.
- [40] S. Kılıç, “Klinik karar vermede ROC analizi,” *Journal of Mood Disorders*, vol. 3, no. 3, pp. 135–140, 2013.
- [41] F. Aydemir and S. Arslan, “A System Design with Deep Learning and IoT to Ensure Education Continuity for Post-COVID,” *IEEE Transactions on Consumer Electronics*, 2023.
- [42] MATLAB, “Classification Learner.” Accessed: Jan. 04, 2024. [Online]. Available: <https://www.mathworks.com/help/stats/classificationlearner-app.html>



E-ISSN: 2687-6167

Number 57, June 2024

RESEARCH ARTICLE

Receive Date: 17.04.2024

Accepted Date: 21.05.2024

Synthesis, characterization, and investigation of antibacterial and antifungal properties of salt and metal complexes of 2-amino-5-chloropyridine and 2,6-pyridinedicarboxylic acid

Ayşe Polat^{a*}, Halil İlkimen^b, Beyza Yılmaz^c, Elif Yurt^d, Aysel Gülbandılar^e

^aKütahya Dumlupınar University, , Faculty of Art and Sciences, Department of Chemistry, 43100 Kutahya, Türkiye, ORCID:0009-0003-6048-7850

^bKütahya Dumlupınar University, , Faculty of Art and Sciences, Department of Chemistry, 43100 Kutahya, Türkiye, ORCID:0000-0003-1747-159X

^cKütahya Dumlupınar University, , Faculty of Art and Sciences, Department of Chemistry, 43100 Kutahya, Türkiye, ORCID:0009-0007-0756-6305

^dKütahya Dumlupınar University, , Faculty of Art and Sciences, Department of Chemistry, 43100 Kutahya, Türkiye, ORCID:0009-0000-7309-3963

^eEskişehir Osmangazi University, Faculty of Agriculture, Department of Food Engineering, 26000 Eskişehir, Türkiye ORCID:0000-0001-9075-9923

Abstract

In this study, the salt (**3**) of 2-amino-5-chloropyridine (**1**) and 2,6-pyridinedicarboxylic acid (**2**) and the complexes of the salt $(H1)_x[M(2)_2].nH_2O$, M = Fe (III), x = 1, n = 3 (**4**); M = Co(II), x = 2, n = 4 (**5**); M = Ni(II), x = 2, n = 5 (**6**); M = Cu(II), x = 2, n = 4 (**7**) were synthesized. The structures of **3-7** were suggested by NMR, AAS, IR, UV, magnetic susceptibility and molar conductivity methods. As a result of spectroscopic analysis, it was observed that all metal complexes had an ionic and octahedral structure. All substances were susceptible to *Candida albicans* (yeast), *Escherichia coli*, *Bacillus subtilis*, *Enterococcus faecalis*, *Pseudomonas aeruginosa*, *Listeria monocytogenes* and *Staphylococcus aureus* bacteria were examined. Antimicrobial activity results were compared with Fluconazole, Ketoconazole, Chloramphenicol, Levofloxacin, Vancomycin and Cefepime. In the activity results, the best values were observed **3**, **5** and **7** in *S. aureus* bacteria, **1** and **5** in *E. coli* bacteria, **1**, **3** and **7** in *P. aeruginosa* bacteria, all compounds in *L. monocytogenes* bacteria, all compounds (except **4**) in *E. faecalis* bacteria, **1** and **3-5** in *B. subtilis* bacteria and **3**, **4** and **7** in *C. albicans* yeast.

© 2023 DPU All rights reserved.

Keywords: 2-Amino-5-chloropyridine, 2,6-pyridinedicarboxylic acid, salt, complex, antimicrobial activity.

1. Introduction

Pyridine derivative compounds are widely acknowledged to be found in numerous pharmaceutical formulations exhibiting diverse biological characteristics. Within this category, 2-aminopyridine derivatives have been identified as important precursors for the production of a variety of heterocyclic compounds. The 2-aminopyridine derivatives showcase a wide range of pharmacological activities such as antiparasitic, anti-inflammatory, antihistamine,

antibacterial, antiviral, anticonvulsant, anti-alzheimer, antifungal, antidiabetic, and analgesic properties [1-4]. These derivatives possess the capacity to engage in coordination interactions with metal ions in either a monodentate or bidentate manner, utilizing the pyridine ring and the nitrogen atom located within the amino group [5,6]. Within the modern context, the rise of microbial resistance emerges as a highly complex global challenge, resulting in increasing rates of mortality and morbidity [7], thus emphasizing the critical need for the creation of new compounds that can effectively combat multidrug-resistant microorganisms with a wide spectrum of efficacy.

Pyridine-2,6-dicarboxylic acid (**2**), known for its various biological activities, is a versatile ligand/chelating agent that can coordinate with metal ions, functioning as a bidentate, tridentate, meridian or bridging ligand [8-14].

Our group examine the antibacterial and antifungal properties of salt and metal complexes of 2-aminopyridine derivatives and carboxylic acid derivatives such as 2,6-pyridinedicarboxylic acid [5,6,15,16], salicylic acid [17], 5-sulfosalicylic acid [18], 4-sulfamoylbenzoic acid [19], 2-methoxy-5-sulfamoylbenzoic acid [20-26], 2,4-dichloro-5-sulfamoylbenzoic acid [27], 3-(3/4-sulfamoylphenylcarbamoyl)acrylic acid [28-30].

2. Experimental

2.1. Methods and materials

All chemicals used were analytical reagents and were commercially purchased from Aldrich. Perkin Elmer AAS PinAAcle 900T for AAS analyses, Agilent Premium Compact NMR (600 MHz) spectrometer for NMR spectra studies, Bruker Optics Vertex 70 FT-IR spectrometer for FT-IR spectra, SHIMADZU UV-2550 spectrometer for UV-Vis spectra, Sherwood Scientific Magway MSB MK1 for magnetic susceptibility measurements and WTW Cond 315i/SET Model conductivity meter for molar conductances were used.

2.2. Preparation of 3-7

10 mmol (1.2856 g) **1** and 10 mmol (1.6712 g) **2** dissolved in 100 mL of absolute ethanol. The white powder solid (**3**) (2.8090 g, 70% yield) precipitated in the reaction was filtered and dried (Fig. 1).

2 mmol (0.5914 g) **3** and 2 mmol metal(II) salt [0.556 g $\text{FeSO}_4 \cdot 7\text{H}_2\text{O}$ or 0.498 g $\text{Co}(\text{OAc})_2 \cdot 4\text{H}_2\text{O}$ or 0.496 g $\text{Ni}(\text{OAc})_2 \cdot 4\text{H}_2\text{O}$ or 0.400 g $\text{Cu}(\text{OAc})_2 \cdot \text{H}_2\text{O}$] was dissolved in ethanol:water solution (2:1) (100 mL) with stirring one week. Yellow power solid (0.1706 g, 60% yield) for **4**, pink power solid (0.2697 g, 75% yield) for **5**, green power solid (0.2027 g, 55% yield) for **6** and turquoise power solid (0.2172 g, 60% yield) for **7** were obtained from the mixtures (Fig. 1).

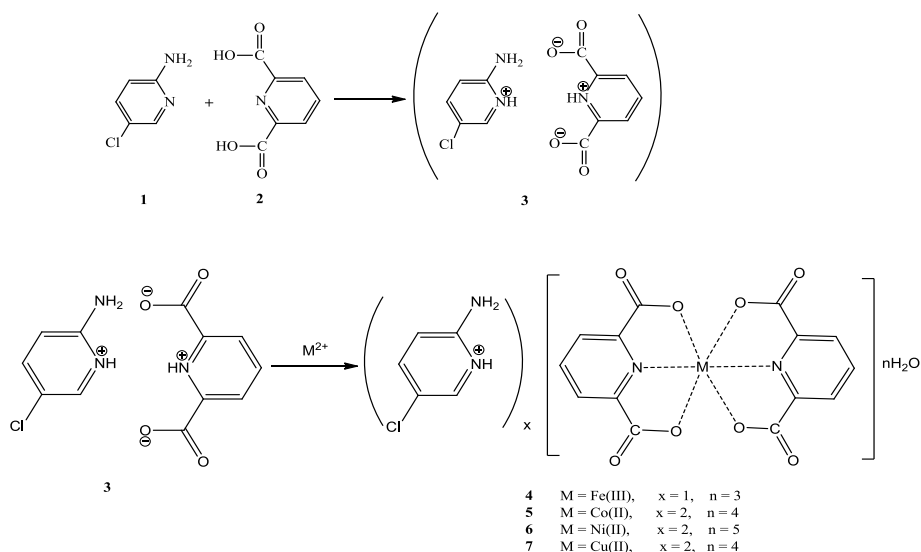


Fig. 1. The structures of 3-7.

2.3. Antimicrobial study

Candida albicans (ATCC 14053) (yeast), *Staphylococcus aureus* (NRRL-B 767), *Listeria monocytogenes* (ATCC 7644), *Bacillus subtilis*, *Enterococcus faecalis* (ATCC 29212), *Pseudomonas aeruginosa* (ATCC 27853), and *Escherichia coli* (ATCC 25922) bacteria microorganisms were used in this study.

The evaluation of the antimicrobial properties of the substances was conducted through the utilization of a microbroth dilution susceptibility test. Stock solutions were prepared using dimethyl sulfoxide. Each compound, totaling 4 mg, was dissolved in 2 mL of dimethyl sulfoxide. Bacteria and yeast suspensions, grown overnight, were standardized to 10^8 Colony Forming Units/mL using McFarland No. 0.5 standard solution in double-strength Mueller-Hinton broth. Subsequently, 100 μ L of each microbe suspension was added to the wells. A well-chain devoid of microbes served as the negative control. The positive growth control was composed of the medium along with sterile distilled water. The determination of the minimum inhibitory concentration (MIC) was based on the observation of the first well exhibiting no turbidity following an incubation period of 18-24 hours at 37 °C.

3. Results and discussion

3.1. Elemental analysis and AAS results

Elemental analysis was conducted for 3-7, while AAS was carried out for 4-7. The obtained results indicated a the 1:2 ratio for 3 and the metal:1:2 ratios for 4-7 were observed to be 1:1 for 3, 1:1:2 for 4 and 1:2:2 for 5-7 (Table 1).

Table 1. Elemental analysis and AAS results of 3-7.

Compound	Formula	Found% Anal. Cald.%			
		C	H	N	M
3	C ₁₂ H ₁₀ ClN ₃ O ₄	48.75(48.74)	3.45(3.41)	14.20(14.21)	-

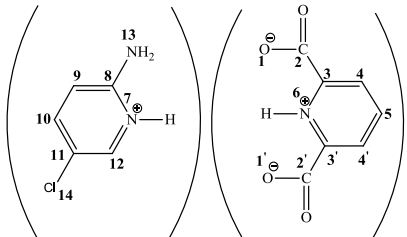
4	C ₁₉ H ₁₈ ClFeN ₄ O ₁₁	40.10(40.06)	3.20(3.18)	9.90(9.84)	9.90(9.80)
5	C ₂₄ H ₂₆ Cl ₂ CoN ₆ O ₁₂	40.00(40.02)	3.65(3.64)	11.65(11.67)	9.90(9.84)
6	C ₂₄ H ₂₆ Cl ₂ NiN ₆ O ₁₃	39.00(39.05)	3.80(3.82)	11.45(11.39)	8.00(7.95)
7	C ₂₄ H ₂₆ Cl ₂ CuN ₆ O ₁₂	39.80(39.76)	3.60(3.61)	11.50(11.54)	8.80(8.77)

3.2. NMR result of 3

In ¹H NMR spectrum in d₆-DMSO of **3** (Table 2, Fig. 2), the protons were observed at 6.42 ppm (H⁹, doublet, ³J_{H⁹-H¹⁰} = 9.00 Hz) with 1H intensity, 7.36 ppm (H¹⁰, doublet-doublet, ³J_{H¹⁰-H⁹} = 9.00 Hz ve ⁴J_{H¹⁰-H¹²} = 2.40 Hz) with 1H intensity, 7.84 ppm (H¹², doublet-doublet, ⁴J_{H¹²-H¹⁰} = 2.40 Hz) with 1H intensity, 6.06 ppm (H¹³, singlet) with 2H intensity, 8.21 ppm (H⁴ and H^{4'}, doublet, ³J_{H⁴/H^{4'}-H⁵} = 7.80 Hz) with 2H intensity and 8.14 ppm (H⁵, triplet, ³J_{H⁵-H⁴,H³} = 7.80 Hz) with 1H intensity.

¹³C NMR spectrum in d₆-DMSO of **3** (Table 2, Fig. 3), the carbon peaks were observed at 165.898 ppm (C², C^{2'}), 148.555 ppm (C³, C^{3'}), 127.902 ppm (C⁴, C^{4'}), 117.790 ppm (C⁵), 158.878 ppm (C⁸), 145.976 ppm (C⁹), 109.741 ppm (C¹⁰), 137.168 ppm (C¹¹) and 139.647 ppm (C¹²).

Table 2. Results of NMR spectra (ppm).

		¹ H-NMR	¹³ C-NMR
H ⁴ , H ^{4'}	8.21 (2H, d) [³ J _{H⁴/H^{4'}-H⁵} = 7.80 Hz]	C ² , C ^{2'}	165.898
H ⁵	8.14 (1H, t) [³ J _{H⁵-H⁴,H^{4'}} = 7.80 Hz]	C ³ , C ^{3'}	148.555
H ⁶	-	C ⁴ , C ^{4'}	127.902
H ⁷	-	C ⁵	117.790
H ⁹	6.42 (1H, d) [³ J _{H⁹-H¹⁰} = 9.00 Hz]	C ⁸	158.878
H ¹⁰	7.36 (1H, dxd) [³ J _{H¹⁰-H⁹} = 9.00 Hz. ⁴ J _{H¹⁰-H¹²} = 2.40 Hz]	C ⁹	145.976
H ¹²	7.84 (1H, d) [⁴ J _{H¹²-H¹⁰} = 2.40 Hz]	C ¹⁰	109.741
H ¹³	6.06 (2H, s)	C ¹¹	137.168
		C ¹²	139.647

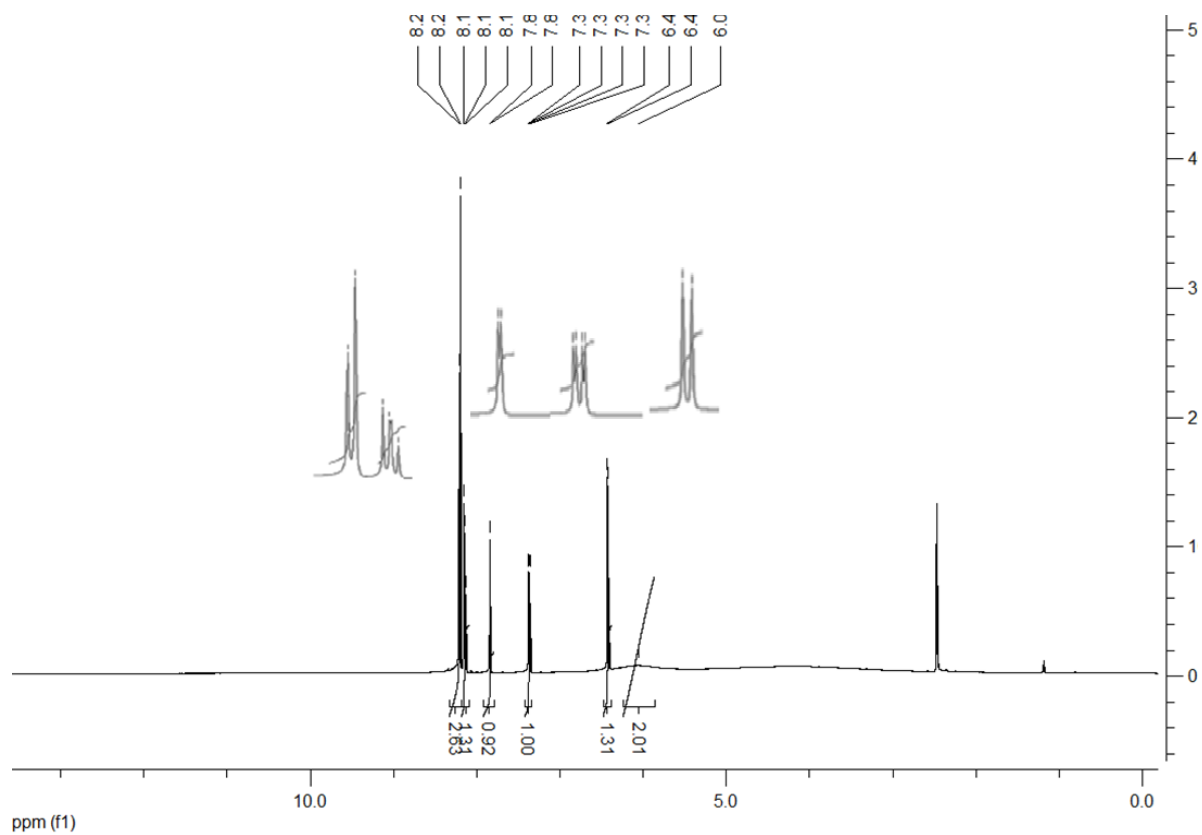
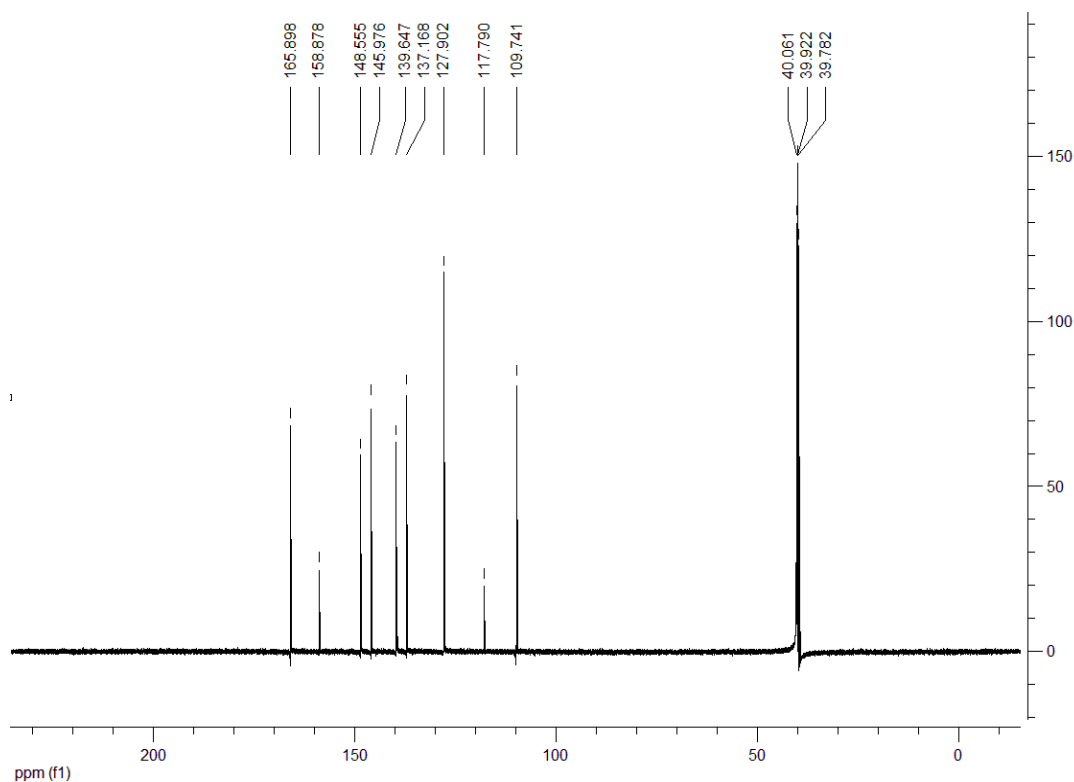


Fig. 2. ¹H NMR spectrum of **3**.

Fig. 3. ^{13}C NMR spectrum of **3**.

3.3. FT-IR results

The FT-IR results of **3-7** are given in Table 3. The water molecules in the structure of **4-7** were the cause of the $\nu(\text{O-H})$ vibrations, which were seen as wide bands between 3416 and 3569 cm^{-1} . The $\nu(\text{N-H})$ vibrations of **3-7** are responsible for bands that appear at 3432 and 3317 , 3408 and 3239 , 3356 and 3236 , 3349 and 3238 and 3379 and 3210 cm^{-1} , respectively. The $\nu(\text{N}^+\text{-H})$ vibrations observed in the range $2549\text{-}2773\text{ cm}^{-1}$ for **3-7** [31]. These peaks observation shows that the **1** molecule is present in the complexes as a complimentary ion outside of coordination. The binding of the COO^- group to the metal ion is indicated by the difference in the lengths of its asymmetric and symmetric oscillations ($\Delta\nu$). The results of **4-7** were calculated to be 195 (1662 and 1467 cm^{-1}), 191 (1660 and 1469 cm^{-1}), 200 (1665 and 1465 cm^{-1}) and 200 (1679 and 1479 cm^{-1}), respectively. These findings imply that the carboxylate group forms a monodentate bond with the metal ion [32]. The absorption bands in the region of $3076\text{-}3107\text{ cm}^{-1}$ for aromatic $\nu(\text{C-H})$, $1419\text{-}1685\text{ cm}^{-1}$ for $\nu(\text{C=N})/\nu(\text{C=C})$, $1070\text{-}1394\text{ cm}^{-1}$ for $\nu(\text{C=O})$, $748\text{-}770\text{ cm}^{-1}$ for $\nu(\text{py})$, $588\text{-}598\text{ cm}^{-1}$ for $\nu(\text{M-O})$ (except **3**) and $469\text{-}506\text{ cm}^{-1}$ for $\nu(\text{M-N})$ (except **3**) are found for all compounds.

3.4. Results of UV/Vis measurements

The electronic spectra of **3-7** (as shown in Fig. 4, dissolved in DMSO at a concentration of $1.10^{-3}\text{ molL}^{-1}$) exhibit both $\pi\text{-}\pi^*$ and $n\text{-}\pi^*$ transitions, which are detected at 298 nm ($27100\text{ Lmol}^{-1}\text{cm}^{-1}$) and 272 nm ($2700\text{ Lmol}^{-1}\text{cm}^{-1}$) for **1**, 290 nm ($30180\text{ Lmol}^{-1}\text{cm}^{-1}$) for **2**, 322 nm ($28730\text{ Lmol}^{-1}\text{cm}^{-1}$) for **3**, 292 nm ($32380\text{ Lmol}^{-1}\text{cm}^{-1}$) and 266 nm ($10110\text{ Lmol}^{-1}\text{cm}^{-1}$) for **4**, 318 nm ($34370\text{ Lmol}^{-1}\text{cm}^{-1}$) and 292 nm ($24070\text{ Lmol}^{-1}\text{cm}^{-1}$) for **5**, 314 nm (26810

$\text{Lmol}^{-1}\text{cm}^{-1}$) and 292 nm ($24150 \text{ Lmol}^{-1}\text{cm}^{-1}$) for **6** and 274 nm ($27000 \text{ Lmol}^{-1}\text{cm}^{-1}$) and 254 nm ($22300 \text{ Lmol}^{-1}\text{cm}^{-1}$) for **7**. The d-d transitions of metal atoms with octahedral structure occurred at wavelengths of 688 nm ($310 \text{ Lmol}^{-1}\text{cm}^{-1}$) for **5**, 702 nm ($290 \text{ Lmol}^{-1}\text{cm}^{-1}$) for **6** and 782 nm ($350 \text{ Lmol}^{-1}\text{cm}^{-1}$) for **7** [15,16].

Table 3. IR data of all compounds (cm^{-1})

	3	4	5	6	7
$\nu(\text{O-H})$	-	3504(br)	3569(br)	3466(br)	3416(br)
$\nu(\text{N-H})$	3432(m)	3408(m)	3356(m)	3349(m)	3379(m)
	3317(m)	3239(m)	3236(m)	3238(m)	3210(m)
$\nu(\text{C-H})_{\text{Ar}}$	3090(w)	3107(w)	3076(w)	3089(w)	3095(w)
$\nu(\text{N}^+-\text{H})$	2703(w)	2773(w)	2733(w)	2677(w)	2708(w)
	2575(w)	2549(w)	2571(w)	2524(w)	2528(w)
$\nu(\text{C=O})$	1762(s)	1662(s)	1660(s)	1665(s)	1679(s)
	1478(s)	1467(s)	1469(s)	1465(s)	1479(s)
$\nu(\text{C=N})$	1685(s)	1622(s)	1637(s)	1639(s)	1655(s)
$\nu(\text{C=C})$	1626(s)	1605(s)	1609(s)	1610(s)	1609(s)
	1562(s)	1577(s)	1563(s)	1585(s)	1555(s)
	1545(s)	1437(s)	1499(s)	1563(s)	1502(s)
	1428(s)		1436(s)	1500(s)	1419(s)
				1437(s)	
$\nu(\text{C-O})$	1385(s)	1384(s)	1394(s)	1394(s)	1374(s)
	1229(s)	1278(s)	1281(s)	1282(s)	1267(s)
	1070(s)	1073(s)	1074(s)	1077(s)	1077(s)
$\nu(\text{py})$	748(s)	770(s)	767(s)	764(s)	770(s)
$\nu(\text{M-O})$	-	597(w)	588(w)	596(w)	598(w)
$\nu(\text{M-N})$	-	494(w)	469(w)	506(w)	490(w)

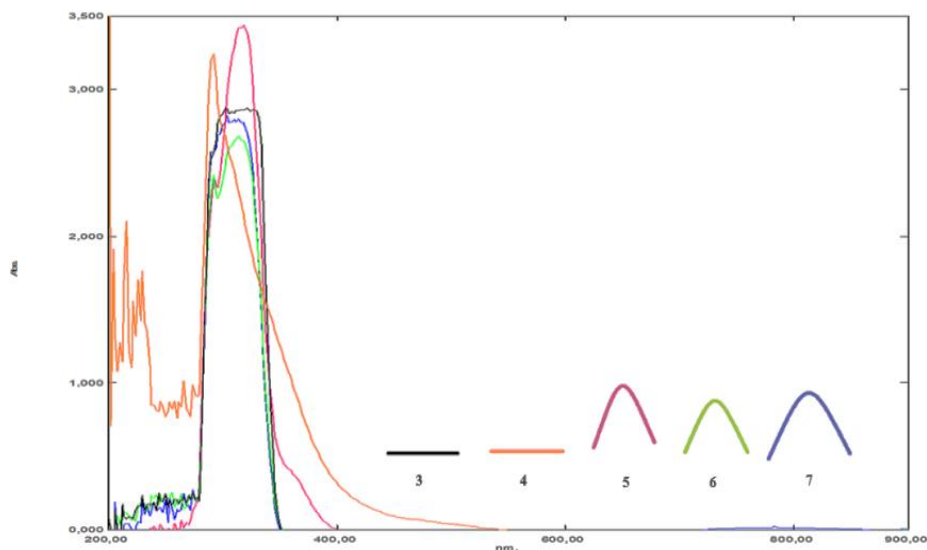


Fig. 4. UV-Vis spectra of 3-7.

3.5. Magnetic susceptibilities

Magnetic susceptibility results of **4-7** were found between 5.84, 3.80, 2.72 and 1.69 BM. These values say that there are five, three, two and one unpaired electrons in the complexes, respectively. The magnetic moment for the metal ion obtained in the octahedral geometry is also consistent with this value [15,16].

3.6. Molar Conductivity

Conductivity measurements of **4-7** (in DMSO) were observed as 68.90 for **4**, 51.50 for **5**, 50.50 for **6** and 59.20 $\mu\text{S}/\text{cm}$ for **7** and these results are 1:1 ionic for **4** and 2:1 ionic for **5-7** [33].

3.7. Antimicrobial activity

The antimicrobial activity of **1-7**, Vancomycin, Levofloxacin, Cefepime, Chloramphenicol, Ketoconazole and Fluconazole were investigated by microdilution method. MIC values of all compounds showing activity against bacteria and yeast are given in Table 4. The observed activity results are similar to 2-aminopyridine derivatives, salt and metal complexes found in the literature [5,6,15,18].

The antifungal drugs (Ketoconazole and Fluconazole) and **1-7** have activity against *C. albicans* when MIC values are compared. Compounds **3** and **4** showed greater activity than according to Ketoconazole and Fluconazole while compounds **1**, **5** and **6** showed equal effective. Compound **2** was found to have a lower degree of action.

Table 4. MIC values of compounds ($\mu\text{g}/\text{mL}$)

	<i>C. albicans</i>	<i>L. monocytogenes</i>	<i>E. coli</i>	<i>B. subtilis</i>	<i>S. aureus</i>	<i>E. faecalis</i>	<i>P. aeruginosa</i>
Ketoconazole	62.50	-	-	-	-	-	-
Fluconazole	62.50	-	-	-	-	-	-

Vancomycin	-	125.00	62.50	250.00	31.25	31.25	62.50
Levofloxacin	-	31.25	62.50	62.50	31.25	31.25	31.25
Cefepime	-	31.25	31.25	62.50	62.50	62.50	31.25
Chloramphenicol	-	62.50	62.50	62.50	62.50	62.50	125.00
1	62.50	62.50	31.25	31.25	62.50	62.50	31.25
2	125.00	62.50	62.50	62.50	62.50	62.50	62.50
3	31.25	62.50	62.50	31.25	31.25	62.50	31.25
4	31.25	62.50	62.50	31.25	62.50	125.00	62.50
5	62.50	62.50	31.25	31.25	31.25	62.50	62.50
6	62.50	62.50	62.50	62.50	62.50	62.50	62.50
7	31.25	62.50	62.50	62.50	31.25	62.50	31.25

All antibacterial drugs (Vancomycin, Levofloxacin, Cefepime and Chloramphenicol) and **1-7** have activity against *L. monocytogenes* when MIC values are compared of all compounds indicated greater activity than according to Vancomycin. All compounds showed equally activity according to Chloramphenicol while all compounds showed lower activity according to Levofloxacin and Cefepime.

All compounds showed greater activity *E. coli* than according to Vancomycin. While compounds **1** and **5** showed equally effective, the other compounds were found to have a lower degree of according to Cefepime. Compounds **1** and **5** showed greater activity than according to Vancomycin, Levofloxacin and Chloramphenicol while the other compounds showed equally effective.

All compounds showed greater activity *B. subtilis* than according to Vancomycin. **1** and **3-5** showed greater activity than according to Levofloxacin, Chloramphenicol and Cefepime the other compounds showed equally effective.

While **3**, **5**, and **7** showed equally effective *S. aureus*, the other compounds were found to have a lower degree of according to Vancomycin and Levofloxacin. **3**, **5**, and **7** showed greater activity than according to Chloramphenicol and Cefepime while the other compounds showed equally effective.

All compounds showed greater activity *E. faecalis* than according to Vancomycin and Levofloxacin. While all compounds (except **4**) showed equally effective, the other compounds were found to have a lower degree of according to Chloramphenicol and Cefepime.

All compounds showed greater activity *P. aeruginosa* than according to Chloramphenicol. **1**, **3**, and **7** showed greater activity than according to Vancomycin while the other compounds equally effective. While **2** and **4-6** showed equally effective, the other compounds were found to have a lower degree of according to Levofloxacin and Cefepime.

4. Conclusions

In this study, the salt (**3**) of 2-amino-5-chloropyridine (**1**) and 2,6-pyridinedicarboxylic acid (**2**) and the metal complexes of the salt $\{(H1)_x[M(2)_2].nH_2O, M = Fe(III), x = 1, n = 3$ (**4**); $M = Co(II), x = 2, n = 4$ (**5**); $M = Ni(II), x = 2, n = 5$ (**6**); $M = Cu(II), x = 2, n = 4$ (**7**) $\}$ were synthesized. The structures of **3-7** were suggested by AAS, IR, UV, NMR (for compound **3**), magnetic susceptibility, and molar conductivity methods. As a result of spectroscopic analysis, it was observed that all metal complexes had an ionic and octahedral structure. All compounds exhibited antimicrobial efficacy against both bacterial and fungal microorganisms. In the activity results, the best values were observed **1** and **5** in *E. coli* bacteria, **3**, **5**, and **7** in *S. aureus* bacteria, all compounds in *L. monocytogenes* bacteria, **1**, **3**, and **7** in *P. aeruginosa* bacteria, all compounds (except **4**) in *E. faecalis* bacteria, **1** and **3-5** in *B. subtilis* bacteria and compounds **3**, **4**, and **7** in *C. albicans* yeast.

Acknowledgements

This investigation received funding as part of the TUBITAK 2209-A program, which aims to support research projects conducted by university students. The funding was granted under application number 1919B012108018.

Author contribution statements

Author 1 Investigation, Writing –review & editing, Author 2 Investigation, Author 3 Investigation, Author 4 Investigation, Author 5 Writing –original draft.

References

- [1] M. Marinescu, "2-Aminopyridine - a classic and trendy pharmacophore," *Int. J. Pharma Bio. Sci.*, vol. 8, no. 2, pp. 338-355, 2017, doi: 10.22376/ijpbs.2017.8.2.p338-355.
- [2] R. N. Rao and K. Chanda "2-Aminopyridine – an unsung hero in drug discovery," *Chem. Commun.*, vol. 58, pp. 343-382, 2022, doi: 10.1039/D1CC04602K.
- [3] K. J. Orié, R. U. Duru and R. I. Ngochindo "Syntheses, complexation and biological activity of aminopyridines: a mini-review," *Am. J. Het. Chem.*, vol. 7, no. 2, pp. 11-25, 2021, doi: 10.11648/j.ajhc.20210702.11.
- [4] P. Sharma and P. Sinha, "Recent advancements in multicomponent reactions of substituted 2- aminopyridines synthesis: a decade review," *Cur. Chinese Chem.*, vol. 3, e061223224235, pp. 18, 2023, doi: 10.2174/0126660016267259231012105113.
- [5] C. Yenikaya, M. Poyraz, M. Sarı, F. Demirci, H. İlkimen and O. Büyükgüngör, "Synthesis, characterization and biological evaluation of a novel Cu(II) complex with the mixed ligands 2,6-pyridinedicarboxylic acid and 2-aminopyridine," *Polyhedron*, vol. 28, no. 16, pp. 3526-3532, 2009, doi: 10.1016/j.poly.2009.05.079.
- [6] C. Yenikaya, N. Büyükkıdan, M. Sarı, R. Keşli, H. İlkimen, M. Bülbül and O. Büyükgüngör, "Synthesis, characterization and biological evaluation of novel Cu(II) complexes with proton transfer salt of 2,6-pyridinedicarboxylic acid and 2-amino-4-methylpyridine," *J. Coord. Chem.*, vol. 64, no. 19, pp. 3353-3365, 2011, doi: 10.1080/00958972.2011.620608.
- [7] Centers for Disease Control and Prevention Facts about Antibiotic Resistance and Antibiotic Prescribing: Attitudes, Behaviors, Trends, and Cost. [(accessed on 21 April 2022)]; Available online: <http://www.cdc.gov/getsmart/community/about/fast-facts.html>
- [8] M. M. Khalil and A. E. Attia, "Potentiometric studies on the binary and ternary complexes of copper(II) containing dipicolinic acid and amino acids," *J. Chem. Eng. Data*, vol. 44, no. 2, pp. 180-184, 1999, doi: 10.1021/je980185d.
- [9] S. Xiang, D. X. Bao, J. Wang, Y.C. Li and X.Q. Zhao, "Luminescent lanthanide coordination compounds with pyridine-2,6-dicarboxylic acid," *J. Lumin.*, vol. 186, pp. 273–282, 2017, doi: 10.1016/j.jlumin.2017.02.037
- [10] M. J. Celestine, J.L. Bullock, S. Boodram, V. H. Rambaran and A.A. Holder, "Interesting properties of p-, d-, and f-block elements when coordinated with dipicolinic acid and its derivatives as ligands: their use as inorganic pharmaceuticals," *Rev. Inorg. Chem.*, vol. 35, vol. 2, pp. 57-67, 2015, doi: 10.1515/revic-2014-0004
- [11] A. M. Kirillov and G. B. Shul'pin, "Pyrazinecarboxylic acid and analogs: highly efficient co-catalysts in the metal-complex-catalyzed oxidation of organic compounds," *Coord. Chem. Rev.*, vol. 257, pp. 732-754, 2013, doi: 10.1016/j.ccr.2012.09.012
- [12] M. V. Kirillova, M. F. C. Guedes da Silva, A. M. Kirillov, J. J. R. Frausto da Silva and A. J. L. Pombeiro, "3D hydrogen bonded heteronuclear CoII, NiII, CuII and ZnII aqua complexes derived from dipicolinic acid," *Inorg. Chim. Acta*, vol. 360, pp. 506-512, 2007, doi: 10.1016/j.ica.2006.07.087.
- [13] N. Büyükkıdan, "Proton transfer salts and their complexes and mixed-ligand complexes of pyridine dicarboxylic acids and piperazines: a short review," *J. Sci. Rep. A*, vol. 49, pp. 198-235, 2022.
- [14] H. Aghabozorg, F. Manteghi and S. Sheshmani, "A brief review on structural concepts of novel supramolecular proton transfer compounds and their metal complexes," *J. Iran. Chem. Soc.*, vol. 5, pp. 184-227, 2008, doi: 10.1007/BF03246111.
- [15] H. İlkimen, S. G. Salün, A. Gülbandır and M. Sarı, "The new salt of 2-amino-3-methylpyridine with dipicolinic acid and its metal complexes: Synthesis, characterization and antimicrobial activity studies," *J. Mol. Struct.*, vol. 1270, pp. 133961, 2022, doi: 10.1016/j.molstruc.2022.133961.
- [16] H. İlkimen, S. G. Salün, A. Gülbandır and M. Sarı, "Synthesis, characterization, antimicrobial activity studies of a novel salt of dipicolinic acid with 2-amino-5-methylpyridine and their metal complexes," *Pharm. Chem. J.*, 2024, (in press).
- [17] H. İlkimen and A. Gülbandır, "Synthesis, characterization, anti-microbial activity studies of salicylic acid and 2-aminopyridine derivatives salts and their Cu(II) complexes," *J. Sci. Rep. A*, vol. 56, pp. 94-104, 2024.
- [18] H. İlkimen, C. Yenikaya and A. Gülbandır, "Investigation of the antimicrobial activities of proton transfer salts of 5-sulfosalicylic acid and 2-aminopyridine derivatives," 3rd International Conference on Innovative Academic Studies, September 26-28, 2023, Konya, Türkiye, pp. 779-783. ISBN: 978-625-6530-66-9.
- [19] H. İlkimen, N. Türken and A. Gülbandır, "Synthesis, characterization, antimicrobial and antifungal activity of studies of two novel aminopyridine-sulfamoylbenzoic acid salts and their Cu(II) complexes," *J. Iranian Chem. Soc.*, vol. 18, no. 9, pp. 1941-1946, 2021, doi: 10.1007/s13738-021-02157-4.

- [20] H. İlkimen and A. Gülbandır, "Synthesis, characterization, anti-microbial activity studies of 2-methoxy-5-sulfamoylbenzoic acid and 2-amino-5/6-picoline salts and their Cu(II) complexes," *Uşak Univ. J. Sci. Nat. Sci.*, 2024, (in press).
- [21] H. İlkimen, C. Yenikaya and A. Gülbandır, "Synthesis, characterization and investigation of antimicrobial activities of salts of 2-aminopyridine derivatives and 2-methoxy-5-sulfamoylbenzoic acid," *Selçuk Univ. J. Sci. Fac.*, vol. 49, no. 2, pp. 53-63, 2023, doi: 10.35238/sufefd.1315568.
- [22] H. İlkimen and A. Gülbandır, "Synthesis, characterization, anti-microbial activity studies of 2-methoxy-5-sulfamoylbenzoic acid and 2-aminopyridine derivatives salts and their Cu(II) complexes," *Pamukkale Univ. J. Eng. Sci.*, 2024, doi. 10.5505/pajes.2024.48196
- [23] H. İlkimen, C. Yenikaya and A. Gülbandır, "Synthesis, characterization, investigation of antimicrobial properties of proton transfer salt and Cu(II) complex of 2-methoxy-5-sulfamoylbenzoic acid and 2,3-diaminopyridine derivatives," III. Baskent International Conference On Multidisciplinary Studies, September 23-25, 2022, Ankara, Türkiye, pp. 105-119, ISBN - 978-625-8246-04-9.
- [24] H. İlkimen, C. Yenikaya and A. Gülbandır, "Synthesis, characterization and investigation of antimicrobial and antifungal activities of 2-methoxy-5-sulfamoylbenzoic acid and 2-aminonitropyridine derivatives," 3rd International Conference on Innovative Academic Studies, September 26-28, 2023, Konya, Türkiye, pp. 784-793. ISBN: 978-625-6530-66-9.
- [25] H. İlkimen and A. Gülbandır, "Synthesis, characterization, and investigation of antimicrobial and antifungal activities of 2-Amino-5-substituted epipyridine derivatives and proton transfer salts of 2-methoxy-5-sulfamoylbenzoic acid," 2nd International Conference on Contemporary Academic Research ICCAR 2023, November 4-5 2023, Konya, Türkiye, pp. 40-47. ISBN: ISBN: 978-625-6530-69-0
- [26] H. İlkimen, C. Yenikaya and A. Gülbandır, "2-Amino-6-substitüepiridin türevleri ile 2-metoksi-5-sulfamoylbenzoik asitin proton transfer tuzlarının sentezi, karakterizasyonu, antimikrobiyal ve antifungal aktivitelerinin incelenmesi," 2nd International Conference on Contemporary Academic Research ICCAR 2023, November 4-5 2023, Konya, Türkiye, pp. 48-55. ISBN: ISBN: 978-625-6530-69-0.
- [27] H. İlkimen and A. Gülbandır, "Synthesis, characterization, antimicrobial and antifungal activity studies of four novel 2-aminopyridine and 2,4-dichloro-5-sulfamoylbenzoic acid salts and their Cu(II) complexes," *Kuwait J. Sci.*, vol. 50, no. 3A, pp. 1-11, 2023, doi: 10.48129/kjs.19163.
- [28] H. İlkimen, C. Yenikaya and A. Gülbandır, "Antimicrobial activity of (E)-3-(4-sulfamoylphenylcarbamoyl)acrylic acid derivatives," *J. Sci. Rep. A*, vol. 52, pp. 365-375, 2023, doi: 10.59313/jsr-a.1126888.
- [29] H. İlkimen, C. Yenikaya and A. Gülbandır, "Synthesis, characterization and investigation of antimicrobial activities of metal complexes of (E)-4-oxo-4-(3-sulfamoylphenyl)amino)but-2-enoic acid," *Bayburt Univ. J. Sci.*, vol. 6, no. 1, 12-19, 2023, doi: 10.55117/bufbd.1137044.
- [30] H. İlkimen, C. Yenikaya and A. Gülbandır, "Antimicrobial activity of proton salts of 3-(sulfamoylphenylcarbamoyl) acrylic acid derivatives with aminopyridine derivatives." *J. Sci. Rep. A*, vol. 54, no. 2, pp. 264-272, 2023, doi: 10.59313/jsr-a.1311495.
- [31] D. Cook, "Vibrational spectra of pyridinium salts," *Canadian J. Chem.*, vol. 39, no. 10, 2009-2024, 1961, doi: 10.1139/v61-271.
- [32] K. Nakamoto, "Infrared and raman spectra of inorganic and coordination compounds," 5th ed. NewYork: Wiley-Interscience, pp. 232 (1997).
- [33] W. J. Geary, "The use of conductivity measurements in organic solvents for the characterisation of coordination compounds," *Coord. Chem. Rev.*, vol. 7, no. 1, pp. 81-122, 1971, doi: 10.1016/S0010-8545(00)80009-0.



Contents lists available at *Dergipark*

Journal of Scientific Reports-A

journal homepage: <https://dergipark.org.tr/tr/pub/jsr-a>



E-ISSN: 2687-6167

Number 57, June 2024

RESEARCH ARTICLE

Receive Date: 06.07.2023

Accepted Date: 15.03.2024

Conway-Maxwell-Poisson profile monitoring with rk -Shewhart control chart: a comparative study

Ulduz MAMMADOVA^{a*}

Çukurova University, Faculty of Science and Letters, Department of Statistics, Adana, Türkiye, ORCID: 0000-0001-5022-4932

Abstract

A control chart is an essential tool in Statistical Quality Control for monitoring the production process. It provides a visual means of identifying process irregularities. In this study, we focus on the Shewhart control chart based on the rk -deviance residuals, namely rk -Shewhart control charts to examine the Conway–Maxwell–Poisson (COM-Poisson) profile, which is used to model the count data with varying degrees of dispersion. The primary goal of this study is to identify the biasing parameter that produces the best result among newly presented biasing parameters developed based on existing ones. It provides a short overview of the COM-Poisson distribution, its modeling, and rk parameter estimation in the case of multicollinearity, as well as the construction of the deviance-residual-based Shewhart chart. To evaluate the performance of the rk -Shewhart, we conduct an analysis using a real-life data set, considering various shift sizes. By employing different biasing parameters, we examine the effectiveness of the rk -Shewhart control chart. The performance evaluation outcomes of the rk -Shewhart charts are compared to the ML -deviance-based Shewhart chart and within themselves based on the biasing parameters. The results demonstrate the advantage of the rk -Shewhart charts over the ML -deviance-based control chart in detecting out-of-control signals. Among the considered biasing parameters, the rk -Shewhart chart utilizing the adjusted biasing parameter k_4 shows the best performance based on the ARL metric.

© 2023 DPU All rights reserved.

Keywords: Control chart; Conway-Maxwell-Poisson model; Multicollinearity; Process monitoring; rk estimation

* Corresponding author

E-mail address: contact@ulduzmammadova.com

1. Introduction

Statistical process control covers a range of tools to examine the production process. One such tool is the control chart. Control charts allow visual inspection and quick identification of the irregularities in the process. The simplicity of the approach has made it attractive to researchers looking to develop new techniques to perform profile monitoring. The profile itself represents the quality of the product/process through a relationship between the response and one or more producers. An extreme similarity of profiles with regression models allows the implementation of the modeling methods into the monitoring. In cases with count response, the data from the process is generally regarded as the Poisson profile. Several studies are dedicated to monitoring Poisson profiles with predictors independent of each other [1] – [7] and with collinear relationship [8] – [10]. But Poisson distribution comes with the specific characterization of the data being equidispersed, in other words, having an equal mean-variance structure. The real-life data do not always fit under this structure by showing a higher mean than variance or vice versa. In the early 1960s, Conway and Maxwell [11] introduced the Conway – Maxwell – Poisson distribution, which can represent the count data with various levels of dispersion. The COM-Poisson distribution is reviewed in the generalized linear models (GLMs) framework by Guikema and Coffelt [12], Lord et al. [13], Jowaheer and Khan [14], and Sellers and Shmueli [15].

The possibility of modeling data with dispersed count response as GLM has led to the emergence of new studies in the context of process monitoring, as well. Inspired by Marcondes Filo and Sant'Anna [8], Park et al. [16] proposed an *R-control* chart based on the combination of regression modeling and principal component analysis, assuming the existence of interrelation among predictors. Later, Park et al. [17] introduced a randomized quantile residual-based control chart. Both studies are focused on monitoring process data with count response that follows Poisson, Negative Binomial, or COM-Poisson distributions. Mammadova and Özkale [9] adopted a different approach. For monitoring Poisson and COM-Poisson profiles, the authors used ridge estimation to lessen the effect of multicollinearity and proposed ridge-deviance-based Shewhart, cumulative sum (CUSUM), and exponentially weighted moving average (EWMA) charts. Jamal et al. [18] took a similar approach and studied deviance and randomized quantile residual-based CUSUM and EWMA charts for COM-Poisson process data and applied them to real-time highway safety surveillance. Mammadova and Özkale [9, 19, 20] also investigated COM-Poisson profile monitoring under multicollinearity by incorporating principal component regression (PCR), Liu, and *rk* estimation methods. Liu – deviance – based control charts proved to be better than the maximum likelihood (ML) and ridge deviance-based control charts, while *rk* deviance-based control charts outperformed ML, ridge, and PCR deviance-based control charts.

In this study, we mainly focused on the Shewhart control chart based on the *rk*-deviance residuals (*rk*-Shewhart). Unlike other methods, biased estimation methods require an optimal biasing parameter that provides an effective estimate without deviating far from its actual value. Since *the rk* estimation method combines PCR and ridge estimators, its value is also affected by the biasing parameter. In this paper, we evaluated the effect of the eight different biasing parameters of *k* on the overall performance of the control chart. The study aims to determine the best biasing parameter among considered ones that results in a good performance.

The rest of the paper is organized as follows: Section 2 covers detailed information about COM-Poisson modeling, an alternative estimation method of *rk* estimation, deviance residuals, and adjusted biasing parameters for *the rk* estimator as well. Monitoring with a residual-based Shewhart control chart is presented in Section 3. An illustrative example is included in Section 4, where the performance of the *rk*-Shewhart control chart with various biasing parameters is compared both among each other and to the performance of the *ML*-deviance-based Shewhart (*ML*-Shewhart) chart in general. Lastly, Section 6 covers the summary and conclusions regarding the study.

2. Conway-Maxwell-Poisson model

The probability density function for the COM-Poisson distribution is defined by

$$f(y_i) = \frac{\mu_i^{y_i}}{(y_i!)^\nu} \frac{1}{Z(\mu_i, \nu)}, i = 1, 2, 3, \dots, n \tag{1}$$

where $y = 0, 1, 2, \dots, \nu$ is the dispersion parameter, and $Z(\mu_i, \nu) = \sum_{s=0}^{\infty} (\mu_i^s / (s!)^\nu)$ is a normalization parameter. $\nu > 1$ indicates an underdispersion and $\nu < 1$ shows that data is overdispersed. $\nu = 1$ is the equidispersed case.

The distribution is known to have three special cases, which are Geometric (when $\nu = 0, \mu_i < 1$), Poisson (when $\nu = 1$), and Bernoulli (when $\nu \rightarrow \infty$) distributions. According to Shmueli et al. [21], the normalization parameter $Z(\mu_i, \nu)$ does not converge when $\nu = 0$ and $\mu_i \geq 1$. Consequently, the distribution is undefined in that case.

As GLM, data with COM-Poisson distributed response is commonly modeled through the log-link function [12, 14, 15]. The log-link function of $\mu_i = \exp(x_i\beta)$ involves i th observation $x_i = [x_{i1}, x_{i2}, \dots, x_{ip}]$ of $X_{n \times p} = [x_1, x_2, \dots, x_n]'$ predictor matrix and unknown $\beta = [\beta_1, \beta_2, \dots, \beta_p]'$ parameters. In the case of independent predictors, these unknown parameters can be estimated iteratively by using the *ML* estimation technique as

$$\hat{\beta}_{ML}^{(t)} = (X' \hat{V}_{ML}^{(t-1)} X)^{-1} X' \hat{V}_{ML}^{(t-1)} \hat{u}_{ML}^{(t-1)} \tag{2}$$

where t indicates the iteration step, $\hat{u}_{ML}^{(t-1)} = X \hat{\beta}_{ML}^{(t-1)} + (\hat{V}_{ML}^{(t-1)})^{-1} (y - \hat{\mu}_{ML}^{(t-1)})$ is the working response, and \hat{V}_{ML} is the weight matrix evaluated at $\hat{\beta}_{ML}^{(t-1)}$. The *ML* estimator at convergence is $\hat{\beta}_{ML} = (X' \hat{V}_{ML} X)^{-1} X' \hat{V}_{ML} \hat{u}_{ML}$. Francis et al. [22] presented a general form of the weight matrix \hat{V}_{ML} for *ML* estimation, initially given by Sellers and Shmueli [15]. It can be calculated as in Appendix A.

The presence of the correlation among predictors requires the utilization of alternative estimation methods. One such method is the *rk* estimation. Initially, the *rk* estimator was proposed by Baye and Parker [23] for linear models and later modified for GLMs by Abbasi and Özkale [24]. To obtain the *rk* estimator first, we perform singular value decomposition to determine the principle components as follows:

Let $X^* = XT$ and $\alpha = T'\beta$, where $T = [t_1, t_2, \dots, t_p]$ is the $p \times p$ orthogonal matrix through $T'X'\hat{V}_{ML}XT = \Lambda$. $\Lambda = \text{diag}(\lambda_i), i = 1, 2, \dots, p$, and λ_i are the eigenvalues of the $X'\hat{V}_{ML}X$ matrix. While λ_1 is equivalent to the maximum eigenvalue, λ_p is the minimum. Then linear predictor in canonical form can be written as $\eta = X\beta = XTT'\beta = X^*\alpha$ and $X^* = [X_r^* X_{p-r}^*]$ where $X_r^* = XT_r$ ($r \leq p$) is the matrix of principal components that corresponds to the large eigenvalues and r is the number of principal components that will be in the model. Accordingly, ω, T , and Λ can be partitioned as $\alpha = [\alpha_r \ \alpha_{p-r}]$, $T = [T_r \ T_{p-r}]$, and $\Lambda = \begin{bmatrix} \Lambda_r & \\ & \Lambda_{p-r} \end{bmatrix}$, where $\Lambda_r = T_r'X'\hat{V}_{ML}XT_r$ and $\Lambda_{p-r} = T_{p-r}'X'\hat{V}_{ML}XT_{p-r}$, respectively.

The number of principal components can be determined via the metric proposed by Jolliffe [25] called the percentage of the total variance (PTV). In this study, we adopted the adjusted version of this metric for GLMs, introduced by Aguilera [26], where $PTV = (\sum_{i=1}^r \hat{\lambda}_i / \sum_{i=1}^p \hat{\lambda}_i) \times 100\%$.

Mammadova and Özkale [20] obtained *rk* estimator for COM-Poisson model as

$$\hat{\beta}_{rk}^{(t)} = T_r (T_r' X' \hat{V}_{ML}^{(t-1)} X T_r + k I_r)^{-1} T_r X' \hat{V}_{ML}^{(t-1)} \hat{u}_{rk}^{(t-1)} \tag{3}$$

where k is the biasing parameter and $\hat{u}_{rk}^{(t-1)} = X T_r T_r' \hat{\beta}_{rk}^{(t-1)} + (\hat{V}_{ML}^{(t-1)})^{-1} (y - \hat{\mu}_{rk}^{(t-1)})$ is the working response. The $\hat{\beta}_{rk}$ estimator at convergence is as $\hat{\beta}_{rk} = T_r (T_r' X' \hat{V}_{ML} X T_r + k I_r)^{-1} T_r X' \hat{V}_{ML} \hat{u}_{rk}$. When $k = 1$, $\hat{\beta}_{rk}$ is the same as PCR estimator.

Once parameters are estimated, we can calculate deviance residuals. Sellers and Shmueli [15] defined the i th deviance-residual (*ML*-deviance) formula for the COM-Poisson model where the *ML* estimation method is utilized as

$$d_{ML,i} = \pm \left[2 \left(L(y_i, y_i; v) - L(\hat{\mu}_{ML,i}, y_i; v) \right) \right]^{1/2} \tag{4}$$

where $L(y_i, y_i; v) = \sum_{i=1}^n y_i \log(y_i) - v \sum_{i=1}^n \log(y_i!) - \sum_{i=1}^n \log(Z(y_i; v))$ is the log-likelihood function of the saturated model, and $L(\hat{\mu}_{ML,i}, y_i; v) = \sum_{i=1}^n y_i \log(\hat{\mu}_{ML,i}) - v \sum_{i=1}^n \log(y_i!) - \sum_{i=1}^n \log(Z(\hat{\mu}_{ML,i}; v))$ is the log-likelihood of the fitted model. When $y_i < \hat{\mu}_{ML,i}$ the sign of the residual is negative, otherwise it is positive.

Mammadova and Özkale [20] modified Eq. (4) and obtained the i th rk -deviance residual as follows

$$d_{rk} = \pm \left[2 \left(L(y_i, y_i; v) - L(\hat{\mu}_{rk,i}, y_i; v) \right) \right]^{1/2} \tag{5}$$

where $L(\hat{\mu}_{rk,i}, y_i; v) = \sum_{i=1}^n y_i \log(\hat{\mu}_{rk,i}) - v \sum_{i=1}^n \log(y_i!) - \sum_{i=1}^n \log(Z(\hat{\mu}_{rk,i}; v))$ is the log-likelihood of the fitted model where the rk estimation method is applied. Similarly, the sign of the residual is negative if $y_i < \hat{\mu}_{rk,i}$ and positive when $y_i \geq \hat{\mu}_{rk,i}$.

2.1. Biasing parameter k

The possibility of obtaining the rk estimator simply by adjusting ridge biasing parameters was mentioned by Abbasi and Özkale [24]. The literature contains numerous studies on the choice of the biasing parameter k for ridge estimation. Hoerl and Kennard [27] and Hoerl et al. [28] presented the early biasing parameters. Several studies focused on the k parameters for linear ridge regression [29] – [34] and eventually, the biasing parameters proposed in these studies adapted to GLMs. [9], [10], [35] – [39] examined the k parameters of models with count response and carried out comparative studies to determine the optimal k . One of the recent studies, Kibria [40] reviewed more than a hundred bias parameters for GLM.

Here we present some of the biasing parameters adjusted for the rk estimation of COM-Poisson model parameters considered in this paper:

$$k_1 = \frac{v}{(\max(\hat{\alpha}_i))^2} \tag{6}$$

$$k_2 = \frac{rv}{\sum_{i=1}^r \alpha_i^2} \tag{7}$$

$$k_3 = \max \left(1 / \sqrt{v / \hat{\alpha}_i^2} \right) \tag{8}$$

$$k_4 = \text{median} \left(\sqrt{v / \hat{\alpha}_i^2} \right) \tag{9}$$

$$k_5 = \max \left(\frac{v}{\hat{\alpha}_i^2} + \frac{1}{\lambda_i} \right) \tag{10}$$

$$k_6 = \text{median} \left(\frac{v}{\hat{\alpha}_i^2} + \frac{1}{\lambda_i} \right) \tag{11}$$

$$k_7 = \min \left(1 / \sqrt{\frac{\max(\lambda_i v)}{(n-r-1)v + \lambda_{\max} \hat{\alpha}_i^2}} \right) \quad (12)$$

$$k_8 = \text{median} \left(1 / \sqrt{\frac{\max(\lambda_i v)}{(n-r-1)v + \lambda_{\max} \hat{\alpha}_i^2}} \right) \quad (13)$$

where λ_i is the eigenvalue of the $T_r' X' V_{ML} X T_r$ matrix.

The formulations for k_1 and k_2 in Eqs. (6) and (7) are based on the biasing parameters introduced by Hearl and Kennard [27] and Hearl et al. [28], respectively. These biasing parameters, known for their simplicity and adaptability, represent the earliest contributions to the literature, establishing a foundation for the development of new biasing parameters for more thorough analysis. k_3 and k_4 are obtained based on the recommendations of Muniz and Kibria [31]. Kibria et al. [36] stated that the earlier version of the k_3 is particularly efficient when high correlation is present among predictors for Poisson ridge estimation. The biasing parameters denoted as k_5 and k_6 derived from the two biasing parameters presented by Alkhamisi and Shukur [30] for linear models. They have proven to produce the best results for Poisson profile monitoring by Mammadova and Özkale [10] in the framework of process control. The final two biasing parameters originated from the biasing parameters for COM-Poisson regression model presented by Sami et al. [39]. The authors suggested using those biasing parameters to overcome the multicollinearity issue based on the findings of the extensive simulation study.

3. Monitoring procedure

In the 1920s, the Shewhart control chart was introduced to the literature as a method to detect abnormalities in the production process caused by various factors [41]. In the following years, these control charts have undergone modifications and adjustments to be able to monitor different process data. In the profile monitoring framework, residuals derived from profiles are monitored through the Shewhart control chart to detect process irregularities assuming that residuals follow the normal distribution. Since deviance residuals derived from GLMs are proven to be closer to the normal distribution than Pearson residuals [42] – [43], most of the studies employed deviance residuals for monitoring generalized linear profiles with Shewhart control charts.

Shewhart control chart based on the deviance residuals can be constructed by using the following control limits

$$LCL = \mu_{ML,0} - L\sigma_{ML,0} \quad (14)$$

$$UCL = \mu_{ML,0} + L\sigma_{ML,0} \quad (15)$$

where LCL is the lower and UCL is the upper control limit, L is the width of the limits, $\mu_{ML,0}$ and $\sigma_{ML,0}$ are the mean and standard deviation of the ML -deviance residuals under an in-control state, respectively. Any observation outside of the control limits indicates an out-of-control state. Following the same approach, Mammadova and Özkale [44] obtained control limits for the rk -Shewhart control chart as

$$LCL = \mu_{rk,0} - L\sigma_{rk,0} \quad (16)$$

$$UCL = \mu_{rk,0} + L\sigma_{rk,0} \quad (17)$$

where $\mu_{rk,0}$ and $\sigma_{rk,0}$ are the in-control mean and standard deviation of the rk -deviance residuals, respectively.

The L value in the control limits for the Shewhart control chart may differ slightly depending on the data set. It is typically selected based on the desired in-control average run length (ARL), which is the average number of data points until the first out-of-control signal. It is usually set to $ARL_0 \approx 370$. This choice ensures a minimal false alarm rate of 0.0027.

4. Illustrative example

4.1. Data set and its initial examination

The comprehensive evaluation of the performances of the control charts is carried out through the SECOM data set [45]. The SECOM data set involves a collection of sensor readings, corresponding test results obtained from the production line, and a precise date-time stamp for each data point. While data from 590 sensors is considered a predictor matrix, test results act as the response.

To ensure that the data set fit the presumptions of the study, we performed data cleaning procedures. These include addressing missing values by replacing them with the previous value and reducing the number of predictors by removing non-continuous variables. Also, given that the response variable is binary (-1 for Pass, 1 for Failure), we rearranged the whole data set to be able to model it with the COM-Poisson regression model. The strategy for rearrangement is given below:

- a) Following the cleaning, the initial predictor matrix became $X_{1567 \times 444}$.
- b) Based on the time stamp, the 24 hours are divided into eight distinct time intervals, referred to as time frames (TF). Time frames are

1 \rightarrow 00:00-02:59,	2 \rightarrow 03:00-05:59,
3 \rightarrow 06:00-08:59,	4 \rightarrow 09:00-11:59,
5 \rightarrow 12:00-14:59,	6 \rightarrow 15:00-17:59,
7 \rightarrow 18:00-20:59,	8 \rightarrow 21:00-23:59.

A new date-time-frame (DTF) column was created by joining TF with the date information. For instance, the DTF of "20-5-2008-2" is the category of the observations for 20th May of 2008 and the time period between 03:00-05:59.

- c) A rearranged response is created by summing the number of passes in the respective DTF. Similarly, the corresponding predictors are calculated by averaging each predictor variable within the corresponding DTF. Consequently, the data set became consist of $X_{476 \times 444}$ predictor matrix and a $Y_{476 \times 1}$ response vector of counts.
- d) Lastly, to ensure the presence of multicollinearity, predictors with the absolute pairwise correlation value between [0.744, 0.756] are selected to be included in the analysis. Only 30 predictors met this condition. The final data set is a matrix of $X_{476 \times 30}$ and vector of $Y_{476 \times 1}$.

A further application is performed following the workflow given by Figure 1.

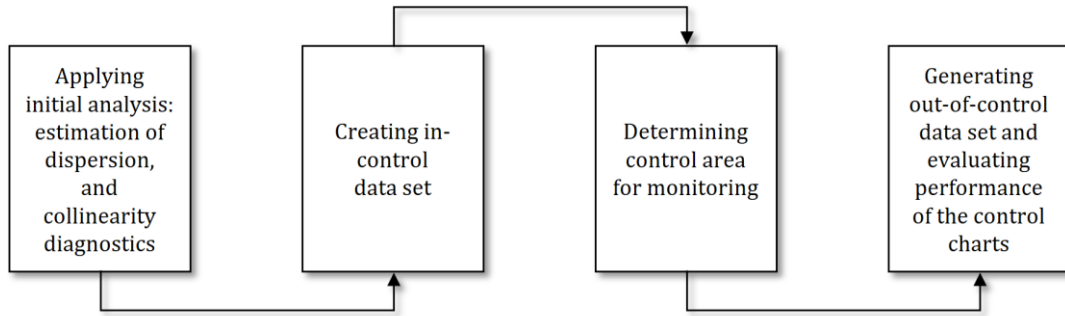


Figure 1. Application process workflow.

Prior to the analysis, we standardized the X matrix such that each column has a zero mean and unit variance. The estimation of the dispersion is carried out using the "COMpoissonReg" package [46], where $\nu = 0.7772$ is obtained, reflecting overdispersion.

Next, we model the relationship between the overdispersed response and predictors through the log-link function. The ML estimator is obtained iteratively, with the initial value being the ordinary least squares estimator. The convergence criterion is set as $\|\hat{\beta}^{(t)} - \hat{\beta}^{(t-1)}\| \leq 10^{-6}$. In the final iteration, we calculated the weight matrix \hat{V}_{ML} together with the ML estimator. Then condition number denoted as CN is calculated by taking the square root of the maximum eigenvalue divided by the minimum eigenvalue of the scaled information matrix to assess collinearity among predictors. The result $CN = 237.2906 > 10$ indicates the presence of severe collinearity among the predictors according to Mackinnon and Puterman [47].

4.2. Monitoring and performance evaluation

For the monitoring process, first, we computed d_{ML} and d_{rk} residuals. The d_{rk} residuals are obtained from models where the model parameters are estimated using rk estimation with the respective biasing parameter. These estimators are calculated iteratively by setting $PTV = 95\%$, $\hat{\beta}^0 = T_r T_r' (X'X)^{-1} X'y$ as the initial value, and $\|\hat{\beta}^{(t)} - \hat{\beta}^{(t-1)}\| \leq 10^{-6}$ as convergence criterion. The biasing parameters are calculated according to Eqs. (6) - (13) and obtained as $k_1 = 9.4355$, $k_2 = 23.1216$, $k_3 = 0.00042$, $k_4 = 77.3809$, $k_5 = 170.9183$, $k_6 = 68.2304$, $k_7 = 2.3757$, and $k_8 = 2.9525$.

Next, we conducted a preliminary analysis because of the absence of information regarding the state of the data set. A control area is established using the estimated mean and standard deviation of residuals to identify potential out-of-control data points outside 3σ control area. The control area is determined based on the estimated standard deviation of the monitored observations using the control limits in Eqs. (14)-(17). Resulted control charts are presented in Figure 2.

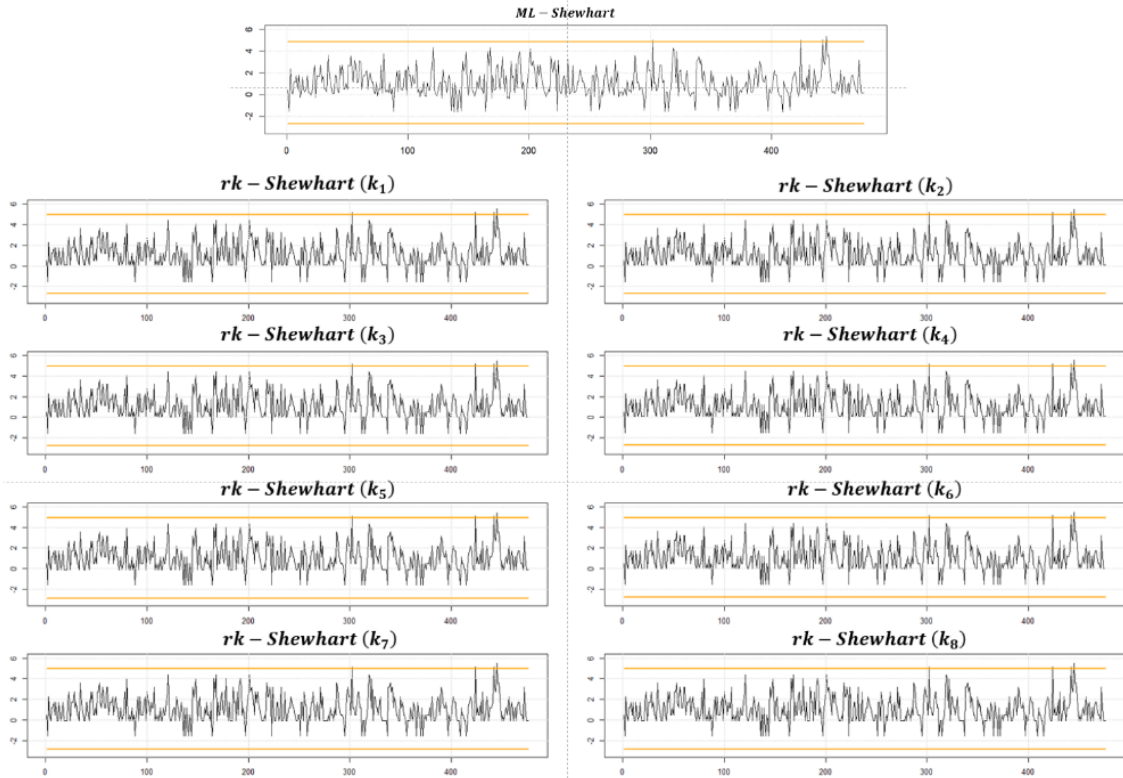


Figure 2. Initial analysis of the SECOM data set with ML-Shewhart and rk -Shewhart control charts.

Four unique data points (302nd, 424th, 442nd, 445th) fall outside the control area of all control charts. These observations are eliminated from the data matrix to create an in-control data set. Afterward, the model is refitted using the updated data set. New biasing parameters are obtained as $k_1 = 11.9482$, $k_2 = 25.9485$, $k_3 = 0.00039$, $k_4 = 58.6119$, $k_5 = 133.3645$, $k_6 = 53.6406$, $k_7 = 2.4283$ and $k_8 = 2.9115$. Then, the model parameters are estimated using the same settings, and residuals are calculated accordingly. Lower and upper control limits for the ML -Shewhart and rk -Shewhart control charts are obtained as in Eqs. (14) - (17) through simulation using these residuals such that they met the condition of $ARL_0 \approx 370$.

The simulation-derived control limits are included in Table 1.

Table 1. Control limits of the ML -Shewhart and rk -Shewhart control charts obtained through simulation.

Control chart	L CL	U CL
ML -Shewhart	- 3.425	2. 870
rk -Shewhart(k_1)	- 3.228	2. 660
rk -Shewhart(k_2)	- 3.282	2. 710
rk -Shewhart(k_3)	- 0.00039	2. 0
rk -Shewhart(k_4)	- 58.6119	2. 58.6119
rk -Shewhart(k_5)	- 133.3645	2. 133.3645
rk -Shewhart(k_6)	- 53.6406	2. 53.6406
rk -Shewhart(k_7)	- 2.4283	2. 2.4283
rk -Shewhart(k_8)	- 2.9115	2. 2.9115

Shewhart(k_3)	3.027	724
<i>rk</i> -	-	2.
Shewhart(k_4)	3.267	747
<i>rk</i> -	-	2.
Shewhart(k_5)	3.138	830
<i>rk</i> -	-	2.
Shewhart(k_6)	3.286	904
<i>rk</i> -	-	2.
Shewhart(k_7)	3.286	779
<i>rk</i> -	-	2.
Shewhart(k_8)	3.408	848

To be able to evaluate the performance of the control charts, we generate a shifted response $y \sim COM - Poisson(\mu_1, v)$, where $\mu_1 = exp(x_i \hat{\beta}_{ML} + \delta \hat{\sigma}_{ML,0})$, δ represents the shift size, and $\hat{\sigma}_{ML,0}$ donates the standard deviation of the in-control d_{ML} . The $\delta = 0.5, 1, 1.5, 2, 2.5, 3$ is considered for a detailed evaluation of the effect of the biasing parameters on the monitoring process. Once the shifted response is generated, we modeled the relationship between predictors and response, estimated the model parameters using the same biasing parameters, and calculated the residuals. Then we compared these residuals to the control limits and calculated ARL_1 following [48]. The results are presented in Table 2.

According to Table 2, regardless of the shift size, the *rk*-Shewhart control chart outperformed the *ML*-Shewhart control chart in terms of ARL_1 . The *rk*-Shewhart control chart with biasing parameter k_4 is the best-performing control chart among *rk* – deviance – based charts. It is followed by *rk*-Shewhart(k_2) when $\delta > 0.5$. Also, with an increase in shift size, the control chart performances show noticeable improvements.

Table 2. Performance of the *ML*-Shewhart and *rk*-Shewhart control charts.

Control chart	$\delta = 0$	$\delta = 0.5$	$\delta = 1$	$\delta = 1.5$	$\delta = 2$	$\delta = 2.5$	$\delta = 3$
<i>ML</i> -Shewhart	370.746	202.478	54.540	17.329	7.050	3.605	2.242
<i>rk</i> -Shewhart(k_1)	370.628	194.907	52.437	16.874	6.898	3.558	2.215
<i>rk</i> -Shewhart(k_2)	372.410	179.159	45.839	15.083	6.235	3.275	2.057
<i>rk</i> -Shewhart(k_3)	371.176	197.257	52.023	16.754	6.868	3.546	2.201
<i>rk</i> -Shewhart(k_4)	371.969	169.111	44.550	14.728	6.058	3.213	2.035
<i>rk</i> -Shewhart(k_5)	370.591	176.780	48.756	15.782	6.478	3.365	2.117
<i>rk</i> -Shewhart(k_6)	370.059	190.232	51.820	16.661	6.816	3.508	2.186
<i>rk</i> -Shewhart(k_7)	369.995	177.014	47.400	15.420	6.356	3.315	2.091
<i>rk</i> -Shewhart(k_8)	370.460	186.037	50.242	16.296	6.645	3.453	2.152

5. Conclusions

This research focuses on the variations of the *rk*-Shewhart control chart for detecting unexpected deviations in the COM-Poisson profile. This monitoring method employs deviance residuals derived from a model with parameters estimated via the *rk* estimation method. Given that the *rk* estimation method integrates PCR and ridge estimators, the choice of biasing parameter influences its performance. In this study, we aimed to investigate the impact of the set of biasing parameters on the performance of the *rk*-Shewhart control chart and determine the one that yields optimal performance of the control chart.

We reviewed eight distinct biasing parameters from the literature and adjusted them to the COM-Poisson profile for rk estimation. The impact of biasing parameters for the COM-Poisson profile is evaluated using a real-life data set. It is modified to reflect the study's assumptions, and shifts in various sizes are added for a thorough comparison. The performance of each rk -Shewhart control chart is evaluated and in addition to being compared among themselves, the performance of the rk -Shewhart charts is also compared to that of the ML -Shewhart chart.

Findings revealed that the rk -Shewhart control chart consistently outperforms the deviance-based Shewhart control chart, regardless of the chosen biasing constant. The superiority of the rk -Shewhart control chart indicates an elevated sensitivity in detecting deviations in the process mean. In particular, the rk -Shewhart chart based on the biasing parameter k_4 , as proposed by Muniz and Kibria [31], demonstrates the best performance among all control charts regarding the ARL metric.

In conclusion, the study highlights the superior performance of the rk -Shewhart control chart, particularly when adapted to the COM-Poisson profile with adjusted biasing parameters. The findings show the importance of modifying statistical procedures for best performance in a variety of data scenarios.

For future research an investigation of additional biasing parameters to improve the effectiveness of the control charts utilizing the rk estimation method may be considered. Furthermore, the implementation of advanced statistical techniques and machine learning algorithms can provide more comprehensive and effective process monitoring.

Acknowledgements

The author would like to thank anonymous reviewers for their valuable feedback and suggestions, which enhanced the quality of this paper.

Author ORCID ID: <https://orcid.org/0000-0001-5022-4932>

References

- [1] K.R. Skinner, D.C. Montgomery, and G.C. Runger, "Process monitoring for multiple count data using generalized linear model-based control charts," *Int. J. Prod. Res.*, vol. 41, no. 6, pp. 1167–1180, Jun. 2003, doi: 10.1080/00207540210163964.
- [2] K.R. Skinner, D.C. Montgomery, and G.C. Runger, "Generalized linear model-based control charts for discrete semiconductor process data," *Qual. Reliab. Eng. Int.*, vol. 20, no. 8, pp. 777–786, 2004, doi: 10.1002/qre.603.
- [3] D. Jearkpaporn, D.C. Montgomery, G.C. Runger, and C.M. Borror, "Process monitoring for correlated gamma-distributed data using generalized-linear-model-based control charts," *Qual. Reliab. Eng. Int.*, vol. 19, no. 6, pp. 477–491, 2003, doi: 10.1002/qre.521.
- [4] A. Amiri, M. Koosha, and A. Azhdari, "Profile monitoring for Poisson responses," in *IEEE Int. Conf. Ind. Eng. Eng. Manag.*, 2011, pp. 1481–1484, doi: 10.1109/IEEM.2011.6118163
- [5] A. Asgari, A. Amiri, and S.T.A. Niaki, "A new link function in GLM-based control charts to improve monitoring of two-stage processes with Poisson response," *Int. J. Adv. Manuf. Technol.*, vol. 72, no. 9, pp. 1243–1256, 2014, doi: 10.1007/s00170-014-5692-z.
- [6] W.Y. Hwang, "Quantile-based control charts for Poisson and gamma distributed data," *J. Korean Stat. Soc.*, pp. 1–18, 2021, doi: 10.1007/s42952-021-00108-6.
- [7] H. Wen, L. Liu, and X. Yan, "Regression-adjusted Poisson EWMA control chart," *Qual. Reliab. Eng. Int.*, vol. 37, no. 5, pp. 1956–1964, 2021, doi: 10.1002/qre.2840.
- [8] D. Marcondes Filho and A.M.O. Sant'Anna, "Principal component regression – based control charts for monitoring count data," *Int. J. Adv. Manuf. Technol.*, vol. 85, no. 5, pp. 1565–1574, 2016, doi: 10.1007/s00170-015-8054-6.
- [9] U. Mammadova and M.R. Özkale, "Profile monitoring for count data using Poisson and Conway – Maxwell – Poisson regression–based control charts under multicollinearity problem," *J. Comput. Appl. Math.*, vol. 388, p. 113275, 2021, doi: 10.1016/j.cam.2020.113275.
- [10] U. Mammadova and M.R. Özkale, "Comparison of deviance and ridge deviance residual-based control charts for monitoring Poisson profiles," *Commun. Stat. – Simul. Comput.*, vol. 52, no. 3, pp. 826–853, 2023, doi: 10.1080.
- [11] R.W. Conway and W.L. Maxwell, "A queuing model with state-dependent service rates," *J. Ind. Eng.*, vol. 12, no. 2, pp. 132–136, 1962. [Online]. Available: <https://tinyurl.com/28cv3brs>
- [12] S.D. Guikema and J.P. Coffelt, "A flexible count data regression model for risk analysis," *Risk Anal.: An Int. J.*, vol. 28, no. 1, pp. 213–223, 2008, doi: 10.1111/j.1539-6924.2008.01014.x.
- [13] D. Lord, S.D. Guikema, and S.R. Geedipally, "Application of the Conway–Maxwell–Poisson generalized linear model for analyzing motor vehicle crashes," *Accident Anal. & Prev.*, vol. 40, no. 3, pp. 1123–1134, 2008, doi: 10.1016/j.aap.2007.12.003.

- [14] V. Jowaheer and N.M. Khan, "Estimating regression effects in COM–Poisson generalized linear model," *Int. J. Comput. Math. Sci.*, vol. 1, no. 2, pp. 59–63, 2009, doi: 10.5281/zenodo.1075883.
- [15] K.F. Sellers and G. Shmueli, "A flexible regression model for count data," *Ann. Appl. Stat.*, vol. 4, no. 2, pp. 943–961, 2010, doi: 10.2139/ssrn.1127359
- [16] K. Park, J.M. Kim, and D. Jung, "GLM-based statistical control r-charts for dispersed count data with multicollinearity between input variables," *Qual. Reliab. Eng. Int.*, vol. 34, no. 6, pp. 1103–1109, 2018, doi: 10.1002/qre.2310.
- [17] K. Park, D. Jung, and J.M. Kim, "Control charts based on randomized quantile residuals," *Appl. Stoch. Models Bus. Ind.*, vol. 36, no. 4, pp. 716–729, 2020, doi: 10.1002/asmb.2527.
- [18] A. Jamal et al., "GLM-based flexible monitoring methods: An application to real-time highway safety surveillance," *Symmetry*, vol. 13, no. 2, p. 362, 2021, doi: 10.3390/sym13020362.
- [19] U. Mammadova and M.R. Özkale, "Conway–Maxwell Poisson regression-based control charts under iterative Liu estimator for monitoring count data," *Appl. Stoch. Models Bus. Ind.*, vol. 38, no. 4, pp. 695–725, 2022, doi: 10.1002/asmb.2682.
- [20] U. Mammadova and M.R. Özkale, "Detecting shifts in Conway–Maxwell–Poisson profile with deviance residual-based CUSUM and EWMA charts under multicollinearity," *Stat. Papers*, pp. 1–47, 2023, doi: 10.1007/s00362-023-01399-z.
- [21] G. Shmueli, T.P. Minka, J.B. Kadane, S. Borle, and P. Boatwright, "A useful distribution for fitting discrete data: revival of the Conway–Maxwell–Poisson distribution," *J. R. Stat. Soc.: Series C (Appl. Stat.)*, vol. 54, no. 1, pp. 127–142, 2005, doi: 10.1111/j.1467-9876.2005.00474.x.
- [22] R.A. Francis, S.R. Geedipally, S.D. Guikema, S.S. Dhavala, D. Lord, and S. LaRocca, "Characterizing the performance of the Conway–Maxwell–Poisson generalized linear model," *Risk Anal.: An Int. J.*, vol. 32, no. 1, pp. 167–183, 2012, doi: 10.1111/j.1539-6924.2011.01659.x.
- [23] M.R. Baye and D.F. Parker, "Combining ridge and principal component regression: a money demand illustration," *Commun. Stat.-Theory Methods*, vol. 13, no. 2, pp. 197–205, 1984, doi: 10.1080/03610928408828675.
- [24] A. Abbasi and M.R. Özkale, "The r-k class estimator in generalized linear models applicable with sim. and empirical study using a Poisson and gamma responses," *Hacettepe J. Math. Stat.*, vol. 50, no. 2, pp. 594–611, 2021, doi: 10.15672/hujms.715206.
- [25] I.T. Jolliffe, *Principal Components in Regression Analysis*. New York: Springer, 2002.
- [26] A.M. Aguilera, M. Escabias, and M.J. Valderrama, "Using principal components for estimating logistic regression with high-dimensional multicollinear data," *Comput. Stat. Data Anal.*, vol. 50, no. 8, pp. 1905–1924, 2006, doi: 10.1016/j.csda.2005.03.011.
- [27] A.E. Hoerl and R.W. Kennard, "Ridge regression: Biased estimation for nonorthogonal problems," *Technometrics*, vol. 12, no. 1, pp. 55–67, 1970, doi: 10.2307/1267351.
- [28] A.E. Hoerl, R.W. Kannard, and K.F. Baldwin, "Ridge regression: some simulations," *Commun. Stat.-Theory Methods*, vol. 4, no. 2, pp. 105–123, 1975, doi: 10.1080/03610927508827232.
- [29] B.M.G. Kibria, "Performance of some new ridge regression estimators," *Commun. Stat.-Simulation Comput.*, vol. 32, no. 2, pp. 419–435, 2003, doi: 10.1081/SAC-120017499.
- [30] M.A. Alkhamisi and G. Shukur, "A Monte Carlo study of recent ridge parameters," *Commun. Stat.-Simulation Comput.*, vol. 36, no. 3, pp. 535–547, 2007, doi: 10.1080/03610910701208619.
- [31] G. Muniz and B.M.G. Kibria, "On some ridge regression estimators: An empirical comparison," *Commun. Stat.-Simulation Comput.*, vol. 38, no. 3, pp. 621–630, 2009, doi: 10.1080/03610910802592838.
- [32] Y. Asar, A. Karaibrahimoglu, and G. Aşır, "Modified ridge regression parameters: A comparative Monte Carlo study," *Hacettepe J. Math. Stat.*, vol. 43, no. 5, pp. 827–841, 2014. [Online]. Available: <https://dergipark.org.tr/en/pub/hujms/issue/43879/536843>
- [33] Y. Asar and A. Genç, "A note on some new modifications of ridge estimators," *Kuwait J. Sci.*, vol. 44, no. 3, 2017. [Online]. Available: <https://journalskuwait.org/kjs/index.php/KJS/article/view/11110>
- [34] M. Qasim et al., "Biased adjusted Poisson ridge estimators – method and application," *Iran. J. Sci. Technol. Trans. A Sci.*, vol. 44, pp. 1775–1789, 2020, doi: 10.1007/s40995-020-00974-5.
- [35] K. Mansson and G. Shukur, "A Poisson ridge regression estimator," *Econ. Model.*, vol. 28, no. 4, pp. 1475–1481, 2011, doi: 10.1016/j.econmod.2011.02.030.
- [36] B.M.G. Kibria, K. Mansson, and G. Shukur, "A simulation study of some biasing parameters for the ridge type estimation of Poisson regression," *Commun. Stat.-Simulation Comput.*, vol. 44, no. 4, pp. 943–957, 2015, doi: 10.1080/03610918.2013.796981.
- [37] A. Zaldivar, "On the performance of some Poisson ridge regression estimators" (Master's thesis). Florida International University, 2018, doi: 10.25148/etd.fidc006538.
- [38] Z.Y. Algamal and M.M. Alanaz, "Proposed methods in estimating the ridge regression parameter in Poisson regression model," *Electron. J. Appl. Stat. Anal.*, vol. 11, no. 2, pp. 506–515, 2018, doi: 10.1285/i20705948v11n2p506.
- [39] F. Sami, M. Amin, and M.M. Butt, "On the ridge estimation of the Conway–Maxwell–Poisson regression model with multicollinearity: Methods and applications," *Concurrency Comput. Pract. Exp.*, vol. 34, no. 1, e6477, 2022, doi: 10.1002/cpe.6477.
- [40] B.M.G. Kibria, "More than hundred (100) estimators for estimating the shrinkage parameter in a linear and generalized linear ridge regression models," *J. Econom. Stat.*, vol. 2, no. 2, pp. 233–252, 2022, doi: 10.47509/JES.2022.v02i02.06.
- [41] W.A. Shewhart, "Some applications of statistical methods to the analysis of physical and engineering data," *Bell Syst. Tech. J.*, vol. 3, no. 1, pp. 43–87, 1924, doi: 10.1002/j.1538-7305.1924.tb01347.x.
- [42] D.A. Pierce and D.W. Schafer, "Residuals in generalized linear models," *J. Am. Stat. Assoc.*, vol. 81, no. 396, pp. 977–986, 1986, doi: 10.1080/01621459.1986.10478361.
- [43] T. Park, C.S. Davis, and N. Li, "Alternative GEE estimation procedures for discrete longitudinal data," *Comput. Stat. Data Anal.*, vol. 28, no. 3, pp. 243–256, 1998, doi: 10.1016/s0167-9473(98)00039-5.

- [44] U. Mammadova and M.R. Özkale, "Deviance residual-based Shewhart control chart for monitoring Conway-Maxwell-Poisson profile under the r-k class estimator," *Qual. Tech. Quan. Manag.* pp. 1-22, 2023, doi: 10.1080/16843703.2023.2259589.
- [45] M. McCann and A. Johnston, "Dataset: SECOM." *UC Irvine Machine Learning Repository*, <https://archive.ics.uci.edu/dataset/179/secom>.
- [46] K. Sellers, T. Lotze, A. Raim, and M.A. Raim, "COMPoissonReg (R package version 3.0)." *A comprehensive R archive network*, <https://cran.r-project.org/web/packages/COMPoissonReg/index.html>
- [47] M.J. Mackinnon and M.L. Puterman, "Collinearity in generalized linear models," *Commun. Stat.-Theory Methods*, vol. 18, no. 9, pp. 3463–3472, 1989, doi: 10.1080/03610928908830102.
- [48] D.C. Montgomery, *Introduction to Statistical Quality Control*. John Wiley & Sons, New Jersey, 2012.

Appendix A. Weight matrix

$$\begin{aligned}
 & V_{ML} \\
 = & \text{diag} \left(\sum_{s=0}^{\infty} \left[\frac{v(v-1)s^2 (\exp(\mu_{i,ML}))^{2s} \left(\frac{(\exp(\mu_{i,ML}))^s}{s!} \right)^{v-2}}{(s!)^2} + \frac{vs^2 (\exp(\mu_i))^s \left(\frac{(\exp(\mu_{i,ML}))^s}{s!} \right)^{v-1}}{s!} \right] \right. \\
 & \left. \frac{\sum_{s=0}^{\infty} \left(\frac{(\exp(\mu_{i,ML}))^s}{s!} \right)^v}{\sum_{s=0}^{\infty} \left(\frac{(\exp(\mu_{i,ML}))^s}{s!} \right)^{2v}} \right) \\
 & - \sum_{s=0}^{\infty} \left[\frac{vs (\exp(\mu_{i,ML}))^s \left(\frac{(\exp(\mu_{i,ML}))^s}{s!} \right)^{v-1}}{(s!)^2} \right]^2
 \end{aligned}$$



Contents lists available at *Dergipark*

Journal of Scientific Reports-A

journal homepage: <https://dergipark.org.tr/pub/jsr-a>



E-ISSN: 2687-6167

Number 57, June 2024

RESEARCH ARTICLE

Receive Date: 24.11.2023

Accepted Date: 02.04.2024

Examination of the effect of ANN and NLPCA technique on prediction performance in patients with breast tumors

Canan DEMİR^{a*}

^aVan Yuzuncu Yıl University, Vocational School of Health Services, 65100, Van, Türkiye, ORCID: 0000-0002-4204-9756

Abstract

Breast cancer is among the most prevalent cancer kinds worldwide. The aim of this study is to examine the effect of combining Artificial Neural Networks and Nonlinear Principal Component Analysis techniques on prediction performance in patients with breast tumors. In the application, a network containing 5 layers, including the input, the coding, the bottleneck, the decoding and the output, was used for the 30 variable data set of 569 breast tumor patients. The training algorithm of choice was the Conjugate Gradient Descent (CGD) algorithm. In this study, artificial neural networks (ANN) and nonlinear principal component analysis were coupled. NLPCA was first applied to dimension reduction in artificial neural networks. Using both the original data set and the decreased size, artificial neural networks were used in the second stage to develop prediction models. By contrasting the performance of these two prediction models with one another, the outcomes were understood. 96.37% of the variation was explained by the two fundamental components that were found using NLPCA. The prediction models developed for the original data set and the dimension-reduced data set have R^2 values of 91% and 87%, respectively. The advantages of the NLPCA and ANN combination for breast tumor patients are demonstrated by this study. It is believed that utilizing principal components as inputs can cut down on complexity and extraneous information.

Keywords: Artificial neural networks, Breast tumor, Dimensional reduction, Nonlinear principal component analysis, Variance

1. Introduction

Breast cancer is among the most prevalent cancer kinds worldwide [1], [2]. Breast cancer, which is encountered especially between the ages of 30-59 and is one of the most important causes of death in women, has become a

* Corresponding author

E-mail address: canandemir@yyu.edu.tr

universal problem despite advances in health, advances in diagnosis and treatment methods, and a conscious society [3], [4]. Compared to developed nations, the incidence of breast cancer is rising more quickly in developing low- and middle-income countries, and the death rate is higher [4]. The reasons for this include the adoption of the western lifestyle, fertility, changes in lactation characteristics, exposure to exogenous factors such as malnutrition, fatty diet, alcohol consumption and hormone therapy, lack of health insurance for all individuals, and economic inadequacies [4], [5]. Early detection of breast cancer is important for increasing overall survival and decreasing mortality. On the other hand, whether the cyst is malignant or benign is determined by various biopsy methods. This prevents the cancer from spreading and reduces the ratio of women who need complementary radiotherapy [6].

Although Principal Component Analysis (PCA) emerged in the 1900s, it is still preferred and used by researchers today. Principal component analysis is a linear method and requires assumptions such as that the variables related to the data set are continuous and the relationships between variables are linear. When these assumptions are not fulfilled, (NLPCA) Nonlinear Principal Component Analysis is used. This descriptive dimension reduction technique, which has a linear or nonlinear relationship between them, yields numerical and graphical results for datasets with continuous, categorical, or discrete variables [7], [8].

Artificial neural networks are a type of computational system designed to mimic the functions of the human brain, like the capacity to learn in order to obtain, produce, and find new knowledge [9]. Machine learning is accomplished by ANNs through the use of examples; their algorithms and modes of operation differ from well-known programming techniques. Before the ANN can function successfully, it needs to be trained and its performance evaluated. Artificial Neural Networks are practical instruments utilized in data-driven process modeling, nonlinear process control, pattern recognition, classification, and prediction [10].

The dimensions of the data indicate the amount characteristics that are measured for every observation. Analyzing high-dimensional data is difficult. Dimension reducing strategies are offered to get rid of unnecessary and unnecessary features. Choosing an appropriate dimensionality reduction process can help increase speed up processing and cut down on the time and work needed to retrieve important data. The purpose of this research is to examine the effect of combining ANN and NLPCA techniques on prediction performance on reduced and non-reduced data sets.

2. Material and methods

In the study, a dataset consisting of 30 variables belonging to 569 breast tumour patients (357 benign, 212 malignant) provided from the free data access site was used as the application material. On July 15, 1992, Olvi Mangasarian provided the dataset, which was generated by Dr. William H. Wolberg, a doctor at the University of Wisconsin Hospital in Madison, Wisconsin, USA [11]. The variables and characteristics of 569 patients with breast tumors are given in Table 1. Matlab (MathWorks. Matlab version R2013b. Natick: 2013) and SPSS (Version 16.0 of IBM SPSS. Spss for Windows. IBM, Chicago, 2010) package program were used for data analysis.

Table 1. Study variables and their characteristics.

No.	Variable name
1.	mean radius
2.	radius Standart Deviation
3.	worst Radius
4.	mean texture
5.	texture SD

6. worst texture
 7. mean perimeter
 8. perimeter SD
 9. worst perimeter
 10. mean area
 11. area SD
 12. worst area
 13. mean smoothness
 14. smoothness SD
 15. worst smoothness
 16. mean compactness
 17. compactness SD
 18. worst compactness
 19. mean concavity
 20. concavity SD
 21. worst concavity
 22. mean concave points
 23. concave points SD
 24. worst concave points
 25. mean symmetry
 26. symmetry SD
 27. worst symmetry
 28. mean fractal dimension
 29. fractal dimension SD
 30. worst fractal dimension
-

2.1 Theory of nonlinear principal component analysis in neural networks

NLPCA has been designed to identify nonlinear interactions in cases when the relationship between the variables is not linear [12]. The NLPCA is implemented using the neural network (or "neuron") shown in Figure 1.

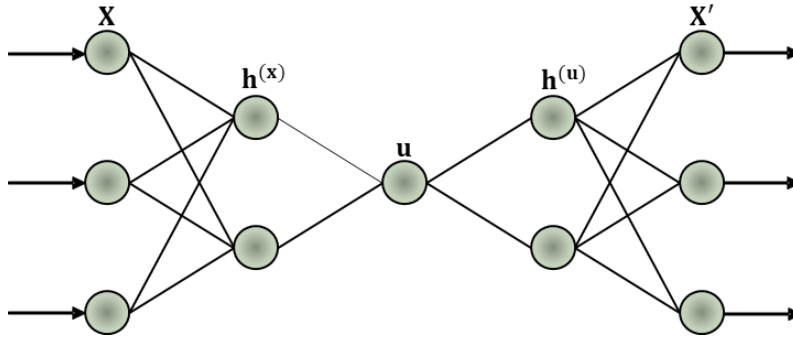


Fig. 1. Nonlinear principal components analysis using a neural network model.

The transfer function is mapped to the input column vector x of length l , or f_1 , by the first hidden layer, denoted by $h^{(x)}$, which is the column vector of length m . Consequently, the expression for $h_k^{(x)}$ is as follows:

$$h_k^{(x)} = f_1 \left[(W^{(x)}x + b^{(x)})_k \right] \quad (1)$$

A weight matrix measuring $m \times l$ is represented by $w^{(x)}$ in equation (1), where $b^{(x)}$ is the column vector in m dimensions containing the bias parameters ($k = 1, \dots, m$). Similar to the first transfer function, f_2 , this one maps the nonlinear basic component (u) from the encoder layer to the hidden layer. It is expressed as follows for this nonlinear basic component:

$$u = f_2 \left(w^{(x)}h^{(x)} + \bar{b}^{(x)} \right) \quad (2)$$

The transformation function f_1 is nonlinear, whereas f_2 is typically assumed to be a linear function (its exact function is unknown, but it can typically be a sigmoid function or hyperbolic tangent). The final hidden layer, $h^{(u)}$, is mapped from u by the transformation function f_3 . Hence, $h_k^{(u)}$ is expressed as follows ($k = 1, \dots, m$):

$$h_k^{(u)} = f_3 \left[(w^{(u)}u + b^{(u)})_k \right] \quad (3)$$

Equation comes after this function (4).

$$x'_i = f_4 \left[(W^{(u)}h^{(u)} + \bar{b}^{(u)})_i \right] \quad (4)$$

The error function $j = \langle \|x - x'\|^2 \rangle$ is used here. By identifying the ideal values, $W(x)$, $b(x)$, $w(x)$, $\bar{b}(x)$, $w(u)$, $b(u)$, $W(u)$ and $\bar{b}(u)$ are minimized [13]. This reduces the mean squared error between the neural network output x' and the original data x .

NLPCA uses the following total parameters: $(m+f+1)(M1+M2)+m+f$. The number of neurons hidden in the decoding and coding is generally regulated by a rule, which also determines which M . Although a bigger M improves the network's capacity for modeling that is nonlinear, it may additionally cause excessively fitting. The accuracy could be low for a lower M because of the network's constrained representation capacity. The complexity of nonlinear functions that the network is capable of producing is indicated by the value of M . Only when f_4 is a linear function and $M = 1$ can there be a linear relationship between the x'_i variables. All of x'_i is linearly related to a single hidden neuron, as shown by Equation (4). Nonlinear solutions have a $M \geq 2$ [14].

Three hidden layers are shown in Figure 1, positioned between input layer x on the left and output layer x' on the right (shown by a circle). The coding layer sits next to the input layer, and is followed by the analysis and "bottleneck" layers (which contain a single neuron, u). The neuron in the bottleneck, u , provides compression or dimension reduction of the data; this is known as the nonlinear principal component [15].

2.2 Backpropagation

A typical backpropagation network consists of an input layer, an output layer, and one or more hidden layers. Even so, the quantity of hidden layers is theoretically unlimited, one or two are typically used. Every layer is completely linked to the layers below it [16].

Supervised learning is the underlying principle of multi-layered networks. During training, the network must be shown both input and output values. For every input, the network's job is to generate the corresponding output. The multilayer network's learning rule is a generalized Delta learning rule that uses the least squares approach as its foundation. The rule of learning is also known as the "Generalized Delta Rule" because of this. There are 2 phases to this rule. The network output is calculated in the first phase, known as forward calculation, and the weights are adjusted in the second phase, known as reverse calculation [17], [18].

Calculation in advance: This stage is where the network output is calculated. The training set's data is now displayed on the network's input layer, marking the start of information processing. As previously stated, the input layer does not process any information. Without any modifications, the newly received entries are routed up to the intermediate stratum. This is what the formula $y_i = x_i$ indicates.

Through the use of connecting weights, every unit in the intermediate layer is given the data from the input unit. The middle layer units' net input is computed as follows:

$$n^1 = \left(\sum_{i=1}^j w_{ir} x_i + b_i \right) \quad (5)$$

In Equality (5)

w_{ir} : i . the input layer element,

r : the connection's weight value to the middle layer unit,

x_i : The input layer's output from the i . processor unit,

n_j : It displays the middle layer unit's output value,

The following is an expression of the output layer's unit's net input;

$$n^2 = \sum_{k=1}^s w_k^2 a_k^1 + b^2 \quad (6)$$

Network output;

$$\hat{y} = g\left\{ \sum_{k=1}^s w_k f\left(\sum_{i=1}^j w_i x_i + b^1 \right) + b^2 \right\} \quad (7)$$

and the following equation is used to calculate the total error [19];

$$E_D = \frac{1}{2} \sum_{i=1}^j (y - \hat{y})^2 \quad (8)$$

The transfer function can be either the hyperbolic tangent function or the sigmoid function, though this is not necessary. It should be mentioned the chosen function can be derived because back propagation requires consideration of the function's derivative [20].

Backward calculation: The network is run entirely backwards during the back propagation phase. The derivative of the transfer function typically modifies the discrepancy between the final layer's output and the intended output, which then propagates back to the previous layer (s). As a result, the error is decreased in the following cycle. Up until the input layer is reached, this process continues for the preceding layer or layers.

2.3 Artificial neural networks (ANN)

Artificial neural networks, which are modeled after the architecture of the brain's nerve cells in humans, are composed of interconnected processing elements of varying weights [21]. The input layer, variable weight factors, summation function, activation function, and output layer are the five primary components that make up an artificial neural network cell in this system (Figure 2).

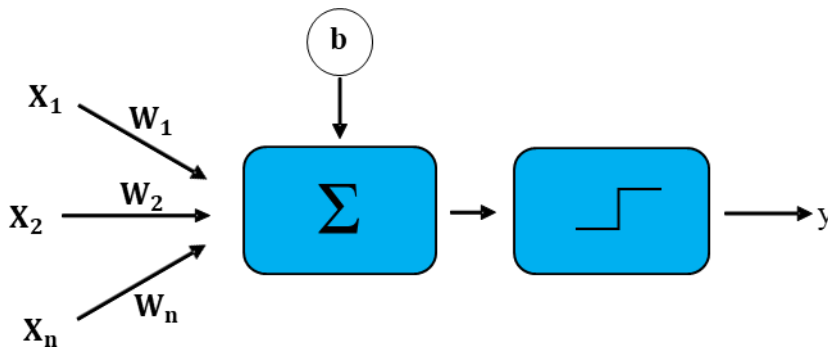


Fig. 2. Artificial neuron.

The data that the artificial nerve cell receives from the outside world is known as an input. The values that establish the significance of information reaching an artificial neuron and its impact on the cell are called weights. When the calculation starts, the weights are given randomly and the weights continue to be changed until the error is minimum according to the process. Learning in artificial neural networks occurs by changing these weights. According to the addition function, each weight in the artificial neuron is multiplied by the input it belongs to. After multiplying these inputs by the weights affecting the inputs, the results are added arithmetically. The result of the addition operation is summed with the threshold value and sent to the activity function. In the calculation, “ w_1, w_2, \dots, w_n ” gives the weights and “ x_1, x_2, \dots, x_n ” gives the values of the input parameters.

$$w_1x_1 + w_2x_2 + \dots + w_nx_n = \sum_{i=1}^n w_i x_i \quad (9)$$

An output value is created by processing the weighted input value with the help of the activation function [8].

2.3.1 Levenberg-marquardt (LM) algorithm

The Hessian matrix does not need to be computed in order to approximate the quadratic training rate using the LM algorithm. The Hessian matrix can be predicted as follows when fed network training frequently uses a sum of squares as the performance function:

$$H = J^T J \quad (10)$$

and can be calculated as gradient.

$$g = J^T e \quad (11)$$

With respect to the weights and deviations, the initial derivatives of the network errors are represented by the Jacobian matrix J , and the network error vector e . It is much simpler to calculate the Jacobian matrix than the Hess matrix, and can be done so with a standard backpropagation technique. The following Newton-like modify is produced by the Levenberg-Marquardt algorithm using this approximation of the Hessian matrix:

$$x_{k+1} = x_k - [J^T J + \mu I]^{-1} J^T e \quad (12)$$

When the scalar μ in equation (11), the Hessian matrix and Newton's method are used. When μ exceeds zero, the function transforms into a gradient with a small step size. The goal is to switch to Newton's method as soon as possible because it is faster, more accurate, and has almost no error. As a result, μ is only raised in the unlikely event that a temporary step would result in an increase in performance function; otherwise, it is lowered after each successful step (decrease in performance function). The outcome is that the performance function continuously decreases with each algorithm iteration [22].

2.3.2 Hyperbolic tangent function

With a marginally larger output space, similar to the sigmoid activation function is the hyperbolic tangent activation function. Although the results of the sigmoid activation function fall within the range of $[0, 1]$, the tangent hyperbolic activation function gives results in the range of $[-1, 1]$ [8].

$$y = \frac{e^x - e^{-x}}{e^x + e^{-x}} \quad (13)$$

In this study, R^2 and MSE were used as accuracy measures. One of these performance measures, R^2 is the accuracy rate decision coefficient of the model. The high value of this coefficient indicates that the predictive relationship is good. MSE, on the other hand, is a measure of high performance because it is an error measure. The error is expressed by the formula et , where t is the time series observed in the time interval rt to show a certain time and pt is the estimated time series [23].

$$MSE = \frac{1}{n} \sum_{i=1}^n e_t^2 \quad (14)$$

3. Results and discussions

NLPCA works by training a feedforward neural network whose inputs are reproduced. Figure 3 depicts the architecture of the neural network that was used to implement NLPCA.

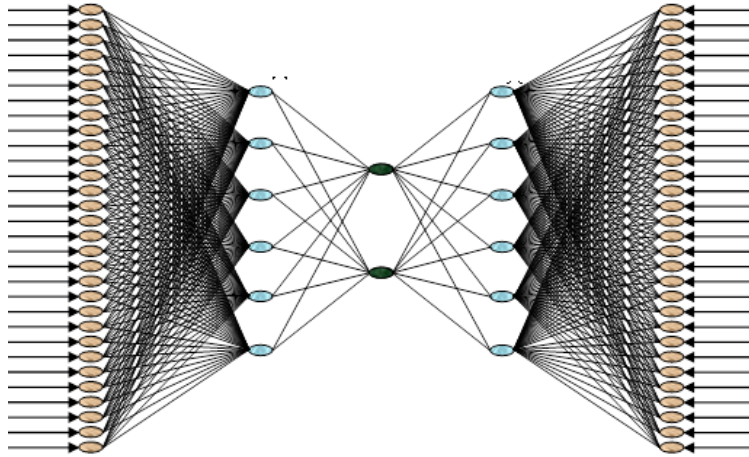


Fig. 3. 30-6-2-6-30 NLPCA model.

In the application, a network containing 5 layers, including the input, the coding, the bottleneck, the decoding and the output, was used for the 30 variable data set of 569 breast tumor patients. The number of iterations in the network architecture, which was selected as the number of neurons 30-6-2-6-30, was determined as 3000. This architecture was decided as a result of trial and error. The coding and decoding layer uses a non-linear hyperbolic tangent function, while the other layers use linear functions. The training algorithm of choice was the Conjugate Gradient Descent (CGD) algorithm.

The original data set consists of a 30x569 matrix. Two main components obtained by NLPCA method in artificial neural networks are a 2x569 dimensional matrix and this matrix explained 96.37% of the total variance (Figure 4).

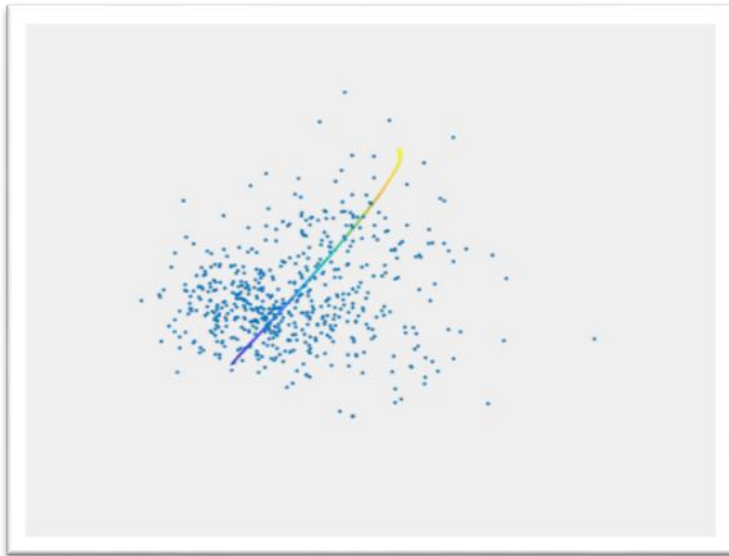


Fig. 4. Two-dimensional Nonlinear Principal Component.

In order to see the effectiveness of NLPCA, prediction models were created with both the original data set and the obtained principal components. (Table 2).

Table 2. Comparison results for two data sets.

	R^2	MSE
Original data set (30x569)	0.91	0.0382
Two principal components (2x569)	0.87	0.0533

The data set was divided into 3 parts as training, verification and testing. Accordingly, the data lines were divided into three as; 70% training, 15% verification and 15% test data. A single hidden layer with 10 neurons in networks and the hyperbolic tangent function in the layers were used. Networks were trained with the Levenberg-Marquardt algorithm. 500 iterations were foreseen for each training. For both data sets, all properties in the networks were kept equal. R^2 shows what percentage of the change in the dependent variable is explained by the independent variables. The high value of the R^2 determination coefficient indicates that our prediction is successful and the prediction is accurate. In feedforward networks, mean square error (MSE) is generally used as a performance function. The MSE function is the average of the sum of squares of the difference between the desired output values and the values produced by the network. The network with the best performance, that is, the network with the smallest test error was evaluated. Accordingly, we found as $R^2 = 0.91$ and $MSE = 0.0382$ for the original data set, and $R^2 = 0.87$ and $MSE = 0.0533$ for the dimension reduced data set.

Many studies have been conducted on the use of PCA as a pre-processor to multi-layer perceptron neural networks in various domains. In order to categorize the quality of food products, O'Farrella et al. employed PCA as a pre-treatment, followed by neural networks with a hidden layer and back propagation algorithm [24]. Bucinski et al. integrated ANN and PCA. They used PCA to reveal some important features in patients with uterine cancer and a back propagation ANN model to classify these patients into two categories [6]. Ayesha et al. stated that most dimensionality reduction applications have a need for classification and prediction accuracy. They also stated that as the size of the data increases, dimensionality reduction is necessary to reduce uncertainty in decision-making [25]. Zebari et al. reported that to improve the accuracy of learning features and reduce training time, dimensionality reduction is necessary as a pre-processing step that can remove irrelevant data, noise, and redundant features [26].

4. Conclusion

In this study, NLPCA was used in artificial neural networks. NLPCA reduced the original data set to two dimensions, with a very high variance explanation rate (96.37%). In dimension reduction methods, original variables contribute to the dimensions to a certain extent. The variables that contribute the most to the dimensions are; radius, perimeter and area variables. Here, variance can be thought as the equivalent of the information in the original data set. In other words, a 30x569 dimensional large matrix was transformed into a much smaller 2x569 dimensional matrix and 96.37% of the information contained was preserved.

In order to see the effectiveness of dimension reduction in patients with breast tumor, prediction models were created in artificial neural networks with both the dimension reduced and non-dimensionally-reduced data set. In practice, multilayer feedforward artificial neural network model was used to see the prediction success of artificial neural networks and malignant tumor was predicted. 30 variable inputs given in the data set variable, and the breast tumor (357 benign, 212 malignant) variable was taken as the target variable. Thus, the probability of predicting malignant tumor for both the original data set and the reduced size data set was determined. Accordingly, when the

prediction models are evaluated, the performance of dimension reduced data seems very close to the performance of non-dimensionally-reduced data.

For the purpose of training machine learning algorithms, not every characteristic in the generated datasets is significant. Certain features might not matter, while others might not have an impact on the prediction's result. Machine learning algorithms are not burdened as much when these unimportant or irrelevant features are ignored or eliminated [27], [28]. In conclusion, this research reveals the benefits of the combination of NLPCA and ANN in dimensionality reduction. It is thought that using basic components as input can reduce unnecessary information and complexity.

Acknowledgement

There is no conflict of interest with any person/institution in the article.

References

- [1] A. Haydaroglu, S. Dubova, S. Özşaran, et al., "Breast Cancer in Ege University "Evaluation Of 3897 Cases"", *The Journal of Breast Health*, vol. 1, pp. 6-11, 2005.
- [2] C. Hocaoglu, G. Kandemir and F. Civil, "The Influence of Breast Cancer to Family Relationships: a Case Report", *The Journal of Breast Health*, vol. 3, pp. 163-165, 2007.
- [3] C. Eroglu, M. A. Eryilmaz, S. Civecik, et al., "Breast Cancer Risk Assessment: 5000 Cases", *International Journal of Hematology and Oncology*, vol. 20, pp. 27-33, 2010.
- [4] N. Akyolcu and G. A. Ugras, "Breast Self-Examination: how Important is it in Early Diagnosis?", *The Journal of Breast Health*, vol. 7, pp. 10-14, 2011.
- [5] A. Tumer, and H. Baybek, "The Risk Level of Breast Cancer at The Working Women", *The Journal of Breast Health*, vol. 6, pp. 17-21, 2010, <https://hdl.handle.net/20.500.12809/4656>.
- [6] A. Buciński, T. Bączek, T. Waśniewski and M. Stefanowicz, "Clinical data analysis with the use of artificial neural networks (ANN) and principal component analysis (PCA) of patients with endometrial carcinoma", *Rep. Pract. Oncol. Radiother*, vol. 10, pp. 239-248, 2005, doi:10.1016/S1507-1367(05)71096-8.
- [7] S. I. V. Sousa, F. G. Martins, M. C. M. Alvim-Ferraz and M.C. Pereira, "Multiple linear regression and artificial neural networks based on principal components to predict ozone concentrations", *Environmental Modelling & Software*, vol. 22, pp. 97-103, 2007, doi:10.1016/j.envsoft.2005.12.002.
- [8] C. Demir and S. Keskin, "Artificial neural network approach for nonlinear principal components analysis", *International Journal of Current Research*, vol. 13, no. 1, pp. 15987-15992, 2021, doi:10.24941/ijcr.40671.01.2021.
- [9] M. O. Kaya, C. Colak and E. Ozdemir, "The Prediction of Prostate Cancer Using Different Artificial Neural Network Models with The Help of Prostate Specific Antigen", *İnönü University Journal of Health Sciences*, vol. 1, pp. 19-22, 2013.
- [10] S. Samarasinghe, "Neural networks for applied sciences and engineering: from fundamentals to complex pattern recognition", *Crc Press*, pp. 245-281. 2006.
- [11] W. Wolberg, O. Mangasarian, N. Street and W. Street, "Breast Cancer Wisconsin (Diagnostic)", *UCI Machine Learning Repository*, 1995, doi:10.24432/C5DW2B.
- [12] M. Scholz, F. Kaplan, C. L. Guy, J. Kopka and J. Selbig, "Non-linear PCA: a missing data approach", *Bioinformatics*, vol. 21, pp. 3887-3895, 2005, doi:10.1093/bioinformatics/bti634.
- [13] W. W. Hsieh, "Nonlinear principal component analysis by neural networks", *Tellus*, vol. 53, pp. 599-615, 2001, doi:10.3402/tellusa.v53i5.12230.
- [14] M.A. Kramer, "Nonlinear principal component analysis using auto-associative neural networks", *AICHE Journal*, vol. 37, pp. 233-43, 1991, doi:10.1002/aic.690370209.
- [15] W. W. Hsieh, "Nonlinear principal component analysis of noisy data", *Neural Networks*, vol. 20, no. 4, pp. 434-443, 2006. doi:10.1016/j.neunet.2007.04.018.
- [16] D. Anderson and G. McNeill, "Artificial Neural Networks Technology", *New York: Rome Laboratory RL/C3C Griffiss AFB*. 83. A011, 1992.
- [17] A. Gülbağ, "Quantitative Determination Of Volatile Organic Compounds By Using Artificial Neural Network And Fuzzy Logic Based Algorithm", [dissertation], Sakarya: Sakarya University, 2006.
- [18] H. Güler, "Prediction of Elements On Corrosion Behavior Of Zinc-Aluminum Alloys Using Artificial Neural Networks", [dissertation]. Sakarya, Sakarya University, 2007.
- [19] H. Okut, "Bayesian Regularized Neural Networks for Small n Big p Data. Rosa JLG", *Artificial Neural Networks-Models and Applications*. London: InTechOpen, 2016.
- [20] V.S.A. Kargı, "Artificial Neural Network Models and an Application at a Textile Firm", [dissertation]. Bursa, Uludağ University, 2013.
- [21] B. Taşar, F. Üneş, M. Demirci and Y. Z. Kaya, "Forecasting of Daily Evaporation Amounts Using Artificial Neural Networks Technique",

Dicle University Engineering Faculty Journal of Engineering, vol. 9, no. 1, pp. 543-551, 2018.

[22] Trainlm [Internet]. [access date 29 november 2021]. Access address:

<https://uk.mathworks.com/help/deeplearning/ref/trainlm.html>

[23] Y. Gültepe, "A Comparative Assessment on Air Pollution Estimation by Machine Learning Algorithms", *European Journal of Science and Technology*, vol. 16, pp. 8-15, 2019, doi:10.31590/ejosat.530347.

[24] M. O'Farrella, E. Lewisa, C. Flanagan, W. B. Lyonsa and N. Jackman, "Combining principal component analysis with an artificial neural network to perform online quality assessment of food as it cooks in a large-scale industrial oven", *Sensors and Actuators B: Chemical*, vol. 107, pp. 104–112, 2005, doi:10.1016/j.snb.2004.09.050

[25] S. Ayesha, M. K. Hanif, and R. Talib, "Overview and comparative study of dimensionality reduction techniques for high dimensional data", *Information Fusion*, vol. 59, pp. 44-58, 2020, <https://doi.org/10.1016/j.inffus.2020.01.005>.

[26] R. Zebari, A. Abdulazeez, D. Zeebaree, D. Zebari and J. Saeed, "A comprehensive review of dimensionality reduction techniques for feature selection and feature extraction", *Journal of Applied Science and Technology Trends*, vol. 1, no. 1, pp. 56-70, 2020, doi:10.38094/jastt1224.

[27] G. T. Reddy, M. P. K. Reddy, K. Lakshmana, R. Kaluri, D. S. Rajput, G. Srivastava and T. Baker, "Analysis of dimensionality reduction techniques on big data", *Ieee Access*, 8, 54776-54788. 2020, doi: 10.1109/ACCESS.2020.2980942

[28] I. K. Omurlu, F. Cantas, M. Ture and H. Ozturk, "An empirical study on performances of multilayer perceptron, logistic regression, ANFIS, KNN and bagging CART", *Journal of Statistics and Management Systems*, vol. 23, no. 4, pp. 827-841, 2020, doi:10.1080/09720510.2019.1696924.



Contents lists available at *Dergipark*

Journal of Scientific Reports-A

journal homepage: <https://dergipark.org.tr/pub/jsr-a>



E-ISSN: 2687-6167

Number 57, June 2024

RESEARCH ARTICLE

Receive Date: 08.02.2024

Accepted Date: 15.04.2024

Chemical structure and characterization of bio-oils isolated from walnut shells by different processes

Yunus Başar^a, Mehmet Salih Nas^b, Mehmet Hakkı Alma^a, İbrahim Demirtaş^a, Mehmet Harbi Calimli^{c*}

^aResearch Laboratory Application and Research Center (ALUM), Iğdır University, Iğdır, Turkey, ORCID:0000-0002-7785-3242,0000-0001-7011-3965, 0000-0001-8946-647X

^bIğdir University, Faculty of Applied Sciences, Department of Organic Agriculture Management, Iğdir, Turkey, ORCID:0000-0003-1092-5237

^cIğdir University, Tuzluca Vocational School, Department of Medical Services and Techniques, Iğdir, Turkey, ORCID:0000-0001-9756-191X

Abstract

In this study, content analyses of the products obtained by pyrolysis and extraction of walnut shells were performed with some advanced analytical methods such as GS-MS, LC/MS-MS, and FTIR. In LC-MS/MS analyses. The presence of phenolic compounds in the pyrolysis liquid and extract liquid of walnut shells was determined using 41 standards. The obtained LC-MS/MS analysis results were compared, and it was found that the type and amount of phenolic compounds in the extracted liquid were more than the type and amount of phenolic compounds in the pyrolysis liquid. As a result of 41 phenolic standards investigations, the presence of a total of 10 phenolic compounds in liquids was detected and 2 of these compounds were detected in the pyrolysis liquid and 8 in the extracted liquid. As phenolic compounds, catechin (770.75 µg/g extract), hydroxy benzaldehyde (140.78 µg/g extract), and vanillic acid (114.95 µg/g compounds) were detected in the walnut extract. The existence of the compounds was supported by FTIR analyses of liquids obtained as a result of two different processes. By GC-MS analysis, linoleic acid methyl ester (44.01%), stearic acid methyl ester (14.93%), palmitic acid methyl ester (24.67%), linolenic acid and methyl ester compounds were detected in walnut shell extract liquid. GC-MS analysis of the pyrolysis liquid showed that compounds such as stearic acid methyl ester (18.97%), palmitic acid methyl ester (18.10%), o-xylene (12.17%), and o-ethyl toluene (8.14%) were formed as a result of pyrolysis. The findings revealed that walnut shell pyrolysis liquid product and extract contain very different phenolic, acid, and ester compounds. A concrete result was revealed about the use of the products obtained in this study in different areas.

© 2023 DPU All rights reserved.

* E-mail address: calimli.6500@gmail.com.

Keywords: : Walnut; Pyrolysis; Extract; LC-MS; GC-MS; Analysis

1. Introduction

Generally, tree species such as walnut, chestnut, and hazelnut are abundant in the Northern Hemisphere. Products obtained from these trees can be used in many industrial areas such as confectionery, chocolate, oil, and liquor. Since it can be consumed directly, the demand for these products is quite high. Some methods such as solvent extraction, microwave-assisted, conventional hydrothermal, and pyrolysis have been used to transform waste into value-added products [1,2]. Among these methods, the pyrolysis process is highly preferred. Pyrolysis is a process of thermally decomposing biomass residue in an airless environment and converting it into bio-oil, biochar, and gas products at different rates [3,4]. During pyrolysis, no waste or any by-products that may harm the environment are formed. Therefore, pyrolysis is a harmless process for the environment [5]. As a result of the pyrolysis process, by-products such as black carbon, coke, pyrolysis oil, and coke are formed [6]. These by-products can be used in different areas such as energy, chemical raw materials, and high-value-added products [7]. For example, black carbon; is used in areas such as fuel cells, the plastic industry, and paint raw materials. In addition, gaseous products such as hydrogen and methane resulting from pyrolysis can be used as fuel. Obtaining and using these products can provide great convenience in daily life. All these products are produced through processes such as cellulosic waste material and pyrolysis process [8]. Analytical methods that can provide highly advanced and accurate results, such as LC-MS/MS, FTIR, and GC, are widely used to elucidate the material structure. Clarifying the structure of matter by using these techniques can provide very important clues about where the materials in question will be used [9]. Additionally, qualitatively and quantitatively complex components can be detected using the solvent extraction method in biomass wastes. Tree bark and other cellulosic materials are rich in various chemicals such as biopolymers, phenolic compounds, and lignite. Detailed analysis of these complex compounds is critical to expand and evaluate the uses of cellulosic materials. Walnut, one of these tree species, belongs to the Juglandacea plant family, which is grown and consumed widely worldwide. Some researchers studies that walnuts have heart-healthy, anti-inflammatory, and cancer-reducing effects [10]. Along with the consumed walnuts, some of the walnut shells produced in large quantities are burned and cannot be adequately utilized in suitable areas [11]. Therefore, these wastes constitute a source of value-added by-products and other areas. Several studies have analyzed the components found in walnut shells. However, studies aiming to reveal the content of walnut shells are limited in the literature [12].

Herein, as far as we know, for the first time, walnut shell residues were pyrolyzed and extracted. The contents of the products obtained from pyrolysis and extraction were investigated and compared using some advanced analytical methods. The presence of various compounds such as phenolic compounds, organic, phenolic, amino acid, and volatile compounds of bio-oils was analyzed with Gas Chromatography-Mass Spectrometry (GC-MS), Liquid Chromatography Mass Spectrometry (LC/MS-MS), and Fourier Transform Infrared Spectroscopy (FT-IR).

2. Material and Method

2.1. Materials

Walnut shells collected in Iğdır province were dried at 105°C for 12 hours. Waste walnut shells were turned into powder with the help of a grinder. The chemical reagents of methanol, acetone, ethyl acetate, ether, and hexane used in this study were purchased from Sigma and were analytically pure. All chemicals used were used without any further purification processes.

2.2. Instruments and Analyses

2.2.1. LC-MS/MS Analysis

Phenolic compounds were analyzed by high-performance liquid chromatography (LC/MS-MS). LC/MS-MS combined with mass spectrometry (MS) was an Agilent Poroshell 120 EC-C18 (100 mm × 3.0 mm, 2.7 μm) reversed-phase analytical column. Eluent A (pure water + 5 mM ammonium formate + 0.1% formic acid) and eluent B (methanol + 5 mM ammonium formate + 0.1% formic acid) were set. Solvent flow rate (0.400 mL/min) and sample injection volume (4 μL) were adjusted [13,14]. The content analysis was performed with 41 standard phenolic compounds (Figure 1).

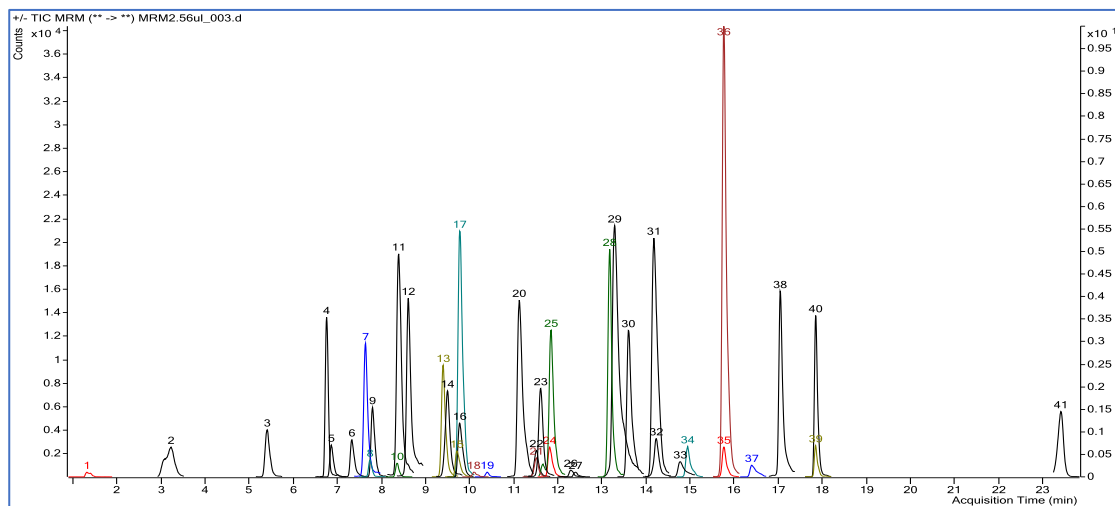


Fig. 1. LC-MS/MS chromatogram. Acids: 1. Shikimic, 2. Gallic, 3. Protocatechuic, 4. Epigallocatechin, 5. Catechin, 6. Chlorogenic, 7. Hydroxy benzaldehyde, 8. Vanillic, 9. Caffeic, 10. Syringic, 11. Caffeine, 12. Vanillin, 13. Orto Coumaric, 14. Salicylic, 15. Taxifolin, 16. Resveratrol, 17. Polydatine, 18. Transferulic acid, 18. Sinapic, 20. Scutellarin, 21. Para Coumaric, 22. Coumarin, 23. Protocatechuic Ethyl Ester, 24. Hesperidin, 25. Isoquercitrin, 26. Rutin, 27. Quercetin -3 - Xyloside, 28. Kaempferol - 3- Glucodide, 29. Fisetin, 30. Baicalein, 31. Chrysin, 32. Trans-cinnamic, 33. Quercetin, 34. Naringenin, 35. Hesperetin, 36. Morin, 37. Kaempferol, 38. Baicalein, 39. Luteolin, 40. Baichanin A, 41. Diosgenin.

2.2.2. GC-MS/MS Analysis

Fixed oil, free oil, and other essential oil components in walnut shell extracts and pyrolysis oil products were examined by GC-MS/MS analysis (Agilent 7000, 7697A Headspace Sampler, 7890 GC, 7693 Autosampler). In GC-MS/MS analysis of the samples, the initial temperature was 50 °C and the retention time was 2 minutes. The temperature was increased to 140 °C at a rate of 3 °C/min and then increased to 220 °C at a rate of 4 °C/min. It was kept at 220 °C for 10 minutes. At a constant temperature increase rate of 4 °C/min, the temperature was increased to 250 °C and finally, the temperature was increased to 270 °C and kept for 30 minutes. The ion temperature of the detector in GC-MS was 280 °C and the carrier gas was He. A 0.22 μm disposable syringe was used for sample analysis (1 μL, 1:10). The analyses were performed on a 30 m x 0.25 mm x 0.25 μm, Agilent MP-5 column (5%-phenyl)-methylpolysiloxane). The process was started by taking 30 mg of the sample and dissolving it in 2 mL methanol and 2 mL n-hexane. 1 mL of 1M KOH was added to the resulting mixture and mixed using a vortex (2500 rpm, 30 sec) to ensure good mixing. 0.22 microns were taken from the upper phase of the mixture and filtered, and the filtered sample was given to the device and analysis started [15].

2.2.3. Analyses of FTIR for walnut shells

Analyses of FTIR for walnut shells were performed to elucidate the bond structure of the compound in the bio-oil samples using the Agilan Carry60 FTIR device.

2.3. Preliminary stages before experimental studies on walnut shells

The collected walnut shells were grounded using the grinding machine until they reached the smallest grain size. Then, the ground walnut shells were washed abundantly in deionized water and dried in the oven at 60 °C for 48 hours. The dried samples were prepared in a moisture-free environment at room conditions for pyrolysis and extra processing.

2.4. Approaches followed to obtain the liquid sample

2.4.1. Liquid sample preparation by extraction process

Pre-prepared ground walnut shells are crushed to a certain amount. Then, the solid sample was added to the prepared glass jar medium with methanol-chloroform (1:1 v/w) solvent. Left indoors and away from light for five days. Then, the solvent mixture was filtered and the solvents were removed with the help of an evaporator device. Finally, the obtained sample was taken into bottles. The samples taken were dissolved in 1 mL methanol and 1 mL hexane was added [13,14]. After phase separation occurred, the hexane phase was analyzed in GC-MS and the methanol phase was analyzed in GC-MS and LC/MS-MS [15].

2.4.2. Liquid sample preparation by pyrolysis process

Walnut shell grinding was carried out with a fixed bed pyrolysis (reactor) device in an inert nitrogen atmosphere. The reactor chamber is manufactured using stainless steel material with a length of 600 mm and an internal diameter of 50 mm. The reactor has a thermocouple temperature sensor design and can be operated with electrical energy. In the pyrolysis study, a 0.1 kg solid sample was taken into the feed reactor basin. Then, Nitrogen gas was exposed to 550 °C for approximately 2 hours under an inert environment at a heating rate of 10 °C/1 min [12]. Then, the liquid sample in the collection tank was taken into airtight bottles. The resulting liquid samples were dissolved in 1 ml of methanol and 1 ml of hexane was added. After phase separation occurred, the hexane phase was analyzed in GC-MS and the methanol phase was analyzed in LC/MS-MS. Additionally, an FTIR device was used to obtain detailed information about the functional structure of the sample.

3. Results and Discussion

3.1. LC-MS/MS analysis results

LC-MS/MS analyses were implemented to examine the phenolic compound content of walnut shells quantitatively and qualitatively. The type of phenolic compounds formed as a result of pyrolysis and the extraction of walnut shells, and the experimental parameters applied during the processes are summarized in Table 1. Among the 41 phenolic compounds investigated, 2 were identified in the pyrolysis sample and 8 in the extract (Fig. 2). The phenolic contents of the chloroform-methanol extract of waste walnut shells and the liquid part obtained by pyrolysis were compared. As seen in Table 1 different results were detected in phenolic compounds of the liquid of extraction and the liquid of pyrolysis of walnut shells.

Table 1. Evaluation of the content profile of the liquid of extraction and the liquid of pyrolysis of walnut shells.

No	Compound	RT	Pyrolysis walnut peel ($\mu\text{g/g}$ extract)	Extract walnut peel ($\mu\text{g/g}$ extract)
1	Protocatechuic acid	5.33	-	24.45
2	Catechin	6.74	-	770.75
3	Hydroxybenzaldehyde	7.50	-	140.78
4	Vanillic acid	8.81	-	114.95
5	p-Coumaric acid	9.40	-	39.84
6	Morin	12.90	-	10.88
7	Naringenin	14.88	11.93	26.92
8	Diosgenin	23.77	4.65	7.20

RT: Retention time.

When looking at the phenolic compound content of the walnut shell extract, catechin (770.75 $\mu\text{g/g}$ extract), hydroxy benzaldehyde (140.78 $\mu\text{g/g}$ extract) and vanillic acid (114.95 $\mu\text{g/g}$ extract) compounds were detected at high levels. Naringenin (11.93 $\mu\text{g/g}$ extract) and diosgenin (4.65 $\mu\text{g/g}$ extract) compounds were detected in the phenolic content of the pyrolysis liquid extract. Compared to the results, it can be seen that the phenolic content decreased significantly after the pyrolysis process. It is thought that this decrease is due to the degradation of phenolic compounds with temperature. The results we obtained are compatible with previous studies. However, it should not be forgotten that differences in the methods applied in the analyses cause differences in the products obtained. For example, while only methanol is used in some studies in the literature, a methanol/hexane mixture can be used in some studies. In this study, a methanol/hexane mixture was used [16].

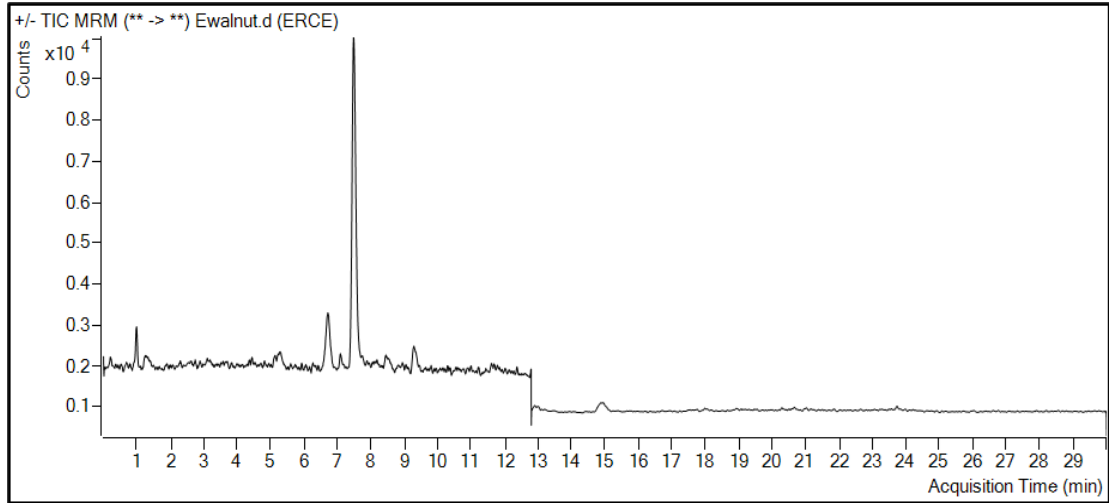


Fig. 2. LC/MS-MS chromatogram of methanol-chloroform extract derived from walnut shell.

3.2. FTIR analysis results

FTIR analysis results of liquid samples obtained from the pyrolysis experiments performed at 550 °C and walnut shells extract are illustrated in Fig. 3. FTIR analyses of the obtained extract and pyrolysis liquid samples show different peaks in the range of 500-400 cm⁻¹. The FTIR results show some considerable differences between the spectra of the solution organics obtained in this study and the bio-oils of the pyrolysis. As can be seen, significant peaks were observed in some regions such as 3300 and 1028 cm⁻¹. The vibration peaks in these ranges show different functional groups such as alcohol, phenols, and carboxylic acid. Moreover, the value of 2922 cm⁻¹ for both aqueous extracts and pyrolytic oils shows a peak band of -CH stretching [17]. A sharp peak around the 1706 cm⁻¹ band was observed especially in the pyrolytic oils and these vibrational peaks indicate that the bio-oils of the pyrolysis contain ketones, carboxylic acids, and aldehydes. The bands at 1214, 1208, 1030, 1028, and 1103 cm⁻¹ indicate the presence of organic and aqueous bio-oils and -CO stretching and -OH bending. This indicates that primary-secondary alcohols, phenolic, ester, and etheric compounds are present in the structures. Finally, the intense peaks between 750 and 600 cm⁻¹ indicate the presence of aromatic groups. It was observed from the band peak values that the pyrolytic organic bio-oils are broader and more intense compared to aqueous extract oils. The observed results are supported by similar results obtained in other studies in the literature [18,19].

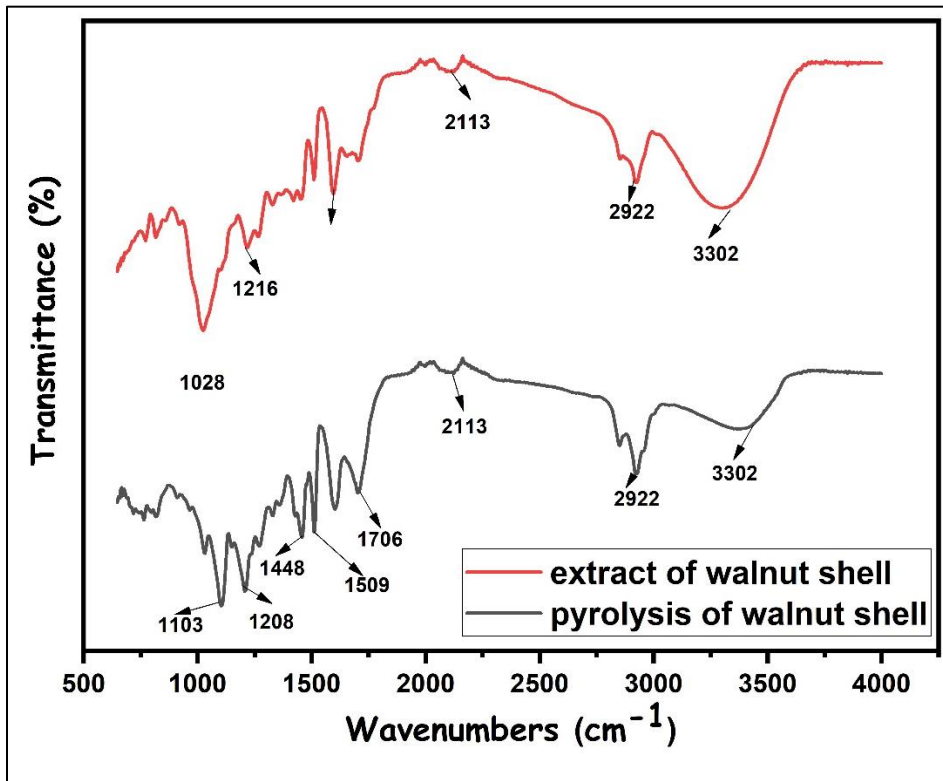


Fig. 3. FTIR analysis results of pyrolysis bio-oil obtained using walnut shells and the products resulting from extraction.

3.3. GC-MS/MS analysis results

GC-MS/MS analysis results of liquids of extracts and pyrolysis of walnut shells are given in Fig.4. According to the analysis results, linoleic acid methyl ester (44.01%), palmitic acid methyl ester (24.67%), stearic acid methyl ester (14.93%), linolenic acid and methyl ester (11.60%) compounds were detected in the liquid of extract. Stearic acid methyl ester (18.97%), palmitic acid methyl ester (18.10%), o-xylene (12.17%), and o-ethyl toluene (8.14%) compounds were determined in high amounts in the liquid of pyrolysis. The comparison between the extract and pyrolysis liquids revealed the presence of free fatty acids in the walnut shell due to the pyrolysis process. We can say that this situation occurs due to the fracture of the sample structure at high temperatures.

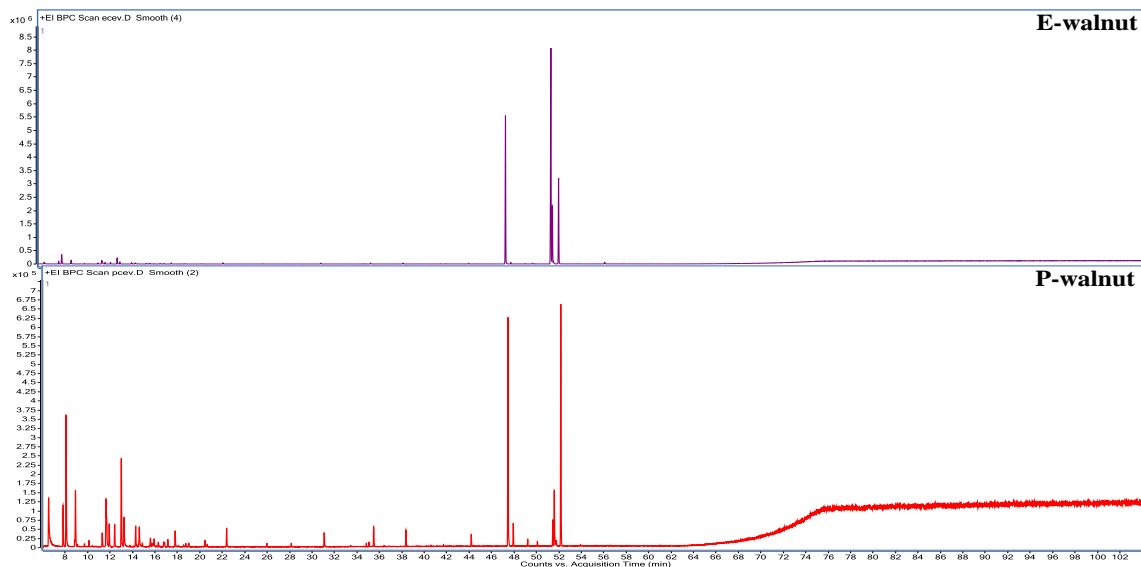


Fig. 4. GC-MS/MS chromatogram of walnut shell methanol-chloroform extract and liquid of pyrolysis liquid.

In addition, it was observed that the percentage amount of stearic acid, methyl ester, and o-ethyl toluene compounds increased as a result of pyrolysis, while the percentage amount of palmitic acid, methyl ester compound decreased (Table 2). Through the pyrolysis process, hemicellulose and cellulose are easily decomposed, resulting in the formation of gaseous products, ketone and hydrocarbon compounds, carboxylic acids, aldehyde products, and other compounds found in bio-oil. Similar results have been found in previous results [20,21].

Table 2. GC-MS analysis results of liquids of pyrolysis and aqueous extract of walnut shells.

No	RT	Compounds	Pyrolysis walnut%	Extract walnut%
1	7.82	m-Xylene	3.18	0.47
2	8.08	o-Xylene	12.17	1.84
3	8.92	???	4.69	-
4	10.12	Cumene	0.42	-
5	11.30	???	1.23	-
6	11.64	m-Ethyltoluene	6.87	0.68
7	11.93	Mesitylene	1.98	-

8	12.41	Pseudocumol	1.91	-
9	13.00	o-Ethyltoluene	8.14	1.24
10	13.25	Decane	2.91	-
11	14.29	Hemimellitene	1.84	-
12	14.60	2-Ethylhexanol	2.16	-
13	15.59	o-Propyltoluene	0.76	-
14	15.93	1,3-Dimethyl-5-ethyl benzene	0.64	-
15	17.80	Undecane	1.37	-
16	22.39	Dodecane	1.54	-
17	31.08	Tetradecane	1.35	-
18	38.37	Hexadecane	1.35	-
19	44.19	Heptadecane	0.88	-
20	47.46	Palmitic acid, methyl ester	18.10	24.67
21	51.46	Linoleic acid, methyl ester	1.90	44.01
22	51.59	Oleic acid, methyl ester	4.94	0.56
23	51.63	Linolenic acid, methyl ester	-	11.60
24	51.76	Oleic acid, methyl ester-isomer	0.70	-
25	52.17	Stearic acid, methyl ester	18.97	14.93

4. Conclusion

Walnut shell is an important environmental problem as an agricultural waste product. Analyzing liquid pyrolysis oil obtained by analytical methods such as LC-MS/MS, GC, and FTIR and determining the usage areas of walnut shells according to the analysis results will reduce waste pollution, which is an environmental problem.

The findings obtained in the study can be summarized as follows;

Pyrolysis of walnut shells and extract preparation of these shells were carried out. GC-MS, LC/MS-MS, and FT-IR analyses of the obtained liquid products were performed and their content analyses were examined. By comparing the analysis results, substance contents with high possible additive values were found. Accordingly, it was concluded that the amount and type of phenolic content in walnut extracts was higher in the pyrolysis liquid. Phenolic compounds and their amounts were found as catechin (770.75 µg/g extract), hydroxy benzaldehyde (140.78 µg/g extract), and vanillic acid (114.95 µg/g compounds). FTIR analysis was performed and it was revealed that walnut extract and pyrolysis liquids had different contents. Volatile component analyses in liquids were performed by GC-MS analyses. GC-MS analysis of the extract revealed the presence of linoleic acid methyl ester (44.01%), stearic acid methyl ester (14.93%), palmitic acid methyl ester (24.67%), linolenic acid and methyl ester compounds. Pyrolysis liquid GC-MS analyses also revealed the presence of the compounds stearic acid methyl ester (18.97%), palmitic acid methyl ester (18.10%), o-xylene (12.17%), and o-ethyl toluene (8.14%). We can probably attribute this to the deterioration of the bonds of the sample exposed to high temperatures in the pyrolysis method. The results showed us that bio-oil yield has a large impact depending on the process used. This study will be useful for those working in various fields such as bioplastics, biofuels, biochemicals, pharmaceuticals, cosmetics, fertilizers, and soil conditioners. In conclusion; this study has shown that wastes such as walnut shells can be evaluated through pyrolysis and pyrolysis products can be used in various areas. These findings could provide solutions to the problem of waste management, contribute to a new bio-economy, and contribute to sustainability.

Acknowledgments

This study did not receive any specific funding or financial assistance from governmental, commercial, or non-profit Organizations.

References

- [1] S. Demirel, M.S Nas, A. Kocyigit, M.H. Calimli and M.H. Alma, "High capacitive pt and NiOx loaded supercapacitors with commercial and green synthesized carbon-based materials," *J Mater Sci Mater Electron*, 35:1–13. 2024. <https://doi.org/10.1007/S10854-023-11885-7/TABLES/4>.
- [2] A. Morales, J. Labidi and P. Gullón, "Hydrothermal treatments of walnut shells: A potential pretreatment for subsequent product obtaining," *Sci Total Environ*, 764:142800. 2021. <https://doi.org/10.1016/J.SCITOTENV.2020.142800>.
- [3] K. Wang and R.C. Brown, "Prospects for Fast Pyrolysis of Biomass," *Green Chem Ser*, 1–11. 2017. <https://doi.org/10.1039/9781788010245-00001>.
- [4] A.V. Bridgwater, "Review of fast pyrolysis of biomass and product upgrading," *Biomass and Bioenergy*, 38:68–94. 2012. <https://doi.org/10.1016/J.BIOMBIOE.2011.01.048>.
- [5] T. Bridgwater, "Biomass for energy," *J Sci Food Agric*, 86:1755–68.2006. <https://doi.org/10.1002/JSFA.2605>.
- [6] M. Schueppel, M. Graebner, "Pyrolysis of Heavy Fuel Oil (HFO) – A review on physicochemical properties and pyrolytic decomposition characteristics for application in novel, industrial-scale HFO pyrolysis technology," *J Anal Appl Pyrolysis*, 106432. 2024. <https://doi.org/10.1016/J.JAAP.2024.106432>.
- [7] T. Li, J. Su, C. Wang, A. Watanabe, N. Teramae and H. Ohtani H, "Advances in the development and application of analytical pyrolysis in biomass research: A review," *Energy Convers Manag.*, 271:116302. 2022. <https://doi.org/10.1016/J.ENCONMAN.2022.116302>.
- [8] Compendium of Chemical Terminology. *IUPAC Compend Chem Terminol.*, 1824. 2009. <https://doi.org/10.1351/goldbook.P04961>.
- [9] H. Li, Y. Zou, J. Liang, Z. Zhao, N. Zhou and Y.Gao Y, "The Potential of Platanus orientalis L. Bark for High-Grade Resource Utilization," *Forests.*,14:2002. 2023. <https://doi.org/10.3390/F14102002/S1>.
- [10] H. Pei, S. He, S. Liu, H. Chen, J. Song and Q. Liu, "Aroma characteristics and odor source analysis of roasted Xinjiang thin-shell walnuts (*Juglans regia* L.) by using multivariate statistical analysis," *Food Biosci*, 56:103312. 2023. <https://doi.org/10.1016/J.FBIO.2023.103312>.
- [11] R. Wang, Z. Liu, L. Li, Y. Zhang, Q. Dong and Z. Huang, "Impact of pretreatment with photocatalysis sequential coupling Fenton oxidation on physicochemical properties, pyrolysis behaviors, and product distribution of walnut shell," *Chem Eng J.*, 148425. 2023. <https://doi.org/10.1016/J.CEJ.2023.148425>.
- [12] Y. Başar, F. Gül, M.S. Nas, M.H. Alma and M.H. Calimli, "Investigation of value-added compounds derived from oak wood using hydrothermal processing techniques and comprehensive analytical approaches (HPLC, GC-MS, FT-IR, and NMR)," *Int J Chem Techno*, 2023. <https://doi.org/10.32571/IJCT.1365592>.
- [13] Y. Başar , S. Yenigün , Y. İpek , L. Behçet , F. Gül and Özen, "DNA protection, molecular docking, enzyme inhibition and enzyme kinetic studies of 1,5,9-epideoxyloganic acid isolated from *Nepeta aristata* with bio-guided fractionation," *J Biomol Struct Dyn*, 2023 <https://doi.org/10.1080/07391102.2023.2250461>.
- [14] S. Yenigün, Y. Başar, Y. İpek, L. Behçet, T. Özen and İ Demirtaş, "Determination of antioxidant, DNA protection, enzyme inhibition potential and molecular docking studies of a biomarker ursolic acid in *Nepeta* species," *J Biomol Struct Dyn.*, 2023.<https://doi.org/10.1080/07391102.2023.2229440>.
- [15] Y. Başar, S. Yenigün, F. Gül, T. Ozen, İ. Demirtaş and M.H. Alma, "Phytochemical profiling, molecular docking and ADMET prediction of crude extract of *Atriplex nitens* Schkuhr for the screening of antioxidant and urease inhibitory," *Int J Chem Technol .*, 2024. <https://doi.org/10.32571/IJCT.1389719>.
- [16] F. Sheng, B. Hu, G. Jin, J. Wang, C. Wu, Z. Luo, "The Analysis of Phenolic Compounds in Walnut Husk and Pellicle by UPLC-Q-Orbitrap HRMS and HPLC," 26, Page 3013 2021;26:3013. 2021. <https://doi.org/10.3390/MOLECULES26103013>.
- [17] A. Oasmaa, T. Sundqvist, E. Kuoppala, M. Garcia-Perez, Y. Solantausta, C. Lindfors, "Controlling the phase stability of biomass fast pyrolysis bio-oils," *Energy & Fuels*, 29:4373–81. 2015. <https://doi.org/10.1021/ACS.ENERGYFUELS.5B00607>.
- [18] F. Abnisa F, W. Daud, J.N. Sahu JN. "Pyrolysis of mixtures of palm shell and polystyrene: An optional method to produce a high-grade of pyrolysis oil," *Environ Prog Sustain Energy*, 33:1026–33. 2014. <https://doi.org/10.1002/EP.11850>.
- [19] J.L. Chukwunke, J.E. Sinebe, D.C. Ugwuegbu and C.C. Agulonu . " Production by Pyrolysis and Analysis of Bio-oil from Mahogany Wood (*Swietenia macrophylla*)," *Curr J Appl Sci Technol*, 17:1–9. 2016. <https://doi.org/10.9734/BJAST/2016/24551>.
- [20] N. Ahmed, M. Zeeshan, N. Iqbal, M.Z. Farooq, S.A. Shah . "Investigation on bio-oil yield and quality with scrap tire addition in sugarcane bagasse pyrolysis.," *J Clean Prod*, 196:927–34. 2018. <https://doi.org/10.1016/J.JCLEPRO.2018.06.142>.
- [21] D.V. Naik, V. Kumar, B. Prasad, M.K. Poddar, B. Behera and R. Bal , "Catalytic cracking of jatropa-derived fast pyrolysis oils with VGO and their NMR characterization," *RSC Adv.*, 5:398–409. 2014. <https://doi.org/10.1039/C4RA08128E>.



Contents lists available at *Dergipark*

Journal of Scientific Reports-A

journal homepage: <https://dergipark.org.tr/pub/jsr-a>



E-ISSN: 2687-6167

Number 57, June 2024

RESEARCH ARTICLE

Receive Date: 02.04.2024

Accepted Date: 28.05.2024

Investigation of the alloying elements effect in the flux-cored wire and submerged arc welding flux combination

Erhan Ozkan^{a,*}

^a*Ege University, Mechanical Engineering Department, 35040, İzmir, Türkiye, ORCID: 0000-0002-3849-6713*

Abstract

In this study, it was aimed to investigate hardfacing weld metals' metallurgical and mechanical properties produced by flux-cored wire and submerged arc welding flux combinations. The usage of the combination for these two methods, which are generally preferred separately, distinguishes this research from other similar studies. In the first stage, the optimum production conditions and physical properties of the submerged arc welding fluxes were determined and then flux-cored wire manufacturing details have been defined. Agglomerated submerged arc welding fluxes and seamed type flux-cored welding wires samples were investigated according to the changing carbon, chromium, niobium, and wolfram ratios, while manganese and silicon values were kept constant. Five different samples have been prepared with this purpose, and the hardness test, wear test, microstructure analysis, chemical analysis, and X-Ray diffraction analysis were carried out respectively. It was observed that the increase in hardness affects the wear resistance directly. The effect of chemical analyses on the microstructure has also been determined. Moreover, while the increasing amount of chromium carbide clearly changed the microstructure, and the addition of refractory metals enabled the formation of the eutectic and dendritic structure. The problems of low efficiency in flux-cored wire and inability to alloy in submerged arc welding flux were solved with this method. Therefore, the production of hardfacing consumables via submerged flux-cored arc welding combination method was achieved firstly by using domestic raw materials, and one TUBITAK project and one PhD thesis were successfully finished with these data.

Click here and insert your abstract text.

© 2023 DPU All rights reserved.

* Corresponding author. Tel.: +90-532-509-5021; fax: +90-232-877-1715
E-mail address: erhanozkan81@icloud.com

Keywords: FCAW, SAW, Hardfacing, Wear resistance, Mechanical properties, Metallurgical properties.

1. Introduction

The process of joining or filling metallic materials by melting them using a heat source with or without pressure is called metal welding. When the history of electric arc welding is researched, it is determined that the oldest one is the Benardos welding method in 1885. Benardos created an arc between a carbon electrode and the workpiece and welded using a wire electrode, as in oxyacetylene welding. Later, in the method developed by Zerener in 1889, an electric arc was created between two carbon electrodes and the arc was blown towards the part with the help of a magnetic coil between the two electrodes. In this method, a welding wire was also required. Also in 1889, Slavianoff developed the method that forms the basis of today's electric arc welding. MMA (Manual Metal Arc) welding is still used in many applications today [1-6].

However, due to the limited development of MMA welding, more emphasis has been given to R&D activities in MIG (Metal Inert Gas) / MAG (Metal Active Gas) [7-10], TIG (Tungsten Inert Gas) [11-13], LB (Laser Beam) welding [14], FS (Friction Stir) welding [15-17], and SAW (Submerged Arc Welding) methods [18]. MIG welding is carried out under inert gas (generally argon or helium) atmosphere. In this method, excellent melting properties can be achieved when working with high current density. The only difference between MIG and MAG welding is doing MAG method under CO₂ atmosphere instead of inert gas. In short, there is no need for additional welding equipment when welding under a CO₂ atmosphere [19]. Since the argon gas used in MIG welding is expensive, a lot of research carried out to use gases obtained at a lower cost, and it was determined that the most suitable gas was CO₂. On the other hand, the arc and molten metal are protected by a powder cover with a granular structure in the SAW method. SAW, which has high melting power, welding speed and is very suitable for welding various types of steels, is used extensively in the production of boilers, profiles, ships, pressure vessels and in fillet welding processes [20-22]. This method, like every method, is existing advantages and disadvantages. The main biggest disadvantage is that flux is applied externally and cannot penetrate directly into the weld pool. Various methods have been tried to be developed to prevent this defect and to provide advantages over MIG/MAG methods.

FCAW is one of these developed methods [23-26]. Academic and technical studies are continuing these products, which are obtained by filling the flux into the void area within the wire. In this method the flux, applied externally in SAW method is placed inside the wire, allowing the welding process to be carried out at higher current densities. In addition, another important effect of FCAW is that the greater penetration obtained in the MAG method and the faster and cleaner weld deposits obtained in MIG welding are provided in a single method more economically [27-31].

The most advanced applications of FCAW are hardfacings. There are still unknowns for hardfacing products, which have a wide range of usage, especially in the repair and maintenance of heavy equipment [32]. The reason for this uncertainty is the complex integration of the system and the limited database on the effect of metallurgical events on the mechanical properties of refractory metals that provide wear resistance. The main goal of this article is to evaluate the microstructure, hardness, and wear behavior in the controlled change of chromium, niobium, and tungsten elements, which increase the wear resistance in hardfacing applications. There are numerous articles in the literature in which the effect of refractory metals on welding ability was investigated by handling them in a controlled manner, but the originality of this study is being the first mechanical and metallurgically detailed investigation of the FCAW method, in which the elements were distributed homogeneously, and the SAW method, in which high-speed welding can be carried out [33-39].

In this article, details of a successfully completed TUBITAK project and a related PhD thesis were included, and it was aimed to present an original study in which the mentioned disadvantages of FCAW, due to too much spatter, and SAW methods, due to the inability to direct high amounts of alloying elements to the weld pool, were eliminated with a synergistic effect. While the amounts of iron, carbon, chromium, niobium, and wolfram were

changed in a controlled manner by keeping manganese and silicon constant, wear tests were carried out according to the hardness values obtained for these variants, microstructure controls and details of the data were conveyed to the readers. As a result, it was determined that the highest hardness and best wear resistance were obtained in the material sample with dendritic structures in the eutectic phase containing 35% chromium, 7% niobium and 3% wolfram.

Nomenclature

FCAW	Flux-Cored-Arc-Welding
FS	Friction-Stir
LB	Laser-Beam
MMA	Manuel-Metal-Arc welding
MAG	Metal-Active-Gas
MIG	Metal-Inert-Gas
SAW	Submerged-Arc-Welding
TIG	Tungsten-Inert-Gas

2. Material and Method

In this section, the preparation methods of welding consumables, the production of welding fluxes whose composition was determined according to different criteria, and the general conditions of flux-cored wire manufacture were included. The production of submerged arc welding fluxes was carried out in the Submerged Arc Welding Flux Production Line with a capacity of 10 tons/day within Oerlikon, and the agglomeration method was preferred in production. On this line, the dry mixtures, which can be changed according to the recipe, was prepared and mixed first, later dried at 100 ± 10 °C for 120 minutes, and last treated at 400-850 °C, depending on the type of recipe, for 2-5 hours, again depending on the type of recipe. After the physical, chemical, and metallurgical properties of the treated products were checked and approved, they were packaged in 25 kg packages and delivered to the laboratory. The prepared SAW products fulfilled the requirements of the EN 760 SA FB 1 55 AC. These regulations describe the characteristics of the powders and mean that fully basic agglomerated SAW flux. The Fig. 1. shows the SAW specimen used for the tests.



Fig. 1. SAW flux.

The production of FCAW wires was carried out in the FCAW Production Line within Oerlikon with a capacity of 15 tons/day. The FCAW production line is given schematically in Fig. 2. In this diagram, (a) represents the state of the strip material before it takes shape, (b) shows the plastic deformation that occurs to fill the strip with flux, (c) defines filling the strip with flux, (d) represents complete closure of the strip, (e) shows joining the tips, (f) defines completing the coverage of the diameter, and (g) represents the final form by thinning the walls.

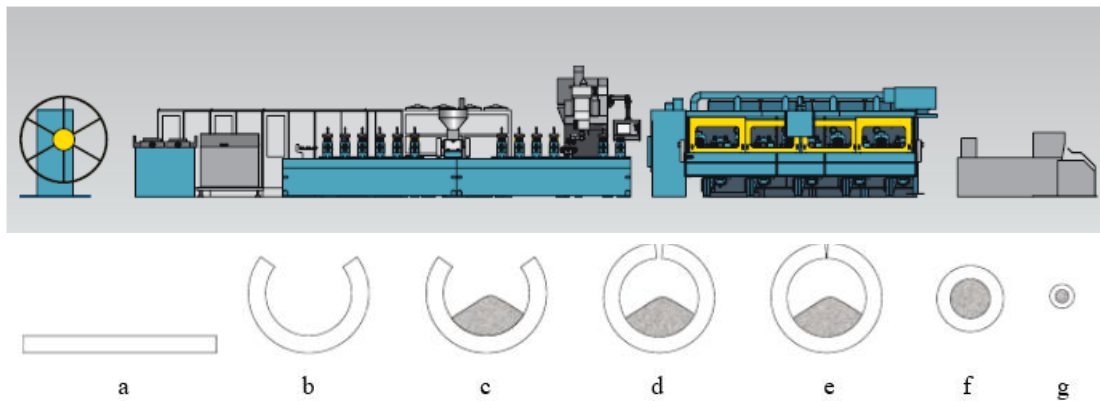


Fig. 2. Schematic representation of FCAW production line step by step.

Mechanical analyzes of FCAW and SAW combinations were carried out on S355JR (EN 10025-2) materials, and metallographic research of the parts on the same material was carried out. Welds on S355JR materials were made with Oerlikon SG100 Inverter Automatic SAW machine. The chemical composition of the weld deposits was defined by using Metavision 10008i optical emission spectrometer (Fig.3.). The microstructures of samples with

varying alloys were examined with Nikon LV150NA Straight Industrial Microscope. The hardness of the samples was measured with the Presi HZ 2-4 device. Wear loss values were determined by calculating the wear losses in the substrate material and the counter friction element, as specified in the ASTM G133-05 standard. Wear amounts were determined by testing weld metal samples, 10 mm high and 40 mm in diameter, prepared for five different samples, with a TRIBOtester Brand friction wear device (Fig. 3.). Tests were carried out at 25.000, 50.000, 75.000 and 100.000 cycles under 10N load. Ø 6 mm 100Cr6 steel balls were selected as counter friction elements (abrasives) in the tests. Moreover, 3.140 meters in the 25.000 cycle stage, and 12.560 meters for 100.000 cycle stage have been covered as the total sliding distance. Before and after each test stage, the steel balls and the weld metal sample were weighed with a precision balance and the wear information was recorded. The wear images of test samples were taken with JEOL-840 A model SEM electron microscope. XRD studies have been carried out to explain the composition effect on stable carbides that give hardness to the sample. Philips Expert Pro model XRD device was used with this purpose. X-Ray diffraction patterns have been clearly obtained with the help of CuK_α rays ($\lambda=0.15418$ nm).



Fig. 3. (a) optical emission spectrometer; (b) wear test device.

3. Results and Discussion

The weight percentages of alloying elements can be easily controlled with the combination of FCAW and SAW. The reason for this condition is that the metals placed in the flux in elemental form were trapped in the weld seam and there was no reaction that would lead to loss of these elements due to slag formation. Table 1 includes the weld metal analysis obtained with the FCAW and SAW combination, which has different chemical analysis values, and the hardness values obtained because of these analyses.

Table 1. Hardness values of products with different chemical analysis.

Element Percentage (%)	S-1	S-2	S-3	S-4	S-5
Carbon	0.1	1.0	3.0	7.0	7.0
Manganese	0.9	0.9	0.9	0.9	0.9
Silicon	0.7	0.7	0.7	0.7	0.7
Chromium	3.0	7.0	35.0	35.0	35.0

Niobium	-	-	-	7.0	7.0
Wolfram	-	-	-	-	3.0
Iron	Rest	Rest	Rest	Rest	Rest
Hardness	S-1	S-2	S-3	S-4	S-5
HR _c	31	59	60	63	67

It has been determined that increasing the amount of chromium and carbon increases the hardness very much, but increasing chromium alone does not increase the hardness much, and added niobium does not affect the hardness as much as tungsten (wolfram), but the main purpose of adding these elements is to increase the wear resistance of the products. For this reason, in the next stage, wear tests were carried out with the products listed in Table 1.

Fig. 4. shows the friction-wear test curves of the products whose hardness and analysis values are given in Table 1. Accordingly, sample 5, which has the highest hardness value, has the highest wear resistance; It is seen that niobium in sample 4 and tungsten in product sample 5 increase the wear resistance.

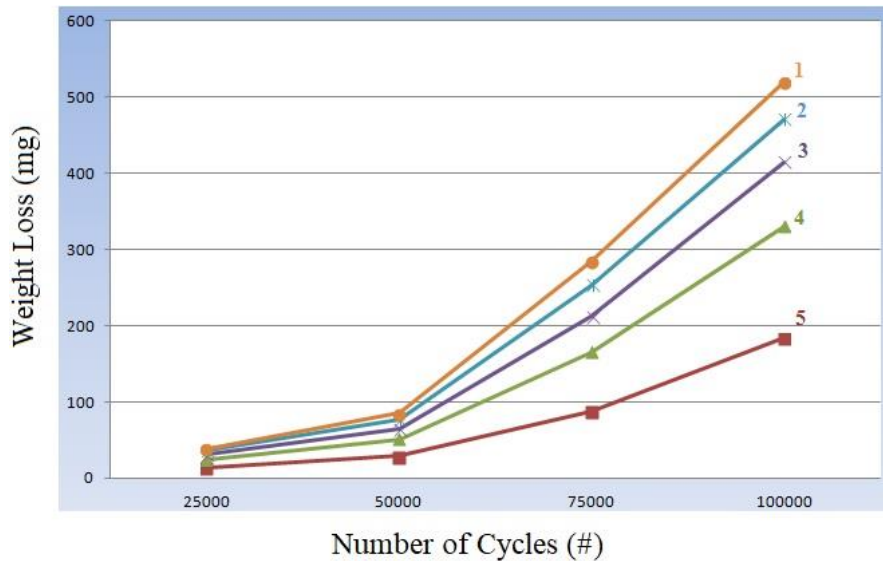


Fig. 4. Friction-wear test results in different chemical analyses.

The amounts of wear losses in milligrams depending on the number of cycles are given in Table 2 to make Fig. 4. more understandable. The difference in wear amounts between the samples increased with the increasing number of cycles. Wear rates of the samples were determined from the Table 2 for highest cycles as S-1: $4.77 \times 10^{-6} \text{ m}^3/\text{Nm}$, S-2: $3.41 \times 10^{-6} \text{ m}^3/\text{Nm}$, S-3: $2.39 \times 10^{-6} \text{ m}^3/\text{Nm}$, S-4: $1.70 \times 10^{-6} \text{ m}^3/\text{Nm}$, and S-5: $1.02 \times 10^{-6} \text{ m}^3/\text{Nm}$, respectively. The reason for this was the increased wear resistance of metallic wolfram and niobium due to their good mechanical properties. Similar results were also reported in the literature which clearly demonstrated the improvement of wear resistance by forming hard layers on the surface of Ni- and Co-based alloys by boriding [40-42].

Table 2. Weight loss amounts depending on the number of cycles.

Number of cycles during the friction-wear test	sample code and mass loss in milligram				
	S-1	S-2	S-3	S-4	S-5
25.000	14	10	7	5	3
50.000	88	72	54	32	18
75.000	274	241	207	166	92
100.000	514	486	415	321	188

The SEM micro images of the worn surfaces were investigated in Fig. 5. to analyze the wear behavior of the samples. It was determined that the wear marks of sample 1 were quite frequent and narrow. It was obtained that there was 14 mg wear loss under 10 N load with 3.140 m sliding distance. However, it was determined that sample 2 had wider and more spaced than sample 1 by considering the wear surfaces. On the other hand, it was observed that the wear marks of sample 3 were narrower than sample 2, and when compared to the hardness value, it was determined that this was proportional to the fact that it was much higher than sample 1. Moreover, much finer wear traces have been observed in the SEM image of sample 4. In the SEM image of sample 5, the wear marks were not quite deep, and it is seen that there was superficial wear on the material.

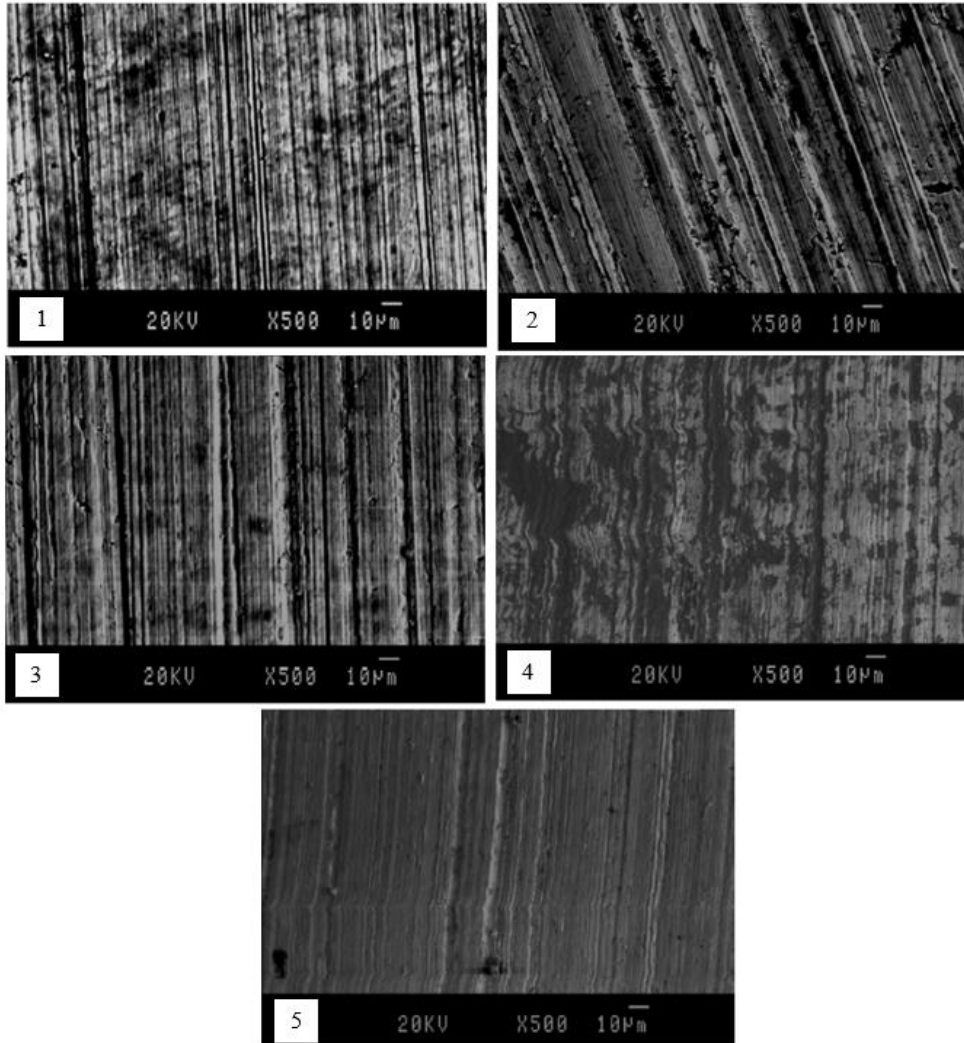


Fig. 5. SEM images of the samples after wear test.

The XRD analysis performed before and after the test to determine the effect of the phases on the wear resistance of the sample showing the highest wear resistance is shown in Fig. 6. This figure represents the XRD patterns obtained before (a) and after (b) wear test. The first striking feature in comparing the XRD patterns was the disappearance of alpha iron and chromium carbide phases after the wear test. Alpha iron is a body-centered cubic allotrope, and it can only dissolve small concentrations of carbon. For this reason, it is soft and able to quickly separate from the material surface in the wear test. The width of the chromium carbide peak provides information about the grain size of the particles. Therefore, big chromium carbide particles' separation from the material during the initial wear of the test explains the disappearance of chromium carbide peak. On the other hand, since alpha iron removed from the system and gamma iron remains in the weld deposit in a more stable state, the intensity of gamma iron's peak increased after the wear test. The niobium and wolfram carbides, which increase the hardness and especially the wear resistance of the samples, show the lowest level of the peaks, because of their less amount in the

total system. They disappeared after the wear test due to fulfilling their duties on the wear and abrasion characteristics.

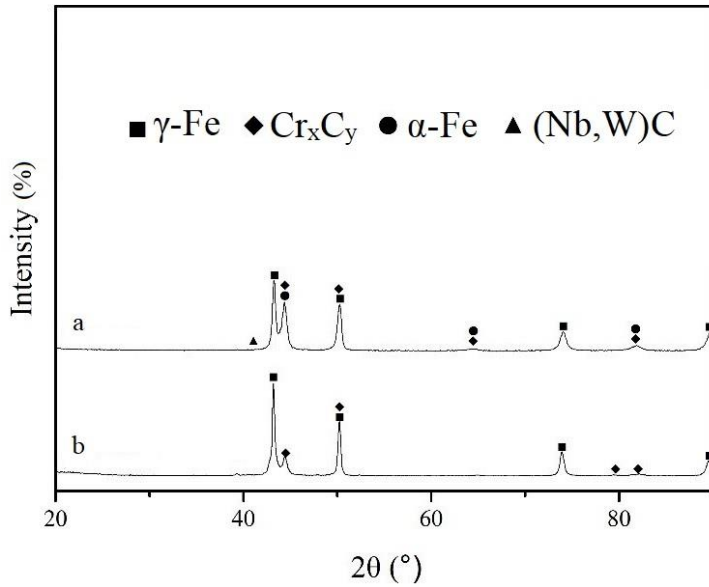


Fig. 6. XRD patterns before (a) and after (b) wear test of the sample with the highest hardness and wear resistance.

The difference in chemical analyses not only affects the mechanical properties at the macro level, but also naturally affects the structure at the micro level. For this reason, the microstructures of all products were examined, and the microstructure of sample 1 at 100x magnification is shown in Fig 7., and the martensitic structure is suited to hardfacings resistant to wear by impact, compression, and slight abrasion [43].

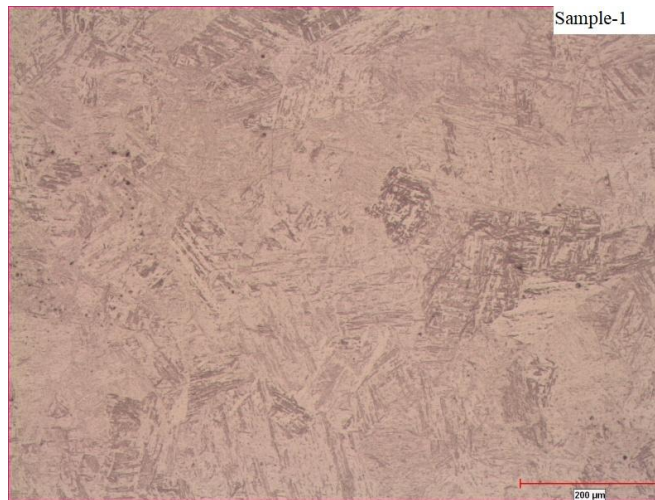


Fig. 7. Microstructure of sample 1.

As seen in Fig. 8., chromium carbides were sparsely distributed in the iron matrix but homogeneously without accumulation. This homogeneous distribution brings a huge advantage by ensuring that the hardness and wear properties of the weld metal are transmitted homogeneously to the construction. This includes also martensitic structure, but carbides are observed more clearly, that makes this sample suited in impact and pressure stress situations, but machining of the weld deposit is available only by grinding [44].

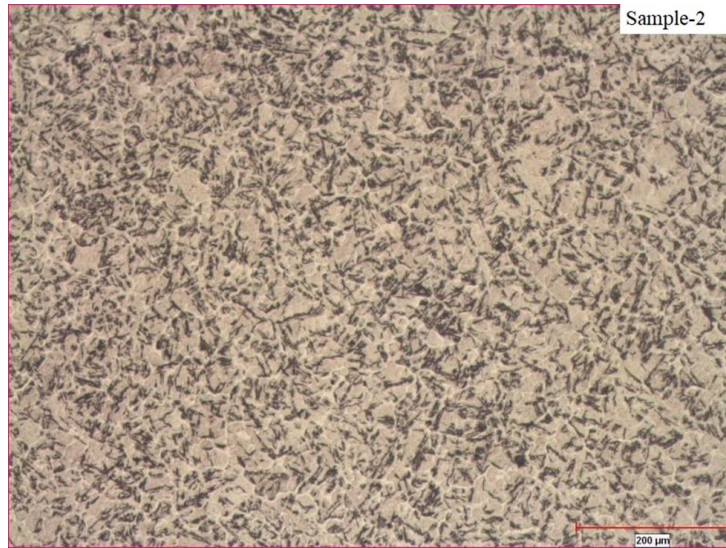


Fig. 8. Microstructure of sample 2.

In Fig. 9., the homogeneous distribution of increasing chromium carbides in the microstructure is clearly detected. It is observed that the chromium carbide density in the grains has increased compared to sample number 1. This increase in the chromium carbide density within the grains is the difference's reason in the hardness values between samples number 1 and 2. The high chromium carbides alloyed hardfacing sample is used for surfacing on parts made of carbon steel, cast steel or Mn-steel, which are subject to grinding wear, such as idlers, digging buckets, digging teeth, ploughshares, mixing wings and conveyor screws [45].

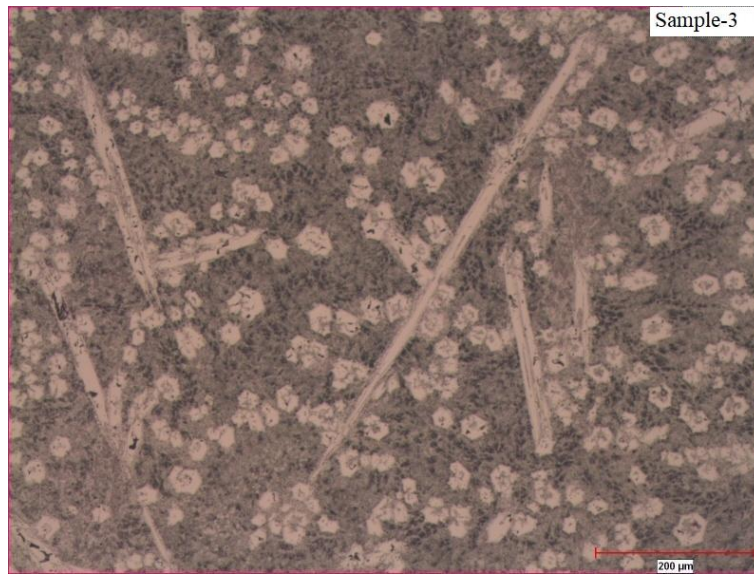


Fig. 9. Microstructure of sample 3.

Graphite formation resulting from increased carbon in the metal matrix in sample number 4 was detected in Fig. 10. The increased amount of carbon did not directly affect the hardness but provided an advantage in wear resistance compared to sample number 3. It is suited for highly wear resistant claddings on parts subject to strong grinding abrasion combined with medium impact, such as conveyor screws, scraper blades, digging teeth, mixer wings, sand pumps [46].

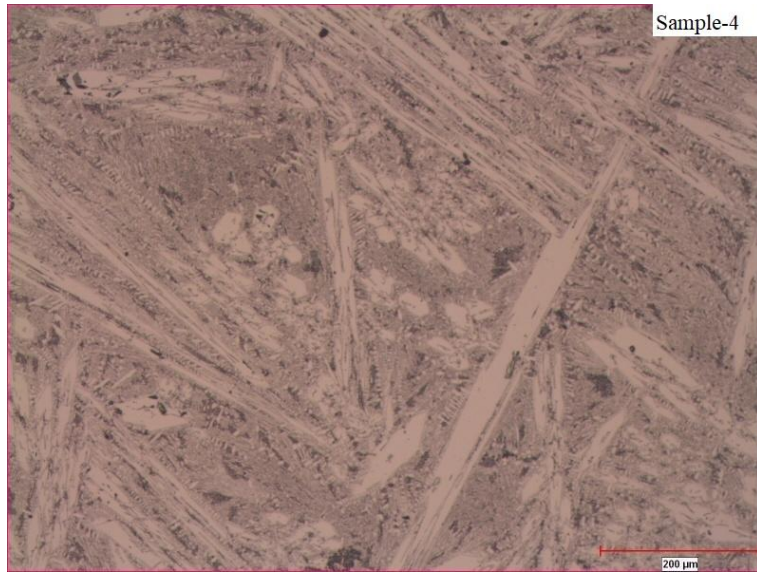


Fig. 10. Microstructure of sample 4.

The increased amount of carbon in sample 5 compared to sample 4 increased the ratio of graphite in the matrix, and the added niobium formed carbides within the grains, creating the eutectic structure. This formation can be seen clearly in the microstructure in Fig. 11.

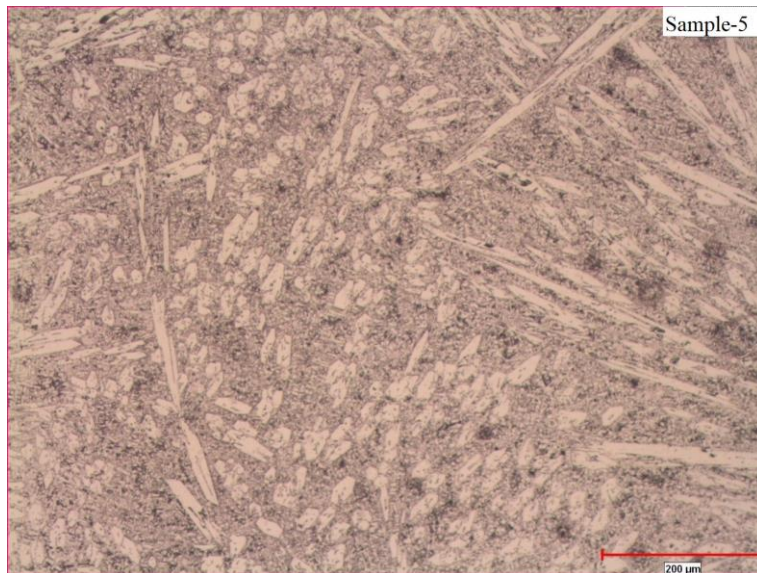


Fig. 11. Microstructure of sample 5.

It was determined that the eutectic phase was formed in sample number 5, resulting from increase in carbon content and the high melting temperature of wolfram added to sample number 4, and this microstructure is shown in Fig. 11. The presence of these structures brings high macro hardness and micro wear resistance. This is suited for highly abrasion resistant claddings on parts subject to extreme sliding mineral abrasion, also at elevated temperatures in the range of 500°C. Elements containing quite high carbides, such as wolfram, cause high abrasion resistance. Main application fields are surfacing on earth moving equipment, working parts in the brick, cement industry or in steel mills for radial breakers and revolving-bar screens of sintering plants [47].

The Fig.12 shows the SEM image comparison of sample 5 before and after the wear test, where small carbides in the metal matrix are visible. In sample 5 compared to other samples, more carbides in the matrix structure and appears to exhibit a more homogeneous distribution. In the SEM image of the same sample, only the abrasive counterpart left the material in fine scratches. The wear marks are not deep, and superficial wear on the material appears to occur.

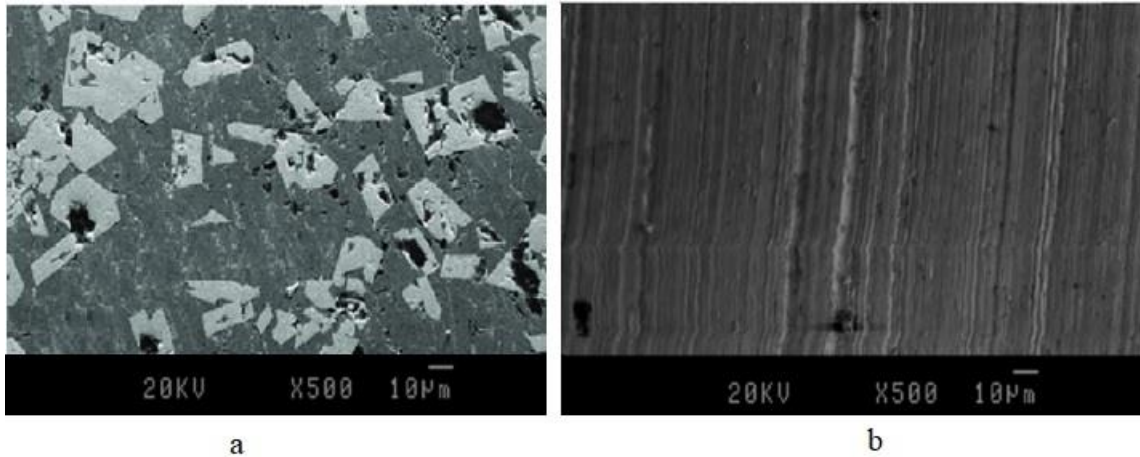


Fig. 12. SEM microstructure of sample 5 before (a) and after (b) wear test.

4. Conclusion

It has become possible to obtain weld fillers with the desired chemical analysis by using the production technique developed with the combination of FCAW and SAW. In this way, an advantageous method has been developed by adjusting the chemical composition homogeneously as desired. The advantage of this process has been clearly observed, especially in refractory metal-based welding fillers due to its high wear resistance. Furthermore, with the increase in the hardness of the samples then their wear resistance also increases, and it has been clearly determined that chemical analyses directly affect the microstructures. While the increasing amount of chromium carbide clearly changed the microstructure, the addition of other refractory metals enabled the formation of eutectic and dendritic structure. Finally, it was determined that the highest hardness and best wear resistance were obtained in the material sample containing dendritic structures in the eutectic phase containing 35% chromium, 7% niobium and 3% wolfram. In conclusion, the problems of low efficiency in FCAW and alloying in SAW were solved by this combination method. In this way, it is possible to prepare recipes that provide the chemical content requested by the end user.

Acknowledgements

This research includes a part of a successfully completed PhD thesis with the support of TÜBİTAK-TEYDEB project number 3130488. I would like to thank TÜBİTAK, Ege University, and Oerlikon for their contributions. However, I would like also to thank to Dikkan R&D Center for the financial support it provided within the scope of the award regulations.

References

- [1] Jamrozik, W., and Jacek G. "Assessing MMA welding process stability using machine vision-based arc features tracking system." *Sensors* 21.1, 2020, 84, <https://doi.org/10.3390/s21010084>.
- [2] Shankhwar, K., and Shana S. "Finite element analysis results visualization of manual metal arc welding using an interactive mixed reality-based user interface." *Journal of Manufacturing Processes* 93, 2023, pp. 153-161, <https://doi.org/10.1016/j.jmapro.2023.03.001>.
- [3] Nalle, C.Y.A., Aditya, M. B., Putra, F. G. A. P., Nalle, M. N., and Sumarta, R. P. "Analysis of Electric Current on Aluminum Plate Welding Using MMA (Manual Metal Arc) Method." *Proceeding of International Conference on Artificial Intelligence, Navigation, Engineering, and Aviation Technology (ICANEAT)*. Vol. 1. No. 1. 2024, Vol. 1, No. 1, pp. 144-146, <https://doi.org/10.61306/icaneat.v1i1.222>.
- [4] Sitorus, M. B. H. "Effect of welding heat input on the corrosion rate of carbon steel MMA welding." *International journal of innovation in mechanical engineering and advanced materials*, 3(1), 2021, pp. 26-31,
- [5] Kóvágó, C., Szekeres, B., Szűcs-Somlyó, É., Májlinger, K., Jerzsele, Á., and Lehel, J. "Preliminary study to investigate the distribution and effects of certain metals after inhalation of welding fumes in mice." *Environmental Science and Pollution Research*, 29(32), 2022, pp. 49147-49160, <https://doi.org/10.1097/00043764-198005000-00007>.
- [6] Faqih, I. A., Ma'arif, S., and Sukarjo, H. "The effect of current variation on mma welding to mechanical properties and microstructure of mild steel." In *Proceeding International Conference on Materials Science and Technology*, Vol. 1, No. 1, 2019, pp. 21-26.
- [7] Silva, R. H. G., Dutra, J. C., and Gohr Jr, R. "Scientific and technological fundamentals for the development of the controlled short-circuiting MIG/MAG welding process: a review of the literature. Part 2 of 3. Metal droplet formation, shield gases, penetration mechanisms, heat input and economical aspects." *Welding International*, 23(2), 2019, pp. 141-149, <https://doi.org/10.1080/09507110802349700>.
- [8] Şenol M. and Çam G., "Investigation into microstructures and properties of AISI 430 ferritic steel butt joints fabricated by GMAW", *International Journal of Pressure Vessels and Piping*, 2023, Vol. 202, Article Number: 104926. <https://doi.org/10.1016/j.ijpvp.2023.104926>.
- [9] Ezer M. and Çam G., "A Study on microstructure and mechanical performance of gas metal arc welded AISI 304L joints", *Materialwissenschaft und Werkstofftechnik (Material Science and Engineering Technology)*, 2022, Vol. 53, Iss. 9, pp. 1043-1052. <https://doi.org/10.1002/mawe.202200050>.
- [10] Serindağ H.T. and Çam G., "Microstructure and mechanical properties of gas metal arc welded AISI 430/AISI 304 dissimilar stainless steels butt joints", *Journal of Physics: Conference Series*, 2021, Vol. 1777, Paper No: 012047. <https://doi.org/10.1088/1742-6596/1777/1/012047>.
- [11] Serindağ H.T. and Çam G., "Multi-pass butt welding of thick AISI 316L plates by gas tungsten arc welding: Microstructural and mechanical characterization", *International Journal of Pressure Vessels and Piping*, 2022, Vol. 200, Article Number: 104842. <https://doi.org/10.1016/j.ijpvp.2022.104842>.
- [12] Serindağ H.T. and Çam G., "Characterizations of microstructure and properties of dissimilar AISI 316L/9Ni low alloy cryogenic steel joints fabricated by GTAW", *Journal of Materials Engineering and Performance (JMEPEG)*, 2023, Vol. 32, pp. 7039-7049. <https://doi.org/10.1007/s11665-022-07601-x>.
- [13] Serindağ H.T., Tardu C., Kirçiçek I.Ö., Çam G., "A study on microstructural and mechanical properties of gas tungsten arc welded thick cryogenic 9% Ni alloy steel butt joint", *CIRP Journal of Manufacturing Science and Technology*, 2022, Vol. 37, pp. 1-10. <https://doi.org/10.1016/j.cirpj.2021.12.006>.
- [14] Çam G., Yeni Ç., Erim S., Ventzke V., and Koçak M., "Investigation into properties of laser welded similar and dissimilar steel joints", *Sci. Technol. Weld. Join.*, 1998, Vol. 3 (Iss. 4), pp. 177-189. <https://doi.org/10.1179/stw.1998.3.4.177>.
- [15] Küçükömeroğlu T., Aktarer S.M., İpekoğlu G., and Çam G., "Investigation of mechanical and microstructural properties of friction stir welded dual phase (DP) steel", *IOP Conf. Series: Materials Science and Engineering*, 2019, Vol. 629, Paper No: 012010. <https://doi.org/10.1088/1757-899X/629/1/012010>.
- [16] İpekoğlu G., Küçükömeroğlu T., Aktarer S.M., Sekban D.M., and Çam G., "Investigation of microstructure and mechanical properties of friction stir welded dissimilar St37/St52 joints", *Materials Research Express*, 2019, Vol. 6, Iss. 4, Article Number: 046537. <https://doi.org/10.1088/2053-1591/aafb9f>.
- [17] Küçükömeroğlu T., Aktarer S.M., İpekoğlu G., and Çam G., "Microstructure and mechanical properties of friction stir welded St52 steel joints", *International Journal of Minerals, Metallurgy and Materials*, 2018, Vol. 25, Iss. 12, pp. 1457-1464. <https://doi.org/10.1007/s12613-018-1700-x>.
- [18] Coetsee, T., and De Bruin, F. "A Review of the Thermochemical Behaviour of Fluxes in Submerged Arc Welding: Modelling of Gas Phase Reactions." *Processes*, 11(3), 2023, p-658, <https://doi.org/10.3390/pr11030658>.
- [19] Jia, Y., Huang, N., Zhang, J., Xiao, J., Chen, S., and Huang, W. "Current research status and prospect of metal transfer process control methods in gas metal arc welding." *The International Journal of Advanced Manufacturing Technology*, 128(7-8), 2023, 2797-2811, <https://doi.org/10.1007/s00170-023-12028-2>.

- [20] Singh, A., and Singh, R. P. "A review of effect of welding parameters on the mechanical properties of weld in submerged arc welding process." *Materials Today: Proceedings*, 26, 2020, 1714-1717, <https://doi.org/10.1016/j.matpr.2020.02.361>.
- [21] Coetsee, T. "Phase chemistry of Submerged Arc Welding (SAW) fluoride based slags." *Journal of Materials Research and Technology*, 9(5), 2020, 9766-9776, <https://doi.org/10.1016/j.jmrt.2020.06.069>.
- [22] Özkan, E. "Investigation of Metallurgical Characterization and Mechanical Behaviour for Submerged Flux Cored Arc Welding Process." *Çelik Araştırma ve Geliştirme Dergisi*, 4(1), 2023, pp.1-9.
- [23] Mohamat, S. A., Ibrahim, I. A., Amir, A., and Ghalib, A. "The effect of flux core arc welding (FCAW) processes on different parameters." *Procedia Engineering*, 41, 2012, pp.1497-1501, doi: 10.1016/j.proeng.2012.07.341.
- [24] Świerczyńska, A., Varbai, B., Pandey, C., and Fydrych, D. "Exploring the trends in flux-cored arc welding: scientometric analysis approach." *The International Journal of Advanced Manufacturing Technology*, 130(1), 2024, 87-110, <https://doi.org/10.1007/s00170-023-12682-6>.
- [25] Costa, P. S., Altamirano-Guerrero, G., Ochoa-Palacios, R. M., Reséndiz-Flores, E. O., Guía-Hernández, L. A., and Ramírez-Luna, L. E. "Optimization of welding parameters in underwater wet FCAW on a structural steel using support vector regression and sequential quadratic programming." *The International Journal of Advanced Manufacturing Technology*, 121(5), 2022, pp. 4225-4236, <https://doi.org/10.1007/s00170-022-09584-4>.
- [26] da Silva, M. S., Souza, D., de Lima, E. H., Bianchi, K. E., and Vilarinho, L. O. "Analysis of fatigue-related aspects of FCAW and GMAW butt-welded joints in a structural steel." *Journal of the Brazilian Society of Mechanical Sciences and Engineering*, 42(1), 2020, 67, <https://doi.org/10.1007/s40430-019-2142-8>.
- [27] Dhas, J. E. R., Lewise, K. A. S., and Laxmi, G. "Submerged arc welding process parameter prediction using predictive modeling techniques." *Materials Today: Proceedings*, 64, 2022, 402-409, <https://doi.org/10.1016/j.matpr.2022.04.757>.
- [28] Wahidi, S. I., Oterkus, S., and Oterkus, E. "Robotic welding techniques in marine structures and production processes: A systematic literature review." *Marine Structures*, 95, 2024, 103608, <https://doi.org/10.1016/j.marstruc.2024.103608>.
- [29] Kumar, R., Biswas, S., Das, S., and Ershad, M. "Experimental Investigation of Welding Parameters on Mild Steel Using Metal Active Gas Welding." *Journal of Mines, Metals & Fuels*, 71, 2023, 11.
- [30] Özkan, E. "Endüstriyel Uygulamalar İçin Gerekli Mekanik ve Metalurjik Özelliklere Sahip Tozaltı Kaynak Tozu ve Özlü Tel Kombinasyonunun Karakterizasyonu" *completed PhD Thesis, Ege Üniversitesi Fen Bilimleri Enstitüsü*, 2015, İzmir.
- [31] Neves, A. C., Sartori M. J. R., Corrêa, C. A., and Trevisani O. E. F. "Study of arc welding stability in flux cored arc welding process and pulsed continuous current." *Welding International*, 35(4-6), 2021, pp. 158-169, <https://doi.org/10.1080/09507116.2021.1971936>.
- [32] Xu, S., Han, Y., Jia, C., Maksymov, S., Kakhovskiy, M., and Wu, C. "Numerical modeling of coupled arc plasma, metal transfer and molten pool evolution for underwater flux-cored arc welding." *The International Journal of Advanced Manufacturing Technology*, 123(7), 2022, pp. 2605-2622, <https://doi.org/10.1179/stw.2001.6.6.387>.
- [33] Xu, S., Han, Y., Jia, C., Maksymov, S., and Wu, C. "3D non-axisymmetric numerical analysis of droplet oscillation, arc drifting and molten pool evolution for underwater wet FCAW." *Journal of Materials Processing Technology*, 320, 2023, 118101, <https://doi.org/10.1016/j.jmatprotec.2023.118101>.
- [34] Gürol, U., Çoban, O., Coşar, İ. C., and Koçak, M. "Effect of the notch location on the Charpy-V toughness results for robotic flux-cored arc welded multipass joints." *Materials Testing*, 64(9), 2022, pp. 1278-1289, <https://doi.org/10.1515/mt-2022-0113>.
- [35] Kumar, A., and Vijayakumar, P. "Comparison of Weld Built-up by FCAW and MIG Welding on Damaged Low Cr-Mo Alloy Steel Tube in Boiler Application." *International Journal of Science and Research Archive*, 8(2), 2023, pp. 492-505, <https://doi.org/10.30574/ijrsra.2023.8.2.0243>.
- [36] Balasubramanian, K., Vikram, R., Sambath, S., Sowrirajan, M., Arunachalashiva, M., Abhijith, P. V., and Deepak, D. "Optimization of flux cored arc welding parameters to minimize the dilution percentage of AISI 316L stainless steel cladding on mild steel." *International Journal on Interactive Design and Manufacturing (IJIDeM)*, 2023, pp. 1-11, <https://doi.org/10.1007/s12008-023-01487-2>.
- [37] Costa, P. S., Altamirano-Guerrero, G., Ochoa-Palacios, R. M., Ramirez-Luna, L. E., Guía-Hernández, L. A., de Luna-Jiménez, I. F., and Buendía-Carrillo, A. "Study of surface porosity of underwater wet welding employing FCAW-S process in structural steels." *MRS Advances*, 8(2), 2023, pp. 34-38, <https://doi.org/10.1557/s43580-022-00477-y>.
- [38] Sharma, S., and Singh, L. "A Review on the Flux Cored Arc Welding through Process Parameter.", *International Journal of Scientific Research in Mechanical and Materials Engineering*, 47, 2023, pp. 777-780.
- [39] Oo, H. Z., and Muangjunburee, P. "Improving microstructure and hardness of softening area at HAZ of thermite welding on rail running surface." *Materials Today Communications*, 34, 2023:105485, <https://doi.org/10.1016/j.mtcomm.2023.105485>.
- [40] Girişken İ. and Çam G., "Characterization of microstructure and high-temperature wear behavior of pack-borided Co-based Haynes 25 superalloy", *CIRP Journal of Manufacturing Science and Technology*, 2023, Vol. 45, pp. 82-98. <https://doi.org/10.1016/j.cirpj.2023.06.012>.
- [41] Günen A., Gürol U., Koçak M., and Çam G., "Investigation into the influence of boronizing on the wear behavior of additively manufactured Inconel 625 alloy at elevated temperature", *Progress in Additive Manufacturing*, 2023, Vol. 8, pp. 1281-1301. <https://doi.org/10.1007/s40964-023-00398-8>.
- [42] Girişken İ. and Çam G., "Boriding of Co-based Haynes 25/L-605 superalloy", *Journal of Characterization*, 2022, Vol. 2, Iss. 3, pp. 206-219. <https://doi.org/10.29228/JCHAR.66388>.
- [43] Srikarun, B., Oo, H. Z., and Muangjunburee, P. "Influence of different welding processes on microstructure, hardness, and wear behavior of martensitic hardfaced cladding." *Journal of Materials Engineering and Performance*, 30(12), 2021, pp. 8984-8995, <https://doi.org/10.1007/s11665-021-06109-0>.
- [44] Rojacz, H., Katsich, C., Kirchgäßner, M., Kirchmayer, R., & Badisch, E. "Impact-abrasive wear of martensitic steels and complex iron-based hardfacing alloys." *Wear*, 492, 2022, 204183 <https://doi.org/10.1016/j.wear.2021.204183>.

- [45] Tippayasam, C., Taengwa, C., Palomas, J., Siripongsakul, T., Thaweechai, T., and Kaewvilai, A. "Effects of flux-cored arc welding technology on microstructure and wear resistance of Fe-Cr-C hardfacing alloy." *Materials Today Communications*, 35, 202, 105569, <https://doi.org/10.1016/j.mtcomm.2023.105569>.
- [46] Oo, H. Z., and Muangjumburee, P. "Hardfacing of thermite welded rail by flux-cored arc welding." *Wear*, 2024, 205314. <https://doi.org/10.1016/j.wear.2024.205314>.
- [47] Wijayanto, B., and Ringan, T. K. "The Effect of Welding Current with Smaw Process for Medium Carbon Steel Hardfacing On Micro Structure, Hardness, and Cracking." *Jurnal Teknik dan Manajemen p-ISSN*, 2(2), 2022, <https://doi.org/10.47577/technium.v4i5.6674>.